UNIVERSIDAD COMPLUTENSE DE MADRID
FACULTAD DE CIENCIAS FÍSICAS

TESIS DOCTORAL

Estudio del acoplamiento entre dinámica y química en la formación de una estrella de masa solar

Study of the chemo-dynamical coupling in the formation of solar-like stars

MEMORIA PARA OPTAR AL GRADO DE DOCTOR

PRESENTADA POR

David Gerardo Navarro Almaida

Directores

Asunción Fuente Juan
Pablo Riviere Marichalar

Madrid

UNIVERSIDAD COMPLUTENSE DE MADRID

Facultad de Ciencias Físicas
Departamento de Física de la Tierra y Astrofísica

DISSERTATION

Estudio del acoplamiento entre dinámica y química en la formación de una estrella de masa solar

Study of the chemo-dynamical coupling in the formation of solar-like stars

A thesis submitted in partial fulfillment of the requirements for the DEGREE OF DOCTOR OF PHILOSOPHY IN ASTROPHYSICS by

David Gerardo Navarro Almaida

Supervisors

Asunción Fuente Juan
Pablo Riviere Marichalar

Estudio del acoplamiento entre dinámica y química en la formación de una estrella de masa solar

Study of the chemo-dynamical coupling in the formation of solar-like stars

Observatorio Astronómico Nacional (OAN)
Instituto Geográfico Nacional (IGN)

Facultad de Ciencias Físicas
Departamento de Física de la Tierra y Astrofísica

A thesis submitted in partial fulfillment of the requirements for the DEGREE OF DOCTOR OF PHILOSOPHY IN ASTROPHYSICS by

David Navarro Almaida

SUPERVISORS
Asunción Fuente Juan
Pablo Riviere Marichalar

TUTOR
Nicolás Cardiel López

Agradecimientos

> "La gratitud no sólo es la más grande de las virtudes, sino que engendra todas las demás"
>
> Marco Tulio Cicerón

Es típico pensar que el éxito en cualquier empeño depende únicamente del trabajo duro y el esfuerzo. Si bien son importantes, el azar también juega un nada despreciable papel y, dado que he tenido la suerte de terminar esta tesis, no se me ocurre mejor manera de reconocer dicha suerte que mostrando gratitud hacia todas las personas que me han acompañado a lo largo de este camino.

Esta tesis ha sido realizada en el Instituto Geográfico Nacional y quiero dar las gracias a esta institución por haberme ofrecido la oportunidad de poder dedicarme a su redacción durante estos cuatro años. Mi más sincero agradecimiento a mis directores de tesis Asunción Fuente y Pablo Rivière por abrirme los ojos a una disciplina científica tan fascinante y por su apoyo moral durante todo este tiempo. Agradezco la ayuda y el apoyo del grupo GEMS, al resto de colegas en el Observatorio Astronómico Nacional y, especialmente, a María y Axel, mis compañeros de fatigas. Quiero además agradecer la amabilidad y la calidez del personal del Observatorio, que me han hecho sentir como en casa.

A día de hoy es impensable hacer ciencia solo, y en este sentido quiero agradecer la labor de todos los colaboradores que han hecho este texto posible. Mi agradecimiento a Valentine Wakelam por su hospitalidad en el Laboratorio de Astrofísica de Burdeos y su excelente labor como colaboradora, a Benoît Commerçon por su inestimable y paciente ayuda durante mi estancia en Lyon y al personal del telescopio de IRAM 30m en Pico Veleta, que hacen de las observaciones una experiencia a querer repetir. Muchas gracias a Aina Palau y Gemma Busquet por aceptar la revisión y evaluación de este texto. Cuentan también con mi gratitud mi tutor, Nicolás Cardiel, la Prof. Elisa de Castro, David Montes y Jesús Gallego de la Universidad Complutense de Madrid por sus sugerencias para la presentación de la tesis y su ayuda a la hora de tramitar el depósito de la tesis y su defensa.

Todo esto no hubiera sido posible sin algo de descanso. Gracias a Álvaro, Daniel, Félix, José y Rafa por sacarme de casa cuando claramente lo necesitaba. Gracias a Bruno por estar ahí durante todo este tiempo. Digo yo que esto se merece un festival de verano por lo menos, ¿no?

Agradezco de corazón el apoyo de mi familia, sin la que nada de esto hubiera pasado:

- Agradezco a mis tios José Luis y Emilio el interés y la motivación para seguir con esto y su apoyo y compañia en momentos muy duros.

- A Raquel, por llenar de alegría y risas (y perros) cualquier momento por difícil que sea.
- A mi hermano, Sergio, por apoyarme, estar siempre ahí y entenderme como nadie.
- A mi madre, porque al final el trabajo duro y el esfuerzo darían igual si no fuera por ti. Gracias por todo, absolutamente todo. Esta tesis es también obra tuya.
- A mi padre y a mi abuela. Habéis formado parte de momentos muy importantes antes y durante los cuatro años de redacción de esta tesis. No todo es buena suerte, y el azar ha querido que no la podáis ver acabada. Va por vosotros.

Contents

Summary

Astrochemistry is the study of the chemical composition of interstellar objects and the chemical reactions occurring in space. How species interact have a great impact in the process of star formation. In fact, determining aspects for the dynamical behavior of interstellar matter are the gas cooling rate and the ionization degree, highly influenced by the gas chemistry and molecular abundances. Indeed, efficient gas cooling diminishes thermal support against gravity, leading to fragmentation and collapse of molecular filaments into pre-stellar cores. Here, elemental depletions of Carbon (C) and Oxygen (O) are key to determine the cooling rate of the gas, as CO and CII are the main coolants in molecular clouds. The ionization fraction of the gas is involved in gas dynamics as well, since it controls the coupling of the gas with the magnetic fields. Magnetic fields thus drive the dissipation of turbulence and angular momentum transfer in the cloud collapse and the dynamics of accretion disks. The ionization fraction of the gas is, in absence of other ionization agents like X-rays, UV photons, and shocks, proportional to ζ_{H_2}, the cosmic-ray ionization rate for H_2 molecules. Other factors that affect the ionization degree of the gas are the molecular abundances and elemental depletion factors. Towards the surface of a cloud ($A_v < 4$ mag), Carbon is the main donor of electrons. Deeper into the cloud however, in the range $A_v \sim 4-7$ mag, Sulphur (S) becomes the main donor of electrons. This range of extinctions encompasses a large fraction of the molecular cloud's mass.

Given the importance of molecular abundances and elemental depletions in the star formation process, our goal is to determine the elemental abundances and, hence, the gas ionization degree in a sample of prototypical starless cores in TMC 1 and Barnard 1 molecular filaments. In a second step we use these parameters to model the chemistry and dynamics of a selected sample of pre-stellar cores in TMC 1 molecular cloud: TMC 1-C and TMC 1-CP. By observing cores at different evolutionary stages within the same cloud, we have a deeper insight into the chemical evolution of these cores, allowing a precise description of the collapse of these objects.

Our methodology combines high quality observations with state-of-the-art chemical models to determine the elemental abundances, molecular depletion, and the gas ionization fraction at different positions belonging to the TMC 1 filament. We characterize the physical properties, density, and temperature of the different positions across the filament, covering a wide range of visual extinctions, using millimeter observations of density tracers. The emission of a selection of key molecules in the chemistry of molecular clouds that includes CO, HCO^+, CS, SO, HCN, and N_2H^+, is used to estimate their fractional abundances. Information about the abundances of these molecules allows the chemical modeling of the region. We use a grid of chemical models with varying values of the elemental abundances of Car-

bon, Oxygen, Nitrogen, and Sulfur, as well as the ionization degree of the gas, the C/O ratio, and the cosmic-ray ionization rate in the translucent gas of the TMC 1 filament. Even in this translucent regime, sulfur is found to be depleted onto grains, due to the attraction forces between ionized sulfur atoms and the negatively charged dust grains (Chapter 4).

Despite its important role in setting the ionization degree of the gas, the determination of the sulfur depletion inside molecular clouds is challenging. Our study suggests a depletion of about an order of magnitude compared to its estimated cosmic abundance in the diffuse gas, but little is known about where the missing sulfur is. This is known as the Sulfur depletion problem. Due to the high hydrogen abundances and the mobility of hydrogen in the ice matrix, sulfur atoms impinging in interstellar ice mantles are expected to form H_2S preferentially. There is no direct evidence of this and there are only upper limits to the solid H_2S abundance. OCS is the only S-bearing molecule unambiguously detected in ice mantles because of its large band strength in the infrared. A possibility would be that most of the sulfur is locked in atomic sulfur in the gas phase. Unfortunately, the direct observation of this atom is difficult and, until now, has only been detected in some bipolar outflows using the infrared space telescope Spitzer. Given the importance of the H_2S molecule in the Sulfur depletion problem and the relevance of gas and grain chemical reactions, we explore the relationship between the gas-phase and grain-phase chemistry, as well as the ice composition of the grain ices, the abundance of H_2S, and its formation pathways. This investigation starts with the physical description of well-known pre-stellar cores in the star-forming regions of Taurus and Perseus. The moderately dense areas of these cores are characterized in density and temperature using molecular tracers of these quantities. Then, the chemistry in the grain phase is explored with the estimation of the gas-phase abundance of H_2S across the sample, as this molecule is only efficiently formed on grain surfaces. Once the H_2S is formed through grain-phase reactions, it must be desorbed. The chemical desorption mechanism is investigated with the aid of state-of-the-art gas-grain chemical models to conclude that H_2S is mainly released via chemical desorption. Furthermore, its gas-phase abundance is sensitive to variations in the chemical desorption efficiency due to changes in the grain surface composition. The gas-grain chemical models also confirm the amount of Sulfur depletion obtained in the diffuse gas of the molecular cloud (Chapter 5).

Once the elemental abundances and the chemistry of the Taurus cores are constrained, we carry out an evolutionary and dynamical study. In fact, the age of the objects of the interstellar medium is an important factor to understanding their chemistry, as the changing physical conditions through the evolution of a pre-stellar object lead to changes in their chemical properties. The analysis of the chemical features of an object thus provides information about its evolutionary stage. We analyze the chemical differences of two pre-stellar cores belonging to the same filament in TMC 1, which can be explained by their different evolutionary stage: TMC 1-C and TMC 1-CP. In dense and cold cores, the depletion of molecules like CO leads to the enhancement of H_2D^+, which is a very efficient deuteration agent through ion-molecule reactions at low temperatures. We analyze the emission of deuterated molecules such as N_2D^+, DNC, and DCN, and molecules like N_2H^+ and CS to trace the densest gas in these pre-stellar cores and estimate their abundances. We then derive the deuterium fraction in these cores, which is linked to the chemical age and, therefore, their evolutionary stage. The comparison between observations and chemical model

predictions allows us to constrain key parameters in the chemical evolution of these targets like the cosmic-ray ionization rate or the initial ortho-to-para ratio of H_2. Furthermore, with the predictions of the chemical model using density and temperature pseudo-time dependent profiles we estimate the dynamical age of these cores. The results show that TMC 1-C seems to be more evolved than TMC 1-CP. To discriminate between possible dynamical models even further, we post-processed each dynamical model to obtain the corresponding line profiles of each one of them. The results are again in agreement with TMC 1-C being more evolved than TMC 1-CP (Chapter 6).

This thesis presents a thorough study of the chemistry of low-mass and intermediate-mass star-forming regions from the diffuse gas to the dense gas surrounding pre-stellar cores. This study is aimed at a better understanding of the influence of chemistry in the star formation process. Chemical and elemental abundances, and external factors play a fundamental role in the dynamics of this process. The analysis of millimeter emission from different molecules allows us to compute the chemical abundances in these regions, and the comparison of these results with chemical models provide invaluable insight on the elemental abundances of Carbon, Oxygen, Nitrogen, and Sulfur, and the chemical processes occurring in the gas and grain-phase. Chemical models help address the sulfur depletion problem in low-mass star-forming regions, highlighting the importance of grain-phase reactions in the production of H_2S and, ultimately, in the sulfur chemistry in dark clouds. Finally, once key chemical parameters of these pre-stellar cores have been established, we perform a dynamical modeling of the regions relying on the information that deuterated molecules provide. We conclude summarizing the implications that these results have in the field, as well as the possible follow-ups to this work that would help in our understanding of the star-formation process even further.

Resumen

La astroquímica es el área de estudio que investiga la composición química de los objetos interestelares y las reacciones químicas que tienen lugar el ellos. La interacción entre especies químicas tiene un gran impacto en el proceso de formación estelar. Dos aspectos fundamentales para el comportamiento dinámico de la materia interestelar son el ritmo de enfriamiento del gas interestelar y su grado de ionización, altamente influenciados por la química en fase gaseosa y las abundancias químicas presentes. En efecto, un enfriamiento eficiente del gas disminuye el soporte térmico de éste contra la fuerza de la gravedad, provocando la fragmentación y colapso de filamentos moleculares en núcleos pre-estelares. La depleción de los elementos carbono (C) y oxígeno (O) es crucial en este aspecto, ya que CO y CII son los principales refrigerantes del gas en nubes moleculares. Al igual que el ritmo de enfriamiento del gas, su fracción de ionización juega un papel importante en su dinámica, ya que controla su acoplamiento con los campos magnéticos. Estos campos dirigen la disipación de la turbulencia y la transferencia de momento angular en el colapso de una nube, y la dinámica de los discos de acreción. La fracción de ionización del gas es, en ausencia de otros agentes ionizantes como los rayos X, fotones ultravioleta o choques, proporcional a ζ_{H_2}, la tasa de ionización por rayos cósmicos para moléculas de hidrógeno. Otros factores que afectan al grado de ionización del gas son las abundancias moleculares y los factores de depleción elementales. Así, en la superficie de una nube molecular ($A_\nu < 4$ mag), el carbono es el principal donador de electrones, mientras que el azufre (S) lo es en regiones internas en las que $A_\nu \sim 4-7$ mag. Este rango de extinciones comprende una fracción importante de la masa de la nube.

Dada la importancia de las abundancias moleculares y depleciones elementales en el proceso de formación estelar, nuestro objetivo es el de determinar dichas depleciones y, por tanto, el grado de ionización del gas en una muestra de núcleos pre-estelares en las nubes moleculares de TMC 1 y Barnard 1. En segundo lugar, utilizamos estos resultados para realizar un modelo químico y dinámico de una muestra de núcleos pre-estelares en TMC 1: TMC 1-C y TMC 1-CP. La observación de estos núcleos en distintos estados evolutivos dentro de la misma nube proporciona un mejor entendimiento de la evolución química de estos objetos y nos permite realizar una mejor descripción del proceso.

Nuestra metodología combina observaciones espectroscópicas de alta calidad con modelos químicos punteros para determinar las abundancias elementales, las depleciones moleculares y la fracción de ionización del gas en distintas posiciones dentro de la nube molecular TMC 1. Primero caracterizamos las propiedades físicas, tanto en densidad como en temperatura, de las posiciones observadas, que cubren un amplio rango de extinciones visuales, utilizando y analizando la emisión espectroscópica de trazadores de densidad y temperatura.

La emisión de moléculas clave en la química de una nube molecular como CO, HCO^+, CS, SO, HCN y N_2H^+ se utilizan para la obtención de sus abundancias. La información que proporcionan las abundancias se compara después con una red de modelos químicos variando las abundancias elementales, el grado de ionización del gas, la razón C/O y la tasa de ionización por rayos cósmicos para obtener los valores más representativos del gas difuso de TMC 1. Incluso en este régimen traslucido, se detecta depleción de azufre producida por las fuerzas electrostáticas de atracción entre el azufre ionizado y los granos de polvo negativamente cargados (Capítulo 4).

A pesar de su importancia ajustando el grado de ionización del gas, la determinación de la depleción del azufre en nubes moleculares es compleja. Nuestros resultados sugieren que en las regiones traslúcidas de una nube molecular la depleción de azufre es aproximadamente de un orden de magnitud comparado con la abundancia cósmica (solar), pero poco se sabe sobre los compuestos que el azufre restante forma. Esto se conoce como el problema de depleción del azufre. Debido a la alta abundancia de hidrógeno y su movilidad en la superficie de los granos, es de esperar que el azufre depletado forme H_2S de forma preferente. Sin embargo, no hay evidencia directa de esto y sólo se han determinado límites superiores a la abundancia de esta molécula en los hielos. OCS es la única molécula portadora de azufre que ha sido detectada directamente en los hielos debido a su gran fuerza de banda en el infrarrojo. Otra posibilidad es que la mayor parte del azufre esté en forma de azufre atómico en el gas. No obstante, la detección directa de este átomo es difícil y, hasta ahora, sólo se ha detectado en algunos flujos bipolares usando el telescopio infrarrojo Spitzer. Dado el papel que la molécula H_2S tiene en el problema de depleción del azufre y la relevancia que las reacciones en fase gaseosa y en la superficie de los granos tienen en la formación de esta molécula, exploramos la relación entre estos dos tipos de química, la composición de los hielos, la abundancia de H_2S, y los mecanismos de su formación. Comenzamos con una descripción física de condensaciones pre-estelares conocidas en las regiones de formación estelar de Tauro y Perseo. La densidad y temperatura de estas regiones es obtenida mediante el uso de trazadores moleculares de estas cantidades. Se explora a continuación la química sobre la superficie de los granos con observaciones espectroscópicas de la molécula H_2S ya que esta molécula sólo se forma eficientemente sobre la superficie del polvo. Los mecanismos de liberación de esta molécula al gas se investigan con ayuda de modelos químicos. Estos modelos permiten concluir que H_2S es principalmente liberado a partir de la desorción química. La abundancia gaseosa de esta molécula es sensible a las variaciones de la eficiencia de desorción a lo largo de las regiones como resultado de un cambio en la composición de la superficie de los granos. Estos modelos además confirman el grado de depleción del azufre obtenido previamente (Capítulo 5).

Una vez que las abundancias elementales y la química de los núcleos pre-estelares de Tauro ha sido constreñida, realizamos un estudio evolutivo y dinámico. De hecho, la edad de los objetos del medio interestelar es un factor importante para entender su química, ya que las condiciones físicas cambiantes de estos objetos llevan consigo cambios químicos notorios. El análisis químico de un objeto puede por tanto ofrecer información acerca de su estado evolutivo. Analizamos las diferencias químicas entre dos núcleos pre-estelares de TMC 1 que pueden ser explicadas mediante diferentes estados evolutivos: TMC 1-C y TMC 1-CP. En las condensaciones pre-estelares se espera una alta depleción de moléculas como CO,

que conlleva un aumento de otras moléculas destruidas por ella como H_2D^+. Esta molécula es eficiente en producir moléculas deuteradas y aumentar la fracción de deuterio de la zona mediante reacciones ion-molécula. Analizamos la emisión de moléculas deuteradas como N_2D^+, DNC y DCN, así como moleculas como N_2H^+ y CS, para calcular sus abundancias, trazar el gas más denso y conocer sus propiedades. A partir de esto calculamos la fracción de deuterio de los núcleos pre-estelares, una cantidad relacionada con la edad de estas regiones y por tanto con su estado evolutivo. La comparación de estos resultados con modelos químicos permite determinar parámetros clave en su evolución como la razoón inicial orto-para del hidrógeno molecular o la tasa de ionización por rayos cósmicos. Además, el modelo químico utilizado junto con modelos dinámicos pseudo-dependientes del tiempo permite estimar la edad de estos núcleos y descartar diferentes escenarios de colapso. Los resultados sugieren que TMC 1-C es más evolucionado que TMC 1-CP. Este resultado se confirma mediante la síntesis de espectros a partir de los modelos en su comparación directa con las observaciones (Capítulo 6).

Esta tesis presenta un estudio exhaustivo de la química de regiones de formación estelar de baja masa desde el gas difuso hasta el interior de núcleos pre-estelares. Este estudio tiene como objetivo mejorar nuestra comprensión de la interacción dinámica-química en este tipo de regiones. Las abundancias químicas, elementales y otros factores externos juegan un papel fundamental en la dinámica de este proceso. El análisis de la emisión de diferentes moléculas permite calcular sus abundancias, y la comparación de estas con modelos químicos proporciona información valiosa sobre las abundancias elementales de carbono, oxígeno, nitrógeno y azufre y sobre los procesos químicos que tienen lugar en el gas y en el polvo. Estos modelos ayudan a dar respuestas al problema de depleción del azufre, resaltando la importancia de las reacciones sobre la superficie de los granos en la producción de H_2S y, por tanto, en la química del azufre en regiones de formación estelar. Una vez determinadas cantidades clave en estas regiones, construimos un modelo dinámico apoyado sobre la información obtenida de la emisión de moléculas deuteradas. Finalizamos la tesis resumiendo los resultados y el impacto que estos tienen en el campo, así como las posibles nuevas avenidas que estos abren.

List of Figures

List of Tables

List of acronyms and commonly used symbols

$\mathbf{A_{ul}}$	Einstein's coefficient of spontaneous emission
$\mathbf{A_v}$	Visual extinction
Å	Ångstrom (10^{-10} m)
AD	Ambipolar Difussion
AGB	Asymptotic Giant Branch
ALMA	Atacama Large Millimetre Array
$\mathbf{B_{lu}}$	Einstein's coefficient of absorption
$\mathbf{B_{ul}}$	Einstein's coefficient of induced emission
BE	Bonnor-Ebert Sphere
$\mathbf{B_{eff}}$	Beam efficiency
CDMS	Cologne Database for Molecular Spectroscopy
CLASS	Continuum and Line Analysis Single-dish Software
CMB	Cosmic Microwave Background
CNM	Cold Neutral Medium
COM	Complex Organic Molecule
CRIR - $\boldsymbol{\zeta(H_2)}$	H_2 Cosmic-Ray Ionization Rate
DEC	Declination
$\mathbf{F_{eff}}$	Forward efficiency
FFTS	Fast Fourier Transform Spectrometer
FHSC	First Hydrostatic Core
FIR	Far-infrared
FUV	Far-ultraviolet
GMC	Giant Molecular Cloud
$\boldsymbol{h}$	Planck's constant
$\boldsymbol{\hbar}$	Reduced Planck's constant ($\hbar = h/2\pi$)
HCL	Heiles Cloud
HFS	HyperFine Splitting
HPBW	Half Power Beamwidth
IMF	Initial Mass Function

IR	Infrared
IRAM	Institut de RadioAstronomie Millimétrique
ISM	Interstellar Medium
$\mathbf{k_B}$	Boltzmann's constant
KIDA	Kinetic Database for Astrochemistry
LH	Langmuir-Hinshelwood (mechanism)
LVG	Large Velocity Gradient approximation
Lyα	Lyman alpha line
MCMC	Markov Chain Monte Carlo
MIR	Mid-infrared
n_{H}	Atomic hydrogen number density
NIR	Near-infrared
OPR	Ortho-to-Para Ratio
OTF	On-The-Fly
PDR	Photodissociation Region – Photon-Dominated Region
RA	Right Ascension
SED	Spectral Energy Distribution
SHSC	Second Hydrostatic Core
τ_{m}	Optical depth of the main hyperfine component
T_{A}	Antenna Temperature
T_{k}	Kinetic Temperature
T_{MB}	Main-beam Temperature
TMC	Taurus Molecular Cloud
UV	Ultraviolet
WIM	Warm Ionized Medium
WNM	Warm Neutral Medium
$\mathrm{Y_{pd}}$	Photodesorption yield
YSO	Young Stellar Object

Part I

Introduction

Chapter 1

The interstellar medium

> "Discworld is real. It's the way worlds should work. Admittedly, it is flat and goes through space on the back of four elephants which stand on the shell of a giant turtle, but consider the alternatives. Consider, for example, a globular world, a mere crust upon an inferno of molten rock and iron. An accidental world, made of the wreckage of old stars..."
>
> *Darwin's Watch* - Terry Pratchett

1.1 General aspects

The evolution of the Universe is intrinsically linked to the interaction of stars and their surrounding medium. The medium between stars is known as the interstellar medium (hereafter ISM), and contains the matter the stars are made of. During their lifetime, the stars return this matter to the interstellar medium, enriched by their own activity. This activity also includes an exchange of energy with their environment, often released as mechanical energy that compress the surrounding gas. This enriched and compressed gas will then form the next generation of stars, starting the cycle again. The evolution of the interstellar medium and the Universe is thus a continuous exchange of matter and energy in a cyclic fashion.

In our Galaxy, the Milky Way, with a baryonic mass of $0.8 - 4 \times 10^{11}$ $M_\odot$ (Nicastro et al. 2016), the 90% of its mass is kept inside stars, while the remaining 10% is in the interstellar matter. The interstellar (baryonic) matter is mainly made up of gas and dust. The interstellar gas is made up of the lightest elements in the Universe: hydrogen (H) and helium (He) represent, respectively, the 70% and 28% of the total ISM mass, whereas heavier elements such as carbon (C), nitrogen (N), oxygen (O), sulphur (S), magnesium (Mg), iron (Fe), silicon (Si), or argon (Ar) account for only about 2% (Ferrière 2001). The several forms in which hydrogen can be found, namely, ionized, atomic, or molecular, as well as its density and temperature, have allowed a classification of the ISM in different phases: cold molecular clouds, cool neutral clouds, and ionized gas (Lequeux 2005). Molecular clouds are cold regions ($T \sim 10$ K) where the hydrogen is found in its molecular and neutral form. Is in these clouds where the star formation takes place. If the hydrogen is found in atomic form, we have H I regions, either as cold neutral medium ($T \sim 100$ K), or warm intercloud gas ($T \sim 8000$ K). In the ISM

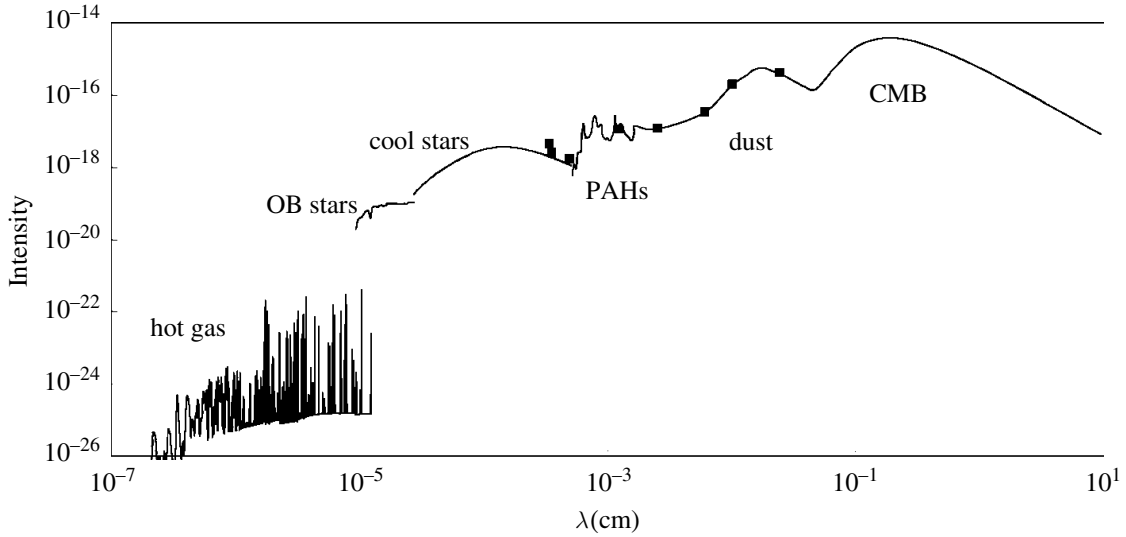

Figure 1.1: Mean intensity (in cgs units) of different interstellar radiation fields (ISRF). PAHs stands for Polycyclic Aromatic Hydrocarbons, large organic molecules formed in molecular clouds. **Credits:** *The Physics and Chemistry of the Interstellar Medium*, Tielens 2005.

near young massive stars with O/B spectral types ($T_{\rm eff} > 25000$ K), or in the event of violent shocks, the hydrogen can be found ionized, constituting H II regions. Finally, the coronal gas is present in the halos of galaxies as a hot, tenuous, and highly ionized gas as the result of the ejection of hot gas from supernova explosions that extend vertically outside the disk of the galaxy (Tielens 2005).

A large fraction of the elements heavier than hydrogen and helium are locked in dust grains. The interstellar dust, with typical sizes of around 100 nm (Kim & Martin 1994), is continuously formed in the circumstellar envelopes of aged stars in the Asymptotic Giant Branch (AGB), in planetary nebulae, supernovae events, or in the outflows of massive stars. It is then released to the ISM by radiation pressure, stellar winds, or in stellar explosions (Evans 1993). Interstellar dust accounts for the remaining < 1% of the ISM baryonic mass, and is mainly composed of silicates, graphite, and amorphous carbon, and is often covered by ices in cold environments like molecular clouds (Zubko et al. 2004). Interstellar dust plays an important role in the emission and absorption of radiation, and the energetic balance of the ISM. The surface of dust grains also acts as catalyst of chemical reactions inside dark molecular clouds (Williams 2005). The presence of dust in the ISM was first identified in its interaction with the radiation of distant stars. Dust absorbs ultraviolet (UV) light and re-emits it at longer wavelengths, thus becoming an important opacity and reddening agent of the ISM (Draine 2003). Dust grains can also be heated by phenomena like gas-grain collisions or by the energy released in chemical reactions occurring over their surfaces (Lequeux 2005). Indeed, interstellar dust plays an important role in the chemistry of the ISM, as it offers a surface on which chemical species can accrete, diffuse, and react, allowing chemical reactions that would not be possible otherwise.

Apart from the exchange of matter, the evolution of the ISM is heavily dependent on the exchange of energy. Various photon fields impregnate the ISM, influencing the physical and

chemical state of the interstellar gas and dust (see Fig. 1.1). The radiation fields heat both gas and dust, and interacts with the chemical species present in the gas phase and those adhered to dust grains. The photon field originated by stars, the stellar photon field, depends on the spectral class of the stars: O and B class stars are bright in the far-ultraviolet (FUV) regime, while A and later spectral types are bright in the visible, and far (FIR) and mid-infrared (MIR) regimes. At shorter wavelengths, stars' radiation is absorbed by neutral hydrogen (Lyman's edge, 912 Å) and thus does not contribute significantly to the total radiation field. Instead, the emission of hot plasmas, like the hot coronal gas, dominate the radiation field at shorter wavelengths. At the longest wavelengths, in the millimeter regime, the Cosmic Microwave Background (CMB) radiation contribution becomes the most important (Tielens 2005). However, in the dense and opaque regions of dark molecular clouds, the stellar photon fields cannot penetrate deep enough due to dust extinction (Hollenbach et al. 1971), and only high-energy particles proceed (Umebayashi & Nakano 1981). Cosmic rays are high-energy particles, mainly relativistic protons (84%), α particles and heavy nuclei (15%), and electrons (1%) (Grenier et al. 2015). The interaction of high-energy cosmic rays with the ISM leads to the production of gamma rays in several ways depending on the energy of the cosmic ray. Highly energetic ($1-10$ GeV) cosmic rays produce gamma radiation via neutral pion decay, whereas less energetic (<1 GeV) cosmic rays produce them via bremsstrahlung and inverse Compton scattering (Tielens 2005). Tracing sources of gamma rays are used to measure the distribution of high-energy cosmic rays. On the other hand, low-energy (<100 MeV) cosmic rays are one of the most efficient heating gas and dust in the ISM. The incoming cosmic rays may produce secondary UV photons as a result of the induced collision cascade (Prasad & Tarafdar 1983; Padovani et al. 2018). This is particularly important for the properties of the gas and dust and the chemical processes inside dense and opaque regions of molecular clouds, where cosmic rays become the main photoionization agent.

Finally, magnetic fields are also an important source of energy in the ISM. The presence of magnetic fields in the ISM is identified in a wide variety of phenomena, namely, the polarization of radiation passing through aligned dust grains, the Faraday rotation, the Galactic cyclotron/synchrotron radiation, and the Zeeman splitting of line emission (Lequeux 2005). Additionally, magnetic fields provide mechanical energy and pressure to the ISM. Such pressure drives the dynamics of the gas and dust, and has a key role in the formation of the complex structures present in the ISM.

1.2 Interstellar objects

The energy and pressure of the different agents discussed in the previous section are responsible for the properties and distribution of interstellar matter over the Galaxy. According to these properties, the ISM has been modeled as a three-phase model, with cold, warm, and hot phases in different ionization states (McKee & Ostriker 1977).

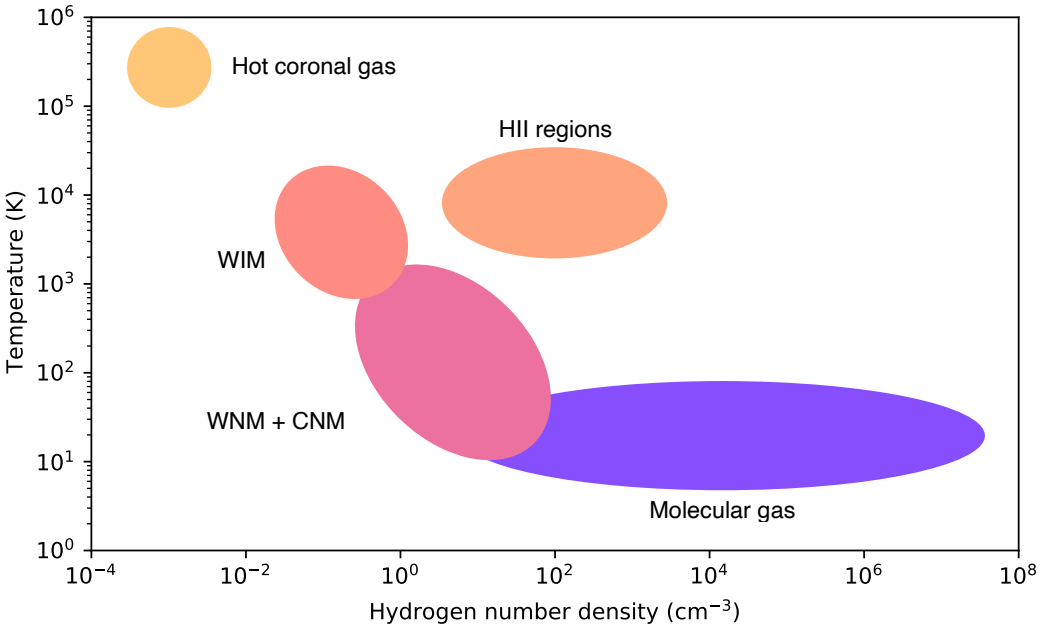

Figure 1.2: Temperature and density of the different components of the ISM

1.2.1 Ionized gas

As discussed previously, the exchange of matter and energy determine the properties of the ISM, from which the new generation of stars are born. One of the feedback processes involved is the ionization of the medium. The ionized medium occupies most of the volume of the Galaxy (70-80%, see, e.g., McKee & Ostriker 1977; Berkhuijsen et al. 2006). Several mechanisms can ionize the interstellar gas, like FUV radiation of hot stars, shocks, X-rays, or cosmic rays. Commonly, three kinds of ionized interstellar medium are defined according to their origin and properties: H II regions, warm ionized medium, and hot coronal gas.

HII regions

A region of ionized hydrogen surrounding a hot star or a cluster of hot stars is called an H II region. In these regions, O- and B-type stars ionize the medium with their UV radiation. The presence of these regions are therefore signatures of massive star formation sites in the Galaxy. Notable examples of H II regions are the Orion Nebula, the Eta Carinae Nebula, or the Tarantula Nebula. These regions are observed in free-free radio continuum radiation, infrared thermal emission from heated dust, optical line emission from ions like [O II], [O III], and [N II], fine-structure forbidden lines, and radio recombination lines (Osterbrock 1989). The balance of ionization and recombination processes defines a sphere around the star or cluster outside of which the gas is neutral (Strömgren 1939). The radius of such a sphere is the Strömgren radius, and sets the typical size of an H II region. H II regions reach temperatures of about 5000 – 10000 K, with a wide variety of sizes in the range ~ 0.5 – 100 pc. The densities found in these areas also varies greatly, from compact ($10^3 - 10^4$ cm^{-3}) to diffuse (~ 10 cm^{-3}) H II regions (Tielens 2005).

Warm ionized medium

Warm ionized medium (WIM), also known as diffuse ionized gas, makes up around 90% of the ionized gas in our Galaxy (10^9 $M_\odot$). Unlike H II regions, WIM can be found far from the galactic plane as a product of the leakage of Lyman continuum radiation from hot stars into the galaxy's disk and halo (Struve & Elvey 1938; Haffner et al. 2009). It is observed by methods such as the dispersion of radio radiation from pulsars, radio continuum free-free emission and absorption, and optical recombination lines (Hα) (Lequeux 2005). This medium is characterized by a low density (≈ 0.1 cm^{-3}), temperatures around 8000 K, and scale heights up to 1 kpc (Hoyle & Ellis 1963).

Hot coronal gas

The existence of a tenuous (10^{-3} cm^{-3}) and hot ($T \sim 10^6$ K) (McCammon & Sanders 1990) component of the ionized gas was first proposed by Spitzer (1956). Later measurements of soft X-rays and absorption lines of highly ionized species (C IV, S VI, N V, O VI, Bowyer et al. (1968); Jenkins & Meloy (1974); Sanders et al. (1998)) helped trace this elusive gas. These hot plasmas also emit free-free and recombination continuum and line radiation in the UV and X-ray regime of the electromagnetic spectrum. This gas is present in the galaxy's halo, distributed in bubbles of ionized gas that is being heated and ionized by the shocks produced in supernova explosions, supernova remnants, or early type stars (Ferrière 2001).

1.2.2 Neutral atomic gas

The neutral atomic gas (H I gas) constitutes the most massive component of the ISM in the Galaxy ($\sim$ 64%, see, e.g., Kalberla et al. 2007). This gas is found in two phases (Spitzer 1968). One phase is the warm neutral medium (WNM), with temperatures around $T \sim 8000$ K and low density (~ 0.2 cm^{-3}). The cold phase of the neutral medium (CNM) is characterized by low temperatures ($\sim$ 100 K) and moderate densities (~ 50 cm^{-3}) (Dickey et al. 1978; Kulkarni & Heiles 1987). This cold phase of the neutral gas is organized in clouds, often called diffuse H I clouds, of typical sizes about 10 pc. The main tracers of this gas are the 21-cm line of atomic hydrogen and optical and UV absorption lines in front of a bright continuum background (Ewen & Purcell 1951). The cold neutral gas dominates the absorption detections of this gas, whereas the WNM is barely seen in absorption (Mebold & Hills 1975). The thermal balance of this two-phase medium is mediated by heating and cooling processes. The neutral medium is heated by the UV radiation of external sources and the emission of electrons via photoelectric effect over dust. Hyperfine atomic line emission is the main cooling agent in the CNM, with the addition of line emission in the WNM (Wolfire et al. 1995). The neutral atomic gas is mainly found in the disk of the galaxy. Observations of the 21-cm line in the disk provides information about the galactic rotation and the spiral structure of the galaxy (Huchtmeier 1975). Additionally, at high latitudes towards the halo of the galaxy, the 21-cm line allows the observation and study of the so called high velocity clouds present in the galactic halo.

1.2.3 Molecular gas

H I clouds may reach sufficiently large densities so that the interior is shielded from UV radiation coming from external sources. In fact, H_2 becomes dominant over the neutral atomic component when the total column density surpass 10^{21} cm^{-2} (Morris & Rickard 1982). In these conditions, hydrogen atoms bind to grain surfaces, where they diffuse and react with other hydrogen atoms, resulting in the H_2 molecule (Gould & Salpeter 1963; Hollenbach et al. 1971). The H_2 molecule is then ejected from the surface due to its large enthalpy of formation. The formation of H_2 is an example of grain surface reactions and, in particular, of chemical (reactive) desorption, an efficient way of production of certain molecules in dense and cold environments where other mechanisms cannot operate.

H_2 molecule destruction is only effective via photodissociation in a line-based process (Stecher & Williams 1967; van Dishoeck 1987) and consequently it is highly inhibited by self-shielding. Therefore, this medium allows the formation of H_2 and other molecules, and thus it is called molecular gas. Depending on the density and temperature of the molecular gas, we distinguish two phases (see, e.g., Larson 1981; Huettemeister et al. 1993). The diffuse molecular gas possesses a density of around ~ 100 cm^{-3}, and cool temperatures ~ 50 K, while the dense molecular gas is colder $\sim 10-50$ K, and denser $\sim 10^3-10^6$ cm^{-3}. Molecular gas in the galaxy is typically concentrated in discrete clouds called molecular clouds. These clouds have typical sizes of $\sim 10-100$ pc, and they are often regarded as "dark" when gas temperature remains low ~ 10 K, and the visual extinction surpasses 3 mag (Myers 1989). In this case, the dust grains are covered with, mainly, H_2O ice mantles (see, e.g., Boogert et al. 2008). Other species also adhere to the grain surfaces, leading to molecule depletion.

Since the physical conditions of dark clouds allow the formation of molecules, molecule emission is used as the main tracer of these regions. However, the H_2 molecule does not possess a permanent electric dipole moment and thus it does not present rotational electric dipole transitions in the radio regime. Instead, CO rotational lines and, in particular, the CO $1 \rightarrow 0$ transition at 2.6 mm, are the most common tracers of molecular gas. In fact, CO is a proxy for the H_2 molecule, since the H_2/CO abundance ratio has been estimated to be in the range of 10^4-10^5 (Allen 1973; Dickman 1978). Many other molecules have been detected in the molecular gas. Indeed, the number of molecules detected in the ISM has been steadily increasing, reaching more than 200 as of February 2021 (CDMS catalogue).

Molecular clouds are interesting, not only due to their role in the chemistry of the ISM, but also as the birthplace of stars. In the densest parts of giant molecular clouds, objects called cores form. Star formation occurs when prestellar cores collapse due to density fluctuations. Energetic events like supernovae explosions may induce such fluctuations leading to the formation of new stars. This process is detailed in the following section.

1.3 The lifecycle of interstellar matter

The interstellar matter evolves in a cyclic manner. Stars play a major role in each cycle, processing the ISM, injecting energy through their activity and death, and providing the matter that a new generation of stars will form from. Nearby stellar activity, large scale events like cloud or galaxy interaction, and the force of gravity are responsible for the compression of

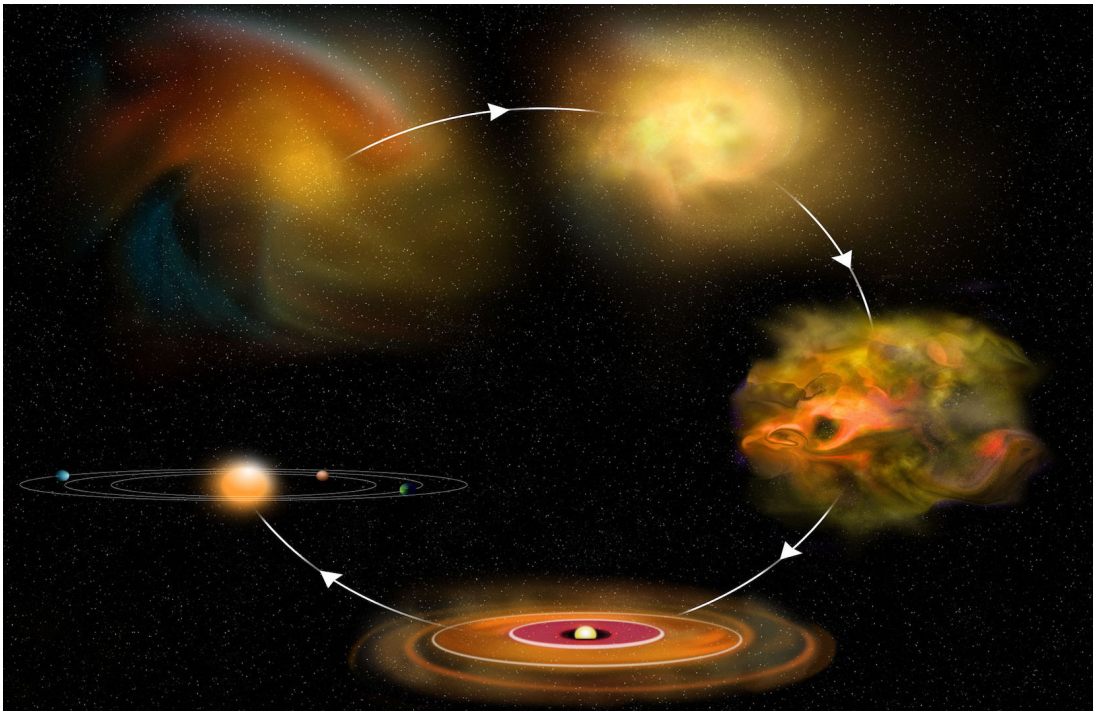

Figure 1.3: The different stages of the ISM matter (clockwise): diffuse cloud, molecular cloud, dense cores, protoplanetary disk, and planetary system. **Credits:** *Bill Saxton*, NRAO/AUI/NSF.

the enriched ISM to form new stars. This cyclic process is depicted schematically in Fig. 1.3, starting with a diffuse cloud.

1.3.1 Diffuse atomic clouds

Most of the volume of our Galaxy is filled by atomic gas. To form stars, we need to understand how this interstellar atomic gas becomes denser. As commented above, two phases of neutral atomic gas are found, the WNM and CNM. To get dense molecular gas from atomic gas, a transition from the WNM to the CNM has to occur. This transition is found to be produced by thermal instabilities due to the atomic cooling of the WMN through Lyman alpha (Lyα), OI, and CII lines (Wolfire et al. 2003). The WNM then contracts and cools, reaching a CNM state. These newly formed CNM clumps, surrounded by the WNM, are the progenitors of molecular clouds. Indeed, the formation of the dense gas in molecular clouds has been proposed as the result of CNM instabilities (Ballesteros-Paredes et al. 2020). These instabilities are seeded, locally, by stellar winds, jets, and supernova ejecta, or by large scale interactions like cloud collisions or the passage of spiral arms (Dobbs & Pringle 2013). Converging flows are formed as a result of these instabilities, leading to increased densities and, ultimately, the formation of molecular clouds (Hennebelle & Pérault 2000).

1.3.2 Molecular clouds

From a dynamical point of view, as the diffuse cloud increases its column density, it becomes gravitationally dominated and thermal pressure cannot overcome the force of gravity (Spitzer 1978). In addition, the mass-to-magnetic flux ratio becomes supercritical (Hartmann et al. 2001), and the magnetic support of the cloud is unable to support its weight. From a chemical point of view, the interior begins to be self-shielded from dissociating UV radiation and therefore the inner gas becomes molecular, forming molecules such as H_2 and CO (Bergin 2004). As commented above, the process of adsorption of hydrogen atoms by dust grains promotes the association reactions that produce the H_2 molecule. CO is the second most abundant molecular species. Its permanent dipole moment allows it to be rotationally excited and become an important coolant for the gas at moderate densities $n \sim 10^3$ cm^{-3}. At much higher densities however, CO is heavily depleted onto grains (Goldsmith 2001).

The most massive structures of molecular gas are the Giant Molecular Clouds (GMC), whose mass ranges from $10^4 - 10^7$ $M_\odot$. The formation of the GMCs we observe in our galaxy is a very active field of research. One of the earliest models proposed their formation via agglomeration and collision of smaller molecular clouds. This was originally proposed by (Oort 1954), who considered molecular clouds as highly mobile objects due to the HII regions inside them. Early models of collisions have been subjected to criticism, since they estimated a timescale of formation much longer ($\sim$ 100 Myr, Kwan (1979)) than the observationally derived estimations ($\sim$ 20 Myr, Blitz & Shu (1980)). Since then, refined simulations have provided lower values of the formation timescale. Indeed, several studies have explored the role of spiral arms in the formation of GMC, suggested by the different properties found between clouds in spiral arms compared to inter-arm ones. The passage of spiral arms would increase the frequency of collisions, reducing the timescale of formation by collisions significantly (Casoli & Combes 1982).

A top-down formation mechanism, the Parker instability, has also been proposed (Parker 1966). In this mechanism, magnetic fields parallel to the disk of the galaxy support the gas against gravity. In this scenario, the giant molecular clouds are the result of perturbations in the mass-to-flux ratio that bend the lines of magnetic fields and produce molecular gas accumulations in the midplane of the galaxy. The scale of the deformations in the magnetic field is proportional to the disk thickness, allowing the gas to be concentrated in scales of several hundred pc (Blitz & Shu 1980). This model does not however contemplate the effect that turbulence may have preventing the accumulation of gas following the magnetic field. Finally, another top-down model proposed for the formation of GMC is the Jeans instability. These instabilities arise when the internal pressure of the molecular cloud is not strong enough to prevent gravitational collapse. This model has been modified to include the influence of the magnetic tension at creating gravitational instabilities in the rotating disk of the galaxy (Lynden-Bell 1966; Elmegreen 1987). This model, however, does not explain the formation of molecular clouds with moderate sizes and masses.

Early estimations of the lifetime of GMCs were based on observations of molecular clouds in arm and inter-arms regions (Scoville et al. 1979). They concluded that GMCs are generated at the passage of an spiral arm from smaller molecular clouds in inter-arm regions. There-

fore, GMCs must have, at least, a lifetime equal to the time between arm passages $\sim 10^8$ yr. However, recent observations of the molecular gas (Engargiola et al. 2003; Blitz et al. 2007) have yielded shorter lifetimes between 10 and 55 Myr. During their lives, GMCs are characterized by clumpy and filamentary structures, in which low-mass and high-mass star formation takes place (André et al. 2010). The origin of these filaments is an open question, with many potential processes involved like convergence of flows, large scale turbulence, or magnetic fields (Larson 1985; Padoan et al. 2001; Audit & Hennebelle 2005; Nagai et al. 1998; Heitsch et al. 2008). The star activity that takes place in the molecular cloud is also responsible for its dispersion and dissolution. As discussed in the general aspects of the ISM, stellar activity provides energy and momentum to the surrounding ISM. This new input of momentum and energy in form of stellar feedback, e.g., photoionization, supernova ejecta, and wind pressure, eventually dominates and disperses the parent cloud (Krumholz et al. 2014, 2019).

1.3.3 Prestellar cores

Turbulence plays a dual role in the GMC evolution. In average GMC conditions, the cloud is supported by turbulence in the large scale (Vázquez-Semadeni et al. 2000). Turbulence also produces local density enhancements, called cores. The atomic hydrogen number density of the newly formed prestellar core typically reaches $\sim 10^6$ cm^{-3}, while the temperature remains low $\sim$ 10 K. When these cores are large enough, they may become gravitationally unstable and collapse due to density fluctuations. If no pressure forces are present during collapse, the timescale of collapse is given by the free-fall time $t_{\rm ff} = \sqrt{3\pi/32G\rho}$. To account for pressure forces, the Bonnor-Ebert solution (Bonnor 1956) to the isothermal hydrostatic equilibrium equation is commonly used. Magnetic fields also play an important role in core collapse, as they remove angular momentum in the so called magnetic braking (Basu & Mouschovias 1994), leading to a lower star formation efficiency (Mouschovias 1976). Nevertheless, the introduction of non-ideal magnetohydrodynamical factors, like ambipolar diffusion, reduces the magnetic support and boosts the core collapse. The efficiency of this phenomenon is, however, linked to the coupling between gas and magnetic fields, that is, the ionization fraction of the gas, itself dependent on the chemical evolution of the cores.

The ionization fraction and the chemical evolution of the core are therefore of fundamental importance in the core collapse and, ultimately, in the star and protoplanetary disk formation process (Padovani et al. 2013). The ionization fraction (also called ionization degree) is defined as ratio between electron and H number densities and, in dark molecular cloud conditions, it is highly influenced by the sulfur chemistry, as it is the main donor of electrons in the range $A_{\rm v} = 2-8$ mag (Goicoechea et al. 2006). The magnetic fields present in the cloud thread the gas, preventing the gravitational collapse. The chemistry of dense cores is also characterized by depletion of gas-phase molecules like CO, which freezes out onto dust grains. CO depletion leads to interesting chemical features like the enhancement of certain gas-phase molecules such as N_2H^+ or H_2D^+. These molecules are therefore able to trace the densest gas in prestellar/starless cores and thus provide information about the physical and chemical conditions in which the stars are born. The enhancement of H_2D^+ leads to high deuterium fractions, another common chemical feature of star-forming regions.

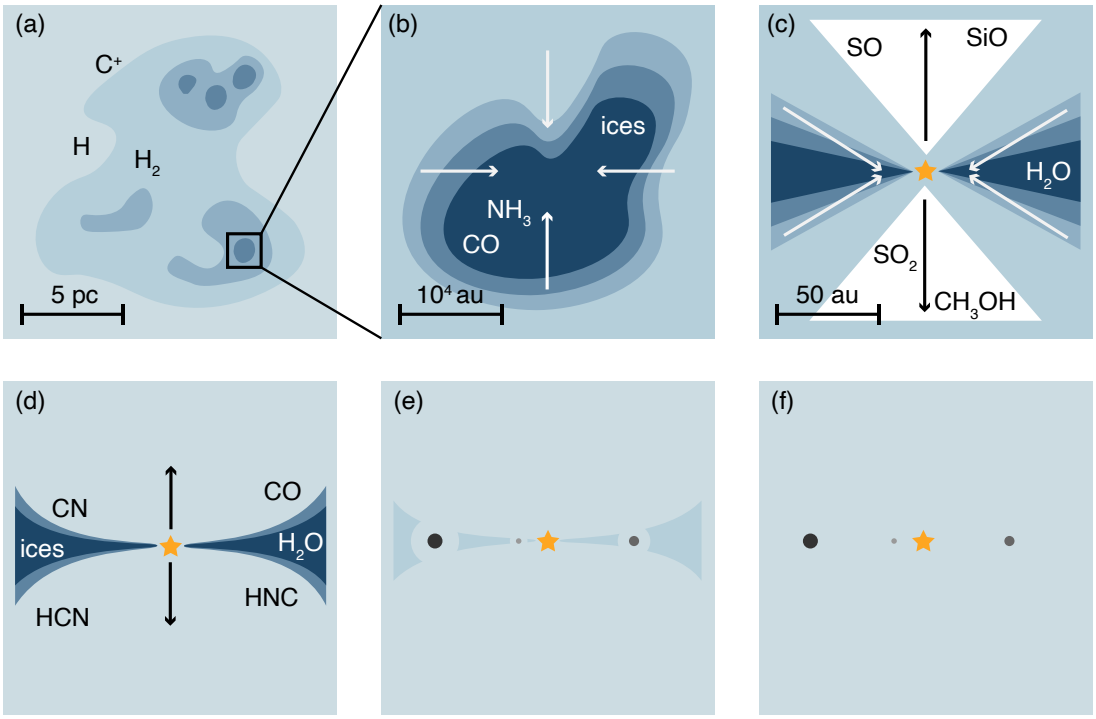

Figure 1.4: The evolution of molecular condensations embedded in neutral diffuse gas present in (a) to dense cores in (b) undergoing collapse and depletion to produce a Class 0 object (c) and, finally, a low-mass star and a protoplanetary disk (d). A planetary system is then formed (e, f). Chemical tracers in each phase are depicted. **Credits:** based on van Dishoeck & Blake (1998)

1.3.4 Protostellar cores

Stars come in a wide variety of masses. The distribution of initial stellar masses is given by the initial mass function (IMF). Traditionally, we distinguish between two types of stars according to their mass: low-mass stars ($\leq 8\ M_\odot$) and high-mass stars ($> 8\ M_\odot$). The mass of the parent cloud determines the mass of the forming star. Low-mass dense cores lead to the formation of isolated low-mass stars, whereas massive dense cores often lead to the formation of stellar clusters. One example of a low-mass star-forming cloud is the Taurus-Auriga complex, including the Taurus Molecular Cloud 1 (TMC 1) and Taurus Molecular Cloud 2 (TMC 2), being the nearest star-forming region to us. Neighboring the Taurus-Auriga complex, the Perseus complex is found an intermediate-mass star-forming region. Finally, the Orion complex is a massive star-forming region, the nearest to us, and one of the most active in the solar neighborhood.

Individual low-mass protostars are thought to be the result of the gravitational collapse of low-mass dense cores present in a molecular cloud (see Fig. 1.4). This picture of star formation is supported by observations and is generally well understood. Once the low-mass dense core collapses, the efficiency of radiation drops significantly as it becomes optically thick, and the collapse becomes adiabatic. This adiabatic core is known as a First Hydrostatic Core (FHSC) or first Larson's core (Larson 1969). Eventually, the FHSC reaches temperatures

high enough to dissociate H_2 molecules, becoming into a Second Hydrostatic Core (SHSC). During the collapse and accretion of matter, the conservation of angular momentum forces the gas to rotate faster and consequently becomes subjected to high centrifugal forces in the plane perpendicular to the rotation axis. This process leads to the development of bipolar flows and a protoplanetary disk. The energy released during collapse clears the envelope, leaving a young T Tauri star. The rising temperatures at the core of the protostar eventually trigger nuclear reactions. The star finally enters its main sequence.

High-mass star formation is not well understood. According to the IMF, high-mass stars are rarely formed in comparison with low-mass stars. They are also shorter-lived (< 1 Myr), and the collapse of the high-mass star parent core often results in the formation of binary systems and stellar clusters. The interaction and feedback between the members of the cluster then plays a crucial role in the formation and evolution of these massive stars. Why the low-mass star formation is favored over its high-mass counterpart and how high-mass young stellar objects (YSOs) can accrete mass against the feedback present in their environments remain as open questions. There are two major scenarios for high-mass star-formation: the turbulent core accretion (McKee & Tan 2002) and competitive accretion (Bonnell et al. 2001). The turbulent core accretion model is commonly referred as a scaled-up version of the low-mass star-formation process where the YSO is formed by the collapse of a single massive dense core. Since the Jeans mass is not high enough to form high-mass stars, the gas must be supported during accretion of mass against gravitational collapse by turbulence or the influence of magnetic fields. On the other hand, the competitive accretion model describes the process of accretion in a common gravitational potential created by clusters. This accretion turns out to be highly non-uniform, resulting in an initial mass segregation across the cluster. Only a few members near the center of the cluster accrete enough mass to become massive stars, while most of the members become low-mass stars.

It becomes apparent that the picture of star formation is far for complete. However, progress is being made, and modern astrophysics is becoming a highly interdisciplinary field, incorporating knowledge from other fields of science for a better understanding of the history of Universe. As we have seen, chemistry plays a fundamental role in the evolution of the ISM. From a practical point of view, the chemical composition of astronomical sources has also been used as a probe to characterize their environment and properties, becoming a powerful diagnostics tool. The growing importance of astrochemistry has also been possible due to the development of new observation techniques in the radio and infrared regimes of the electromagnetic spectrum. The wealth of knowledge that chemical species provide about the ISM turned astrochemistry into the promising field that it is today.

Part II

Astrochemistry in star-forming regions

Chapter 2

Astrochemistry

> "It is a pretty structure, isn't it? It makes you think of something solid, stable, well-linked. In fact it happens also in chemistry as in architecture that "beautiful" edifices, that is, symmetrical and simple, are also the most sturdy: in short, the same thing happens with molecules as with the cupolas of cathedrals or the arches of bridges."
>
> *The Periodic Table* - Primo Levi

2.1 Molecules in space

The existence of interstellar molecules was first realized by the detection of absorption features of the CN and CH molecules against bright stars (Swings & Rosenfeld 1937; McKellar 1940). CH^+ was discovered in interstellar clouds shortly after (Douglas & Herzberg 1941) and since then, more and more molecules have been detected as detector technology improves.

Indeed, most molecules have been detected by their microwave rotational lines, while some others have been detected by their infrared or ro-vibrational emission. As of February 2021, more than 200 molecules have been detected (218, CDMS catalogue), shown in Table 2.1. We may group these molecules into simple neutral molecules, cations and anions, carbon chains, or complex organic molecules (COMs). The nature of the molecules present in a particular region is highly dependent on the characteristics of the environment and therefore the detection of certain molecules offers insight about the region of interest. Different processes take place in the different phases of the ISM, leading to a differentiated chemistry.

2.2 Processes

The chemical processes occurring in the ISM that lead to the formation of molecules can be divided into gas-phase reactions and grain-phase reactions.

Table 2.1: Molecules detected in the interstellar medium or circumstellar shells, including tentative detections. CDMS as of May, 2021

2 atoms
H_2 AlF AlCl C_2 CH CH^+ CN CO CO^+ CP SiC HCl KCl NH NO NS NaCl OH PN SO SO^+ SiN SiO SiS CS HF HD FeO O_2 CF^+ SiH PO AlO OH^+ CN^- SH^+ SH HCl^+ TiO ArH^+ N_2 NO^+ NS^+ HeH^+
3 atoms
C_3 C_2H C_2O C_2S CH_2 HCN HCO HCO^+ HCS^+ HOC^+ H_2O H_2S HNC HNO MgCN MgNC N_2H^+ N_2O NaCN OCS SO_2 c-SiC_2 CO_2 NH_2 $H_3{}^+$ SiCN AlNC SiNC HCP CCP AlOH H_2O^+ H_2Cl^+ KCN FeCN HO_2 TiO_2 C_2N Si_2C HS_2 HCS HSC NCO CaNC NCS
4 atoms
c-C_3H l-C_3H C_3N C_3O C_3S C_2H_2 NH_3 HCCN HCNH$^+$ HNCO HNCS $HOCO^+$ H_2CO H_2CN H_2CS H_3O^+ c-SiC_3 CH_3 C_3N^- PH_3 HCNO HOCN HSCN H_2O_2 C_3H^+ HMgNC HCCO CNCN HONO MgC_2H HCCS
5 atoms
C_5 C_4H C_4Si l-C_3H_2 c-C_3H_2 H_2CCN CH_4 HC_3N HC_2NC HCOOH H_2CNH H_2C_2O H_2NCN HNC_3 SiH_4 H_2COH^+ C_4H^- HC(O)CN HNCNH CH_3O $NH_4{}^+$ H_2NCO^+ $NCCNH^+$ CH_3Cl MgC_3N NH_2OH HC_3O^+ HC_3S^+ H_2C_2S C_4S HC(O)SH
6 atoms
C_5H l-H_2C_4 C_2H_4 CH_3CN CH_3NC CH_3OH CH_3SH HC_3NH^+ HC_2CHO NH_2CHO C_5N l-HC_4H l-HC_4N c-H_2C_3O H_2CCNH C_5N^- HNCHCN SiH_3CN C_5S MgC_4H CH_3CO^+ H_2C_3S
7 atoms
C_6H CH_2CHCN CH_3C_2H HC_5N CH_3CHO CH_3NH_2 c-C_2H_4O H_2CCHOH C_6H^- CH_3NCO HC_5O $HOCH_2CN$ HCCCHNH HC_4NC
8 atoms
CH_3C_3N HC(O)OCH_3 CH_3COOH C_7H C_6H_2 CH_2OHCHO l-HC_6H CH_2CHCHO CH_2CCHCN H_2NCH_2CN CH_3CHNH CH_3SiH_3 $H_2NC(O)NH_2$ $HCCCH_2CN$ HC_5NH^+
9 atoms
CH_3C_4H CH_3CH_2CN $(CH_3)_2O$ CH_3CH_2OH HC_7N C_8H $CH_3C(O)NH_2$ C_8H^- C_3H_6 CH_3CH_2SH CH_3NHCHO HC_7O HCCCHCHCN H_2CCHC_3N
10 atoms
CH_3C_5N $(CH_3)_2CO$ $(CH_2OH)_2$ CH_3CH_2CHO CH_3CHCH_2O CH_3OCH_2OH
11 atoms
HC_9N CH_3C_6H C_2H_5OCHO $CH_3OC(O)CH_3$ $CH_3C(O)CH_2OH$
12 atoms
c-C_6H_6 n-C_3H_7CN i-C_3H_7CN $C_2H_5OCH_3$ 1-c-C_5H_5CN 2-c-C_5H_5CN
> 12 atoms
C_{60} C_{70} $C_{60}{}^+$ c-C_6H_5CN $HC_{11}N$ 1-$C_{10}H_7CN$ 2-$C_{10}H_7CN$

Table 2.2: Gas phase reactions and typical rates.

	Reaction	Rate
Photodissociation	$AB + \gamma \rightarrow A + B$	10^{-9} s^{-1} $^{(a)}$
Neutral-neutral	$A + B \rightarrow C + D$	4×10^{-11} cm^3 s^{-1} $^{(b)}$
Ion-molecule	$A^+ + B + \rightarrow C^+ + D$	10^{-9} s^{-1} $^{(c)}$
Radiative association	$A + B + \rightarrow AB + \gamma$	$^{(d)}$
Dissociative recombination	$A^+ + e^- \rightarrow C + D$	10^{-7} cm^3 s^{-1}
Charge transfer	$A^+ + B \rightarrow A + B^+$	10^{-9} cm^{3}s^{-1} $^{(c)}$
Associative detachment	$A^- + B \rightarrow AB + e^-$	10^{-9} cm^{3}s^{-1} $^{(c)}$

$^{(a)}$ Rate in the unshielded radiation field.
$^{(b)}$ Rate in the exothermic direction with no activation barrier.
$^{(c)}$ Rate in the exothermic direction.
$^{(d)}$ Rate highly dependent on the reaction.

2.2.1 Gas-phase chemistry

Although gas-phase reactions are ubiquitous in the ISM, the conditions of the environment favors certain reactions over others. For example, in the cold environment of a dark cloud, gas-phase reactions with a high activation barrier would turn inefficient, even if they were exothermic. The rate coefficient of this kind of reaction is typically given by the Arrhenius equation:

$$k(T) = A(T) \exp\left(\frac{-E_a}{k_B T}\right),$$

where $A(T)$ is a function of the temperature, E_a is the activation energy, T is the temperature, and k_B is the Boltzmann's constant. Likewise, endothermic reactions would not take place and exothermic reactions would dominate the medium. In a warmer region, reaction rates increase and both endothermic and exothermic reactions proceed.

Gas-phase reactions cover a wide variety of processes. These are found in Table 2.2. These reactions include bond-forming reactions, like the radiative association. On the other hand, bond-destruction reactions include processes such as photodissociation/photoionization, dissociative recombination, and collisional dissociation. Finally, molecular bonds can be rearranged, leading to ion-molecule exchange reactions, charge transfer reactions, and neutral-neutral reactions. Some of them are detailed in the following.

Radiative association

Radiative association reactions are reactive processes in which the two reactants collide to form a larger molecule, called activated complex, that stabilizes after the emission of a photon or the interaction with a third reactant. Stabilization through photon emission is preferred though, as ternary reactions are very unlikely in the ISM conditions. This process is shown in Table 2.2.

Radiative association reactions are key reactions in the synthesis of diatomic and polyatomic molecules in diffuse and dense interstellar clouds (Bates 1951; Herbst & Klemperer 1973). There are two major types of radiative association reactions: those that involve ions and neutral species as reactants, or those with collision between neutrals. The ion and neutral radiative associations do not normally possess an activation barrier and proceed much faster in cold environments. Neutral-neutral radiative association reactions offer a high activation barrier and therefore are slower in the same conditions.

An example of radiative association between ion and neutral species is the efficient formation of CH_2^+ and ultimately CH via electron recombination. They are therefore thought to be an important step in the formation of hydrocarbons (Black & Dalgarno 1973; Bates & Herbst 1988).

Neutral-neutral reactions

Neutral-neutral reactions involve two neutral species as reactants and products:

$$A + B \leftrightharpoons C + D + \Delta E,$$

where it is assumed to be exothermic to the right. Since this kind of reaction involves bond rearrangement, many of them possess significant activation barriers (Smith 2013). High activation barriers exclude them from the gas-phase chemistry in low-temperature conditions. Not all neutral-neutral reactions have activation barriers. Atom-radical and radical-radical reactions usually proceed without any activation barrier (Smith 2013), and could, in fact, be quite fast at low temperatures (Herbst et al. 1994).

These reactions are key in the formation of, for example, cyanopolyynes (HC_nN), cyanothiopolyynes (Cernicharo et al. 2021b), and hydrocarbon cycles (Cernicharo et al. 2021a) in the low temperatures prevailing in molecular clouds (Herbst & Leung 1990). Examples of neutral-neutral reactions in warmer gas are those that lead to the formation of water: $O + H_2 \rightarrow OH + H$, $OH + H_2 \rightarrow H_2O + H$ (Charnley 1997).

(Photo)dissociation and (photo)ionization

As discussed in Chapter I, when interstellar gas is shielded from the FUV interstellar radiation, molecules like H_2 or CO form. On the contrary, in diffuse environments where UV interstellar radiation penetrates into the gas, photodissociation becomes the main destruction agent for molecules. Photodissociation might also be viewed as a molecular formation agent via dissociation of bigger molecules.

Regions of neutral gas where the FUV radiation controls the chemistry and dominates the gas heating are referred as photodissociation regions (alternatively, photon-dominated regions, PDR) (Hollenbach 1990). The structure of these regions is fundamentally determined by its density and the FUV radiation flux. The flux of the radiation field is often given in units of the Habing field G_0 (Habing 1968), or Draine field χ, such that $G_0 = 1.71\chi$ (Draine 1978).

The FUV interstellar radiation is not the only ionization agent. Cosmic rays and shocks are also ionization agents that could be present in self-shielded environments. In molecular clouds, cosmic rays are in fact responsible for the ionization of H_2 to form H_2^+. H_2^+ then

reacts with H_2 to yield H_3^+, an important driver of gas-phase chemistry. As H_3^+ reacts with other species, it produces positive ions that will be part of other fast ion-molecule reactions, leading to a rich gas-phase chemistry (McCall 2001).

Ion-molecule reactions

Ion-molecule reactions involve ionized species. These ionized species result from ionization processes in the ISM like photoionization or cosmic-ray ionization. The ionization fraction accounts for the presence of ionized species in a medium. Diffuse clouds where UV fields penetrate are characterized by a higher ionization degree than, for example, molecular clouds, where the main ionization agent are cosmic-rays.

The reaction rates of ion-molecule reactions are generally several orders of magnitude higher than those of neutral-neutral reactions and have lower activation barriers. In absence of activation barrier, the rate of an ion-molecule reaction is well-described by the Langevin coefficient (Langevin 1905):

$$k_L = 2\pi e\sqrt{\frac{\alpha}{\mu}}$$

where α represents the polarizability of the neutral molecule and μ the reduced mass between the reactants.

The rich chemistry that emerges from the H_3^+ ion is regulated by ion-molecule reactions like

$$H_3^+ + X \rightarrow XH^+ + H_2.$$

This reaction takes place depending on the proton affinity of X. Ion-molecule reactions are key in the gas-phase production of ammonia (NH_3), a chemical thermometer. Ammonia is however not produced exclusively by gas-phase reactions, and grain-surface association reactions are key in the production of this molecule.

Dissociative recombination

Dissociative recombination reactions are found in multitude of environments, including molecular clouds, planetary ionospheres, and cometary comae. These reactions constitute the final step in the synthesis of neutrals. Together with hydrogen abstraction, they are key processes in the gas formation of most hydrides, among the first molecules detected in the ISM (Gerin et al. 2016).

The absence of activation barrier and the fact that they are a two-body process, make this kind of reaction proceed fast. They however compete with ion-molecule reactions with abundant species like the molecular hydrogen in dark clouds. One example of dissociative recombination is the formation of methane after the radiative association of CH_3^+ and H_2:

$$CH_3^+ + H_2 \rightarrow CH_5^+ + \gamma$$
$$CH_5^+ + e^- \rightarrow CH_4 + H.$$

Methane is in fact involved in the formation of the carbon monosulphide (CS), a density tracer in molecular clouds, via its ion-molecule reaction with S^+ and a dissociative recombination (Millar et al. 1986):

$$\begin{aligned} S^+ + CH_4 &\rightarrow HCS^+ + H_2 + H \\ HCS^+ + e^- &\rightarrow CS + H. \end{aligned}$$

CS is also produced in the neutral-neutral reactions (Millar et al. 1986; Bulut et al. 2021):

$$\begin{aligned} SO + C &\rightarrow CS + O \\ S + C_2 &\rightarrow CS + C \\ CH + S &\rightarrow CS + H. \end{aligned}$$

Despite its role in the formation of hydrides, dissociative recombination reactions are not very efficient in the formation of certain sulphur hydrides. HS^+ is produced by the ion-molecule reaction of ${H_3}^+$ with sulphur:

$${H_3}^+ + S \rightarrow HS^+ + H_2.$$

H_3S^+ is then a product of the radiative association of HS^+ with H_2. H_3S^+ finally yields H_2S and HS (Yamamoto 2017):

$$\begin{aligned} SH^+ + H_2 &\rightarrow H_3S^+ + \gamma \\ H_3S^+ + e^- &\rightarrow H_2S + H \quad (17\%) \\ &\rightarrow HS + H_2 \quad (58\%) \\ &\rightarrow HS + H + H \quad (15\%). \end{aligned}$$

The branching ratio that correspond to the H_2S formation route is low. The production of H_2S is not very high in the gas-phase, and the observed abundances in dark clouds cannot be explained only with gas-phase reactions. Instead, H_2S is thought to be produced through grain-surface reactions (Duley et al. 1980).

2.2.2 Grain-phase reactions

Dust grains have a fundamental role in the chemistry of the ISM. As commented in Chapter I, the surface of dust grains acts as catalyst of reactions that would not normally take place in the gas phase. The formation of the H_2 molecule is the paradigmatic example of grain-phase chemistry.

The gas phase interacts with dust grains. The collision between molecules and dust grains lead to the adsorption of gas-phase molecules into the grain surface. The probability of adsorption after a collision is enhanced in cold environments. In fact, the sticking probability is ~ 1 at gas temperatures ~ 10 K (see, e.g., Mayo Greenberg 1982; Sandford & Allamandola 1993; Le Petit et al. 2006). A certain gas-phase species is said to be depleted when the gas-phase molecules are being removed from the gas-phase efficiently via adsorption onto grains. Molecules stick to grains and react fundamentally in two ways. Molecules can

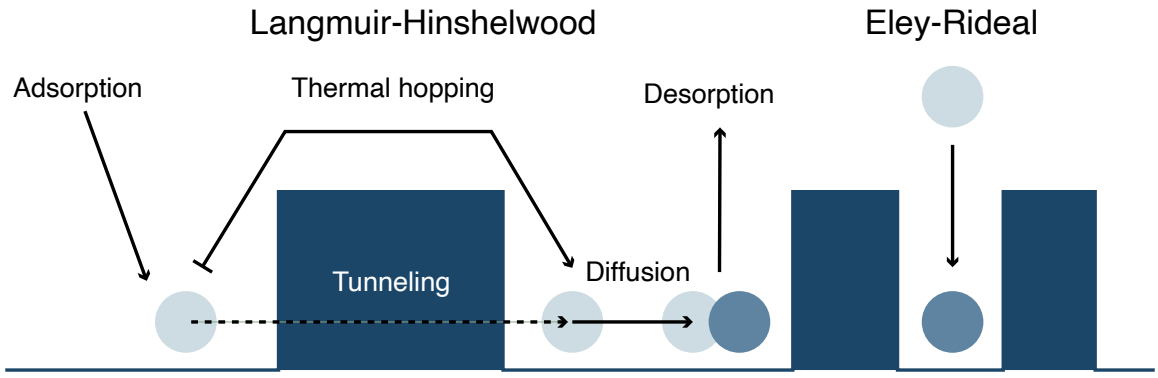

Figure 2.1: Grain-surface reaction mechanisms. *Left:* the Langmuir-Hinshelwood mechanism of reaction via accretion, diffusion, and encounter of two species. Tunneling between adsorption sites and desorption processes are also depicted. *Right:* the Eley-Rideal mechanism, consisting in the direct reaction between a gas-phase molecule and an adsorbed one.

be adsorbed on grain surfaces by van der Waals forces or they can form chemical bonds with the chemical compounds over their surface. The first case is termed physisorption while the latter is termed chemisorption.

The grain surface is often thought as a matrix of adsorption sites (see Fig. 2.1). These sites are actually local surface potential minima, to which molecules adhere. The timescale of accretion of molecules onto grains in a molecular cloud is estimated to be $\sim 10^5$ yr (Tielens & Allamandola 1987), two orders of magnitude below the typical timescale of molecular cloud evolution $\sim 10^7 - 10^8$ yr. Once adhered, molecules move on the surface from one adsorption site to another. The adhered molecule may have enough kinetic (thermal) energy to overcome the potential well present at the adsorption site. If this thermal energy is higher than the desorption energy between the surface and the molecule, the molecule is desorbed and leaves the surface. This process is called thermal desorption, and might be caused by, for example, cosmic ray grain heating. Otherwise, the thermal energy allows the molecule to move on the surface by thermal hopping between sites. Eventually, this molecule meets and reacts with other molecules adhered to the grain surface. This mechanism of reaction is called the Langmuir-Hinshelwood (LH) mechanism (Laidler et al. 2002), and the associated timescale for thermal hopping is given by:

$$t_{th} = \frac{1}{\nu_0} \exp\left(\frac{E_b}{k_B T}\right),$$

where ν_0 is the characteristic frequency of desorption, E_b is the well depth, and T is the temperature. If the molecule is not energetic enough to overcome the potential well, it can still move through the surface of the grain. Quantum tunneling between adjacent potential wells allows molecules to move, meet, and react even in conditions of low temperatures (Tielens & Allamandola 1987). The probability of quantum tunneling through a potential well depends on the mass of the molecule m, the characteristic frequency of desorption ν_0, the height of the well E_b, and the physical separation between adsorption sites a:

$$t_q = \frac{1}{\nu_0} \exp\left(\frac{2a}{\hbar}\sqrt{2mE_b}\right).$$

An alternative to the LH mechanism is the Eley-Rideal mechanism, and consists in the direct interaction between the gas-phase species and a molecule adhered to the surface (Laidler et al. 2002). The Rideal mechanism does not depend on diffusion of species, and is more efficient in regions where collisions between gas and grains are energetic and frequent, that is, in regions of warm gas and dust (Le Bourlot et al. 2012).

The chemical processes occurring on the surface of dust grains are mainly association reactions with hydrogen (Whittet et al. 2011; Watanabe & Kouchi 2002), given its high mobility over surfaces. The association of hydrogen with oxygen gives water as a product. In a similar way, the association reactions of hydrogen with nitrogen produces ammonia (NH_3), while the association of hydrogen with carbon monoxide leads to the formation of formaldehyde (H_2CO). In cold $T \sim 10$ K conditions, thermal desorption proceeds extremely slow. Once the species present in dust grains react, they may become a part of the ice covering over the grain or be desorbed from it. Besides thermal desorption, there are other mechanisms of desorption that are crucial to release reaction products back to the gas-phase.

Photodesorption

Desorption of molecules is possible by the FUV radiation at the edge of molecular clouds or by the cosmic ray-induced FUV radiation present in the interior of molecular clouds. These mechanisms have been proposed to explain the gas-phase abundances of several molecules (Shen et al. 2004; Roberts et al. 2007; Öberg et al. 2009) present in environments where they are expected to be removed from the gas-phase in a significant fraction via depletion. The flux of desorbed particles of a species due to photodesorption is given by

$$F_{\mathrm{pd},i} = Y_i F_{\mathrm{FUV}} f_{s,i},$$

where F_{FUV} is the incident FUV photon flux on the grain surface, $f_{s,i}$ the fraction of adsorption sites occupied by the species, and Y_i is the photodesorption yield. The incident FUV photon flux reaches its maximum value when the extinction becomes negligible, as

$$F_{\mathrm{FUV}} = G_0 F_0 \exp\left(-1.8 A_V\right),$$

where G_0 is the Habing field, A_V is the visual extinction in magnitudes, and $F_0 \sim 10^8$ photons cm^{-2} s^{-1} is the local interstellar flux of FUV photons. In unshielded regions, despite the high photodesorption rate, the abundance of the photodesorbed species decreases as it is also being photodissociated by the FUV field. As the extinction increases, the photodesorption rate remains high while the desorbed molecules are protected from the FUV field and thus their abundance increases. In inner, dense, and cold regions, the molecular abundances decrease again due to depletion and a lower FUV illumination. The abundances predicted by these models have a characteristic inverted U-shape (see, e.g., Hollenbach et al. 2009).

Photodesorption yields are not constant and vary with the composition of the surface from which the species are being desorbed. Consequently, these quantities are tightly related to the extent of ices over dust grains in the ISM. The presence of ices over grain surfaces is key to understand the efficiency of other desorption mechanisms, like chemical desorption, that are essential for the production of certain molecules in molecular clouds.

Chemical (reactive) desorption

Complex organic molecules (COMs) are large organic saturated molecules. Some of these molecules have been detected in pre-stellar/starless cores, e.g., formaldehyde (H_2CO), methyl formate ($HCOOCH_3$), and dimethyl ether (CH_3OCH_3). The presence of unexpected amounts of complex organic molecules in the gas-phase becomes a challenge for the desorption mechanisms presented so far, as these species are expected to be depleted given the cold temperatures in these regions (Bacmann et al. 2012). Thermal desorption is inefficient at the low temperatures $T \sim 10$ K prevailing in pre-stellar/starless cores and therefore its contribution is negligible. Photodesorption by FUV photons is also inefficient due to the large extinctions present in the interior of pre-stellar/starless cores. Moreover, due to their large size, photodesorption of any kind would likely dissociate the desorbed COMs and thus they will not reach the gas-phase intact.

An alternative mechanism is the chemical, or reactive, desorption (Dulieu et al. 2013). In associative reactions occurring over grain surfaces, energy is released. This energy is typically larger than the binding energy. When the reaction takes place, the energy is released and transferred to the surface resulting in the desorption of the newly created molecule. This transference of energy to the surface is, however, strongly dependent on its composition. The presence of ice layers reduce the efficiency of reactive desorption as part of the energy resulting from the reaction is transferred to them. This mechanism is now thought to be part of the processes that release complex organic molecules into the gas-phase in a multitude of environments (see, e.g., Vasyunin & Herbst 2013; Vastel et al. 2014; Esplugues et al. 2016; Jiménez-Serra et al. 2016).

There are several treatments of chemical desorption used in astrochemistry, with different considerations to calculate the desorption efficiency. The Rice-Ramsperger-Kassel-Marcus formalism, which takes into account the different internal degrees of freedom in the computation of reaction rates, is one of those approaches (Garrod et al. 2006; Garrod et al. 2007). This formalism yields a low fraction of molecules desorbed ~ 0.01. Another approach was taken by Minissale et al. (2016) based on a collisional model. This model was found to be in a reasonable agreement with experimental results in bare surfaces. Further experiments allowed to estimate the desorption efficiency in ice-covered surfaces, which was found to be 10% of that on bare grains.

Sputtering and shocks

Molecules also leave grain surfaces when energetic ions interact with dust. This process is called sputtering, and it is particularly important in outflows. Outflows are a common feature in the earliest stages of stellar evolution. Outflows are launched from protostars as supersonic flows of gas that have two components: an ionized jet and a molecular outflow. These outflows interact with the environment producing strong shocks that increase the temperature of the gas and dust, and a bombardment with energetic particles. These phenomena have an important effect on the chemical composition of gas and grain mantles. One of them is the desorption of molecules from dust grains. The ice mantles present over grain surfaces can be both thermally sublimated or sputtered by the ionized particles of the outflow.

Gas-phase abundances of molecules efficiently formed via grain-phase reactions are commonly used as tracers of shocks. Methanol (CH_3OH) is an example of such a molecule (Bachiller & Pérez Gutiérrez 1997). As discussed before, COMs are good tracers of these events due to their formation in grain surfaces (Sugimura et al. 2011). In strong shocks, even the refractory elements that make up dust grains can be released into the gas phase, resulting in gas-phase abundance enhancements of molecules like SiO (Bachiller et al. 1991; Martin-Pintado et al. 1992; Gueth et al. 1998).

It becomes apparent that the chemistry in the ISM is very rich and diverse. Some of the processes described thus far may become relevant in certain phases of the ISM while others do not, leading to a differentiated chemistry among regions. In the following, we shall give a brief summary of the features the chemistry that each region of the ISM presents.

2.3 Chemistry of diffuse gas

Diffuse gas is often defined by its total hydrogen density, ranging from 10 to 100 cm^{-3} in the case of diffuse atomic gas, and 100 to 500 cm^{-3} for diffuse molecular gas (Snow & McCall 2006). The typical temperatures of this component lie between 30 and 100 K, and low extinctions $A_v < 1$ mag prevail in this medium. This allows FUV to penetrate deeply into the cloud, strongly impacting the chemistry inside them. Since photodissociation and photoionization are important processes in this kind of medium, the chemistry of these regions is mainly driven by ionized species (Bettens & Herbst 1996).

The diffuse atomic gas is completely exposed to the FUV radiation field and therefore the majority of molecules are destroyed by photodissociation. On the other hand, diffuse molecular gas is still heavily exposed to the interstellar radiation field but also sufficiently attenuated to allow the presence of H_2. As introduced at the beginning of this chapter, CN, CH, and CH^+ molecules were among the first detected in the ISM. Their detection was possible due to the observation of UV absorption features of the radiation coming from diffuse clouds against a bright star. Present in the first molecules detected towards this medium, the chemistry of carbon is of great importance. In fact, the low extinction of the diffuse gas leads to the photoionization of carbon, predominantly found as C^+ (Snow & McCall 2006), whose fine-structure transitions are the main coolant of this medium.

The carbon chemistry of diffuse gas starts with the reaction of C^+ and H_2 through a radiative association, forming $CH_2{}^+$ (Dalgarno 1988). Further reactions with H_2 produce carbon hydrides. Carbon monoxide CO is formed by reactions of carbon hydrides with the neutral oxygen and destroyed by photodissociation. The photodissociation of CO in diffuse clouds leads to interesting chemical features. If the incident photons over the diffuse gas are consumed by, for example, the photodissociation of CO, inner CO molecules are shielded (self-shielding) from photodissociation. In a similar manner, the dissociation of abundant molecules like CO and H_2 may shield less abundant species from dissociation (mutual shielding). This effect varies among isotopologues, and can be quantified measuring different isotopic ratios across the cloud. This is known as isotope-selective photodissociation (Federman et al. 2003). This phenomenon hinders the determination of isotopic ratios in the ISM.

Unlike carbon, oxygen and nitrogen are not ionized and they mainly exist as neutrals. The oxygen chemistry in diffuse clouds involve the charge transfer with the H^+ and $H_3{}^+$ ions, ionized by cosmic rays. Indeed, the abundance of the $H_3{}^+$ ion has been used to estimate the cosmic-ray ionization rate in diffuse gas (Indriolo & McCall 2012). The charge transfer reaction $H^+ + O \rightarrow H + O^+$ yields O^+. Successive ion-molecule reactions with O^+ lead to OH_n^+ ions. In the case of H_3O^+, its electron recombination yields water, destroyed by photodissociation. Given its importance in the formation of water, H_3O^+ and other OH_n^+ ions have been the target of numerous observations (Neufeld et al. 2010; Gerin et al. 2010). Finally, nitrogen reactions in this medium are mainly neutral-neutral reactions. These are responsible for the formation of HCN and CN

$$CH_2 + N \rightarrow HCN + H$$
$$CH + N \rightarrow CN + H.$$

However, nitrogen hydrides require the ionization of N atoms. Hydrogenation of N^+ leads to the formation of $NH_2{}^+$, $NH_3{}^+$, and $NH_4{}^+$. The formation of $NH_4{}^+$, the precursor of ammonia, via hydrogenation is inefficient due to an activation barrier. The competing electron recombination reaction of $NH_3{}^+$ takes over and thus ammonia is not efficiently produced in this medium via gas-phase reactions.

2.4 Chemistry in the star formation process

Molecular clouds are the sites of star formation. Throughout the process of star formation, the physical conditions of the environment suffer great changes that impact the chemical processes that might occur. Consequently, molecular species become probes to study the birth of stars, with different molecules to be more relevant in different stages of stellar formation. In the following, we summarize the main stages of star formation and briefly describe the most relevant chemistry in each stage.

2.4.1 Molecular clouds and dense cores

In molecular clouds, a significant fraction of hydrogen is found in its molecular form. Further classification of molecular gas is often found depending on the presence of carbon mainly in either atomic neutral form or in the CO molecule. In the first case we have translucent clouds, with total hydrogen volume densities of $n_{\rm H} \sim 10^2 - 10^3$ cm^{-3} and temperatures $T \sim 30 - 100$ K, whereas in the other case we have dark clouds, with typical densities of $n_{\rm H} \sim 10^4 - 10^8$ cm^{-3}, and lower temperatures $T \sim 10 - 30$ K (Snow & McCall 2006). Molecular clouds have been extensively studied by molecular line emission, the dominant cooling agent of this medium. The properties of this medium have a profound effect in the chemistry of these regions, being qualitatively different from that in diffuse gas.

Due to the high extinction present in the molecular medium, the gas is shielded from the interstellar FUV field, and therefore cosmic rays and their induced UV radiation become the main ionization agents. They are responsible for the ionization of $H_2{}^+$ and the formation of $H_3{}^+$, which initiates gas-phase reactions that produce several molecules via ion-molecule

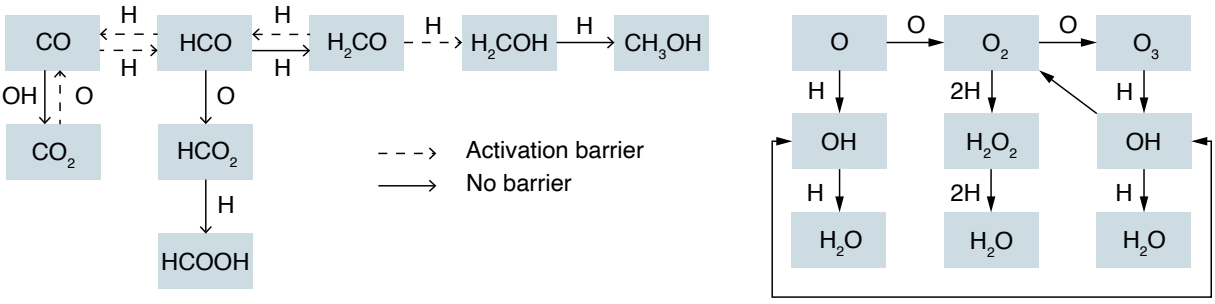

Figure 2.2: The different formation routes of COMs and water occurring over grain surfaces. Based on Tielens & Hagen (1982).

and dissociative recombination reactions. Molecules produced inside molecular clouds are not subjected to photodissociation by FUV photons and therefore live much longer than in diffuse gas. Instead, reactions with ions are the main destruction mechanisms of molecules.

Cosmic rays and the ionization of H and H_2 initiates the oxygen chemistry in molecular clouds. The H_3^+ ion reacts with neutral oxygen to produce OH^+, which, after rapid ion-molecule reactions, produces the radical OH, and the molecules CO and H_2O. These molecules play important roles inside the carbon chemistry and the production of hydrocarbons. The carbon chemistry and the formation of hydrocarbons start with the ion-molecule reaction of C with H_3^+ to produce CH_2^+. Then, CH_2^+ reacts with H_2 molecules to produce carbon hydrides. The reaction of CH_3^+ with atomic oxygen O leads to the formation of HCO^+, and the reaction of CH_3 with oxygen produces H_2CO (formaldehyde). This is not the case, however, of other complex organic molecules like methanol, since its formation through gas-phase reactions is very inefficient. The reaction

$$CH_3^+ + H_2O \rightarrow CH_3OH_2^+$$

proceeds at a slow rate. Moreover, the branching ratio of the dissociative recombination reaction that yields methanol

$$CH_3OH_2^+ + e^- \rightarrow CH_3OH + H$$

is very low $\sim 3\% \pm 2\%$ (Geppert et al. 2006). The low efficiency of the gas-phase formation of methanol does not account for the abundances of this molecule detected in dark clouds. It is firmly established now that chemical reactions over grain surfaces and the following desorption via chemical desorption constitute the main source of this molecule (Watanabe & Kouchi 2002; Fuchs et al. 2009; Garrod et al. 2006). Surface chemistry is therefore also responsible for the formation of methanol and other molecules. For example, water (H_2O), formaldehyde (H_2CO), CO_2, and formic acid (HCOOH) are produced by association reactions of oxygen and carbon monoxide with hydrogen and oxygen atoms happening on grain surfaces, as depicted in Fig. 2.2.

Dust grain surfaces therefore play a fundamental role in the chemistry of molecular gas. As mentioned in Section 2.2.2, the dense and cold properties of the molecular gas in dark clouds lead to a sticking probability of gas-phase species onto grain surfaces of ~ 1. Thus, the chemistry of dense molecular clouds is characterized by depletion of molecules. Indeed,

in prestellar and starless cores, the CO depletion reaches up to a 80-90% (Caselli et al. 1999; Bacmann et al. 2002). This is not the case, however, of nitrogen-bearing molecules, which are less subjected to depletion and some species like N_2H^+ and NH_3 may remain in the gas-phase deeper into the cloud (Bergin et al. 2002). The depletion of molecules leads to the presence of ices over dust grains, also an important feature of molecular cloud chemistry. Spitzer observations have identified the most abundant species in the ices covering dust grains as H_2O, CO, CO_2, as well as other complex ices such as CH_3OH (Sandford & Allamandola 1988, 1990a,b).

The depletion of certain families of molecules is not well understood. This is the case of sulphur-bearing molecules in the so-called sulphur depletion problem. The gas-phase abundance of atomic sulphur in the diffuse medium has been observed to be around its cosmic value $\sim 10^{-5}$ (Jenkins 2009). The sulphur depletion problem in molecular clouds arises as an incomplete picture of the detected sulphur-bearing molecules in both gas and grain phases, which in total only accounts for a $1-5\%$ of the cosmic abundance (see, e.g., Vastel et al. 2018). The main reservoir of sulphur in this medium is therefore unknown. This is a longstanding issue that shall be addressed in detail in the following sections.

Depletion of species in the densest areas of molecular clouds leads to other interesting features. In fact, the depletion of CO in this medium enhances the gas-phase abundance of other species. N_2H^+ gas-phase abundance is enhanced when CO is depleted, becoming an excellent tracer of dense gas. The absence of CO also induces the fractionation of deuterated species, as the H_2D^+ ion is also enhanced when CO and O are significantly depleted (Dalgarno & Lepp 1984). This ion reacts with neutrals to form deuterium substituted molecules, leading to an abnormal ratio between the abundance of a hydrogenated molecule and its deuterated counterpart, much higher than the elemental D/H ratio. This ratio is known as deuterium fraction. A high deuterium fraction is therefore linked to dense and cold areas of molecular clouds, and has been used as a chemical clock to study the evolutionary stage of dense cores.

The subsequent stages of stellar formation have their own chemical signatures. The characterization of the different stages these objects go through is usually realized by their spectral energy distribution (SED) across the mm, sub-mm, infrared, and visible regimes of the electromagnetic spectrum.

2.4.2 The chemistry of young stellar objects

Low-mass young stellar objects (YSO) are commonly classified in different classes according to their SED shape and its slope (Lada & Wilking 1984; Adams et al. 1987; André 1994). The SED of most YSOs typically falls in one of the four classes designated as Class 0, I, II, and III (see Fig. 2.3). This change in the peak of the spectral distribution is shown in Fig. 2.3, where examples of SED shapes represent each one of the classes. The peak of the distribution follows a general trend, moving from the mm range typical of cold dust emission of protostars to the infrared and visible regimes as the dust heats due to the radiation of the pre-main sequence star.

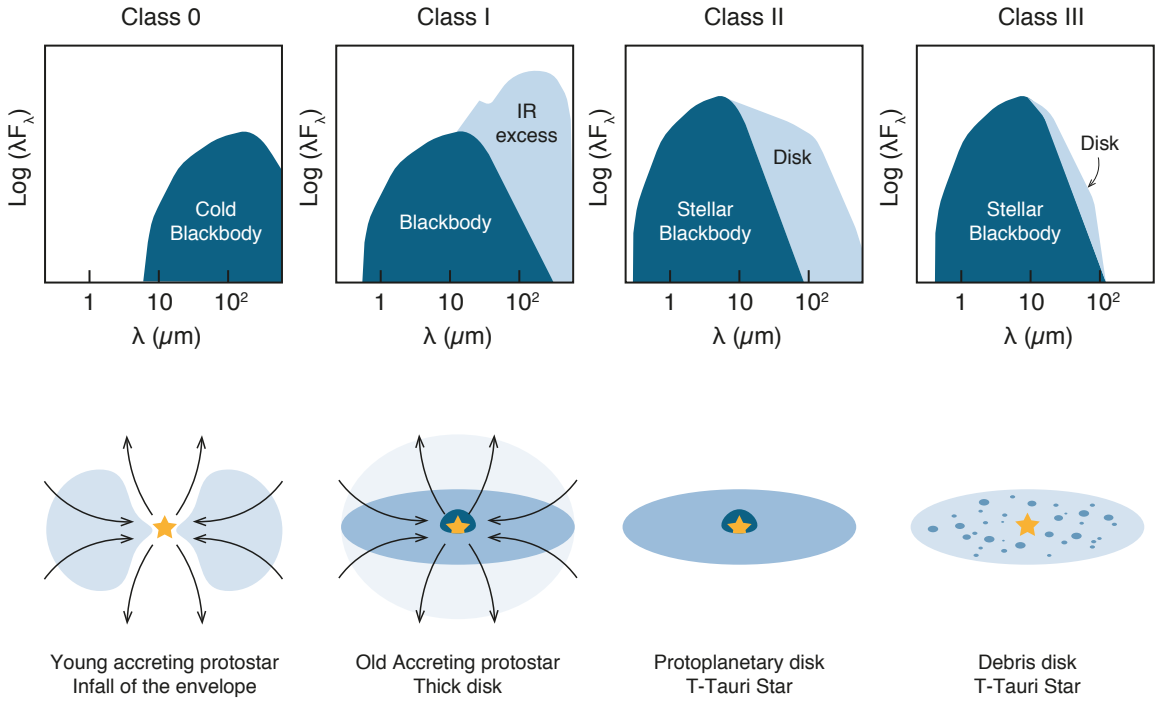

Figure 2.3: Classification of young stellar objects according to their spectral energy distribution. Each one of them represents a different stage of evolution from the collapsing envelope around a protostar to the emerging protostar around a debris disk.

Class 0 objects: hot core/corino chemistry, molecular outflows, and circum-protostellar disks

Class 0 sources are characterized by thick envelopes surrounding the protostellar object. Since the envelope of these objects is optically thick, their SED shapes peak in the mm and sub-mm portions of the electromagnetic spectrum, with a shape similar to that of a single temperature blackbody, typical of cold dust. This kind of object represents the earliest stage of gravitational collapse. Chemically, at the beginning of the collapse, they are characterized by heavy depletion of molecules, build up of ices, and chemical reactions over grain surfaces.

As the envelope material falls, the gravitational energy released heats the inner parts of the envelope. This leads to a stratification of the object in different layers with different properties that have been studied via molecular line emission. Indeed, line profiles are key probes of the physical and chemical processes in the collapsing envelope. For example, observations of HCO^+, CS, or H_2CO have been used to search for infalling signatures at the earliest stages (Zhou et al. 1993; Choi et al. 1995). Additionally, several studies of embedded objects in Taurus have concluded that the HCO^+ molecule is an excellent tracer of the envelope structure and mass (Hogerheijde et al. 1997). The outermost areas of a Class 0 object envelope resembles that of a molecular cloud, with moderate densities and cold temperatures that allows freeze-out of species, in particular CO. The presence of CO-depleted cold envelopes is in fact a common feature of Class 0 objects (Jørgensen et al. 2005). Deeper layers of the envelope get warmer as they approach the protostar. At certain point, dust tempera-

tures reach high temperatures that exceed the grain mantle evaporation temperature. When dust temperature rises beyond ~ 100 K, the ice mantles evaporate, releasing the ice content into the gas-phase, enriching the chemistry of these objects with the complex compounds formed in the ice, and creating what it is known as a hot core/corino.

Hot core/corino refers to a small < 200 au and warm > 100 K inner region around a protostar (Walmsley 1992; van Dishoeck & Blake 1998). While a hot core is present around high-mass protostars, hot corino is the low-mass analog. Chemically, hot cores and corinos are characterized by high gas-phase abundances of saturated species like H_2O (Cernicharo et al. 1990), NH_3 (Genzel et al. 1982), H_2S (Minh et al. 1991), and COMs (Millar et al. 1995; Ohishi 1997; Hatchell et al. 1998b), which have been unequivocally linked to the evaporation of ice mantles. Indeed, gas-phase species detected in hot cores/corinos like methanol are only efficiently produced via grain reactions, and the high amount of saturated species necessitates the efficient hydrogenation reactions occurring on grain surfaces. Additionally, significant deuterium fractions have been detected towards these objects (Jacq et al. 1990; Helmich et al. 1996; Mangum et al. 1991; Turner 1990; Ohishi 1997), a feature understood to reflect the chemical processes at low temperatures. Given the high temperatures in hot cores/corinos, deuterium fractionation is not expected to occur in the gas phase and therefore detection of deuterated molecules would be, again, the result of ice evaporation. These detections include singly, doubly, or even triply deuterated molecules (Tielens 1983; Taquet et al. 2012; Parise et al. 2002).

Other features appear as the collapse proceeds. The gravitational energy of the infalling material is released through bipolar outflows. This release of energy allows the surrounding material to lose angular momentum, enabling the accretion of material onto the protostar. The ionized material ejected through the outflows interacts with the surrounding gas creating shocks. Shocks are very efficient at desorbing species from ice mantles, thus showing similar chemical features to that of hot cores/corinos. This molecular component of the outflow is usually called molecular outflow. Moreover, shocks also produce sputtering of dust grains. According to their velocities, these shocks can release species only from the ice, or in the case of most eneregetic ones, the refractory elements of the grain core. Detections of molecules towards outflows include COMs and hot core/corino molecular tracers like methyl formate ($HCOOCH_3$) or formic acid (HCOOH). Other detections include shock tracers like SiO (Dutrey et al. 1997), and species not detected in any other source like phosphorus nitride (PN, Rivilla et al. (2018)) or hydrogen chloride (HCl, Codella et al. (2012)).

Outflows in Class 0 objects are often linked to the presence of a young disk being formed around the protostar as a result of the initial rotation of the prestellar core and the influence of magnetic fields. Due to the embedded nature of these disks in Class 0 objects, their direct observation is difficult (Chiang et al. 2008). The chemical characterization of the disks has been possible with interferometric observations. An example of detections of molecules in disks is ammonia (NH_3) (Choi et al. 2007, 2010), detected in a 130 au-wide disk around the protostar NGC1333 IRAS4A2, member of the protobinary system IRAS4. In the same cloud, a 25 au-wide disk of water vapor ($H_2{}^{18}O$) has been measured. COMs have also been detected in circum-protostellar disks of binary systems in Ophiuchus (Pineda et al. 2012). Recent chemical models of disk show that the innermost parts of the disks can be traced with H_2O, HNO, and NH_3 molecules, whereas other molecules like H_2CO and HCO^+ trace outer parts

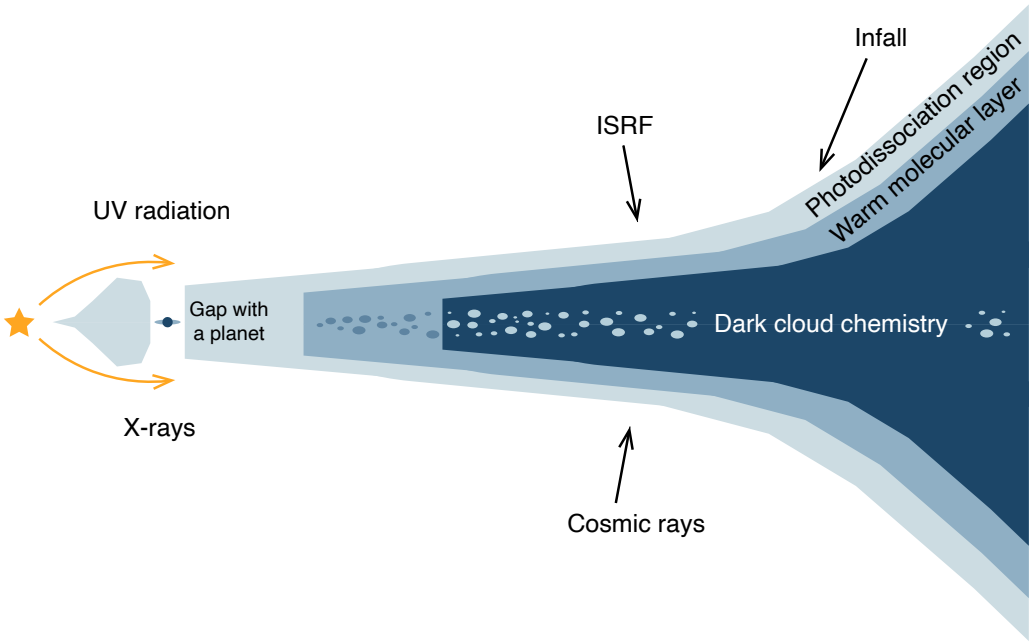

Figure 2.4: Cross section of a protoplanetary disk with its different regions according to the radiation exposure and their typical temperatures. Radiation from both the protostar and the interstellar medium have an impact in the physical properties and chemistry of the different layers.

of the disks (Fuller et al. 1991; Langer et al. 1996; van Dishoeck & Blake 1998).

Class I and II objects: from protostars to pre-main sequence stars, protoplanetary disks, and comets

As the young stellar object evolves, the accretion of matter around the protostar and the action of bipolar outflows and protostellar winds contribute to the progressive fading of the envelope. Consequently, the circum-protostellar warm dust emission becomes apparent in the infrared excess emission that the SED shape of Class I and II objects show. This excess causes the SED of these objects to be broader than the blackbody profile typical of Class 0 objects. The SED of Class I objects is characterized by a positive slope in the MIR and FIR regimes while Class II objects show a negative slope as a result of the amount of dust in the disk and envelope (André 1994).

Disks of Class I and II objects are characterized by a low mass compared to the star, only a few % the stellar mass (Andrews & Williams 2005; Andrews & Williams 2007), and a small size of a few hundred au (Vicente & Alves 2005). Due to their small size, observations at high angular resolution are preferred to study their structure and chemistry. Their structure is divided in several layers parallel to the disk plane according to their exposure to radiation (see Fig. 2.4), leading to a vertical temperature gradient decreasing towards the midplane (Dartois et al. 2003; Piétu et al. 2007). The radiation coming from the protostar indeed plays a key role in the chemistry of these objects (Bergin 2003). The variety of species detected in disks so far include molecules, radicals, and ions such as CO, CS, H_2S, SO, SO_2, HCN, HNC,

DCN, H_2CO, H_2O, HCO^+, DCO^+, and N_2H^+ (Kastner et al. 1997; Dutrey et al. 2007; Riviere-Marichalar et al. 2012; Rivière-Marichalar et al. 2021; van Dishoeck et al. 2003; Booth et al. 2021).

The most exposed layer to the interstellar radiation and the optical, ultraviolet, and X-ray radiation coming from the star constitutes the photodissociation layer of the disk. The chemistry of this layer is dominated by the photodissociation of molecules. This region has been studied with the comparison of, for example, HCN and CN abundances, showing chemical gradients from the outer disk, more exposed to radiation, where CN is more abundant than HCN, to the inner disk, less exposed to radiation, where HCN is more abundant than CN (Bergin et al. 2003; Guilloteau et al. 2016). Below the photodissociation layer, the warm molecular layer is present. Towards the inner disk, photochemistry becomes less and less effective, and molecules survive in the gas phase. Still, a part of the radiation reaches this layer (Aikawa & Herbst 1999) and initiates a rich chemistry ionizing gas and desorbing surface species, with radicals and ions dominating the gas composition. In this region, temperatures are typically higher than the CO evaporation temperature, while H_2O is mostly frozen onto grains, trapping much of the oxygen in the ice phase. This leads to a relatively high C/O ratio and a rich carbon chemistry. Below the warm molecular zone, the midplane is found. The cold temperatures and high densities of this medium lead to a chemistry similar to that in dark clouds. The conditions of density and temperature produce the freeze-out and depletion of molecules like CO, CN, CS, SO, or even N_2H^+ (Dutrey et al. 1996, 1997, 2007; Fuente et al. 2010). Deuterated molecules have been observed towards the midplane of disks. Observations of DCO^+ and DCN towards TW Hya (van Dishoeck et al. 2003; Qi et al. 2008) and DM Tau (Guilloteau et al. 2006) have allowed the estimation of deuterium fractions across disks, increasing with the radius up to a fraction of 0.1 at 70 au from the center of TW Hya (Qi et al. 2008), and disappearing rapidly at further distances.

Protoplanetary disks evolve into debris disks and, ultimately, into planetary systems. How the chemical composition of the protoplanetary disks is transferred to the chemical composition of the planets is an unanswered question. Hints of this connection seems to be given by comets, as their molecular content is thought to be the least modified from the earlier stages of star formation (Mumma et al. 1993; Irvine et al. 2000). Measurements in the radio and infrared regimes of the electromagnetic spectrum have allowed the identification of molecules present in cometary atmospheres and nuclei that link their origin to star-forming regions. A first example is the presence of complex organic molecules similar to those found in molecular clouds (Öberg et al. 2015). The deuterium fraction of water and HCN detected in comets have also been found to be in agreement with that measured towards hot cores close to massive protostars (Jacq et al. 1990; Hatchell et al. 1998a), showing that comets carry well-preserved material from the earliest stages of star formation.

Cometary composition is key to understand planet formation, as comets are among the planetesimals that remain after the formation of planets in a planetary system and, as we have seen, their composition is kept relatively unchanged since then. Moreover, the composition of these bodies as they fall into planets in the heavy bombardment phase help shape the chemistry and composition of the newly created planets. Even water, a key ingredient for life, and whose origin on Earth is under debate, could have formed from hydrogen delivered by meteorites (Piani et al. 2020).

Chapter 3

Data analysis and processing tools

> "En aquel imperio, el arte de la cartografía logró tal perfección que el mapa de una sola provincia ocupaba toda una ciudad, y el mapa del imperio, toda una provincia. Con el tiempo, esos mapas desmesurados no satisficieron y los colegios de cartógrafos levantaron un mapa del imperio, que tenía el tamaño del imperio y coincidía puntualmente con él. Menos adictas al estudio de la cartografía, las generaciones siguientes entendieron que ese dilatado mapa era inútil y no sin impiedad lo entregaron a las inclemencias del sol y de los inviernos."
>
> *Del Rigor en la Ciencia* - Jorge Luis Borges

3.1 Column density estimation and radiative transfer

The analysis of molecular emission is key to derive physical and chemical properties of interstellar regions. As we have seen, chemical abundances provide valuable information about interstellar clouds. The determination of column densities, that is, the number of atoms or molecules per square centimeter (cm^{-2}) along the line of sight in a particular direction, is the first step to derive chemical abundances from observations.

There are numerous methods to compute column densities, each one having different assumptions. One of the most used methods is the rotational diagram technique, which relies on the assumption of local thermodynamical equilibrium to obtain the column density of a species and the so-called rotation temperature $T_{\rm rot}$, which describes the population of the energy levels of the molecule assuming Maxwell-Boltzmann statistics.

3.1.1 Local Thermodynamic Equilibrium (LTE) approximation: rotational diagrams

To apply the rotational diagram technique (Goldsmith & Langer 1999), the observation of several transitions of the same molecule is needed. The interaction of the radiative field with

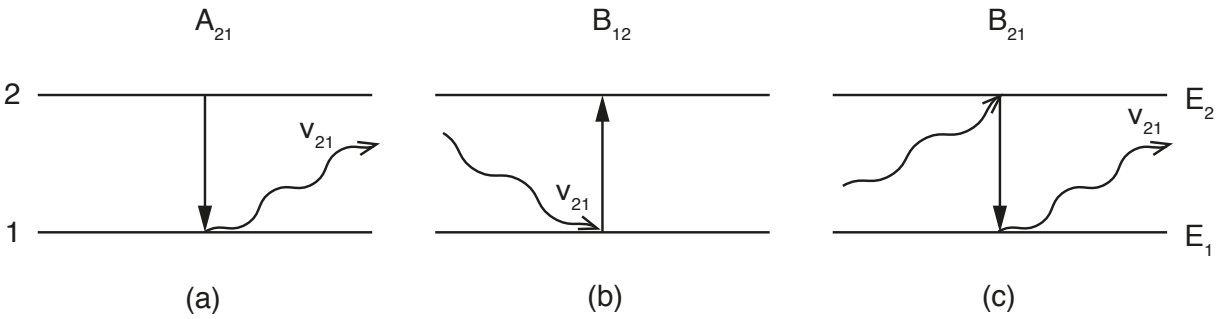

Figure 3.1: Possible processes of interaction between radiation and an atom or molecule, described by a two level system. The spontaneous emission process is depicted in (a), absorption is depicted in (b), and induced emission in (c).

the molecule can be described in a microscopic way with the Einstein coefficients. These coefficients contemplate all possible processes of interaction between radiation and the energy levels of an atom or molecule (see Fig. 3.1).

In a two level system with energy levels E_2 and E_1, such that $E_2 > E_1$, a photon of energy $E_2 - E_1 = h\nu_{21}$ may be emitted after a de-excitation transition from the higher energy level 2 to the lower energy level 1. This is called spontaneous emission and it is described by the Einstein coefficient A_{21} [s^{-1}]. This coefficient measures the probability of transition between the two levels, and its inverse gives the average lifetime of the initial quantum state. The Einstein coefficient A_{21} is related to the emission coefficient j_ν, defined as

$$j_\nu = \frac{n_2 A_{21}}{4\pi} h\nu_{21}\phi(\upsilon),$$

where n_2 is the particle density of the upper level, ν_{21} is the frequency of the emitted photon, h is the Planck's constant, and $\phi(\nu)$ is the line profile. The particle density of the upper n_2 and lower n_1 levels are related to the A_{21} coefficient as well:

$$\frac{\partial n_1}{\partial t} = A_{21} n_2.$$

Another possible process in a two level system is the absorption of a photon with frequency ν_{21} and the consequent excitation of the atom or molecule from the lower level E_1 to the upper level E_2. The probability of this excitation is proportional to the incident radiation intensity I_ν and the Einstein coefficient of absorption B_{12} [$erg^{-1}cm^2$ sr s^{-1}], related by

$$\frac{\partial n_2}{\partial t} = n_1 B_{12} I_\nu. \tag{3.1}$$

Finally, de-excitation of the two level system could be induced by an incident photon. This incident photon is absorbed, triggering the de-excitation of the system with the emission of another photon. This process is called induced emission, and it is described by the Einstein coefficient B_{21}. Both absorption B_{12} and induced emission B_{21} involve the absorption of radiation, and thus they enter in the definition of the absorption coefficient κ_ν:

$$\kappa_\nu = \frac{n_1 B_{12} - n_2 B_{21}}{4\pi} h\nu_{21}\phi(\nu). \tag{3.2}$$

The Einstein coefficients are not independent in the thermodynamic equilibrium approximation. Given an equal number of excitations and de-excitations in the two-level system, we have

$$n_2 A_{21} = (n_1 B_{12} - n_2 B_{21}) B_\nu(T), \tag{3.3}$$

where T is the temperature of the system and $B_\nu(T)$ is the Planck's law. In this case, the relationship between level populations is described by the Boltzmann's law at temperature T

$$\frac{n_2}{n_1} = \frac{g_2}{g_1} \exp\left(-\frac{h\nu_{21}}{k_B T}\right), \tag{3.4}$$

where g_1 and g_2 are the degeneracy of the lower and upper levels, respectively. In the limit $T, B_\nu(T) \to \infty$, eq. 3.4 results in $n_2 g_1 = n_1 g_2$. This limit also forces the parenthesis in the right hand side of eq. 3.3 to be zero, and therefore $n_1 B_{12} = n_2 B_{21}$. These two results yield the following relationship: $g_1 B_{12} = g_2 B_{21}$. Introducing this equality into eq. 3.3, we obtain the relationship

$$A_{21} = \frac{2h{\nu_{21}}^3}{c^2} B_{21}. \tag{3.5}$$

In general, outside of thermodynamical equilibrium, the population of energy levels is not given by the Boltzmann's law at a fixed temperature T. We can, however, define the excitation temperature T_{ex} as the temperature that would describe the level populations using the Boltzmann's law. In such a general case, the relationship in eq. 3.5, the eq. 3.4 with $T = T_{ex}$, and the equality $g_1 B_{12} = g_2 B_{21}$ can be incorporated into eq. 3.2 to yield

$$\kappa_\nu = \frac{c^2}{8\pi{\nu_{21}}^2} A_{21} n_2 \left[\exp\left(\frac{h\nu_{21}}{k_B T_{ex}}\right) - 1\right] \phi(\nu). \tag{3.6}$$

The optical depth τ_ν is the integration of κ_ν along the line of sight. Since the integration of n_2 along the line of sight is the column density of the upper level N_2 [cm^{-2}], it results in

$$\tau_\nu = \frac{c^2}{8\pi{\nu_{21}}^2} A_{21} N_2 \left[\exp\left(\frac{h\nu_{21}}{k_B T_{ex}}\right) - 1\right] \phi(\nu) \approx \frac{A_{21} h c^2}{8\pi\nu_{21} k_B T_{ex}} N_2 \phi(\nu), \tag{3.7}$$

where the approximation assumes $h\nu_{21} \ll k_B T_{ex}$ (Rayleigh-Jeans regime). Switching now from frequency to velocity units $\nu_{21}\tau_\nu = c\tau_v$, we obtain

$$\tau_v = \frac{A_{21} h c^3}{8\pi{\nu_{21}}^2 k_B T_{ex}} N_2 \phi_v(v). \tag{3.8}$$

Finally, assuming optically thin transitions, the observed line temperature is given by the product of the excitation temperature and the opacity. The integrated intensity is given by the product of the observed temperature, the line width, and the line profile:

$$\tau_v T_{ex} = T_A \phi_v(v)\, \Delta v, \tag{3.9}$$

where T_A is the observed temperature. Therefore, the column density of the upper level is

$$N_2 = \frac{8\pi{\nu_{21}}^2 k_B}{hc^3 A_{21}} T_A \Delta v \phi_v(v). \tag{3.10}$$

To derive the rotational diagram equation, we assume local thermodynamic equilibrium. The population of the energy levels follows the Boltzmann's law and can be described by a single value of temperature $T_{\rm rot}$. We introduce the partition function $Q(T_{\rm rot})$ of the system so that the probability to occupy the upper level 2 is given by

$$P_2(T_{\rm rot}) = \frac{1}{Q(T_{\rm rot})} \exp\left(\frac{-E_2}{k_{\rm B}\,T_{\rm rot}}\right) \tag{3.11}$$

The column density of the upper level 2 can therefore be related to the total column density N as

$$N_2 = g_2 P_2(T_{\rm rot}) N = g_2 \frac{N}{Q(T_{\rm rot})} \exp\left(\frac{-E_2}{k_{\rm B}\,T_{\rm rot}}\right). \tag{3.12}$$

Rearranging terms and taking logarithms in both sides of the equation we arrive at the rotational diagram equation:

$$\log\left(\frac{N_2}{g_2}\right) = \log\left(\frac{N}{Q(T_{\rm rot})}\right) - \frac{E_2}{k_{\rm B}\,T_{\rm rot}} \tag{3.13}$$

From the integrated intensity observed in a transition, the weighted column density of the upper level N_2/g_2 can be calculated using eq. 3.10. The logarithm of these column densities can be plotted against the energy of the upper level E_2 of the transition to find a linear relationship. According to eq. 3.13, the slope of the linear regression is the inverse of the rotation temperature $T_{\rm rot}$, while the intercept provides information about the total column density of the molecule. With the rotation temperature, this method offers an estimate of the excitation temperature, equal to the kinetic temperature assuming local thermodynamic equilibrium.

Although widely used, this method is not suitable in cases where the local thermodynamic equilibrium approximation does not hold. Diffuse gas is an example of a medium where thermodynamic equilibrium is a poor approximation (Genzel 1991; Black 2000).

3.1.2 Non-LTE radiative transfer: the RADEX code

More sophisticated methods do not assume thermodynamical equilibrium and solve the so-called statistical equilibrium, that is, the balance of excitation and de-excitation, taking into account the radiative transfer and collisional interactions while retaining the assumption of local excitation. The best-known methods of this type are the escape probability and the Large Velocity Gradient (LVG) method (Sobolev 1960; de Jong et al. 1975).

The escape probability method is suitable when the assumption of optically thin transitions does not hold. In this case, there are varying degrees of photon trapping, that is, part of the emitted photons are re-absorbed along their trajectory while others leave the region without being absorbed or scattered. The escape of photons is enhanced when a velocity gradient larger than the local line width is present. The size of the gradient is often measured in terms of the Sobolev length L. This length is defined as the length over which the line profile has suffered a shift greater than its line width. This implies that the matter that might reabsorb a photon is confined in a region whose radius is the Sobolev length. The large velocity gradient therefore defines regions of size L that are radiatively disconnected from each other, and the excitation becomes a local problem. The probability of escape is commonly

denoted by β, and relates the intensity $\bar{I}_\nu$ of the medium integrated over a solid angle $d\Omega$

$$\bar{J}_\nu = \frac{1}{4\pi}\int \bar{I}_\nu \, d\Omega,$$

with the source function S_ν:

$$\bar{J}_\nu = S_\nu(1-\beta), \qquad S_\nu = B_\nu(T_{\rm ex}).$$

The radiative transfer problem in conditions of local excitation becomes easy to solve. RADEX (van der Tak et al. 2007) is a radiative transfer code that uses the escape probability formalism and the LVG method in spherical symmetry to solve the statistical equilibrium equations iteratively. In the case of LVG approximation in an expanding spherical shell, the expression for β is (Mihalas 1978; de Jong et al. 1980)

$$\beta_{\rm LVG} = \frac{1-\exp(-\tau)}{\tau}.$$

Other expressions may be used for other geometries like a static and spherically symmetric medium or a plane-parallel medium (Osterbrock & Ferland 2006; de Jong et al. 1975):

$$\beta_{\rm sph} = \frac{1.5}{\tau}\left[1-\frac{2}{\tau^2}+\left(\frac{2}{\tau}+\frac{2}{\tau^2}\right)\exp(-\tau)\right] \qquad \beta_{\rm pl} = \frac{1-\exp(-3\tau)}{3\tau}.$$

Several quantities are needed as inputs for the code. RADEX reads the molecular data files that contain the collisional information of the molecule of interest with different collisional partners. The number of collisional partners, the density of the first collisional partner, the kinetic temperature, and the weighted column density of the species of interest $N/\Delta v$, Δv being the line width, are also needed for RADEX to perform the calculations.

The output of RADEX consists in the radiation peak temperatures and fluxes of the transitions of the molecule of interest once the background contribution is subtracted. These can be compared to the observed antenna temperatures to estimate the column density of a species, provided that the physical properties of the region are well-known. Additionally, if a sufficient number of transitions have been observed, both the physical conditions of the region and the column densities can be estimated by finding the RADEX input parameters that best fit the observations.

Searching for the appropriate inputs to reproduce the observed antenna temperatures is a computationally expensive task. To restrict this search to physically sensible quantities and incorporate prior knowledge of the region under study, we used a Markov Chain Monte Carlo (MCMC) methodology with a Bayesian inference approach.

3.1.3 Parameter space sampling: Markov Chain Monte Carlo

The Markov Chain Monte Carlo method is a procedure to explore a parameter space. It can be used to find an appropriate set of distributions of inputs that, after performing the radiative transfer with them, best reproduce the observed antenna temperatures (see Fig. 3.2).

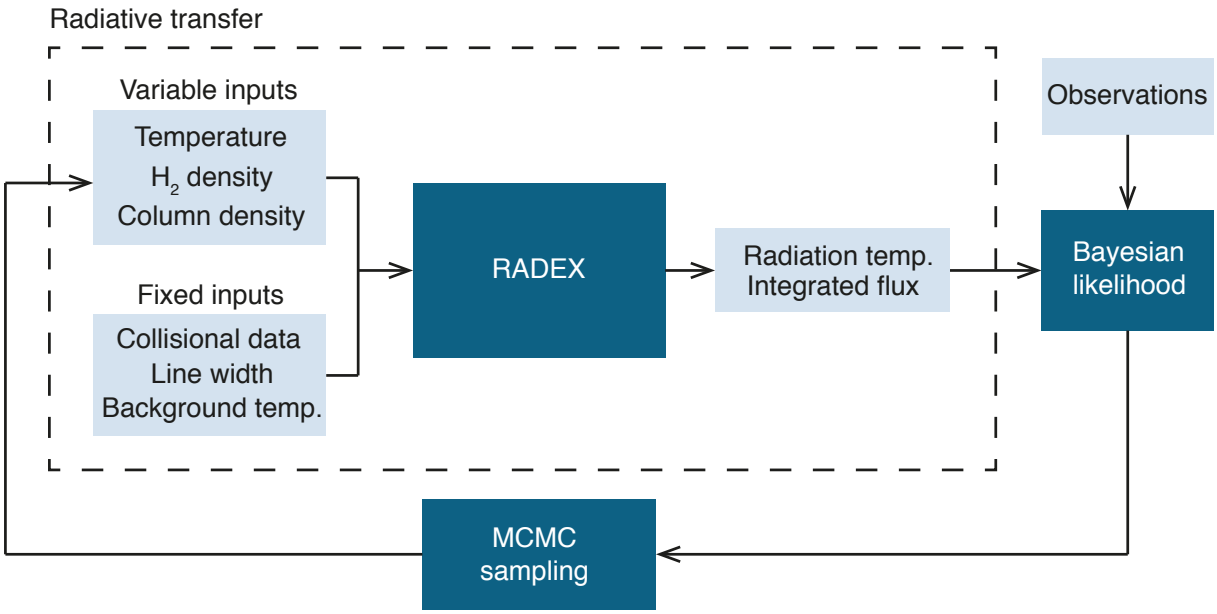

Figure 3.2: Scheme showing the steps to obtain distribution of physical parameters that are representative of a region from observational data. Following the MCMC sampling method with Bayesian inference, the parameter space is explored to compare the radiative transfer of the samples with observations to obtain the parameters whose likelihood is maximum.

This method first extracts a sample from the parameter space. Each parameter of the sample is drawn from a distribution that accounts for any prior information of the parameter. If no previous knowledge is available, this prior is set as uninformative. Once a sample of the parameter space has been extracted, Bayesian inference is used. For each sample, its goodness of fit to the empirical data is evaluated through the estimation of the likelihood function. The goal of the parameter space exploration and the computation of the likelihood for each sample is to find the maximum likelihood, which represents the set of parameters of a probability distribution such that the empirical data is most probable.

The RADEX radiative transfer code can be used with this approach. If enough empirical data is available, the exploration of a parameter space consisting in the kinetic temperature $T_{\rm kin}$, molecular hydrogen volume density $n_{\rm H_2}$, and the column density of a molecule $N(X)$ helps to determine the physical properties of the environment and the column density of the species. Recent work uses this methodology to find column densities and characterize the region under consideration (Fuente et al. 2019; Rivière-Marichalar et al. 2019).

3.1.4 Three-dimensional radiative transfer: RADMC-3D

Radiative transfer codes usually assume a simple geometry like spherical symmetry in order to perform fast computations. While useful in plenty of cases, this simplified approach raises limitations over the radiative transfer in physically or dynamically complex structures. Other radiative transfer codes, while more computationally expensive, allow a fine tuning of more complex model setups. RADMC-3D (Dullemond et al. 2012) is a multipurpose software pack-

age for radiative transfer in one, two, or three dimensions that performs dust continuum, gas continuum, and gas line radiative transfer computations.

RADMC-3D input files contain spatial, velocity, radiative, and molecular information. The spatial distribution is given by the grid. The grid can be set in one, two, or three dimensions, and defines how the space is split in regions called cells. The cell size is flexible in such a way that the grid can be adapted to situations where a fine or coarse spacing is needed. The remaining input files provide molecular, thermic, velocity, and radiative information to each cell defined by the grid. The code offers different ways to perform the radiative transfer over the grid, including local thermodynamic equilibrium, LVG approximation, or user-defined level populations.

RADMC-3D outputs take advantage of its three-dimensional capabilities to produce images. The production of images in the line radiative transfer allows to compare with data cubes obtained during telescope observations. Therefore, these images become an additional way to test different aspects of complex models of interstellar regions.

3.2 Chemical models

The estimation of column densities and abundances derived from observations and the methods described thus far reveal important aspects of the chemical processes occurring in the ISM. To understand these processes, they are studied from both experimental and theoretical points of view.

The development of chemical networks is an essential part of chemical modeling and the theoretical study of the chemistry in the ISM. Chemical networks include a set of relevant species depending on the properties of the region under consideration. The abundance of these species will increase or decrease according to the different reactions included in the network. The rates governing these reactions depend on the initial conditions given to the model, which typically are those appropriate for diffuse atomic clouds. Given a set of initial and physical conditions, the abundance of each molecule in the gas phase follows a system of time-dependent differential equation, which are then integrated through time accounting for all the possible creation and destruction pathways:

$$\frac{\mathrm{d}n_{\mathrm{g}}(i)}{\mathrm{d}t} = \underbrace{-\, n_{\mathrm{g}}(i)\sum_j n_{\mathrm{g}}(j)k_{ij}}_{\substack{\text{Destruction of } n(i) \text{ via}\\ \text{reactions with } n(j)}} \underbrace{+\sum_{j,k} n_{\mathrm{g}}(j)n_{\mathrm{g}}(k)k_{kj}}_{\substack{\text{Bimolecular reactions}\\ \text{forming } n(i)}} \underbrace{+\sum_j n_{\mathrm{g}}(j)k_j}_{\substack{\text{Unimolecular}\\ \text{formation of } n(i)}} \underbrace{-\, n_{\mathrm{g}}(i)\sum_j k_j}_{\substack{\text{Unimolecular}\\ \text{destruction of } n(i)}}$$
$$+ \underbrace{k_{\mathrm{des,i}}\, n_s(i)}_{\substack{\text{Desorption of } i\\ \text{into the gas phase}}} - \underbrace{k_{\mathrm{acc,i}}\, n_{\mathrm{g}}(i)}_{\substack{\text{Adsorption of } i\\ \text{onto grain surfaces}}}, \tag{3.14}$$

where $n_{\mathrm{g}}(i)$ is the gaseous abundance of the i species, $n_{\mathrm{s}}(i)$ is the ice (solid) abundance of i, k_{ij} is the reaction rate of the appropriate reaction involving i and j species, and k_i is the reaction rate that only involves the i species in unimolecular reactions of production or destruction, including desorption $k_{\mathrm{des,i}}$ or accretion $k_{\mathrm{acc,i}}$. The solution of this system of equations gives the evolution of all the species in the gas phase through time. The abundance of

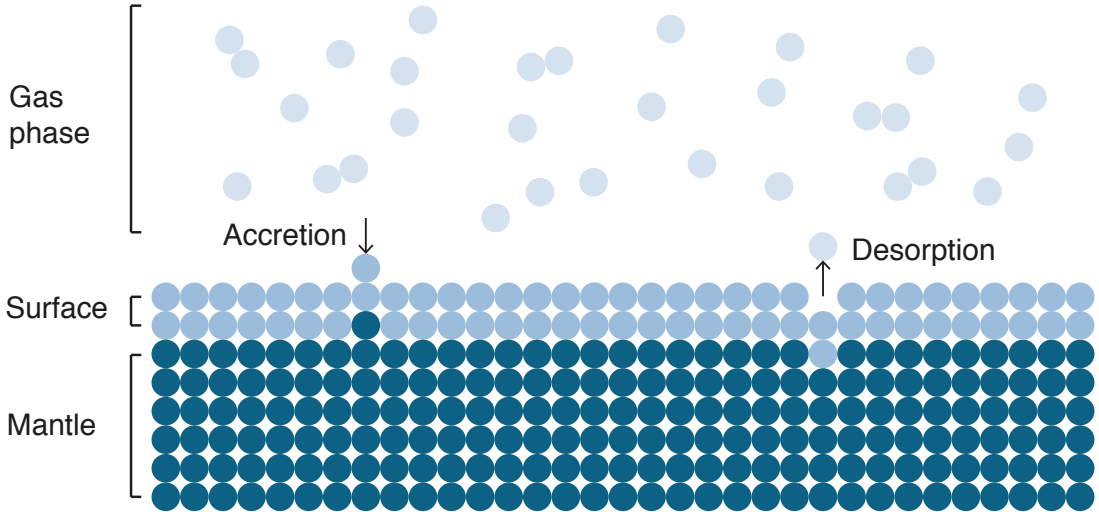

Figure 3.3: 3-phase model of gas and ice phases. The ice phase is divided in surface and mantle. The surface of the ice covering comprises the first two monolayers of ice, allowed to react with the gas phase via accretion and desorption of species. Below the ice surface, the ice mantle is found. Reactions of diffusion with species in the mantle and the surface are allowed.

i in ices $n_s(i)$ obeys its own differential equations that depend on the treatment of the icy phase in the model.

The treatment of ices in chemical models varies greatly. State-of-the-art chemical models distinguish between different icy components based on their possible interactions and reactivity. The pioneering work of (Hasegawa & Herbst 1993) served as starting point to develop the three-phase model of the gas-grain chemical code Nautilus (see Fig. 3.3).

3.2.1 Nautilus chemical model

Nautilus chemical model (Hasegawa et al. 1992; Semenov et al. 2010; Ruaud et al. 2016) is a gas-grain chemical code. This code computes the chemical evolution of up to ~ 1100 species in different phases. This three-phase model includes the gas phase, an icy surface phase, and an icy mantle phase. The icy surface phase is limited to the first two monolayers of ice, and this is the only phase to where species can accrete or from where species can desorb. The icy mantle, while being the most massive icy component, is not as chemically active due to smaller diffusion rates compared to the surface phase.

The rate of bimolecular reactions appearing in eq. 3.14 is given by the modified Arrhenius equation (Reboussin et al. 2014)

$$k_{ij}(T) = \alpha_{ij}\left(\frac{T(K)}{300}\right)^{\beta}\exp\left(-\frac{\gamma}{T(K)}\right),$$

where T is the temperature, α_{ij} is the value of the reaction rate, β controls the temperature dependence of the rate, and γ is the activation barrier. Moreover, unimolecular reaction rates

of formation or destruction due to cosmic rays and FUV radiation are given by, respectively,

$$k_{\mathrm{CR}} = A_i\, \zeta_{\mathrm{CR}},$$
$$k_{\mathrm{FUV}} = A \exp\left(-C A_{\mathrm{V}}\right)\, \chi,$$

where A and A_i are rate coefficients, ζ_{CR} is the cosmic ray ionization rate, C controls the attenuation by dust, A_{V} is the visual extinction in magnitudes, and χ is the FUV flux in Draine units. Finally, the accretion and desorption rates are given by

$$k_{\mathrm{acc}} = \sigma_g \langle v(i) \rangle n(i) n_d$$
$$k_{\mathrm{des}} = \nu_0(i) \exp\left(-\frac{E_D(i)}{T_g}\right),$$

where σ_g is the cross-section of the grain, $\langle v(i) \rangle$ is the mean velocity of i, $n(i)$ its density, n_d the number density of the grains, ν_0 is the characteristic frequency of vibration of the adsorbed species, T_g is the grain temperature, and $E_D(i)$ is the desorption energy of i.

The information needed by Nautilus to perform calculations is given in several input files. The input parameters file sets the main characteristics of the model like the gas and grain density, visual extinction, total H number density, cosmic-ray ionization rate, the FUV flux, and the time. This file also allows to specify the dimensionality and time dependence of the model, being possible to predict chemical abundances in zero-dimensional, one-dimensional, and time-dependent zero-dimensional models. The initial abundances, the possible gas and grain reactions, the gas and grain species present in a given phase, the grain surface parameters, and the activation energies are found in additional input files.

Zero-dimensional models

Nautilus allows zero-dimensional models consisting in a single cell whose physical conditions may vary with time or be fixed. How the physical conditions of density and temperature evolve with time is given as an input file. The predicted chemical abundances in the cell are given at each time step.

One-dimensional models

Nautilus also allows time-independent (static) one-dimensional structures, typically the radial profile of a spherically symmetric model. The abundances are calculated from the outermost parts of the profile to the innermost, taking into account the total extinction along the profile in the computation of the efficiency of photoprocesses at each point of the profile.

The abundances computed by Nautilus in one-dimensional models are given locally, that is, the abundance is given only at each point. The influence of the abundances along the line of sight are therefore not taken into account, becoming a crucial issue when comparing with observations.

Comparison with observations: projection along the line of sight

When part of an interstellar region is observed from Earth using radiotelescopes, the detected emission comes from the different layers of matter at different physical conditions

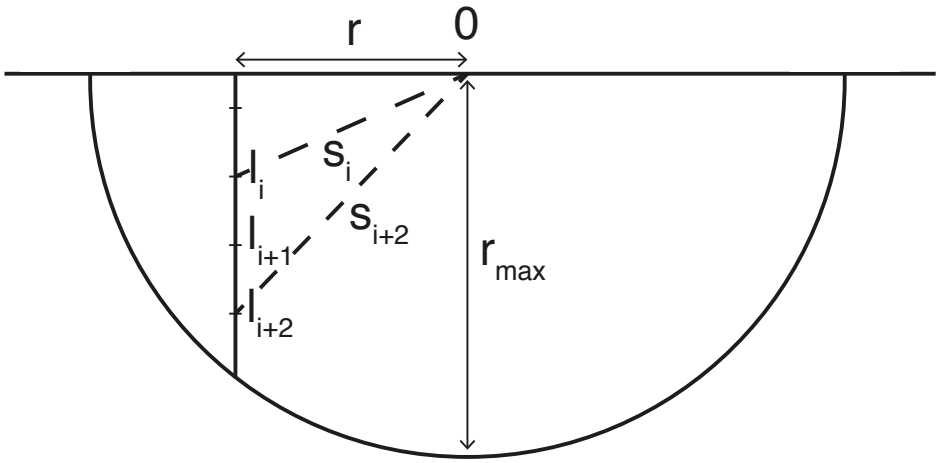

Figure 3.4: Geometric construction of a spherically symmetric region. The line of sight at different impact parameters r is discretized in segments l_i. The distance from the center to each one of the segments is defined as s_i. The total size of the region is $r_{\max}$.

contained in our line of sight. When the column density of a species is estimated from this emission, we measure the total number of molecules along our line of sight. The column density of a certain species is then divided by the total hydrogen column density in order to obtain the abundance of the species as an average of the number of molecules per hydrogen atom.

This issue needs to be taken into account when comparing observational results with Nautilus chemical abundances in one-dimensional models. In the simplest case of spherical symmetry, the average column density of a species X is

$$N_{\text{av, }X}(r) = 2 \times \sum_i \Delta l_i \frac{n_{\text{H}}(s_i)[X](s_i) + n_{\text{H}}(s_{i+1})[X](s_{i+1})}{2},$$

where r is the impact parameter, $[X]$ is the abundance of the especies X, $\Delta l_i = l_{i+1} - l_i$, $s_i = \sqrt{r^2 + l_i^2}$, l_i is a discretization of the segment along the line of sight $l_{\max} > \cdots > l_{i+1} > l_i > \cdots > 0$, with $l_{\max} = \sqrt{r_{\max}^2 - r^2}$, and $r_{\max}$ the radius of the density profile (see Fig. 3.4). Similarly, the total hydrogen average column density is given by

$$N_{\text{av, H}}(r) = 2 \times \sum_i \Delta l_i \frac{n_{\text{H}}(s_i) + n_{\text{H}}(s_{i+1})}{2},$$

so that the projected abundance of X is the ratio

$$[\text{X}]_{\text{av}}(r) = \frac{N_{\text{av, }X}(r)}{N_{\text{av, H}}(r)} = \frac{\sum_i \Delta l_i \left(n_{\text{H}}(s_i)[\text{X}](s_i) + n_{\text{H}}(s_{i+1})[\text{X}](s_{i+1})\right)}{\sum_j \Delta l_j \left(n_{\text{H}}(s_j) + n_{\text{H}}(s_{j+1})\right)}.$$

Part III

The research

Chapter 4

Gas-phase elemental abundances: the prototypical dark cloud TMC 1

Adapted from Fuente, A., Navarro-Almaida, D., Caselli, P., et al. 2019, A&A, 624, A105

Abstract

Context and aims: GEMS is an IRAM 30m Large Program aimed at determining the elemental depletions and the ionization fraction in a set of prototypical star-forming regions. This paper presents the first results from the prototypical dark cloud TMC 1.

Methods: extensive millimeter observations have been carried out with the IRAM 30m telescope (3 mm and 2 mm) and the 40m Yebes telescope (1.3 cm and 7 mm) to determine the fractional abundances of CO, HCO^+, HCN, CS, SO, HCS^+ and N_2H^+ in three cuts that intersect the dense filament at the well-known positions TMC 1-CP, TMC 1-NH3 and TMC 1-C, covering a visual extinction range from $A_v \sim 3-20$ mag.

Results: two phases with differentiated chemistry can be distinguished: i) the translucent envelope with molecular hydrogen densities of $1-5\times10^3$ cm^{-3}; and ii) the dense phase, located at $A_v > 10$ mag, with molecular hydrogen densities higher than 10^4 cm^{-3}. Observations and modeling show that the gas phase abundances of C and O progressively decrease along the C^+/C/CO transition zone ($A_v \sim 3$ mag) where C/H$\sim 8\times10^{-5}$ and C/O $\sim 0.8-1$, until the beginning of the dense phase at $A_V \sim 10$ mag. This is consistent with the grain temperatures being below the CO evaporation temperature in this region. In the case of sulfur, a strong depletion should occur before the translucent phase where we estimate a S/H $\sim 0.4-2.2\times10^{-6}$, an abundance $\sim 7-40$ times lower than the solar value. A second strong depletion must be present during the formation of the thick icy mantles to achieve the values of S/H measured in the dense cold cores (S/H $\sim 8\times10^{-8}$).

Conclusions: based on our chemical modeling, we constrain the value of ζ_{H_2} to $\sim 0.5-1.8\times10^{-16}$ s^{-1} in the translucent cloud.

4.1 Introduction

In recent years, space telescopes such as Spitzer and Herschel have revolutionized our view of star-forming regions. Images of giant molecular clouds and dark cloud complexes have revealed spectacular networks of filamentary structures where stars are born (André et al. 2010). Interstellar filaments are almost everywhere in the Milky Way and are the preferred site for star formation. Now we believe that filaments precede the onset of most star formation, funneling interstellar gas and dust into increasingly denser concentrations that will contract and fragment leading to gravitationally bound pre-stellar cores that will eventually form stars.

Gas chemistry has a key role in the star formation process by regulating fundamental parameters such as the gas cooling rate, and the gas ionization fraction. Molecular filaments can fragment into pre-stellar cores to a large extent because molecules cool the gas, thus diminishing the thermal support relative to self-gravity. The ionization fraction controls the coupling of magnetic fields with the gas, driving the dissipation of turbulence and angular momentum transfer, and therefore it plays a crucial role in the cloud collapse (isolated vs clustered star formation) and the dynamics of accretion discs (see Zhao et al. 2016; Padovani et al. 2013). In the absence of other ionization agents (X-rays, UV photons, J-type shocks), the steady state ionization fraction is proportional to $\sqrt{\zeta_{H_2}/n}$, where n is the molecular hydrogen density and ζ_{H_2} is the cosmic-ray ionization rate for H_2 molecules, which becomes the key parameter in the molecular cloud evolution (Oppenheimer & Dalgarno 1974; McKee 1989; Caselli et al. 2002b). The gas ionization fraction, $X(e^-)=n(e^-)/n_H$, as well as the molecular abundances depend on the elemental depletion factors (Caselli et al. 1998). In particular, Carbon (C) is the main donor of electrons in the cloud surface (A_v<4 mag) and, because of its lower ionization potential and as long as it is not heavily depleted, Sulfur (S) is the main donor in the ~3.7−7 magnitudes range that encompasses a large fraction of the molecular cloud mass (Goicoechea et al. 2006). Since CO and CII are the main coolants, depletions of C and O determine the gas cooling rate in molecular clouds. Elemental depletions also constitute a valuable piece of information for our understanding of the grain composition and evolution. For a given element X, the missing atoms in gas phase are presumed to be locked up in solids, i.e., dust grains and/or icy mantles. The knowledge of the elemental depletions would hence provide a valuable information to study the changes in the dust grain composition across the cloud. Surface chemistry and the interchange of molecules between the solid and gas phases have a leading role in the gas chemical evolution from the diffuse cloud to the prestellar core phase.

GEMS (Gas phase Elemental abundances in Molecular CloudS) is an IRAM 30m Large Program aimed at estimating the S, C, N, O depletions and $X(e^-)$ as a function of visual extinction, in a selected set of prototypical star-forming filaments. Regions with different illumination are included in the sample in order to investigate the influence of UV radiation (photodissociation, ionization, photodesorption) and turbulence (grain sputtering, grain-grain collisions) on these parameters, and eventually in the star formation history of the cloud. This is the first of a series of GEMS papers and it is dedicated to the prototypical dark cloud TMC 1.

Table 4.1: Molecular tracers used in this study

Parameter	$A_v < 10$ mag	$A_V > 10$ mag
X(e^-)	^{13}CO, HCO^+, $H^{13}CO^+$	$C^{18}O$, $HC^{18}O^+$, N_2H^+
n(H_2)	CS, $C^{34}S$	$C^{34}S$, ^{13}CS, SO
C/H	^{13}CO, HCN, CS	$C^{18}O$, $H^{13}CN$
O/H	^{13}CO, SO	$C^{18}O$, SO, ^{34}SO
N/H	HCN	$H^{13}CN$, N_2H^+
S/H	CS, $C^{34}S$, SO, HCS^+	$C^{34}S$, ^{13}CS, SO, ^{34}SO

4.2 TMC 1

The Taurus molecular cloud (TMC), at a distance of 140 pc (Elias 1978; Onishi et al. 2002), one of the closest molecular cloud complexes, is considered an archetype of low-mass star-forming regions. It has been the target of several cloud evolution and star formation studies (Ungerechts & Thaddeus 1987; Mizuno et al. 1995; Goldsmith et al. 2008), being extensively mapped in CO (Cernicharo & Guelin 1987; Onishi et al. 1996; Narayanan et al. 2008) and visual extinction (Cambrésy 1999; Padoan et al. 2002). The most massive molecular cloud in Taurus is the Heiles cloud 2 (HCL 2) (Onishi et al. 1996). TMC 1 was included in the Herschel Gould Belt Survey (André et al. 2010). One first analysis of these data were carried out by Malinen et al. (2012) who generated visual extinction maps of the two long filaments in HCL 2 based on near-IR (NIR) extinction and Herschel data. As one of the most extensively studied molecular filament, TMC 1 is also included in the Green-Bank Ammonia Survey (PIs: R. Friesen & J. Pineda) (Friesen et al. 2017).

TMC 1 has been also the target of numerous chemical studies. In particular, the positions TMC 1-CP and TMC 1-NH3 (the cyanopolyne and ammonia emission peaks) are generally adopted as templates to compare with chemical codes (Fehér et al. 2016; Gratier et al. 2016; Agúndez & Wakelam 2013). Less studied from the chemical point of view, TMC 1-C has been identified as an accreting starless core (Schnee et al. 2007, 2010).

4.3 Observational Strategy

In order to derive the elemental gas abundance of C, O, N and S, we need to determine the abundances of the main gas reservoirs (see Table 4.1). Essentially, most of the carbon in molecular clouds is locked in CO and the C depletion is derived from the study of CO and its isotopologues. Several works have studied the depletion of CO in dense starless cores and young protostars (Caselli et al. 1999; Kramer et al. 1999; Bacmann et al. 2002; Alonso-Albi et al. 2010; Hernandez et al. 2011; Maret et al. 2013; Miettinen & Offner 2013; Lippok et al. 2013). The main reservoirs of nitrogen are atomic nitrogen (N) and molecular nitrogen (N_2) which are not observable. The nitrogen abundance needs to be derived by applying a chemical model to fit the observed abundances of nitriles (HCN, HNC, CN) and N_2H^+. The HCN abundance is also dependent on the amount of atomic C in gas phase and hence, on

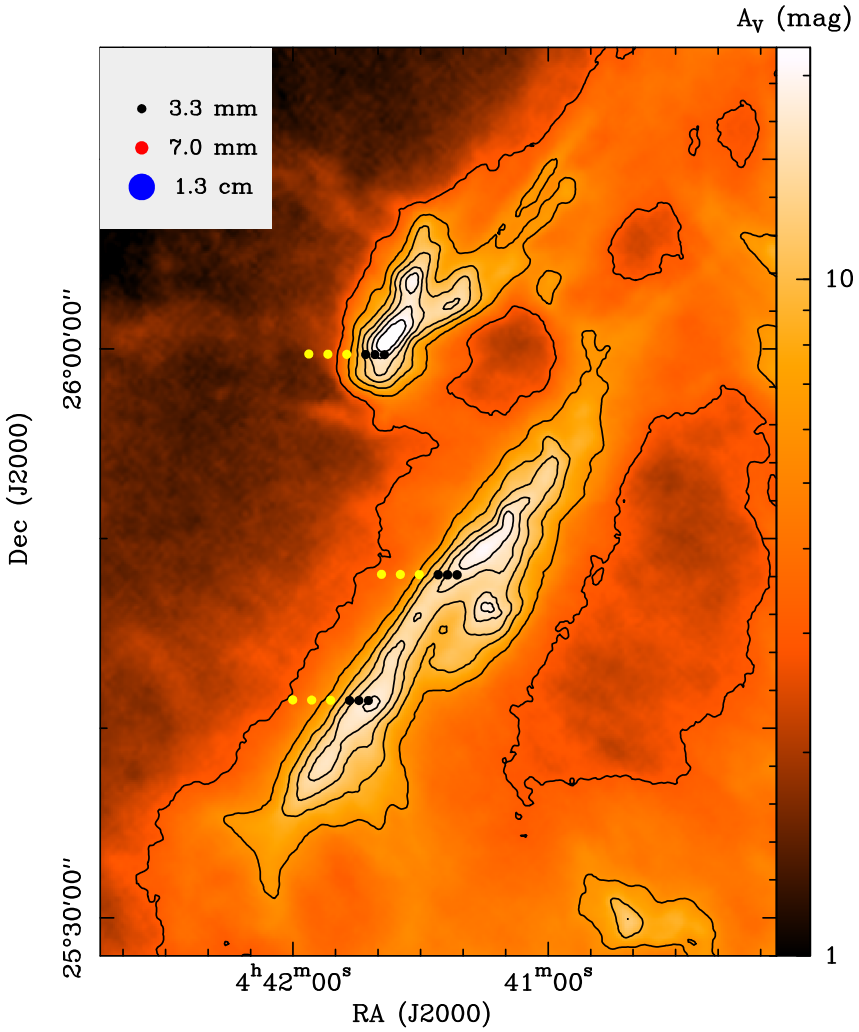

Figure 4.1: Visual extinction map of TMC 1 (Kirk et al., in prep). The positions observed with the 30m telescope are indicated with circles. Black circles mark positions observed only with the 30m telescope while yellow circles show the positions observed also with the Yebes 40m telescope. In the upper left corner, we show the beam of the IRAM telescope at 3 mm (beam~29") and of Yebes 40m telescope at 1.3 cm (beam~84") filled and at 7 mm (beam~42"). Contours are 3, 6, 9, 12, 15, and 18 mag.

the C/O ratio (Loison et al. 2014). Abundant oxygenated species such as O, O_2, H_2O and OH, cannot be observed in the millimeter domain and the oxygen depletion should be indirectly derived through comparison with chemical models, as well. In the case of sulfur, depending on the local physical conditions and the chemical age, atomic S and/or SO are expected to be the main gas phase reservoir in dense clouds (Fuente et al. 2016; Vidal et al. 2017). Unfortunately, the direct observation of atomic S is difficult and, thus far, has only been detected in some bipolar outflows using the infrared space telescope Spitzer (Anderson et al. 2013). Sulfur can also be traced by sulfur recombination lines but they are very weak and not easy to interpret (Roshi et al. 2014). Sulfur depletion in molecular clouds is determined from the observation of a few molecular compounds, mainly CS, HCS^+ or SO (see, e.g. Goicoechea et al. 2006), whose abundances are very sensitive to the C/O gas-phase ratio and also time evolution. Its determination hence requires a good characterization of the gas physical and chemical conditions.

For the present study, we selected a subset of species (CO, HCO^+, HCN, CS, SO, HCS^+, and N_2H^+) that are essential to derive the elemental abundances in the molecular gas. The observations were performed using the receiver setups listed in Table 4.8 and the observed molecular transitions are shown in Table 4.9. When possible we observe several lines of the same species in order to accurately determine the molecular abundance. When only one line was observed, we use the molecular hydrogen density derived from the fitting of the CS (and their rarer isotopologues $C^{34}S$ and ^{13}CS) 3→2 and 2→1 lines. Towards the edge of the cloud, the densities are lower and the CS 3→2 line is not detected. For this reason we complement the 30m observations with the CS 1→0 line as observed with the 40m Yebes telescope. The 40m configuration allows us to observe simultaneously the NH_3 (1,1) and (2,2) lines in band K. We use these observations to constrain the gas kinetic temperature at the cloud edges.

The high sensitivity required by our project, prohibits the mapping of a large area. Instead, we observe the three right-ascension cuts covering visual extinctions between $A_V \sim 3$ mag to ~ 20 mag (see Fig 4.1). In details, we have observed 6 positions per cut which corresponds to the offsets (0",0"), (+30",0), (+60",0"), (+120",0"), (+180",0") and (+240",0") relative to the positions listed in Table 4.2. In addition to the 30m observations, we carried out observations with the 40m Yebes telescope towards the positions marked with yellow circles in Fig 4.1.

4.4 Data acquisition

4.4.1 IRAM 30m telescope

The 3 mm and 2 mm observations were carried out using the IRAM 30-m telescope at Pico Veleta (Spain) during three observing periods in July 2017, August 2017 and February 2018. The telescope parameters at 3 mm and 2 mm are listed in Table 4.8 with the beam size varying with the frequency as HPBW(")=2460 /ν where ν is in GHz. The observing mode was frequency switching with a frequency throw of 6 MHz well adapted to remove standing waves between the secondary and the receivers. The Eight MIxer Receivers (EMIR) and the Fast Fourier Transform Spectrometers (FTS) with a spectral resolution of 49 kHz were used for these observations. The intensity scale is T_{MB} which is a good estimate of T_B as long as

Table 4.2: Source coordinates

Source	RA(J2000)	Dec (J2000)	V_{lsr} (km s^{-1})
TMC 1-CP	$04^h41^m41^s.90$	$25°41'27''.1$	5.8
TMC 1-NH3	$04^h41^m21^s.30$	$25°48'07''.0$	5.8
TMC 1-C	$04^h41^m38^s.80$	$25°59'42''.0$	5.2

the source size is comparable to the observational beam. In our case, the emission is expected to be more extended. In the limiting case of the source being extended through the whole sky, the correct intensity scale would be T_A^*, where T_{MB} and T_A^* are related by $T_{MB} = (F_{eff}/B_{eff})T_A^*$ (see Table 4.8). Since the difference between one scale and the other is not large, ≈ 17 % at 86 GHz and 27% at 145 GHz, we adopt the T_{MB} scale. The uncertainty in the source size is included in the line intensity errors which are assumed to be ~20%. Although numerous lines are detected in the range of frequencies covered by our observations, in this paper we concentrate on the most abundant molecules (and their isotopologues): CO, HCO^+, HCN, CS, SO, HCS^+, and N_2H^+. Other species will be analyzed in forthcoming papers.

4.4.2 Yebes 40m telescope

The RT40m is equipped with HEMT receivers for the 2.2-50 GHz range, and a SIS receiver for the 85-116 GHz range. Single-dish observations in K-band (21-25 GHz) and Q-band (41-50 GHz) can be performed simultaneously. This configuration was used to observe the positions marked with a yellow-red circle in Fig 1. The backends consisted of FFTS covering a bandwidth of ~2 GHz in band K and ~9 GHz in band Q, with a spectral resolution of ~38 kHz. Central frequencies were 23000 MHz and 44750 MHz for the K and Q band receivers, respectively. The observing procedure was position-switching, and the OFF-positions are RA(J2000) = $04^h42^m24^s.24$ Dec(2000):$25°41'27''.6$ for TMC 1-CP, RA(J2000) = $04^h42^m29^s.52$ Dec(2000):$25°48'07''.2$ for TMC 1-NH3, RA(J2000) = $04^h42^m32^s.16$ Dec(J2000):$25°59'42''.0$ for TMC 1-C. These positions were checked to be empty of emission before the observations. The intensity scale is T_{MB} with conversion factors of 4.1 Jy/K in band K (T_{MB}/T_A^*=1.3) and in 5.7 Jy/K in band Q (T_{MB}/T_A^*=2.1). The HPBW of the telescope is 42" at 7 mm and 84" at 1.3 cm.

4.4.3 Herschel Space Observatory: A_V and T_d maps

In this work, we use the column density and dust temperature maps of TMC 1 created following the process described in Kirk et al. (2013) and Kirk et al. (in prep). In the following, we give a brief explanation of the methodology. The PACS and SPIRE (Poglitsch et al. 2010; Griffin et al. 2010) data were taken as part of the Herschel Gould Belt Survey (André et al. 2010) and were reduced as described in Kirk et al. (in prep). The absolute calibration (median flux level) of the maps was estimated using data from Planck and IRAS (c.f.Bernard et al. 2010). The data was then convolved to the resolution of the longest wavelength 500 μm (36 arcsec).

A modified blackbody function of the form $F_\nu = MB_\nu(T)\kappa_\nu/D^2$ was fitted to each point

where M is the dust mass, $B_\nu(T)$ is the Planck function at temperature T, and D = 140 pc was the assumed distance to Taurus. The dust mass opacity was assumed to follow a standard law, $\kappa_\nu \propto \nu^\beta$, with $\beta = 2$ and a reference value of 0.1 cm^2 g^{-1} at λ=1 THz (Beckwith et al. 1990). When using the same dust assumptions, the resulting dust map agreed well with the Planck 353 GHz Optical Depth map above $N(H_2) \sim 1.5 \times 10^{21}$ cm^{-2} (Kirk et al., in prep). The typical uncertainty on the fitted dust temperature was 0.3-0.4 K. The uncertainty on the column density was typically 10% and reflects the assumed calibration error of the Herschel maps (Kirk et al., in prep).

4.5 Spectroscopic data: line profiles

Figures 4.15 to 4.20 show a subset of our spectra across the cuts TMC 1-CP, TMC 1-NH3 and TMC 1-C. The lines of the most abundant species are optically thick at $A_v > 7$ mag and present self-absorbed profiles. However, only the lines of the main isotopologue are detected towards positions with $A_v < 7$ mag. Linewidths vary between ~0.3 to ~1.5 km s^{-1} depending on the transition. The largest line widths are measured in the ^{13}CO 1→0 lines with Δv~1.5±0.5 km s^{-1}. The higher excitation lines of species like CS and SO, and those of the high dipole moment tracers HCS$^+$, N_2H^+ and HCN, show Δv ~0.4± 0.1 km s^{-1}. Similar linewidths are observed in the NH_3 (1,1) and (2,2) inversion lines. Line broadening because of high optical depths might explain, at least partially, the large linewidths observed in the ^{13}CO and CS lines. High optical depths are also measured in the HCN 1→0 lines but the linewidth remains narrow, Δv ~0.4± 0.1 km s^{-1}. The narrow HCN linewidths are better understood as the consequence of the existence of layers with different excitation and hence chemical conditions along the line of sight.

Several authors have discussed the complex velocity structure of the TMC 1 cloud (Lique et al. 2006a; Fehér et al. 2016; Dobashi et al. 2018). Based on high velocity resolution (δv_{lsr} = 0.0004 km s^{-1}) observations of the HC_3N J=5→4 line, Dobashi et al. (2018) propose that the dense TMC 1 filament is composed of at least 4 velocity components at v_{lsr}=5.727, 5.901, 6.064 and 6.160 km s^{-1} with small linewidths, ~0.1 km s^{-1}, and a more diffuse component at 6.215 km s^{-1} with a linewidth of ~0.5 km s^{-1}. The velocity resolution of our observations (from 0.27 km s^{-1} at 7mm, to 0.16 km s^{-1} at 3 mm and 0.09 km s^{-1} at 2 mm) is not enough to resolve these narrow velocity components. In spite of this, in order to have a deeper insight in the velocity structure of the region, we have fitted the observed profiles using 5 velocity components centered at v_{lsr} = 5.0, 5.5, 6.0, 6.5, 7.0 km s^{-1} and with a fixed Δv = 0.5 km s^{-1}. Fig 4.2 shows the result of our fitting for three positions, offsets (+240",0), (+120",0) and (0,0) in the cut across TMC 1-CP. Interestingly, the number of velocity components detected in each transition remains constant with the position, even when the position (+240",0) is located 0.16 pc away from TMC 1-CP. However, the number of detected velocity components does vary from one transition (and species) to another. The five velocity components appear in the spectra of ^{13}CO 1→0, C^{18}O 1→0, and HCO$^+$ 1→0. The CS 2→1 and SO $2_3 \rightarrow 1_2$ spectra present intense emission in the 5.5 km s^{-1} and 6.0 km s^{-1} components and weak wings at the velocity of the other components. Interestingly, only the 5.5 km s^{-1} component presents intense emission in the HCN spectra. As a first approximation, in this paper we use the in-

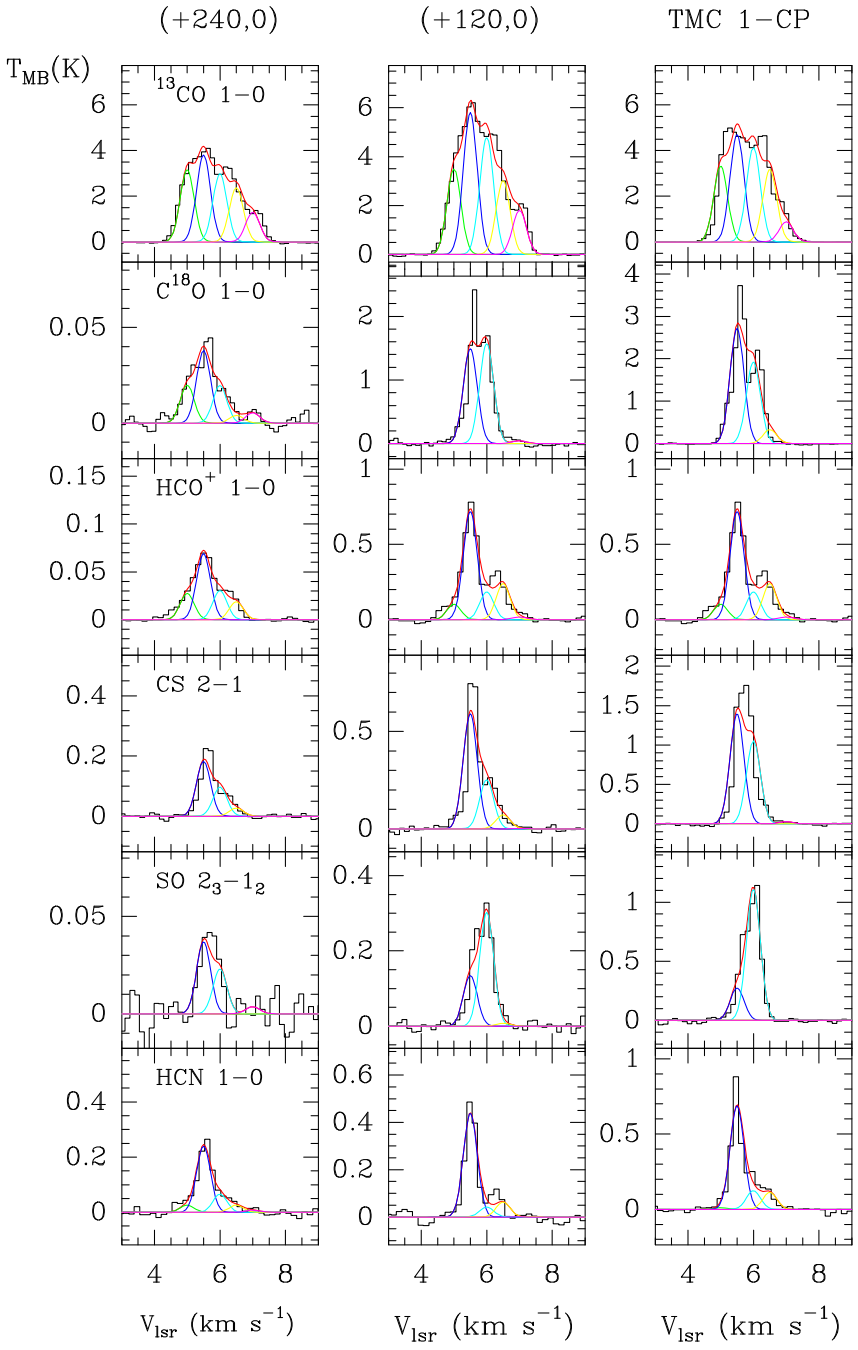

Figure 4.2: Selection of 30m spectra towards the offsets (+240",0), (120",0) and (0,0) in the TMC 1-CP cut. In order to investigate the velocity structure we have fitted the observed line profiles with 5 Gaussians with a fixed linewidth of 0.5 km s^{-1}, each centered at the velocities 5.0 (green), 5.5 (dark blue), 6.0 (light blue), 6.5 (yellow), 7.0 km s^{-1} (fuchsia).

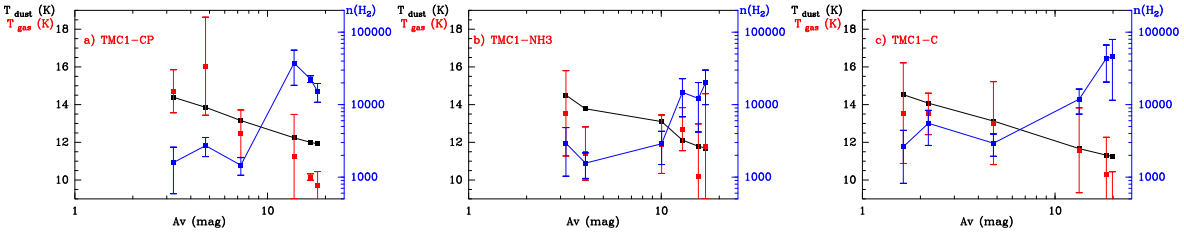

Figure 4.3: Estimated values of the dust temperature (black) as derived from Kirk et al. (in prep), gas temperature (red) and molecular hydrogen density (blue) across the cuts through TMC 1-CP (a), TMC 1-NH3 (b) y TMC 1-C (c).

Table 4.3: Physical conditions

Position	HSO (Kirk+19)		GEMS (This work)		NH_3 (Fehér+16)		Species and transitions used in the calculations
	T_d (K)	$N(H_2)$ ($\times10^{21}$ cm^{-2})	T_k (K)	$n(H_2)$ ($\times10^4$ cm^{-3})	T_k (K)	$n(H_2)$ ($\times$ 10^4 cm^{-3})	
TMC1-CP+0	11.92	18.20	9.7±0.8	1.5±0.4	10.6±1.1	1.0±0.3	^{13}CS - C^{34}S J=2→1, 3→2
TMC1-CP+30	12.00	16.71	10.2±0.2	2.3±0.3			^{13}CS - C^{34}S J=2→1, 3→2
TMC1-CP+60	12.24	13.74	11.2±2.0	3.7±1.9			^{13}CS - C^{34}S J=2→1, 3→2
TMC1-CP+120	13.16	7.27	12.5±1.2	0.15±0.04			C^{34}S - CS J=1→0, 2→1, 3→2
TMC1-CP+180	13.86	4.77	16.0±3.0	0.27±0.09			C^{34}S - CS J=1→0, 2→1, 3→2
TMC1-CP+240	14.39	3.25	14.7±1.1	0.16±0.10			CS J=1→0, 2→1, 3→2
TMC1-NH3+0	11.70	16.97	11.8±2.8	2.0±1.0	11.0±1.1	1.2±0.3	^{13}CS - C^{34}S J=2→1, 3→2
TMC1-NH3+30	11.79	15.58	10.2±2.8	1.2±0.8			^{13}CS - C^{34}S J=2→1, 3→2
TMC1-NH3+60	12.12	12.88	12.7±1.1	1.5±0.8			^{13}CS - C^{34}S J=2→1, 3→2
TMC1-NH3+120	13.10	10.04	11.9±1.6	0.29±0.14			C^{34}S - CS J=1→0, 2→1, 3→2
TMC1-NH3+180	13.78	4.04	11.4±1.4	0.16±0.06			CS J=1→0, 2→1, 3→2
TMC1-NH3+240	13.10	2.18	13.5±2.3	0.19±0.19			CS J=1→0, 2→1, 3→2
TMC1-C+0	11.26	19.85	8.5±2.0	4.5±3.4			^{13}CS - C^{34}S J=2→1, 3→2
TMC1-C+30	11.32	18.47	10.3±2.0	4.3±2.3			^{13}CS - C^{34}S J=2→1, 3→2
TMC1-C+60	11.67	13.34	11.6±2.2	1.19±0.45			^{13}CS - C^{34}S J=1→0, 2→1, 3→2
TMC1-C+120	13.13	4.79	11.1±1.9	0.54±0.25			C^{34}S - CS J=1→0, 2→1, 3→2
TMC1-C+180	14.08	2.20	13.5±1.1	0.55±0.28			C^{34}S - CS J=1→0, 2→1, 3→2
TMC1-C+240	14.53	1.63	13.5±2.7	0.26±0.18			CS J=1→0, 2→1, 3→2

tegrated line intensities to derive column densities and abundances. This is motivated by the limited spectral resolution (at 3 mm) and sensitivity (at 2 mm) of our observations that would introduce large uncertainties in the multi-velocity analysis. Taking into account the analysis of the line profiles described in this section, we can conclude that our results probe the moderate to high density gas detected at V_{lsr}=5.5 km s^{-1} and 6.0 km s^{-1}.

4.6 Physical conditions: Gas kinetic temperature and molecular hydrogen density

A detailed knowledge of the physical conditions is required for an accurate estimate of the molecular column densities and abundances. This is specially important in those positions where we have observed only one line and a multi-transition study is not possible. In these cases, the knowledge of the gas kinetic temperature and density is imperative. CS is a diatomic molecule with well known collisional coefficients (Denis-Alpizar et al. 2018; Lique

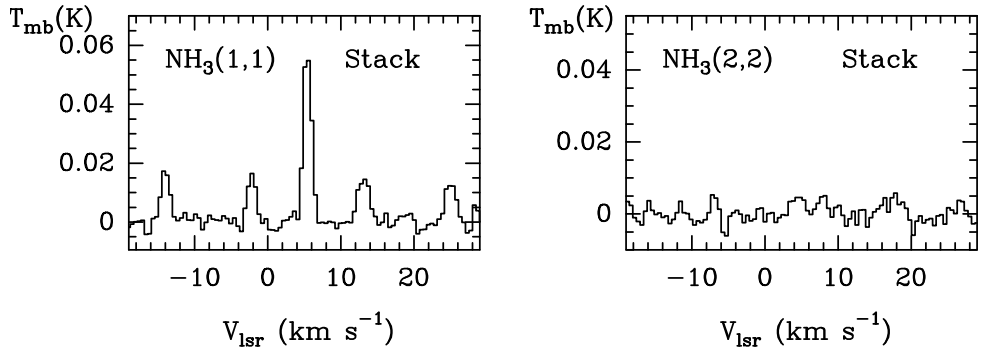

Figure 4.4: NH_3 (1,1) and NH_3 (2,2) lines profiles obtained by stacking all the band-K spectra observed with the 40m Yebes telescope ($A_V < 10$ mag) towards TMC 1.

et al. 2006b) that has been largely used as density and column density tracer in the interstellar medium. Moreover, the velocity-component analysis presented in Sect. 5 shows that CS is detected in the 5.5 km s^{-1} and 6.0 km s^{-1} components, which encompass the bulk of the dense molecular gas (compare, e.g., the $C^{18}O$ and CS profiles in Fig 4.2). Therefore, we consider that CS and its isotopologues are good tracers of the average physical conditions in this cloud.

In order to derive the gas physical conditions, we fit the line intensities of the observed CS, $C^{34}S$ and ^{13}CS lines using the molecular excitation and radiative transfer code RADEX (van der Tak et al. 2007). During the fitting process, we fix the isotopic ratios to $^{12}C/^{13}C$=60, $^{32}S/^{34}S$= 22.5 (Gratier et al. 2016) and assume a beam filling factor of 1 for all transitions (the emission is more extended than the beam size). Then, we let T_k, $n(H_2)$ and N(CS) vary as free parameters. The parameter space (T_k, $n(H_2)$ and N(CS)) is then explored following the Monte Carlo Markov Chain (MCMC) methodology with a Bayesian inference approach. In particular, we used the emcee (Foreman-Mackey et al. 2013) implementation of the Invariant MCMC Ensemble sampler methods by Goodman & Weare (2010). While $n(H_2)$ and N(CS) are allowed to vary freely, we need to use a prior to limit the gas kinetic temperatures to reasonable values in this cold region and hence break the temperature-density degeneracy that is usual in this kind of calculations.

The prior in the gas kinetic temperature is based on our knowledge of the dust temperature from Herschel maps (Kirk et al., in prep). Gas and dust are expected to be thermalized in regions with $n(H_2)>10^4$ cm^{-3}. Friesen et al. (2017) estimated the gas kinetic temperature in a wide sample of molecular clouds based on the NH_3 (1,1) and (2,2) inversion lines, and obtained that the gas temperature is systematically ~1-2 K lower than the dust temperature obtained from the Herschel maps. This discrepancy is interpreted as the consequence of the single-temperature SED fitting procedure which assumes that all the dust is at the same temperature along the line of sight. Towards a starless core in which the dust in the surface is warmer than in the innermost region, this approximation would produce an overestimation of the dust temperature. In order to account for these effects, in our MCMC calculations we use a flat prior to the gas kinetic temperature with constant probability for T_k=T_d±5 K and zero probability outside.

In Table 4.3, we show the gas temperature and the density derived from the multi-line

fitting of CS and its isotopologues. Across the cuts, there are two differentiated regions: i) for Av<7.5 mag, the density is quite uniform and similar to a few 10^3 cm^{-3} and gas temperatures are about 13-15 K which corresponds to gas thermal pressure of ~5 × 10^4 K cm^{-3}. Hereafter, we will refer to this moderate density envelope as the *translucent* component; and ii) for Av>7.5 mag, the density is an order of magnitude larger, T_k~10 K and the density keeps increasing towards the extinction peak. Hereafter, we will refer to this region as the *dense* component. The gas pressure in the dense phase is about 10 times larger than in the translucent phase. The transition from one phase to the other occurs in < 60" (~0.04 pc) and it is not well sampled by our data (see Fig 4.3).

The low densities found in the translucent phase, n(H_2)~ a few10^3 cm^{-3}, might cast some doubts about our assumption of gas and dust thermal equilibrium. In order to check this hypothesis, we have tried to independently derive the gas kinetic temperature in this region using our NH_3 data. For that, we have stacked all the NH_3 (1,1) and (2,2) spectra obtained with the 40m Yebes telescope towards the positions with A_v < 10 mag of the three cuts. The stacked spectra are shown in Fig 4.4, with a good detection of the NH_3 (1,1) line while the NH_3 (2,2) line remains undetected. Even assuming a density as low as n(H_2)=10^3 cm^{-3}, a RADEX calculation shows that the non-detections of the (2,2) line implies an upper limit of < 15 K for the gas temperature, slightly lower than the dust temperature. It is remarkable that NH_3 is only detected in the 5.5 km s^{-1} velocity component while CS is detected in the 5.5 km s^{-1} and 6.0 km s^{-1} components. The upper limit to the gas kinetic temperature is only valid for the 5.5 km s^{-1} component that is very likely the densest and coldest component. We consider, therefore, that the temperature derived from the CS fitting is more adequate for our purposes and it is used hereafter in the molecular abundance calculations. In Sect. 8, we show that the temperatures obtained with our CS fitting are in good agreement with those predicted with the Meudon PDR code.

Another important assumption in our density estimate process is that the beam filling factor is 1 for all the transitions. This is based on the morphology of the Herschel maps that present smooth and extended emission in the translucent part. This assumption is questionable towards the extinction peaks where the column density map presents a steeper gradient (see Fig. 4.1). In Table 4.3 we also compare our estimates with previous ones by Fehér et al. (2016) towards TMC 1-CP and TMC 1-NH3, finding excellent agreement. The good agreement between our estimates and those derived from NH_3, which are not affected by different beam sizes, suggests that our assumption is not far from the reality. The derived densities for the translucent component are in good agreement with previous estimates of the envelope density by Schnee et al. (2010) and Lique et al. (2006a).

4.7 Molecular abundances

Beam averaged molecular column densities and abundances have been derived using RADEX and the collisional rate coefficients shown in Table 4.4. In the following, we add more details of the abundance calculations.

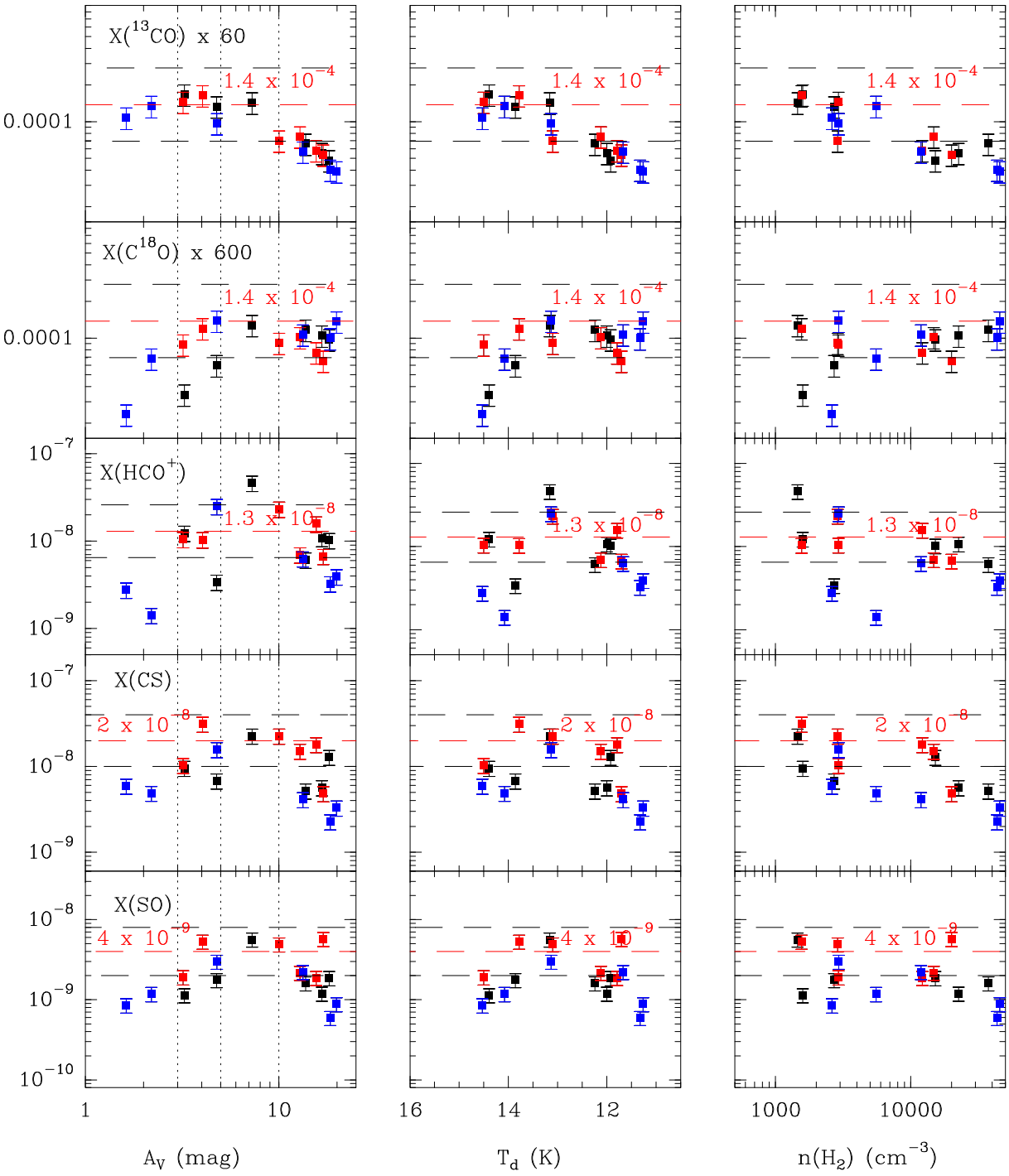

Figure 4.5: Estimated molecular abundances with respect to H_2 for the three studied cuts, TMC 1-CP (black squares), TMC 1-NH3 (red) and TMC 1-C (blue) as a function of the visual extinction (left column), dust temperature (center panel) and molecular hydrogen densities (right panel). The horizontal lines indicate a representative value in the translucent part (red dashed line) and a variation of a factor of 2 relative to it (black dashed lines). Vertical lines mark the A_V=3 mag, 5 mag and 10 mag positions.

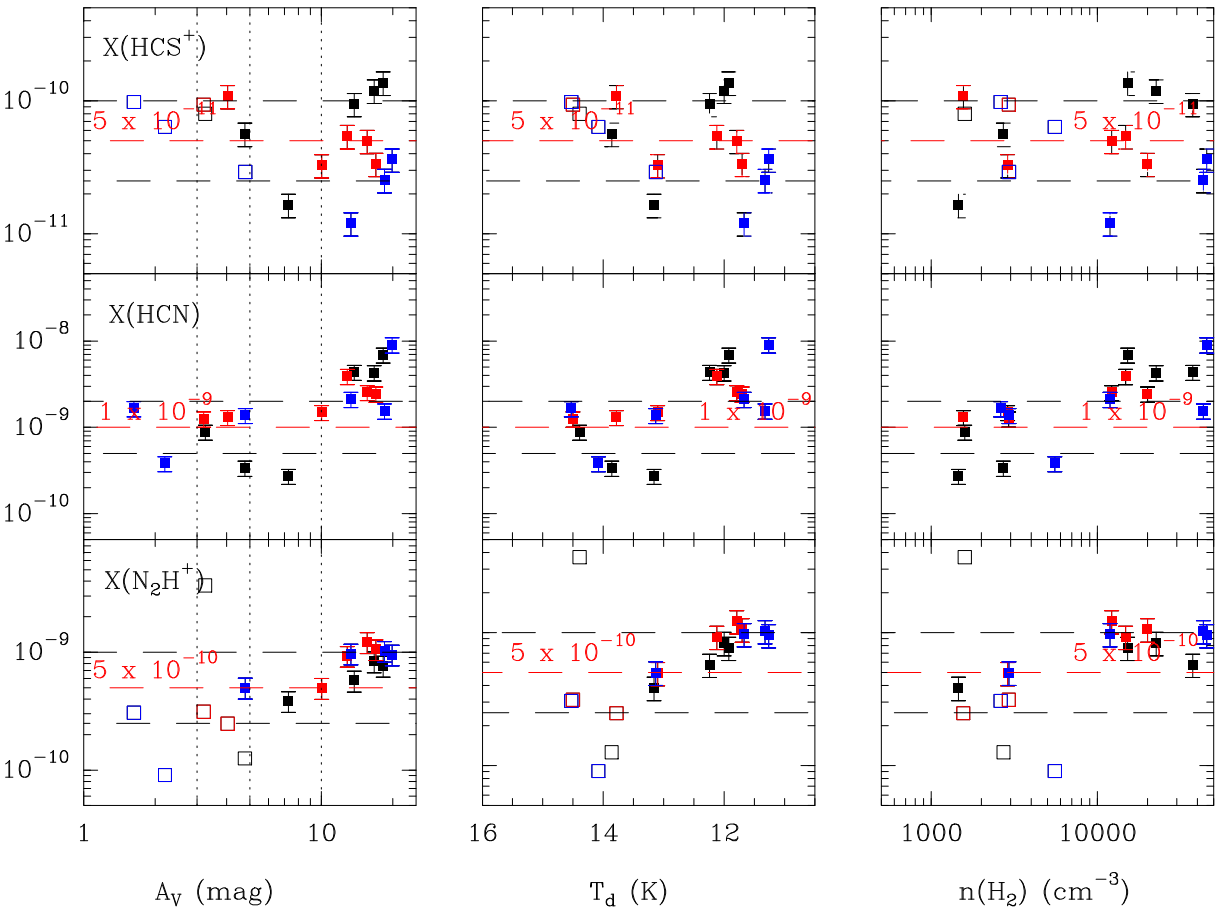

Figure 4.6: Estimated molecular abundances with respect to H_2 for the three studied cuts, TMC 1-CP (black squares), TMC 1-NH3 (red) and TMC 1-C (blue) as a function of the visual extinction (left column), dust temperature (center panel) and molecular hydrogen densities (right panel). Empty symbols correspond to upper limits. The horizontal lines indicate a representative value in the translucent part (red dashed line) and a variation of a factor of 2 relative to it (black dashed lines). Vertical lines mark the A_V = 3 mag, 5 mag and 10 mag positions.

Table 4.4: Collisional rate coefficients

Molecule		Reference
CO	p-H_2	Yang et al. (2010)
HCO^+	p-H_2	Flower (1999)
HCN	p-H_2	Ben Abdallah et al. (2012)
CS	p-H_2	Denis-Alpizar et al. (2018)
	He	Lique et al. (2006b)
SO	p-H_2	Lique & Spielfiedel (2007)
N_2H^+	p-H_2	Daniel et al. (2016)

4.7.1 ^{13}CO, C^{18}O

In this work, we use ^{13}CO and C^{18}O as tracers of CO by assuming fixed isotopic ratios. We use the physical conditions in Table 4.3 to derive ^{13}CO and C^{18}O column densities from the observations of the J=1→0 rotational line. This line is thermalized in the range of densities considered, therefore we do not expect any uncertainty in the molecular abundances because of the adopted densities. The major uncertainty comes from the opacity effects and possible variations in the CO/C^{18}O and CO/^{13}CO ratios.

For $A_V > 7$ mag, the ^{13}CO 1→0 line is expected to be optically thick ($\tau > 1$). In this region, we use C^{18}O as tracer of the CO abundance by assuming ^{16}O/^{18}O=600 (Wilson & Rood 1994). For A_V<7 mag, the ^{13}CO line is expected to be optically thin. In this region we have separately estimated the ^{13}CO and C^{18}O column densities which allows us to investigate the N(^{13}CO)/N(C^{18}O) ratio. Interestingly, this ratio increases from ~10 at A_V~7 mag to ~40 at A_V~ 3 mag. This result is not the consequence of the numerous velocity components along the line of sight. As shown in Fig 4.2, the T_b(^{13}CO 1→0)/T_b(C^{18}O 1→0) is >20 in all the velocity components towards the offset (240",0). Similarly T_b(^{13}CO 1→0)/T_b(C^{18}O 1→0)~4 in all velocity components towards the offset (120",0). The high N(^{13}CO)/N(C^{18}O) ratio is more likely the consequence of selective photodissociation and isotopic fractionation in the translucent cloud (Liszt & Lucas 1996; Bron et al. 2018). Because of isotopic fractionation in the external part of the cloud, a reliable estimate of N(^{12}CO) requires the comparison with a chemical model that includes a differentiated chemistry for the CO isotopologues. We will discuss this phenomenon in Sect. 8 when we compare our results with the Meudon PDR code predictions.

In Fig. 4.5, we plot the CO abundance derived as X(^{13}CO)×60 and X(C^{18}O)×600 as a function of visual extinction, dust temperature and density in the three observed cuts. The decrease of the ^{13}CO abundance for $A_V > 10$ mag is not real but the consequence of the high optical depth of the observed lines. In these dense regions, the rarer isotopologue C^{18}O is a better tracer of the CO abundance. The C^{18}O abundance sharply decreases for $A_V < 3$ mag. This is consistent with the threshold of $A_V = 1.5$ mag proposed by Cernicharo & Guelin (1987) for the C^{18}O detection. The CO abundance presents a peak of ~1.4×10^{-4} at Av ~ 3 mag (T_d=14 K) and seems to decrease towards the dense core phase. This is the expected behavior in this dark cloud where the dust temperature is lower than the evaporation temperature (T_{evap}=15-25 K), so that freeze-out is expected.

4.7.2 HCO$^+$, H^{13}CO$^+$, HC^{18}O$^+$

We have observed the J=1→0 rotational lines of HCO$^+$, H^{13}CO$^+$ and HC^{18}O$^+$. Column densities of all isotopologues have been derived using RADEX and the physical parameters in Table 4.3. In our column density calculations, we only use the H^{13}CO$^+$ and HC^{18}O$^+$ spectra because the HCO$^+$ J=1→0 line presents self-absorbed profiles. Then, we derive the HCO$^+$ column density from the rarer isotopologs assuming the isotopic ratios N(HCO$^+$)/N(H^{13}CO$^+$) = 60 or N(HCO$^+$)/N(HC^{18}O$^+$) = 600. The results are shown in Fig 4.5. The HCO$^+$ abundance is maximum at A_V~5−10 mag, i.e., 2 mag deeper than CO in the translucent cloud. The abundance of HCO$^+$ further decreases towards the dense high extinctions peaks.

4.7.3 CS, $C^{34}S$, ^{13}CS

The CS column densities have been derived as explained in Sect. 6. We find that the CS abundance is maximum at A_V~5−10 mag, with abundances with respect to H_2, X(CS) ~ 2×10^{-8}. The dispersion in the derived CS abundances in translucent cloud is of a factor of 2. For A_v >10 mag, the CS abundance sharply decreases suggesting a rapid chemical destruction or freeze out on the grain mantles.

4.7.4 SO, ^{34}SO

Several lines of SO and ^{34}SO lie in the frequency range covered by our setups (see Table 4.9). Regarding ^{34}SO, only the J=$2_3\rightarrow1_2$ has been detected towards the high extinction positions of the TMC 1-CP, TMC 1-NH3 and TMC 1-CP cuts. Towards the positions where we detect this ^{34}SO line, we measure T_b(SO $2_3\rightarrow1_2$)/T_b(^{34}SO $2_3\rightarrow1_2$) of 10−20. This implies opacities <2, i.e. the emission is moderately optically thick in the dense region. We have estimated the SO column density based on the RADEX fitting of the main isotopologue lines in the dense and translucent phases. Towards the high extinction peaks, we estimate an uncertainty of a factor of 2 in the column density estimates because of the moderate opacity. The derived SO abundances are ~1.8×10^{-9}, 0.9×10^{-9} and 2.9×10^{-9} for TMC 1-CP, TMC 1-C and TMC 1-NH3, respectively. Towards the dense phase, we have been able to derive the density from the T_b(SO $3_4\rightarrow2_3$)/T_b(SO $2_3\rightarrow1_2$) ratio, obtaining values fully consistent with those in Table 4.3. Our abundance estimate towards TMC 1-CP is consistent with previous estimates by Ohishi & Kaifu (1998), Agúndez & Wakelam (2013) and Gratier et al. (2016). The overabundance of SO towards TMC 1-NH3 has been already pointed out by several authors (Lique et al. 2006a and references therein). Similarly to HCO^+ and CS, SO presents its maximum abundance at A_v~5-10 with a peak value of ~5×10^{-9}.

4.7.5 HCS^+

Because of the weak intensities of the HCS^+ lines, we have only detected one line per position which prevents a multi-transition study. In order to estimate the HCS^+ abundances we have assumed the physical conditions in Table 4.3 and used the HCO^+ collisional rate coefficients. We obtain a large scatter in the HCS^+ abundances in the whole range of visual extinctions (see Fig 4.6), without any clear trend of the HCS^+ abundance with the visual extinction, dust temperature or gas density. Interestingly, we find differences among the HCS^+ abundance towards the different cuts, being larger towards TMC 1-CP than towards TMC 1-NH3 and TMC 1-C (see Fig 4.6).

4.7.6 HCN, $H^{13}CN$, $HC^{15}N$, N_2H^+

All the N-bearing species included in this subsection share some characteristics: i) they are only detected in the 5.5 km s^{-1} component and ii) present larger abundances towards the dense phase than towards the outer part of the cloud.

The hyperfine splitting of HCN allows us to estimate the opacity and excitation temperature (assuming a beam filling factor of 1 and equal excitation temperature for all the hyper-

fine components) and hence, to obtain an estimate of the density and column density. In the dense region, the HCN 1→0 line presents deep self-absorption features (see Fig. A2, A4 and A6). Thus, we use the isotopologue $H^{13}CN$ to calculate the gas density and X(HCN) assuming $N(HCN)/N(HC^{13}CN)=60$. We obtain HCN abundances of $2-10 \times 10^{-9}$ and molecular hydrogen densities of a few $\times 10^5$ cm^{-3} in the dense cloud. It is remarkable that the densities derived from the HCN data are larger than those derived from CS and NH_3 by a factor of >10.

Relatively intense emission of the HCN 1→0 line is detected in the translucent cloud. Because of the large dipole moment of HCN, molecular hydrogen densities $>10^4$ cm^{-3} are required to achieve excitation temperatures > 5 K and hence detectable emission. One possibility is that the densities in the 5.5 km s^{-1} component of the translucent cloud are $n(H_2)>10^4$ cm^{-3}. In fact, following the procedure described above, we derive densities ~a few 10^4 cm^{-3} and $X(HCN)\sim 1\times10^{-9}$ (see Fig 4.6) in the $3<A_V<10$ mag range. Alternatively, radiative trapping could have an important role in the excitation of the HCN 1→0 line in TMC 1. Radiative excitation would explain the excitation of the HCN line without invoking higher densities in the 5.5 km s^{-1} velocity component. Assuming a core/envelope system (two-phase model) and using a Monte Carlo radiative transfer code, Gonzalez-Alfonso & Cernicharo (1993) explained the line intensities in TMC 1 with HCN abundances of $\sim 5\times10^{-9}$ all across the cloud. In this two-phase model, the HCN molecules in the envelope are excited by the photons coming from the core which is a bright source in the HCN 1→0 line without the need of invoking higher densities. The value thus derived by Gonzalez-Alfonso & Cernicharo (1993) is similar to that we have derived for the dense gas and a factor of ~5 larger than the HCN abundances we derive in the translucent cloud. Comparing with these results, we consider that our estimates of the HCN abundance based on one-phase molecular excitation calculations are accurate within a factor of 5−10.

Similarly to HCN, we have fitted the excitation temperature and opacity of the N_2H^+ 1→0 line based on the hyperfine splitting, and hence the total N_2H^+ column densities. This molecular ion has been almost exclusively detected towards the dense region with abundances of about 1×10^{-9} and densities of a few 10^4 cm^{-3}, quite consistent with those derived from CS. Towards the translucent cloud, we have detections only for $A_V > 5$ mag with abundances of $\sim 5\times10^{-10}$.

4.8 Chemical modeling of the translucent cloud

The increase in dust temperature at the edges of molecular clouds is understood as the consequence of dust heating by the surrounding interstellar radiation field (IRSF). Moreover, the high $N(^{13}CO)/N(C^{18}O)$ ratio measured in TMC 1 testifies that UV radiation has an active role in the molecular chemistry. To determine the value of the ambient UV field is hence a requisite for the appropriate chemical modelling of the region.

4.8.1 Estimate of the incident UV field in TMC 1: Dust temperature

Herschel has provided extensive H_2 column density and dust temperature maps, with high angular resolution (~36"), of nearby star-forming regions. These maps constitute an un-

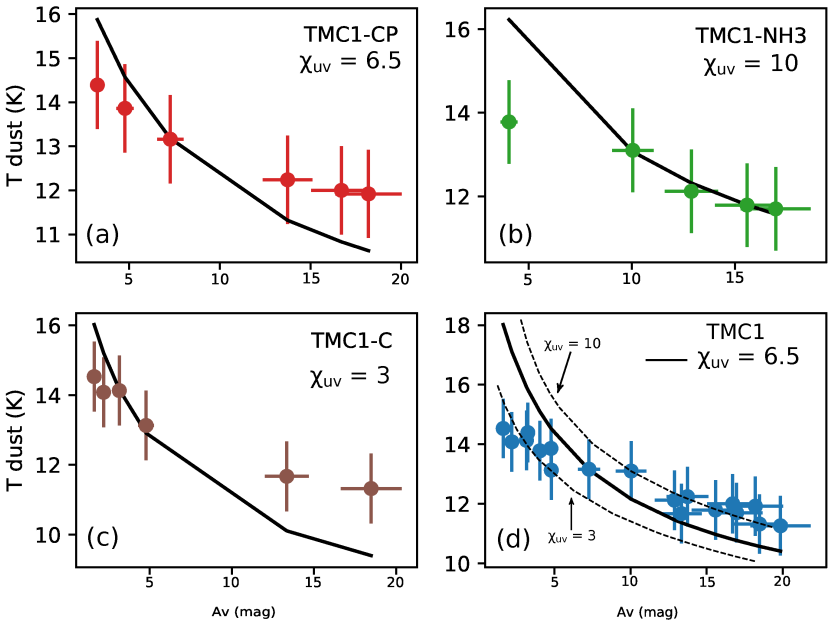

Figure 4.7: T_d-A_V fit following the parametric expression published by Hocuk et al. (2017) for the observed cuts: TMC 1-CP in (a), TMC 1-NH3 in (b), and TMC 1-C in (c). In panel (d), we try to fit all the positions from the three cuts together. For $A_V < 7.5$ mag, the best fit is found for $\chi_{UV} \sim 3$. For $A_V > 7.5$ mag, the best fit corresponds to $\chi_{UV} \sim 10$. The average value of $\chi_{UV} \sim 6.5$ is found to provide the best fit for the whole TMC 1 region.

Table 4.5: PDR chemical models

	ζ_{H_2} (s^{-1})	C/H	C/O	S/H
A	5×10^{-17}	1.38×10^{-4}	0.4	1.5×10^{-5}
B	5×10^{-17}	7.90×10^{-5}	0.4	1.5×10^{-5}
C	5×10^{-17}	3.90×10^{-5}	0.4	1.5×10^{-5}
D	5×10^{-18}	1.38×10^{-4}	0.4	1.5×10^{-5}
E	1×10^{-16}	1.38×10^{-4}	0.4	1.5×10^{-5}
F	5×10^{-17}	1.38×10^{-4}	1.0	1.5×10^{-5}
G	5×10^{-17}	1.38×10^{-4}	0.8	1.5×10^{-5}
H	5×10^{-17}	7.90×10^{-5}	1.0	1.5×10^{-5}
I	5×10^{-17}	7.90×10^{-5}	1.0	8.0×10^{-7}
Best-fit	5×10^{-17}	7.90×10^{-5}	1.0	8.0×10^{-7}

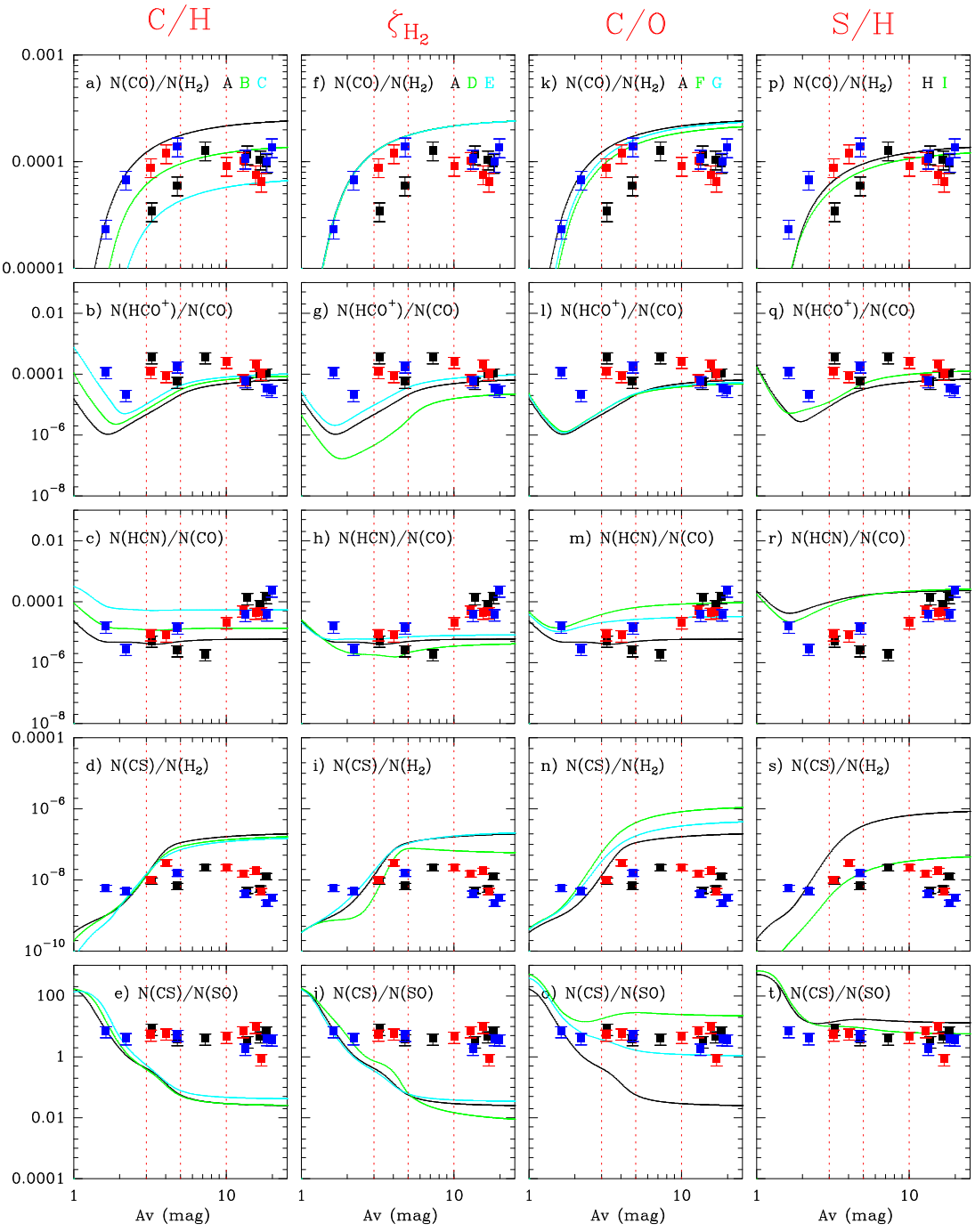

Figure 4.8: Comparison between the predictions of models listed in Table 4.5 and the cumulative column densities derived in TMC 1. In this Figure, we have selected N(CO)/N(H_2), N(HCO^+)/N(CO), N(HCN)/N(CO), N(CS)/N(H_2) and N(CS)/N(SO) to explore the parameter space, where N(CO) has been derived from our observations as N(CO)=600×N($C^{18}O$) and N(H_2)=A_V(mag)×10^{21} cm^{-2}. The observational points are indicated with squares and different colors correspond to the three observed cuts as follows: black for TMC 1-CP, red for TMC 1-NH3 and blue for TMC 1-C. Dashed red lines indicate A_V = 3 mag (C^+/C/CO transition region), A_V = 5 (translucent cloud) and A_V =10 mag (dense region).

precedented opportunity to determine the incident UV field and its local variations due to the nearby star formation activity. Dust temperatures are established by the radiative equilibrium balance between the absorption of UV/visible photons and the emission at a given temperature, T_d. In the cloud border, the exact value of T_d depends on the local IRSF and the absorption efficiencies of grains that are dependent on the grain composition and size. Deeper in the cloud, grain heating is produced by near and mid-infrared emission coming from the warm dust layer at the surface of the cloud (Zucconi et al. 2001). The direct calculation of the local UV field as a function of the dust temperature is hampered by our poor knowledge of the grain composition and its detailed variation across the cloud. Another fundamental problem is that in our part of the Galaxy the dust heating is dominated by the visible part of the ISRF, and the visible/IR part of the ISRF does not scale in a simple way with the ultraviolet part. Hence, the UV field derived from the dust temperature can only be considered as a first guess of the local UV flux.

Alternatively, we can try to fit the observational data with a simple analytical expression. Different attempts have been done to derive parametric expressions that relates the UV ambient field and the dust temperature as a function of the visual extinction (Hollenbach et al. 1991; Zucconi et al. 2001; Garrod & Pauly 2011; Hocuk et al. 2017). Most of them provide a good fitting of the observed T_d as a function of the incident UV field, χ_{UV}, in a given range of visual extinctions but have problems to fit the whole range, from A_V=0.01 to A_V>50 mag. We have used the most recent parametric expression by Hocuk et al. (2017) to obtain an estimate of the incident UV field. This expression is well adapted to the range of visual extinctions relevant to this paper (3 mag < A_V < 20 mag) and is consistent with what one would expect for a mixed carbonaceous-silicate bared grains.

$$T_d = [11 + 5.7 \times \tanh(0.61 - \log10(A_V))]\chi_{UV}^{1/5.9} \tag{4.1}$$

where χ_{UV} is the UV field in Draine units and the the visible/IR part of the IRSF is assumed to scale with χ_{UV}.

Fig 4.7 shows the T_d-A_V plots for the 3 cuts considered in this paper. None of the cuts can be fitted with a single value of the UV field. In fact, the dense cloud (A_V> 7.5 mag) is better fitted with χ_{UV}~10 while the translucent cloud is fitted with χ_{UV}~ 3. Moreover, the three observed cuts share the same behavior without any hint of variation of χ_{UV} from one cut to another (see Fig 4.7). One compelling possibility is that this break at A_V~ 7.5 mag is caused by a change in the grain properties. A thick layer of ice would allow the dust to be warmer by up to 15% at visual extinctions > 10 mag, i.e., the dense component (Hocuk et al. 2017). In fact, if we decrease the dust temperature in the dense regions by this factor, we could explain all the positions with χ_{UV}~3. This interpretation is also consistent with the sharply decrease in the abundances of the C- and S- bearing molecules with visual extinction in the dense phase. We cannot discard, however, local variations with the local UV field being lower in the northern cut (TMC 1-C) than in the southern cuts TMC 1-NH_3 and TMC 1-CP. As commented above, this is a first guess of the local χ_{UV}. In next section, we will confirm the derived values of χ_{UV} by comparing gas temperatures and chemical abundances with the predictions of the Meudon PDR code.

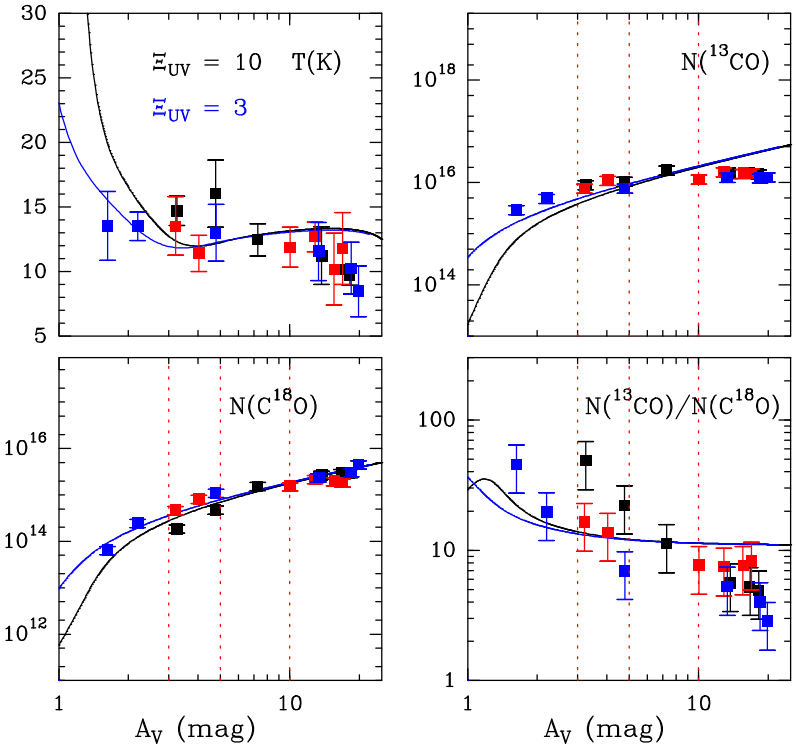

Figure 4.9: Comparison between our "Best-fit" model (see Table 4.5) and the molecular abundances derived in this work. The black line corresponds to the side with χ_{UV}=10 and the blue line to χ_{UV}=3. Dashed red lines indicate A_V=3 mag, 5 mag and 10 mag. The observational points are indicated with squares as in Fig 4.8.

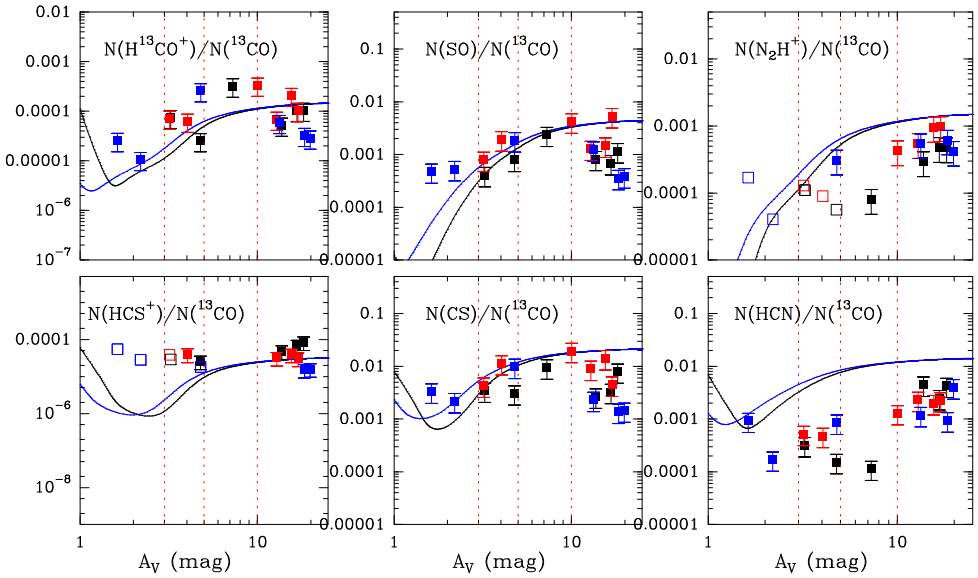

Figure 4.10: Comparison between our "Best-fit" model (see Table 4.5) and the molecular abundances derived in this work. The black line corresponds to the side with χ_{UV}=10 and the blue line to χ_{UV}=3. Dashed red lines indicate A_V=3 mag, 5 mag and 10 mag. The observational points are indicated with squares as in Fig 4.8.

4.8.2 Chemical code

We use the steady state gas-phase Meudon PDR code 1.5.2 (Le Petit et al. 2006; Goicoechea & Le Bourlot 2007; Gonzalez Garcia et al. 2008; Le Bourlot et al. 2012) to estimate the C, O and S elemental abundances. This code computes the steady-state solution to the thermal balance and gas-phase chemical network using accurate radiative transfer calculations and a plane-parallel geometry. The model explicitly considers the H_2 formation on the grain surfaces and adsorption/desorption of H and H_2 from grains. It does not include the accretion/desorption mechanisms for other gas-phase molecules. We assume gas phase elemental abundances below the solar values to take approximately into account depletion effects. The Meudon PDR code uses an extensive gas-phase chemical network which includes the reactions for the ^{13}C and ^{18}O isotologues allowing the direct comparison of chemical predictions with the observed ^{13}CO and C^{18}O column densities.

As a first step, we run a series of models in order to explore the parameter space to determine the values of the cosmic ray ionization rate and elemental abundances that best fit our observations (see Table 4.5). The adopted physical structure is based on our previous calculations, the 'a priori' knowledge of the source (see Ebisawa et al. 2019 and references therein) and the assumption of pressure equilibrium. In practice, we carried out the calculations for an isobaric plane-parallel 30 mag cloud with a constant pressure of 5×10^4 K cm^{-3}, consistent with the physical parameters derived from our observations. Our cloud is illuminated by a UV field, $\chi_{\rm UV}^{\rm front}$, from the front side and $\chi_{\rm UV}$ =1 from the back. We consider two values of $\chi_{\rm UV}^{\rm front}$, $\chi_{\rm UV}^{\rm front}$=10 and 3, which is the range of values derived in Section 8.1. This simple plane-parallel geometry mimics the scenario of a compressed gas layer illuminated from the front proposed by Ebisawa et al. (2019) on the basis of OH 18cm observations.

Fig. 4.8 shows the predicted N(CO)/N(H_2), N(HCO$^+$)/N(CO), N(CS)/N(H_2), and N(CS)/N(SO) ratio as a function of the visual extinction for $\chi_{\rm UV}$ =10, where N(X) is the cumulative column density from 0 to A_V mag of the species X. In general, any line of sight passes through the illuminated cloud surface and the cumulative column density is the parameter directly related with the observed line intensities. In the first column, we show the behavior of the observed abundances under changes in C/H. Here we compare the predicted cumulative column density N(CO) with the observed column density of C^{18}O×600 to avoid isotopic fractionation effects. For A_V >3 mag, all the carbon atoms are basically locked in CO and C/H is well determined from the measured CO abundance. Our peak CO abundance, ~1.4 × 10^{-4}, shows that even at the low extinction of A_V = 3 mag, carbon is depleted by a factor of ~2. Beyond A_V = 3 mag, the carbon depletion progressively increases to reach values of ~3 at A_V ~10 mag.

In the second column, we investigate the chemical effect of varying $\zeta(H_2)$. The value of $\zeta(H_2)$ mainly affects the predicted N(CS) and the N(HCO$^+$)/N(CO) abundance ratios. The abundance of CS is also dependent on the value of S/H (third column of Fig. 4.8) which justifies to use N(HCO$^+$)/N(CO) as a probe of $\zeta(H_2)$. Values of $\zeta(H_2)$ >(5−10) ×10^{-17} s^{-1} are required to fit the observed values of the N(HCO$^+$)/N(CO) ratio in TMC 1. The fit is, however, not perfect with several points being over model predictions for all the considered values of $\zeta(H_2)$. We will discuss the value of $\zeta(H_2)$ in more details in Sect 8.5.

The N(HCN)/N(CO) as well as N(CS)/N(SO) abundance ratios are highly dependent on the C/O gas phase elemental ratio (third column of Fig. 4.8). We have not been able to fit

both ratios with a single C/O value. While the observed N(HCN)/N(CO) is well explained with C/O~0.4, N(CS)/N(SO) points to a value of the C/O ~0.8−1. As commented in Sect. 4.5, the HCN abundance might be underestimated in this moderate density gas. Therefore, we consider that N(CS)/N(SO) is a more reliable tracer of the C/O ratio. Note also that the N(CS)/N(SO) ratio is not very dependent on the S/H value (column 4 of Fig. 4.8) which supports the usage of this ratio to determine C/O. Interestingly, there is not a systematic trend of the N(CS)/N(SO) ratio in the translucent cloud that could be identified with a preferential oxygen depletion in this range of visual extinctions. Our data are best fit with C/O$\sim 0.8-1$. Once the values of $\zeta(H_2)$ and C/O are fixed, the abundances of CS and SO depend almost linearly with S/H (column 4). The abundance of CS is well fitted with S/H~8×10^{-7}, i.e., a factor of 20 lower than the solar value, S/H ~1.5×10^{-5}.

Following the analysis described above, we propose that C/H~7.9×10^{-5}, C/O~1, and S/H~8×10^{-7}, are the most likely values in the translucent cloud, hereafter our "Best-fit" model. In the following we extensively compare this model with our observations.

4.8.3 Carbon depletion and gas temperature

The gas kinetic temperature is determined by the balance between the heating and cooling processes at a given distance from the cloud border. In molecular clouds, CO is the main coolant and carbon depletion is determining the gas temperature. The CO lines are optically thick even at moderate visual extinctions and the CO line profiles usually present self-absorption features. For this reason, we have used the rarer isotopologue $C^{18}O$ to estimate the total CO column density by assuming a fixed N(^{12}CO)/N($C^{18}O$) ratio. The CO abundances thus obtained were used to compare with observations in Fig. 4.8.

The Meudon PDR code computes the abundances of CO, ^{13}CO and $C^{18}O$ taking into account the self-shielding effects for ^{12}CO and ^{13}CO, and the effects of the possible overlap between H, H_2, CO and ^{13}CO UV transitions, as well as the isotopic fractionation reactions. Here, we directly compare the predicted ^{13}CO and $C^{18}O$ abundances with observations. In Fig 4.9 we show our "best-fit" model with χ_{UV}=10 (black) and χ_{UV}=3 (blue) predictions with the observed ^{13}CO and $C^{18}O$ column densities. For further comparison, we also plot the gas temperature as computed by the Meudon code. We find quite good agreement of the observed T_{gas} and N($C^{18}O$) in the TMC 1-CP and TMC 1-NH3 cuts for χ_{UV}=10 and 3. In these cuts, we do not have any observed position with $A_V < 3$ mag. On the other hand, the gas kinetic temperature in the cut across TMC 1-C are better fitted with χ_{UV}=3. These results support the interpretation of a lower UV field towards in the northern part of the filament than towards the south. In this plot we also represent N(^{13}CO) and the N(^{13}CO)/N($C^{18}O$) ratio as a function of the visual extinction from the cloud border. Although we have a good qualitative agreement between the derived N(^{13}CO) and observations, the model underestimates N(^{13}CO) in the outer $A_V < 5$ mag. We consider that this disagreement is due to the fact that, at these low visual extinctions, N(^{13}CO) is very sensitive to the uncertainties in the UV illuminating field and the detailed cloud geometry.

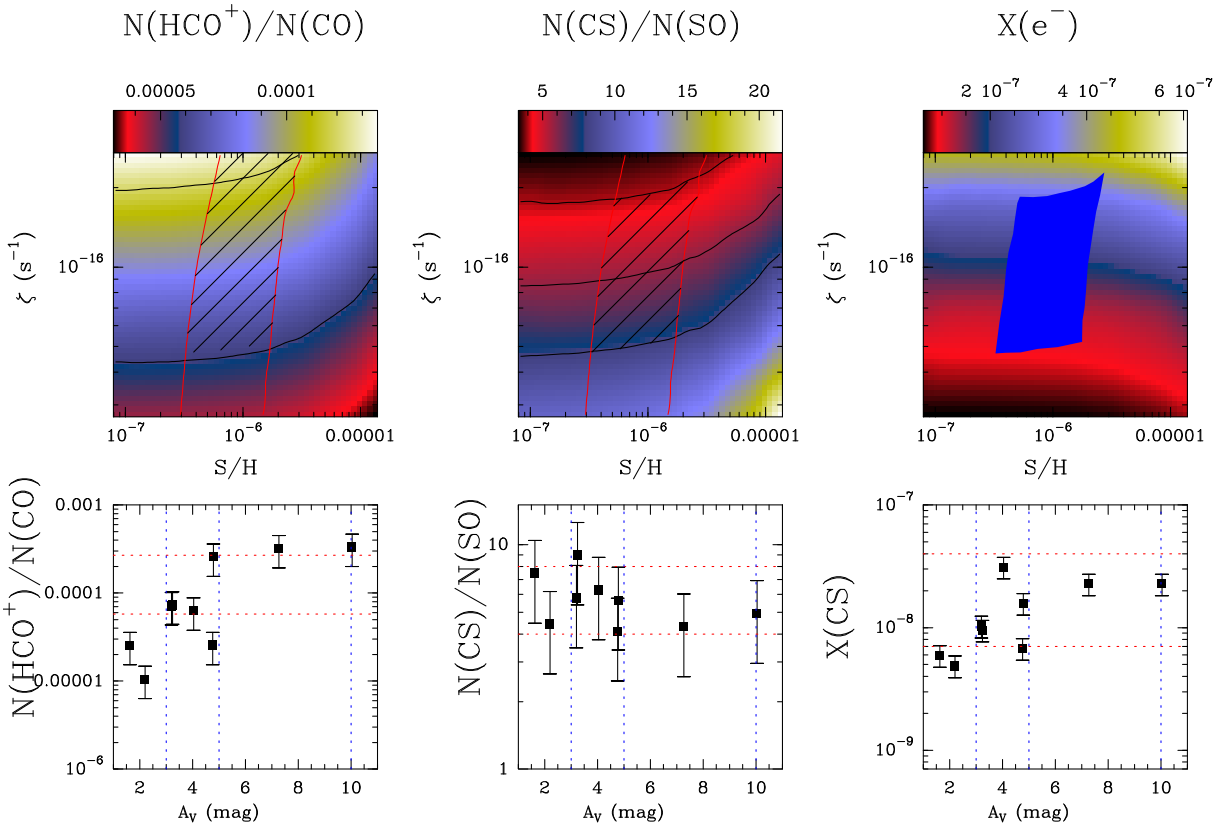

Figure 4.11: *Left:* The color map shows the N(HCO$^+$)/N(CO) ratio as a function of ζ_{H_2} and S/H. Black contours correspond to N(HCO$^+$)/N(CO)=5.8×10^{-5} and 1.2×10^{-4}. Red contours indicate X(CS)=1×10^{-8} and 4×10^{-8}, which is the range of CS abundances derived in the translucent part. *Center:* The color map shows the N(CS)/N(SO) ratio as a function of ζ_{H_2} and S/H. Contours are N(CS)/N(SO)=4, 5.8, and 8. Red contours are the same as in the left panel. *Right:* Gas ionization fraction, X(e$^-$)=n(e$^-$)/n$_H$, as a function of ζ_{H_2} and S/H. According with our data, the blue region marks the range of values expected in the translucent part of TMC 1. Bottom panels show the observed values in the translucent cloud. Dashed red lines are: 5.8×10^{-5} and 2.7×10^{-4} in the N(HCO$^+$)/N(CO) panel; 4 and 8 in the N(CS)/N(SO) panel and 7×10^{-9} and 4×10^{-8} in the X(CS) panel.

4.8.4 Depletion of oxygen and sulfur

The determination of the O and S depletions is very likely the most challenging part of this project. The main oxygen reservoirs, O, H_2O and OH, cannot be observed in the millimeter domain and oxygen depletion has to be derived indirectly from the C/O ratio. As commented above N(HCN)/N(CO) and N(CS)/N(SO) are good tracers of the C/O ratio. Since we have problems to account for observed abundances of HCN and N_2H^+, we prefer to use N(CS)/N(SO) as a proxy of the C/O ratio.

Atomic S in the outer layers of the cloud and solid-H_2S in the dense cores are predicted to be the main sulfur reservoirs and both of them are difficult to observe. Thus, we need to derive the S abundance indirectly by observing minor sulfur compounds. The most abundant easily observable S-species in gas phase are CS, SO and H_2S. Out of them, only CS and SO are thought to be formed in gas phase while the formation of H_2S is only understood as the product of the hydrogenation of S on the grain surfaces. Our team has been working in improving the sulfur chemical network by revising the rates of important reactions in the CS and SO chemistry at low temperatures. Fuente et al. (2016) already presented calculations of the S + O_2 → SO + O rate at temperatures <50 K. In this paper, we include new calculations of the SO + OH → SO_2 + O reaction rate for temperatures below 300 K (see Appendix A). These new rates have been included in the gas-phase chemical network used by the Meudon code to obtain the most accurate determination of the amount of sulfur in gas phase. Fig. 4.10 shows the comparison of the CS, SO, HCS^+, HCN, and N_2H^+ column densities with model predictions. We have a fair agreement for all the species except for the N-bearing compounds HCN and N_2H^+ using C/O=1 and S/H=8×10^{-7}.We also include HCS^+ in our comparison although we have very few detections of this species in the translucent phase.

4.8.5 Gas ionization fraction, X(e^-)

The gas ionization fraction determines the coupling of the gas dynamics with the magnetic field and it is, therefore, a key parameter in star formation studies. At the scale of the molecular cloud, UV photons and cosmic rays are the main ionization agents in the diffuse/translucent phase, and carbon and sulfur are the main electron donors. At the scale of protostellar disc formation, the dust is the main contributor to the magneto-hydrodynamics resistivity. In the following, we discuss the uncertainties in our estimate of X(e^-) and the implications of our results in this context.

Over the past three decades, several attempts have been carried out to estimate ζ_{H_2} in dense cores from measurements of the abundances of various chemical species (see compilation by Padovani et al. 2009). The values of ζ_{H_2} derived by Caselli et al. (1998) through DCO^+ and HCO^+ abundance ratios span a range of about two orders of magnitudes from $\sim10^{-17}$ s^{-1} to $\sim$ 10^{-15} s^{-1}. This large scatter may reflect intrinsic variations of the cosmic rays flux from core to core but, as discussed by the authors, might be the consequence of the sensitivity of the results to several model assumptions, mainly the value of specific chemical reaction rates and elemental depletions. In order to minimize these uncertainties, Fuente et al. (2016) used a gas-phase chemical model to fit the abundances of 22 neutral and ionic species in order to determine the local value of the cosmic ray ionization rate together with

the depletion factors towards Barnard 1b. They estimated a value of ζ_{H_2} between 3×10^{-17} s^{-1} and 10^{-16} s^{-1}, i.e., an uncertainty of a factor of 4.

Several works have been dedicated to estimate ζ_{H_2} in diffuse clouds. The discovery of significant abundances of H_3^+ in diffuse clouds by McCall et al. (1998) led to values of ζ_{H_2} $> 2 \times 10^{-16}$ s^{-1}. Given the simplicity of H_3^+ chemistry, this value was widely accepted as considered more reliable than previous estimates. Neufeld et al. (2010) found $\zeta_{H_2} \approx 1.2$ to 4.8×10^{-16} s^{-1} from observations of OH^+ and H_2O^+in clouds with low molecular fraction. A recent comprehensive work by Neufeld & Wolfire (2017) established that the ionization rate per H_2 in diffuse molecular gas is $\zeta_{H_2} = (5.3\pm1.1)\times10^{-16}$ s^{-1}.

In this work we have estimated the elemental abundances and $X(e^-)$ in the translucent part of TMC 1. Our observations highlight the low density (~ a few 10^3 cm^{-3}) cloud envelope, i.e., the transition from the diffuse medium to the dense cores. In the translucent envelope where most of the carbon is already in molecular form, $X(e^-)$ is mainly dependent on ζ_{H_2} and the elemental abundance of S. In order to obtain the range of values of ζ_{H_2} and S/H consistent with our observations we have run a grid of models with ζ_{H_2} = (1, 5.1, 8.6, 14.4, 24.4) $\times10^{-16}$ s^{-1} and S/H=(0.01, 0.018, 0.058, 0.10, 0.19, 0.34, 0.61 and 1.1) $\times10^{-5}$. All the other parameters are fixed to the values in the "Best-fit" model and χ_{UV}=3. We select the model predictions and observations at A_V=5 mag, as representative of the translucent phase. From our observations, we have derived values of $N(HCO^+)/N(CO) = 0.2 - 2.7 \times 10^{-4}$ at this visual extinction (see Fig. 4.11). Values of $N(HCO^+)/N(CO) > 1.3 \times 10^{-4}$ cannot be fitted with our grid of models (see Fig. 4.11). It is noticeable that an increase of ζ_{H_2} of a factor of 10, from ~3 $\times10^{-17}$ s^{-1} to ~2.2 $\times10^{-16}$ s^{-1}, only produces an increase of a factor of ~2–3, from ~5×10^{-5} to ~1.2×10^{-4}, in the predicted $N(HCO^+)/N(CO)$ ratio which makes it very difficult to estimate the value of ζ_{H_2} with an accuracy better than a factor of 10 based only on the $N(HCO^+)/N(CO)$ ratio. To further constrain the values of ζ_{H_2} and S/H, we have tried to fit X(CS) and N(CS)/N(SO) ratio, as well. The range of the observed values of N(CS)/N(SO) is of ~4 to 8 which is best fitted with ζ_{H_2} of ~ $0.5 - 1.8 \times10^{-16}$ s^{-1} and S/H ~ 0.4–2.2×10^{-6} (see Fig. 4.11). Taking all into account, we conclude that ζ_{H_2} = 0.5 - 1.8×10^{-16} s^{-1} in the TMC 1 translucent envelope. This value is similar to that found by Fuente et al. (2016) in Barnard 1b and it is within the range of the values obtained by Caselli et al. (1998) in dark cores. It is also consistent with the accepted value in diffuse clouds (McCall et al. 1998; Neufeld et al. 2010). Therefore, we do not add any evidence of variation of ζ_{H_2} within a factor of 3.

It is also interesting to find the relationship between ζ_{H_2} and $X(e^-)$, that is dependent on the local density and the elemental abundances. With the physical and chemical conditions derived in the studied region, we need S/H =$0.04 - 0.2 \times10^{-5}$ to account for the measured CS abundance (see Fig. 4.11a). As shown in Fig. 4.11, this would imply that $X(e^-) \sim 9.8 \times 10^{-8}$ - 3.6×10^{-7} in the transition from the diffuse to the dense medium in TMC 1.

4.9 Dense phase

In the following, we carry out a phenomenological analysis of the chemical changes observed across the cuts in the dense phase. The abundance of most molecules decreases with the visual extinction from A_V = 10 to ~20 mag. In Table 4.6 we show the estimated molecular abun-

Table 4.6: TMC 1 physical conditions and chemical abundances

Molecule	TMC 1-CP	TMC 1-NH3	TMC 1-C
X(CO)	9.7×10^{-5}	6.5×10^{-5}	1.4×10^{-4}
X(HCO^+)	1.0×10^{-8}	6.7×10^{-9}	3.9×10^{-9}
X(HCN)	7.0×10^{-9}	2.4×10^{-9}	9.0×10^{-9}
X(CS)	1.3×10^{-8}	4.8×10^{-9}	3.3×10^{-9}
X(SO)	1.8×10^{-9}	2.9×10^{-9}	8.8×10^{-10}
X(HCS^+)	1.4×10^{-10}	3.3×10^{-11}	3.6×10^{-11}
X(N_2H^+)	7.7×10^{-10}	1.0×10^{-9}	9.6×10^{-10}
R_{TD}(CO)	1.7	2.6	1.2
R_{TD}(HCO^+)	1.3	1.9	3.3
R_{TD}(HCN)	0.1	0.4	0.1
R_{TD}(CS)	1.5	4.2	6.0
R_{TD}(SO)	2.2	1.4	4.5
R_{TD}(HCS^+)	0.3	1.5	<1
R_{TD}(N_2H^+)	<0.8	<0.6	<0.6

Notes:
Molecular abundances with respect to H_2 towards the (0",0") positions of TMC 1-CP, TMC 1-NH3 and TMC 1-C. R_{TD}(X) is the ratio between the abundance of the species X in the translucent phase (red lines in Fig 4.5 and 4.6) over the abundance towards each cut extinction peak [i.e. offset (0",0")].

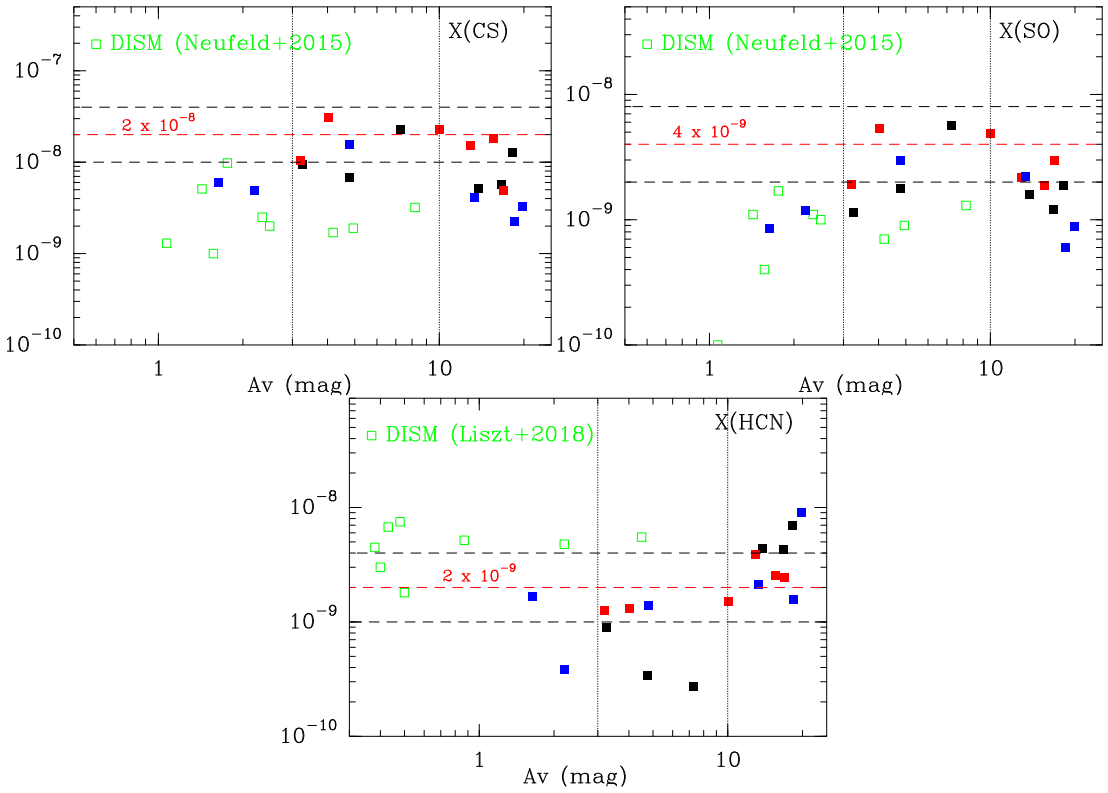

Figure 4.12: Comparison between the abundances in TMC 1 with those observed in the diffuse gas by Neufeld et al. (2015) and Liszt et al. (2018).

dances and the values of $R_{TD}(X)$, defined as the ratio between the abundance of the species X in the translucent phase (red lines in Fig 4.5 and 4.6) over the abundance towards each cut extinction peak [offset (0",0")]. Values of $R_{TD}(CO)$, $R_{TD}(HCO^+)$, $R_{TD}(CS)$ and $R_{TD}(SO)$ >1 are found in the three studied cuts. We cannot derive any conclusion, however, on HCS^+ with very few detections in the translucent phase and an abundance a factor of ~4 larger towards TMC 1-CP than towards the TMC 1-NH3 and TMC1-C. The value of $R_{TD}(HCO^+)$ is very dependent on the CO depletion and the change in the gas ionization fraction in the higher density core center, $X(e^-) \propto \sqrt{\zeta_{H_2}/n}$. The variations in the CO, CS and SO abundances are better understood as the consequence of the freeze-out of S- and O-bearing molecules onto the grain mantles. The depletions of these molecules are slightly higher towards TMC 1-C than towards TMC 1-NH3 and TMC1-CP, suggesting a different density structure and/or a more evolved chemical state for the former.

4.10 Gas chemical composition from the diffuse to the translucent phase

In general we refer to the gas with densities of $n_H < 100$ cm^{-3} and T_k~100 K as diffuse gas. In this phase, the gas is partially atomic and CO is not a good tracer of the total mass of

Table 4.7: Elemental gas phase abundances

	Solar[1]	DIFF$_{min}$[2]	DIFF$_{max}$[3]	TRANSLUCENT[4]	TMC 1-CP[5]	Orion KL[6]	L1157-B1[7]
C/H	2.88×10^{-4}	2.20×10^{-4}	1.76×10^{-4}	$\mathbf{8.00\times10^{-5}}$	9.00×10^{-5}	1.79×10^{-4}	1.79×10^{-4}
O/H	5.75×10^{-4}	5.50×10^{-4}	3.34×10^{-4}	$\mathbf{8.00\times10^{-5}}$	6.40×10^{-5}	4.45×10^{-4}	4.45×10^{-4}
S/H	1.50×10^{-5}	1.25×10^{-5}	3.50×10^{-6}	$\mathbf{8.00\times10^{-7}}$	$<8.00\times10^{-8}$	1.43×10^{-6}	6.00×10^{-7}

Refs: [1] Lodders et al. (2003); [2] Minimum depletion case of Jenkins (2009); [3]Maximum depletion case of Jenkins (2009); [4] This work; [5] Agúndez & Wakelam (2013); Vidal et al. (2017); [6] Esplugues et al. (2014); [7] Holdship et al. (2016).

molecular gas. The molecular content of the diffuse gas has been determined by a series of studies based on the molecular absorption lines at mm wavelengths which revealed a surprisingly rich chemistry (see Liszt et al. 2018 and references therein). Translucent clouds are characterized by n_H ~ a few 1000 cm^{-3}, T_k~20−30 K, the gas is mostly in molecular form and CO is a good mass tracer. The higher densities of this phase permit the detection of low-excitation molecular emission lines. Although difficult, the comparison of the chemical composition of the diffuse and translucent phases might provide important clues for the understanding of the chemical evolution of the gas in the interstellar medium. All the species studied in this paper, except N_2H^+, have been detected in the diffuse gas. Interestingly, we have only one detection of N_2H^+ at A_V~5 mag with $N(N_2H^+)/N(HCO^+)$ ~0.02. Liszt & Lucas (2001) measured $N(N_2H^+)/N(HCO^+) < 0.002$ towards 3C111. This quasar is actually seen through a small hole (region of lower than average extinction) in an outlying cloud in the Taurus cloud complex (Lucas & Liszt 1998) and hence A_V~ 5 mag can be considered as a threshold for the N_2H^+ detection in Taurus.

In Fig 4.12 we show the comparison of the abundances with respect to H_2 of the studied molecules with those from our survey. The data towards 3C111 are indicated. There is a large dispersion in the plot of the molecular abundances as a function of the visual extinction. We recall that diffuse clouds are not only characterized by low values of the visual extinction but also for low hydrogen densities. Besides, in the diffuse gas, with several clouds along the line of sight, the visual extinction is not necessarily related to the local UV field. One can find a better correlation if one considers the abundances vs the local density and assumes that in the diffuse gas the local density is around 50-100 cm^{-3}. For HCO^+, SO and CS we find a trend with their abundances increasing with density from the diffuse to the translucent phase. All these molecules present their peak abundances in the translucent region. HCN might be the one exception to this rule with lower abundances in the translucent phase than in the diffuse gas. As discussed above, the HCN column densities might be severely underestimated in the translucent cloud. It is also interesting the case of HCS^+ which was detected in the diffuse medium by Lucas & Liszt (2002) with an abundance ratio $X(CS)/X(HCS^+)$~13±1 that is ~40 times lower than the value of $X(CS)/X(HCS^+)$~400 we have measured in the translucent cloud. This unveils a different formation path of CS in diffuse (dissociative recombination of HCS^+) and translucent (SO + C→CS + O) clouds.

4.11 Elemental depletions and grain growth

The depletion of an element X in the ISM is defined in terms of its reduction factor below the expected abundance relative to that of hydrogen if all of the atoms were in the gas phase,

$$[Xgas/H] = logN(X)/N(H) - log(X/H)_{\odot}. \quad (4.2)$$

In this expression, N(X) is the column density of element X and N(H) represents the column density of hydrogen in both atomic and molecular form, i.e., N(H I) + 2N(H_2). The missing atoms of element X are presumed to be locked up in solids within dust grains or in the icy mantle. In the diffuse gas, atomic absorption lines can be used to determine abundances by comparison with the atomic and molecular hydrogen column densities measured through Lyman alpha and Lyman-Werner transitions. Jenkins (2009) presents a comprehensive study of the elemental depletions in diffuse clouds. In general, depletions increase with the average density along the line of sight. However, depletions are observed to vary from one line of sight to another. Savage & Sembach (1996) interpreted these variations in terms of averages of warm (presumably low density) gas and cool (denser) gas. In his review, Jenkins (2009) distinguishes between two cases, “minimum” and "maximum" depletion to characterize the range of these variations in diffuse clouds.

In Table 4.7 we compare our estimates in the translucent part of TMC1 with the “minimum” and “maximum” depletion cases, in diffuse clouds. Our value of C/H is consistent within a factor of 2 with the “maximum” depletion diffuse case. A significant difference is found, however, in the O and S depletions which are ~4 times larger in the translucent phase than in the “maximum” depletion case. Although we observe a smooth increase in the C and O depletions with visual extinction in the translucent phase, the C/O ratio remains quite constant (~1). The scatter in the measured X(CS)/X(SO) values can hinder a smooth variation in the derived C/O value but an almost constant C/O ratio can be understood if the freeze-out of CO is the main process that changes the grain composition in this region. Regarding sulfur, we measure a depletion factor of ~7-40 in the translucent cloud. Although some authors like Jenkins (2009) casts doubts on this interpretation, it is widely accepted that sulfur is not depleted in diffuse clouds (see also Neufeld et al. 2015). Adopting this scenario, sulfur atoms (or ions) should be massively incorporated to dust grains from the HI/H_2 (A_V~1) to the C^+/C/CO transition phases to explain a depletion factor of ~7-40 in the translucent medium.

In Table 4.7 we also compare the depletions estimated in the translucent part of TMC 1 with the chemical composition towards TMC 1-CP. We have estimated the C and O depletions from the CO abundance reported by Agúndez & Wakelam (2013) and assumed C/O~1. The S depletion is based on recent results of Vidal et al. (2017). While C and O depletions agree within a factor of 2 with the values in the translucent cloud, sulfur depletion needs to be increased by at least a factor 10 (depletion of ~200 compared to solar) to account for the observed abundances of S-bearing molecules.

Following these findings, we propose that two strong S depletion events should occur across the cloud. The first one occurs in the transition from the diffuse to the translucent phase. In this transition, ~90% of the sulfur is incorporated into dust grains while ~10% of sulfur is hidden as atomic sulfur in the gas phase. The second strong depletion occurs in the

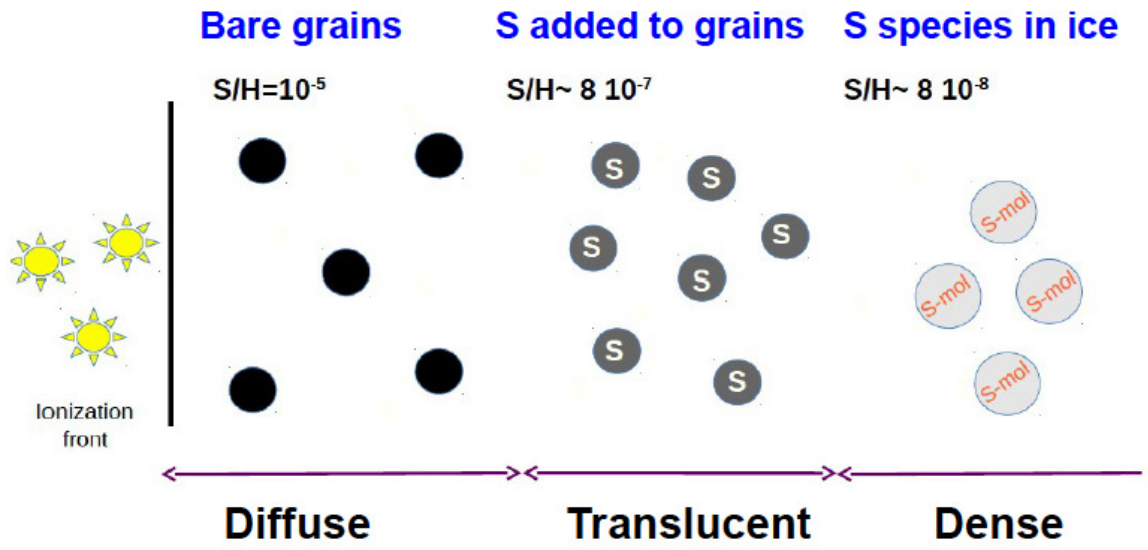

Figure 4.13: Scheme of the proposed scenario of the sulfur gas-phase/solid state evolution in TMC 1 (courtesy of S. Cazaux).

dense gas where a thick ice mantle is formed on the grain surfaces (an illustrative scheme of the proposed scenario is shown in Fig 4.13). The exact composition of the icy mantle is not well established yet. For large values of C/O and early times, atomic sulfur would remain as the main sulfur reservoir in the dense gas. These S atoms would become adsorbed on the icy surface, and would react with hydrogen atoms to produce solid HS and H_2S in ices. These latest reservoirs are supported by observations from the comet 67P with Rosetta showing that H_2S is the most important S-bearing species in cometary ices (Calmonte et al. 2016). For low C/O ratios and close to the steady-state, chemical models predict that most sulfur is in molecular form as SO and SO_2. These molecules are rapidly frozen onto dust grains at high densities and temperatures below ~50 K (see e.g. Pacheco-Vázquez et al. 2016), trapping the sulfur in the solid phase. Observationally, OCS is the only S-bearing molecule unambiguously detected in ice mantles because of its large band strength in the infrared (Palumbo et al. 1995) and, tentatively, SO_2 (Boogert et al. 1997). H_2S has not been detected in interstellar ices through infrared absorption experiments (Jiménez-Escobar & Muñoz Caro 2011).

Regardless of the exact chemical composition, the sulfur budget in the ice is expected to return to the gas phase in hot cores and bipolar outflows. The study of the sulfur chemistry in these environments can, therefore, provide some clues on the fate of sulfur. In Table 4.7, we show the values of sulfur depletion derived towards the hot core Orion KL (Esplugues et al. 2014) and the shocked region L1157-B1 (Holdship et al. 2016). Interestingly, the sulfur depletion in these two sources is ~10-30 relative to the solar value, i.e., similar to the value we have measured in the translucent phase. A similar value of sulfur depletion was measured in bipolar outflows by Anderson et al. (2013) using observations of the infrared space telescope Spitzer. This suggests that the fraction of sulfur incorporated to the grains in the

diffuse-translucent transition (~90%) is not released to the gas phase when the icy mantles are destroyed. This has important implications for star and planet formation studies. During the formation of a low-mass star, the grain cores are not destroyed except in the bow-shocks formed at the tip of high-velocity jets. If our hypothesis is correct, 90% of S atoms would remain locked in the grains in the inner regions of proto-planetary discs where planet formation occurs.

4.12 Summary and conclusions

This paper is based on the GEMS observations (Gas phase Elemental abundances in Molecular CloudS, PI: A. Fuente) of the prototypical dark cloud TMC 1. The Taurus molecular cloud (TMC) is one of the closest, low-mass star-forming regions at 140 pc. In this paper we investigate the chemistry to derive the elemental gas-phase abundances and the gas ionization fraction in the translucent part ($A_V < 10$ mag) of this molecular cloud. The chemistry in this transition from the diffuse to the dense gas determines the initial conditions for the formation of the dense contracting cores.

- We use mm observations of a selected sample of species carried out with the IRAM 30m telescope (3 mm and 2 mm) and the 40m Yebes telescope (1.3 cm and 7 mm)) to determine the fractional abundances of CO, HCO^+, HCN, CS, SO, HCS^+ and N_2H^+ in positions along 3 cuts intersecting the main filament at positions TMC 1-CP, TMC 1-NH3 and TMC 1-C over which the visual extinction vary between peak values of A_V~20 mag and 3 mag.

- None of the studied molecules present constant abundance across the studied cuts. According with their variations with visual extinction, we can differentiate three groups: i) the first group is formed by the abundant molecule ^{13}CO. This molecule reaches its peak value at $A_V \sim 3$ mag and then progressively decreases with visual extinction; ii) the second group is formed by HCO^+, CS and SO; the abundances of these molecules increases with visual extinction until $A_V \sim 5$ mag where they present a narrow peak and then progressively decreases towards the extinction peak; iii) The abundance of the N-bearing molecules HCN and N_2H^+ increases from A_V~3 mag until the extinctions peaks at A_V~20 mag.

- By comparison of the molecular abundances with the Meudon PDR code, we derive the C, O, and S elemental depletions, and hence the gas ionization degree as a function of the visual extinction at each position. Our data show that even at $A_V \sim 3-4$ mag where the transition C^+/C/CO occurs, significant depletions of C, O and S are found. In fact, C/H varies between ~8 10^{-5} to ~4 $\times$ 10^{-5} in the translucent cloud ($3 < A_V <$ 10 mag). Moreover the C/O ratio is $\sim 0.8-1$, suggesting that the O is preferentially depleted in the diffuse phase ($A_V < 3$ mag). Regarding sulfur, we estimate S/H $\sim 0.4 - 2.2 \times 10^{-6}$ in this moderately dense region.

- The detailed modeling of the chemistry in the translucent phase and our estimate of the elemental abundances allow us to constrain the value of ζ_{H_2} to $\sim 0.5-1.8\times10^{-16}$

s^{-1}. This value is slightly lower (a factor of ~3) than that derived by Neufeld & Wolfire (2017), $\zeta_{H_2} = (5.3\pm1.1)\times10^{-16}$ s^{-1}, in the diffuse medium.

Based on our results, we propose that the freeze out of CO is the main process that changes the grain composition in the translucent part of the cloud producing a progressive depletion of C and O from A_V~ 3 mag to A_V~ 10. Regarding sulfur, we measure a constant depletion of ~7−40 across the translucent cloud. This suggests that sulfur atoms (or ions) would have been massively incorporated to dust grains from the HI/H_2 (A_V~1) to the C^+/C/CO transition to reach a depletion of ~7-40 in the translucent medium. In order to account for the chemical composition in the TMC 1-CP core, a second strong S depletion should occur in the dense cloud. Interestingly, the S atoms incorporated into grains during the diffuse and translucent phase are not returned back to the gas phase during the formation of a low-mass star.

4.13 New calculations of the SO + OH → SO_2 + H reaction rate

The potential energy surface (PES) of the ground electronic state of HSO_2 system have been developed by Ballester & Varandas (2005) by fitting very accurate *ab initio* calculations. According to this PES, the SO($^3\Sigma$) + OH($^2\Pi$) → SO_2+ H reaction is exothermic by ≈ 1.3 eV, with two deep wells, of ≈ 3 eV for HOSO and of ≈ 2 eV for HSO_2. There is a barrier between the two wells, of energy very close to the SO + OH asymptote. The HOSO is directly connected to the SO + OH with no barrier, with the attractive dipole-dipole long-range interaction.

There have been several quasi-classical trajectory (QCT) calculations of the SO + OH → SO_2+ H rate (Ballester & Varandas 2007; Ballester et al. 2010; Pires et al. 2014) finding that this reaction presents a capture-like behavior due to the dipole-dipole interaction and a very good agreement with the available experimental rates (Blitz et al. 2000; Jourdain et al. 1979; Fair & Thrush 1969). All these experimental and theoretical results were obtained at temperatures above 200 K, and in this work we extend the simulations to lower temperatures, down to 10 K, of interstellar interest.

QCT calculations have been performed at temperatures in the 10-500K interval, using the miQCT code (Dorta-Urra et al. 2015; Zanchet et al. 2018). For each temperature batches of 50000 trajectories were run, starting at a distance between SO and OH center-of-mass of 125 Bohr. The initial impact parameter, b, was randomly chosen between 0-90 Bohrs according to a b^2 distribution. The initial translational and rotational energy of the two reactants was randomly chosen according to a Boltzmann distribution, while the vibrations of the two reactants was described using a adiabatic switching method (Grozdanov & Solovev 1982; Johnson 1987; Qu & Bowman 2016; Nagy & Lendvay 2017) corresponding to the ground vibrational state of the two reagents. The reactivity of this reaction does not depend on the initial vibrational excitation of the reactants(Ballester & Varandas 2007; Ballester et al. 2010; Pires et al. 2014). For this reason, we can consider that the vibrational state selected rate calculated here is essentially the thermal rate constant. The reactive rate constant is calculated as

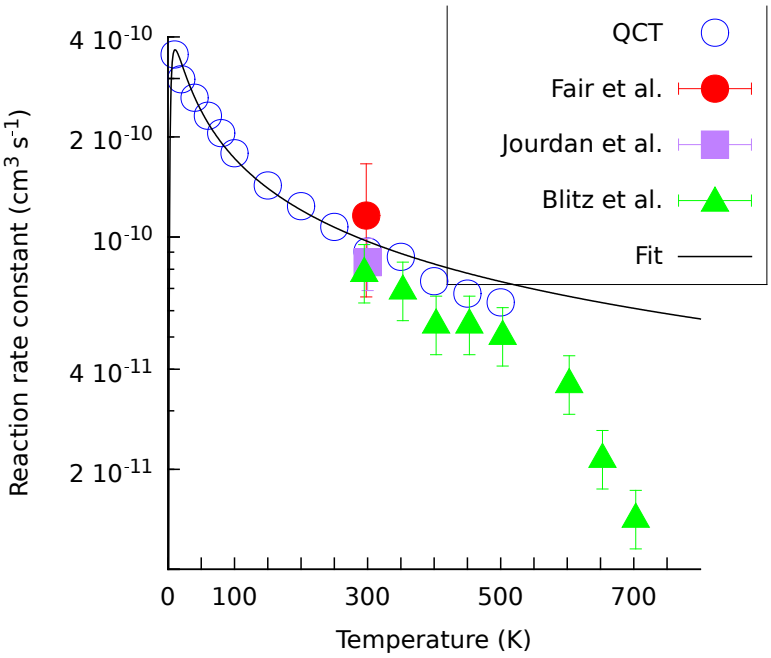

Figure 4.14: State-selected reaction rates for SO($v = 0$) + OH(v=0) → SO_2 + H collisions as a function of temperature obtained in this work (QCT), and compared with the experimental results of previous works (Blitz et al. 2000; Jourdain et al. 1979; Fair & Thrush 1969). The calculated rate has been fitted to the expression $K(T) = a(T/300)^b e^{-c/T}$, with a=1.24211 10^{-10} cm^3/s,b=−0.56049 and c=6.58356 K. This expression is adequate in the 10−300 K interval.

$$k_{vj}(T) = g_e(T)\sqrt{\frac{8k_BT}{\pi\mu}}\frac{N_r}{N_t}\pi b_{max}^2, \tag{4.3}$$

where N_r denotes the number of reactive trajectories and b_{max} is the maximum impact parameter for which reaction takes place. Finally, g_e is the electronic partition function

$$g_e(T) = \left\{3\left(1+e^{-209/T}\right)\right\}^{-1}, \tag{4.4}$$

where the factor 3 arises because only one combination of total spin 1/2 is reactive, when combinaing the triplet state of SO and the double state of OH, and that the OH($^2\Pi$) splits into two spin-orbit states ($^2\Pi_{3/2}$ and $^2\Pi_{1/2}$, with an energy difference of 209 K. The results obtained are shown in Fig. 4.14 and compared with the experimental results available.

The QCT results made in this work are in rather good agreement with the experimental data in the interval 300-500 K. The rate increases by a factor of 3-4 when decreasing the temperature from 300 to 10 K. This may have some consequences in astrophysical objects at low temperatures. Note that the fit presented in he caption of Fig. 4.14 is only adequate for temperatures between 10 and 300 K.

4.14 Tables and Figures

Table 4.8: Telescope parameters

Telescope	Setup	Freq. band	HPBW(")	$F_{\rm eff}$	$B_{\rm eff}$
IRAM 30m	Setup 1	L106	24	0.95	0.80
	Setup 2	L89	29	0.95	0.81
		L147	16	0.93	0.74
	Setup 3	L101	25	0.95	0.80
		L138	17	0.93	0.74
	Setup 4	L92	17	0.95	0.81
		L168	14	0.93	0.74
Yebes 40m	Setup 0	L23000	84	0.93	0.70
		L44750	42	0.90	0.49

Table 4.9: Spectral setups

	Line	Freq.(MHz)	E_u(K)	$A_{ul}(s^{-1})$	g_u
		L89			
HCS^+	2→1	85347.87	6.1	$1.110\ 10^{-5}$	5
HCN	1→0	88631.85	4.3	$2.406\ 10^{-5}$	3
$H^{13}CN$	1→0	86340.18	4.1	$2.224\ 10^{-5}$	3
$HC^{15}N$	1→0	86054.97	4.1	$2.202\ 10^{-5}$	3
HCO^+	1→0	89188.53	4.3	$4.234\ 10^{-5}$	3
$H^{13}CO^+$	1→0	86754.29	4.2	$3.897\ 10^{-5}$	3
$HC^{18}O^+$	1→0	85162.22	4.1	$3.686\ 10^{-5}$	3
HNC	1→0	90663.56	4.4	$2.690\ 10^{-5}$	3
OCS	7→6	85139.10	16.3	$1.715\ 10^{-6}$	15
SO	2_2→1_1	86093.96	19.3	$5.250\ 10^{-6}$	5
		L92			
^{13}CS	2→1	92494.27	6.7	$1.412\ 10^{-5}$	5
$C^{34}S$	2→1	96412.95	6.9	$1.600\ 10^{-5}$	5
CH_3OH	2,-1→1,-1	96739.36	4.6	$2.558\ 10^{-5}$	5
CH_3OH	2,1→1,1	96741.37	7.0	$3.408\ 10^{-6}$	5
		L101			
CS	2→1	97980.95	7.1	$1.679\ 10^{-5}$	5
SO	2_3→1_2	99299.89	9.2	$1.125\ 10^{-5}$	7
^{34}SO	2_3→1_2	97715.40	9.1	$1.073\ 10^{-5}$	7
H_2CS	3(1,2)→2(1,2)	101477.81	8.1	$1.260\ 10^{-5}$	7
		L106			
^{13}CO	1→0	110201.35	5.3	$6.336\ 10^{-8}$	3
$C^{18}O$	1→0	109782.17	5.3	$6.263\ 10^{-8}$	3
N_2H^+	1→0	93173.77	4.5	$3.628\ 10^{-5}$	3
SO	3_2→2_1	109252.18	21.1	$1.080\ 10^{-5}$	5
^{34}SO	3_2→2_1	106743.37	20.9	$1.007\ 10^{-5}$	5
NH_2D	1(1,1)→1(0,1)	110153.59	21.3	$5.501\ 10^{-6}$	9
CH_3OH	0,0→1,-1	108893.94	5.2	$1.471\ 10^{-5}$	3
		L138			
^{13}CS	3→2	138739.26	13.3	$5.107\ 10^{-5}$	7
SO	3_4→2_3	138178.66	15.9	$3.166\ 10^{-5}$	9
OCS	11→10	133785.90	38.5	$6.818\ 10^{-6}$	23
H_2CS	4(0,4)→3(0,3)	137371.21	16.5	$3.647\ 10^{-5}$	9
HDCO	2(1,1)→1(1,0)	134284.90	17.6	$4.591\ 10^{-5}$	5
		L147			
CS	3→2	146969.03	14.1	$6.071\ 10^{-5}$	7
$C^{34}S$	3→2	144617.10	13.9	$5.784\ 10^{-5}$	7
		L168			
H_2S	1(1,0)→1(0,1)	168762.75	8.1	$2.677\ 10^{-5}$	3
$H_2{}^{34}S$	1(1,0)→1(0,1)	167910.52	8.1	$2.616\ 10^{-5}$	3
HCS^+	4→3	170691.62	20.5	$9.863\ 10^{-5}$	9
$HC^{34}S^+$	4→3	167927.25	20.1	$7.805\ 10^{-5}$	9
SO	4_4→3_3	172181.42	33.8	$5.833\ 10^{-5}$	9
^{34}SO	4_4→3_3	168815.11	33.4	$5.498\ 10^{-5}$	9
		L23000			
NH_3	(1,1)a→(1,1)s	23694.49	1.1	$1.712\ 10^{-7}$	12
NH_3	(2,2)a→(2,2)s	23722.63	42.3	$2.291\ 10^{-7}$	20
		L44500			
CS	1→0	48990.96	2.4	$1.749\ 10^{-6}$	3
$C^{34}S$	1→0	48206.94	2.3	$1.666\ 10^{-6}$	3
^{13}CS	1→0	46247.56	2.2	$1.471\ 10^{-6}$	3
HCS^+	1→0	42674.19	2.0	$1.156\ 10^{-6}$	3
OCS	4→3	48651.60	5.8	$3.047\ 10^{-7}$	9

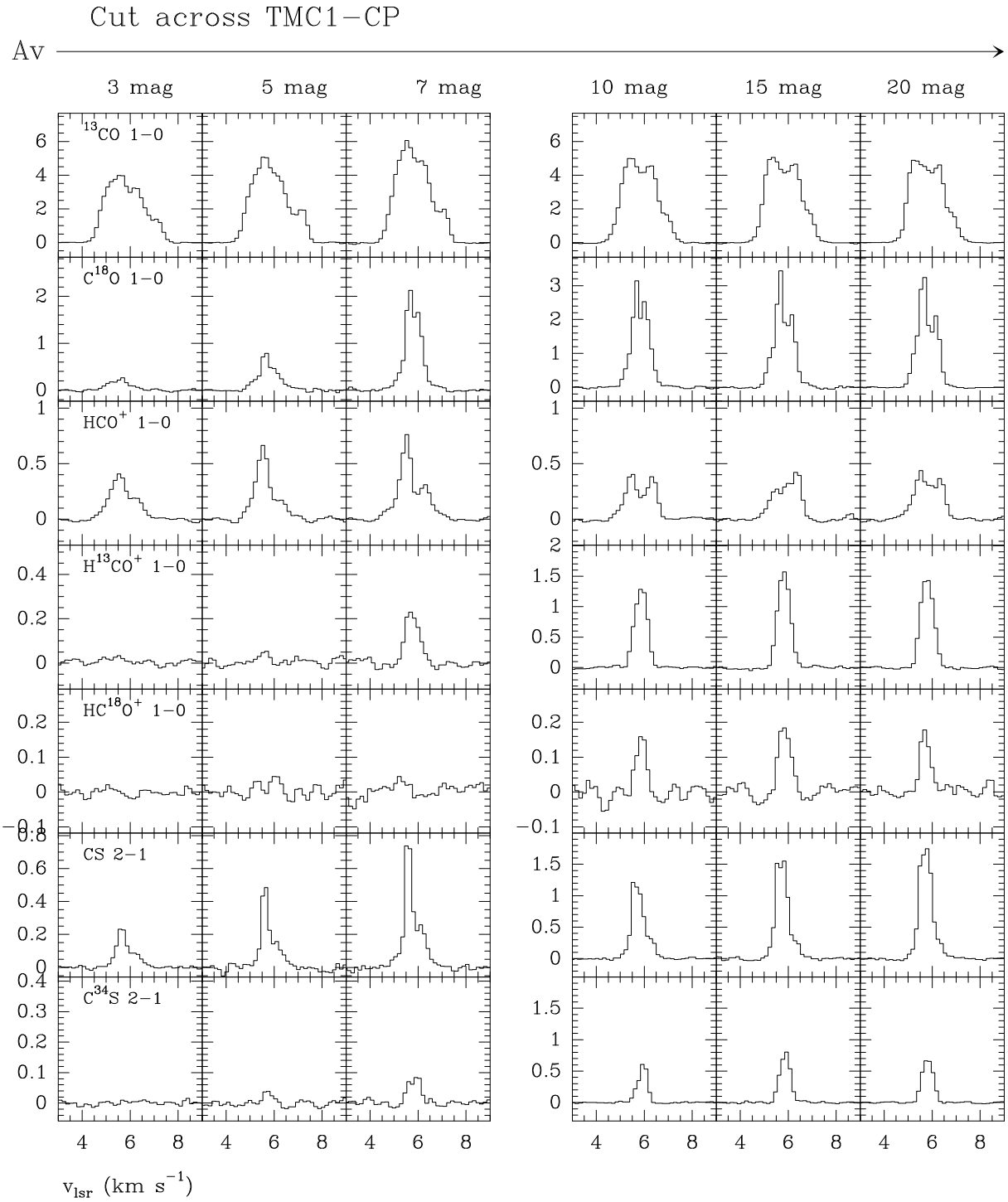

Figure 4.15: Selected sample of spectra as observed with the 30m telescope towards the TMC 1-CP cut (in T_{MB}).

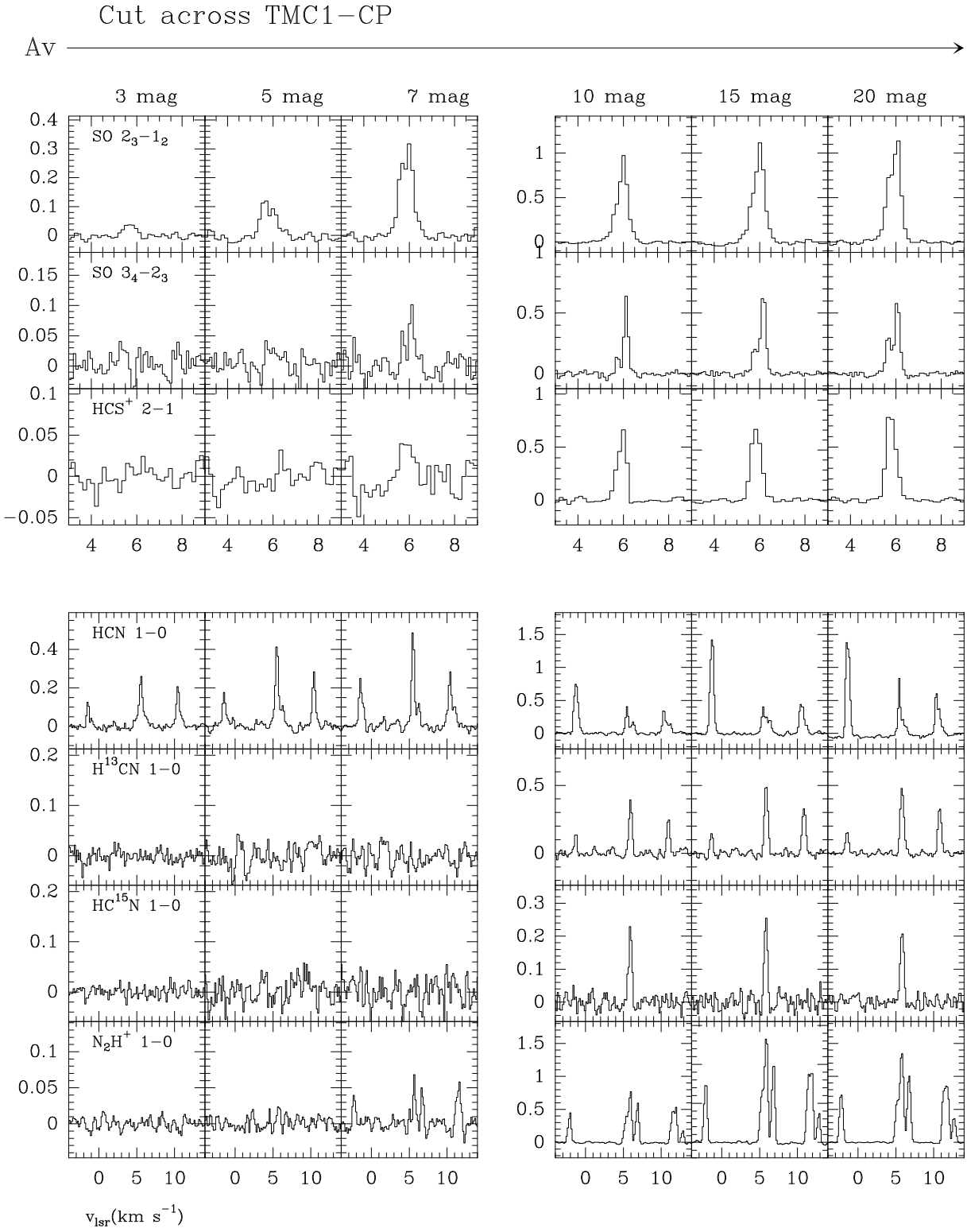

Figure 4.16: The same as Fig. B.1

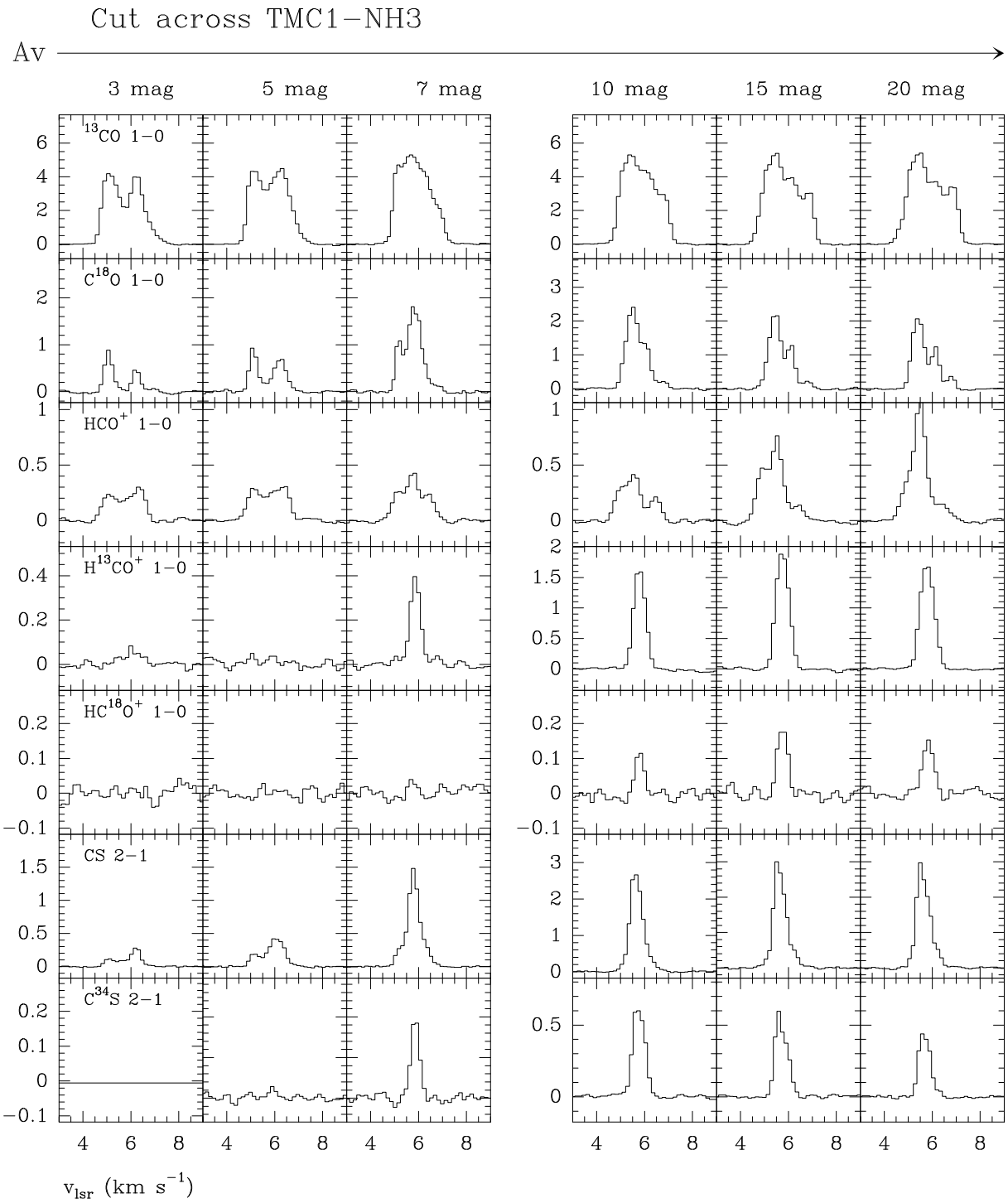

Figure 4.17: Selected sample of spectra as observed with the 30m telescope towards the TMC 1-NH3 cut (in T_{MB}).

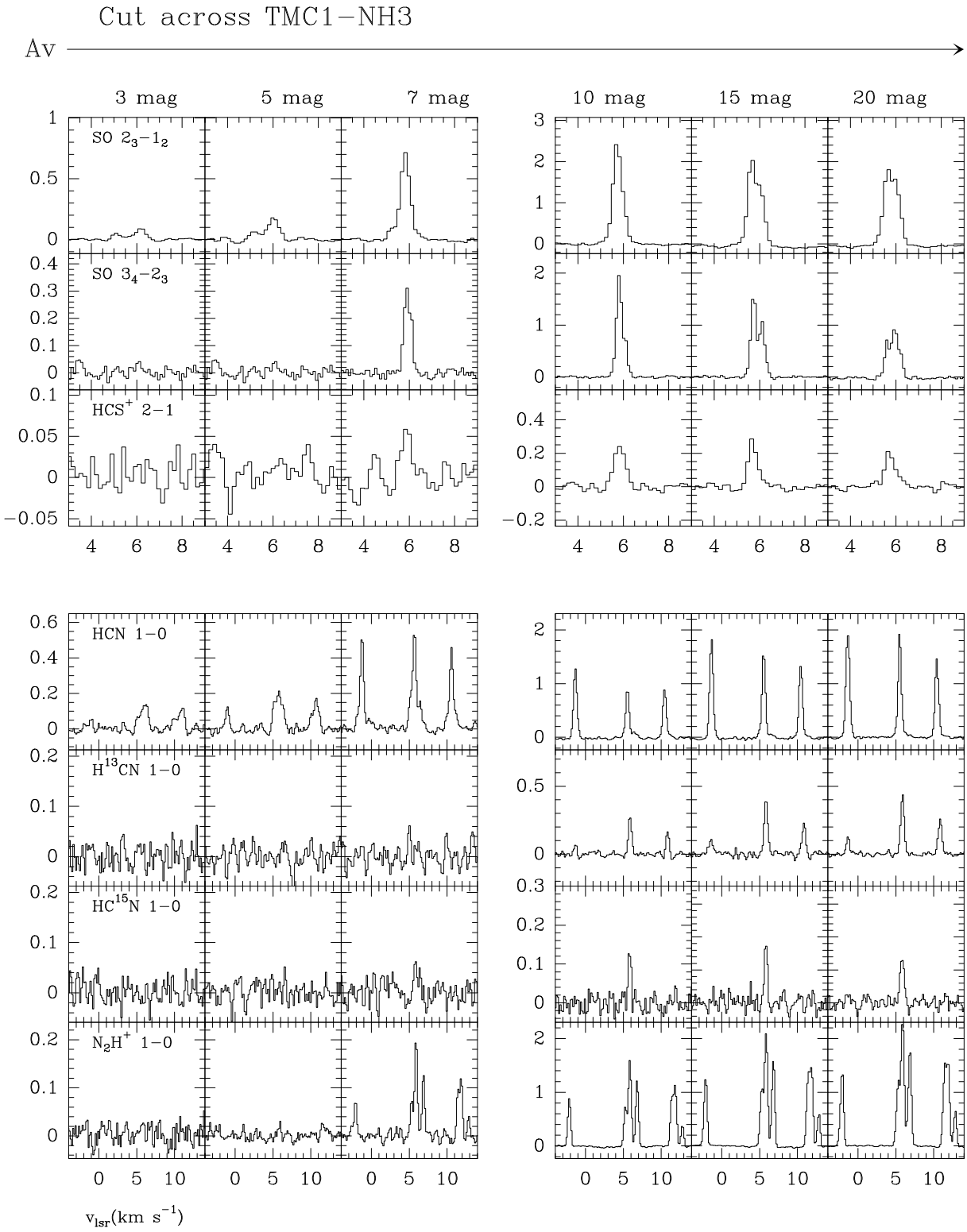

Figure 4.18: The same as Fig. B.3

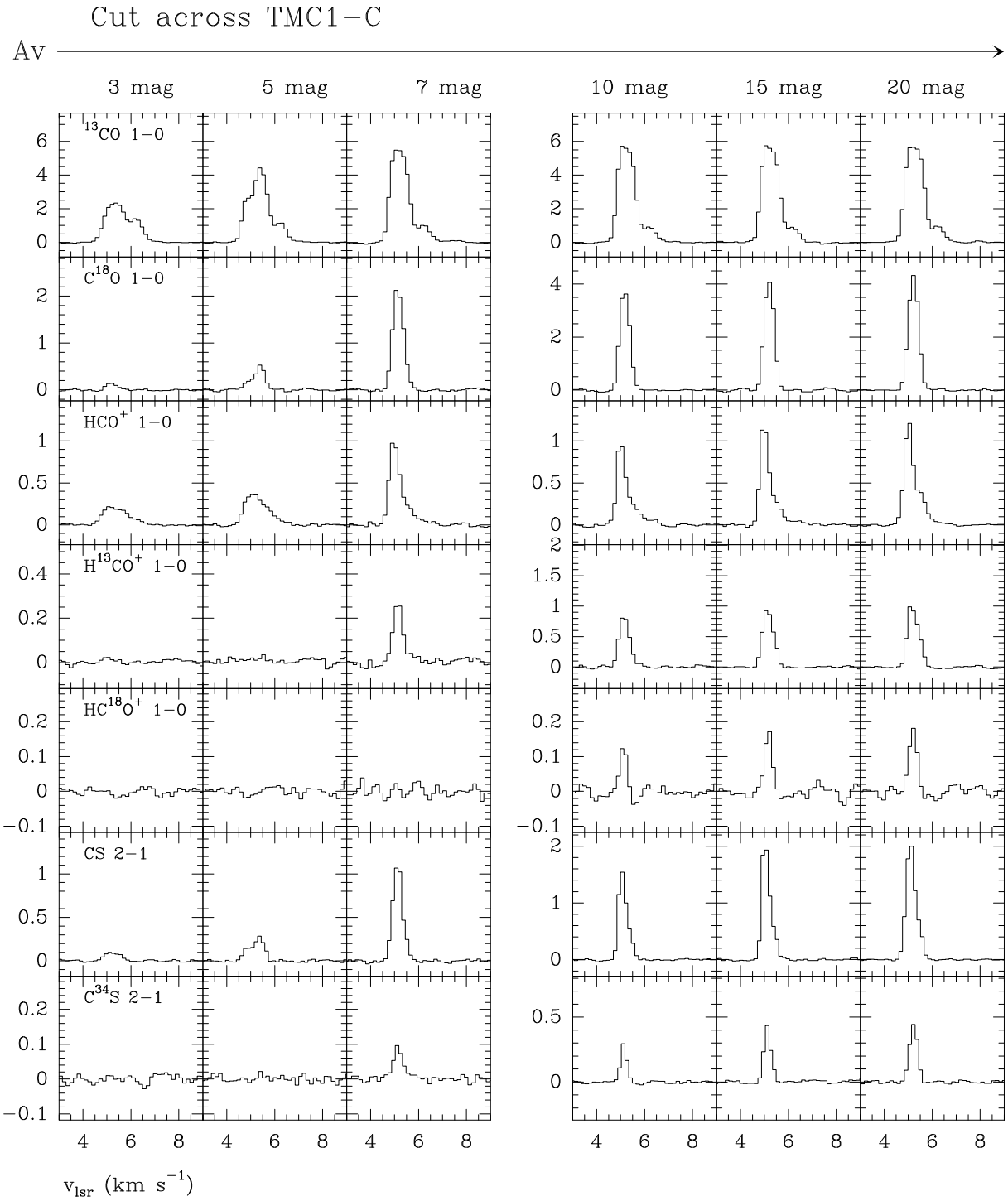

Figure 4.19: Selected sample of spectra as observed with the 30m telescope towards the TMC 1-C cut (in T_{MB}).

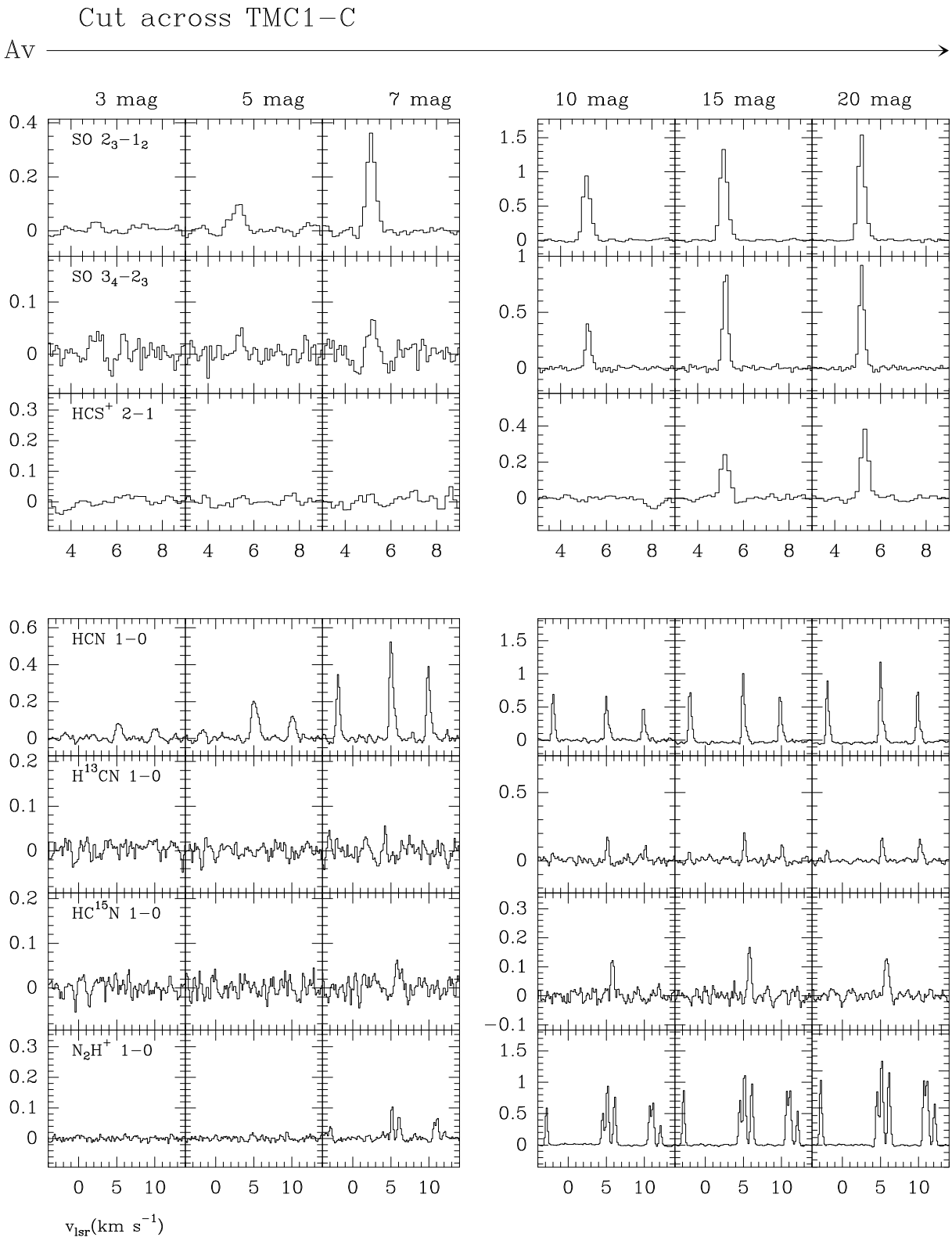

Figure 4.20: The same as Fig. B.5

Chapter 5

On the quest for the sulphur reservoir in molecular clouds: the H_2S case

Adapted from Navarro-Almaida, D., LeGal, R., Fuente, A., et al. 2020, A&A, 637, A39

Abstract

Context: Sulphur is one of the most abundant elements in the Universe. Surprisingly, sulphuretted molecules are not as abundant as expected in the interstellar medium and the identity of the main sulphur reservoir is still an open question.

Aims: Our goal is to investigate the H_2S chemistry in dark clouds, as this stable molecule is a potential sulphur reservoir.

Methods: Using millimeter observations of CS, SO, H_2S, and their isotopologues, we determine the physical conditions and H_2S abundances along the cores TMC 1-C, TMC 1-CP, and Barnard 1b. The gas-grain model NAUTILUS is used to model the sulphur chemistry and explore the impact of photo-desorption and chemical desorption on the H_2S abundance.

Results: Our modeling shows that chemical desorption is the main source of gas-phase H_2S in dark cores. The measured H_2S abundance can only be fitted if we assume that the chemical desorption rate decreases by more than a factor of 10 when $n_H > 2 \times 10^4$. This change in the desorption rate is consistent with the formation of thick H_2O and CO ice mantles on grain surfaces. The observed SO and H_2S abundances are in good agreement with our predictions adopting an undepleted value of the sulphur abundance. However, the CS abundance is overestimated by a factor of $5-10$. Along the three cores, atomic S is predicted to be the main sulphur reservoir.

Conclusions: The gaseous H_2S abundance is well reproduced, assuming undepleted sulphur abundance and chemical desorption as the main source of H_2S. The behavior of the observed H_2S abundance suggests a changing desorption efficiency, which would probe the snowline in these cold cores. Our model, however, highly overestimates the observed gas-phase CS abundance. Given the uncertainty in the sulphur chemistry, we can only conclude that our data are consistent with a cosmic elemental S abundance with an uncertainty of a factor of 10.

5.1 Introduction

Sulphur is one of the most abundant elements in the Universe (S/H ~ 1.35×10^{-5}, Yamamoto 2017) and plays a crucial role in biological systems on Earth, so it is important to follow its chemical history in space (i.e., toward precursors of the Solar System). Surprisingly, sulphuretted molecules are not as abundant as expected in the interstellar medium (ISM). A few sulphur compounds have been detected in diffuse clouds, demonstrating that sulphur abundance in these low-density regions is close to the cosmic value (Neufeld et al. 2015). This is also the case towards the prototypical photodissociation region (PDR) in the Horsehead Nebula, where the sulfur abundance is found to be very close to the undepleted value observed in the diffuse ISM (Goicoechea et al. 2006), with an estimate of S/H = $(3.5 \pm 1.5) \times 10^{-6}$. A wide variety of S-bearing molecules, including the doubly sulphuretted molecule S_2H, were later detected in the HCO peak in this PDR (Fuente et al. 2017; Rivière-Marichalar et al. 2019). However, sulphur is thought to be depleted inside molecular clouds by a factor of 1000 compared to its estimated cosmic abundance (Graedel et al. 1982; Agúndez & Wakelam 2013). The depletion of sulphur is observed not only in cold pre-stellar cores, but also in hot cores and corinos (Wakelam et al. 2004). We would expect that most of the sulphur is locked on the icy grain mantles in dense cores, but we should see almost all sulphur back to the gas phase in hot cores and strong shocks. However, even in the well-known Orion-KL hot core, where the icy grain mantles are expected to sublimate releasing the molecules to the gas phase, one needs to assume a sulphur depletion of a factor of ~ 10 to reproduce the observations (Esplugues et al. 2014; Crockett et al. 2014). Because of the high hydrogen abundances and the mobility of hydrogen in the ice matrix, sulphur atoms impinging in interstellar ice mantles are expected to form H_2S preferentially. To date, OCS is the only S-bearing molecule unambiguously detected in ice mantles because of its large band strength in the infrared (Geballe et al. 1985; Palumbo et al. 1995) and, tentatively, SO_2 (Boogert et al. 1997). The detection of solid H_2S (s-H_2S hereafter) is hampered by the strong overlap between the 2558 cm^{-1} band with the methanol bands at 2530 and 2610 cm^{-1}. Only upper limits of s-H_2S abundance could be derived by Jiménez-Escobar & Muñoz Caro (2011), with values with respect to H_2O ice of 0.7% and 0.13% in W33A and IRAS 18316-0602, respectively.

Sulphur-bearing species have been detected in several comets. Contrary to the interstellar medium (ISM), the majority of cometary detections of sulphur-bearing molecules belongs to H_2S and S_2 (Mumma & Charnley 2011). Towards the bright comet Hale Bopp, a greater diversity has been observed, including CS and SO (Boissier et al. 2007). The brighter comets C/2012 F6 (Lemmon) and C/2014 Q2 (Lovejoy) have also been shown to contain CS (Biver et al. 2016). Currently, some of the unique in-situ data are available from the Rosetta mission on comet 67P/Churyumov-Gerasimenko. With the Rosetta Orbiter Spectrometer for Ion and Neutral Analysis (ROSINA; Balsiger et al. 2007) onboard the orbiter, the coma has been shown to contain H_2S, atomic S, SO_2, SO, OCS, H_2CS, CS_2, S_2, and, tentatively, CS, as the mass spectrometer cannot distinguish the latter from CO_2 gases (Le Roy et al. 2015). In addition, the more complex molecules S_3, S_4, CH_3SH, and C_2H_6S have now been detected (Calmonte et al. 2016). Even with the large variety of S-species detected, H_2S remains as the most abundant, with an ice abundance of about 1.5% relative to H_2O, which is similar to the upper limit measured in the interstellar medium (Jiménez-Escobar & Muñoz Caro 2011).

Gas phase Elemental abundances in Molecular CloudS (GEMS) is an IRAM 30m Large Program aimed at estimating the depletions of the most abundant elements (C, O, S, and N) in a selected set of prototypical star-forming filaments located in the molecular cloud complexes Taurus, Perseus, and Orion A. The first chemical study using GEMS data concluded that only 10% of the sulphur is in gas phase in the translucent part ($A_v \sim 3-10$ mag, Fuente et al. 2019, hereafter Paper I) of TMC 1. These conclusions were based on millimeter observations of CS, SO and HCS^+. Here we investigate the chemistry of H_2S, a key piece in the sulphur chemistry, which is still poorly understood.

The formation of H_2S in the gas phase is challenging at the low temperatures prevailing in the interstellar medium. None of the species S, SH, S^+, and SH^+ can react exothermically with H_2 in a hydrogen atom abstraction reaction which greatly inhibits the formation of sulphur hydrides (Gerin et al. 2016). Alternatively, H_2S is thought to form on the grain surfaces where sulphur atoms impinging in interstellar ice mantles are hydrogenated, forming s-H_2S and potentially becoming the most important sulphur reservoir in dark cores (Vidal et al. 2017). Recent modeling and experimental studies suggest an active sulphur chemistry within the ices where s-H_2S might be converted in more complex compounds such as OCS or CH_3SH (e.g., Laas & Caselli 2019, El Akel et al. in prep). Unfortunately, both the surface chemistry reaction rates and the desorption processes are not well constrained, which makes a reliable prediction of both solid and gas phase H_2S abundance difficult. This paper uses a subset of the complete GEMS database to investigate the H_2S abundance in dark cores TMC 1 and Barnard 1b as prototypes of molecular clouds embedded in low-mass and intermediate-mass star forming regions, respectively.

5.2 Source sample

5.2.1 TMC 1

The Taurus molecular cloud (TMC), at a distance of 140 pc (Elias 1978), is one of the closest molecular cloud complexes and is considered an archetypal low-mass star forming region. It has been the target of several cloud evolution and star formation studies (see e.g., Goldsmith et al. (2008)), being extensively mapped in CO (Cernicharo & Guelin 1987; Narayanan et al. 2008). The most massive molecular cloud in Taurus is the Heiles cloud 2 (HCL 2, Tóth et al. 2004), which hosts the well-known region TMC 1 (Fig. 5.1). As one of the most extensively studied molecular filaments, TMC 1 was included in the IRAM 30m Large Program GEMS. Fuente et al. (2019) modeled the chemistry of the translucent filament, deriving the gas phase elemental abundances (C/O $\sim 0.8-1$, S/H $\sim 0.4-2.2\times10^{-6}$) and constraining the cosmic rays molecular hydrogen ionization rate to $\sim 0.5-1.8\times10^{-16}$ s^{-1} in this moderate dense ($n_{H_2} < 10^4$ cm^{-3}) phase. Here, we will focus on the chemistry of the dense cores TMC 1-CP and TMC 1-C (see Fig. 5.1). TMC 1-CP has been extensively observed at millimeter wavelengths and is often adopted as template of C-rich (C/O > 1) dense cores (Fehér et al. 2016; Gratier et al. 2016; Agúndez & Wakelam 2013). Less studied, TMC 1-C was proposed as an accreting starless core with high CO depletion by Schnee et al. (2007, 2010).

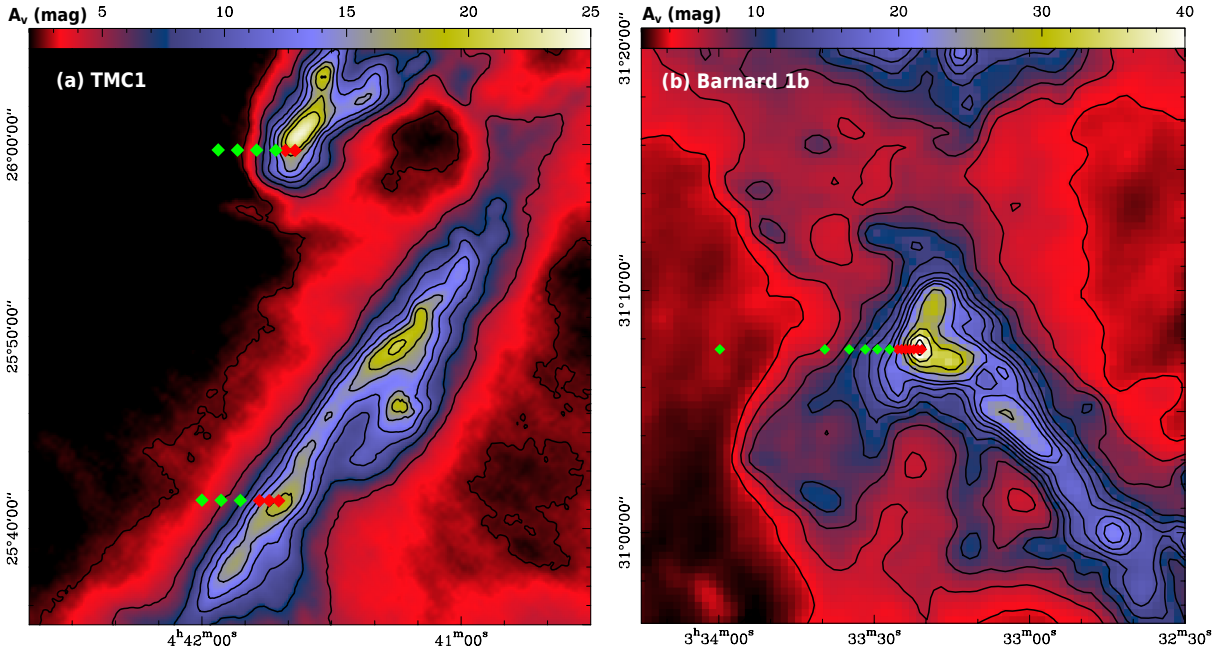

Figure 5.1: *Left panel:* TMC 1 total visual extinction (the visual extinction along the line of sight) map based on Herschel dust emission maps from Jason Kirk (private communication). *Right panel:* Visual extinction map of Barnard 1 from the opacity at 850 μm derived by Zari et al. (2016). In both maps the observed positions are in lines of constant declination, or cuts, where the red squares mark those positions in which only IRAM 30 m telescope data is obtained, and green squares mark positions with additional Yebes 40 m data.

5.2.2 Barnard 1b

Barnard 1 is a young, intermediate-mass star forming cloud, embedded in the western sector of the 30 pc wide molecular cloud complex Perseus (see Fig. 5.1). It hosts several dense cores in different evolutionary stages (Hatchell et al. 2005), out of which Barnard 1b is the youngest. The Barnard 1b region was mapped in many molecular tracers, such as CS, NH_3, ^{13}CO (Bachiller et al. 1990), N_2H^+ (Huang & Hirano 2013), $H^{13}CO^+$ (Hirano et al. 1999), or CH_3OH (Hiramatsu et al. 2010; Öberg et al. 2010). Interferometric observations of Barnard 1b revealed that this compact core hosts two young stellar objects (YSOs), B1b-N and B1b-S (Huang & Hirano 2013; Marcelino et al. 2018), and a third more evolved source, hereafter B1b-Spitzer, with deep absorption features from ices (Jørgensen et al. 2006). The three sources are deeply embedded in the surrounding protostellar envelope, that seems essentially unaffected by the inlaid sources, as shown by the large column density, $N(H_2) \sim 7.6 \times 10^{22}$ cm^{-2} (Daniel et al. 2013) and cold kinetic temperature, $T_K = 12$ K (Lis et al. 2002).

From the chemical point of view, Barnard 1b has a rich chemistry. Indeed, many molecules were observed for the first time in this object, like HCNO (Marcelino et al. 2009) or CH_3O (Cernicharo et al. 2012). Additionally, Barnard 1b shows a high degree of deuterium fractionation and has been associated with first detections of multiple deuterated molecules, such as ND_3 (Lis et al. 2002) or D_2CS (Marcelino et al. 2005), consistent with the expected chemistry in a dense and cold core. Recently, Fuente et al. (2016) proposed that this core is characterized by a low depletion of sulphur, S/H$\sim 10^{-6}$. They proposed that peculiar initial conditions due to the proximity of the bipolar outflows, a rapid collapse of the parent cloud, or the imprint of the two deeply embedded protostellar objects, might be the causes. Within GEMS, we have studied the nine-point cut depicted in Fig. 5.1, with visual extinctions (extinctions along the line of sight) ranging from ~ 3 mag to ~ 76 mag.

5.3 Observations

This paper is based on a subset of the GEMS observations carried out with the IRAM 30m telescope and the 40m Yebes telescopes. The TMC 1 data used in this paper were already presented in Paper I, where we gave a detailed description of the observational procedures used within the GEMS project. The observations towards Barnard 1b were carried out using the same observational strategy as in TMC 1 (see Paper I). We select three lines of constant declination, or cuts, through the three extinction peaks of TMC 1-C, TMC 1-CP, and Barnard 1b. We define the origin of each line as the point of highest extinction in that line. Fig. 5.1 shows the positions observed across the dense cores TMC 1-C, TMC 1-CP, and Barnard 1b. All the positions were observed in setups 1 to 4 (see Paper I) using the 30m telescope. These observations were done using frequency-switching in order to optimize the detection sensitivity. In addition to the 30m observations, the positions with $A_v < 20$ mag were also observed with 40m Yebes telescope (setup 0). During the 40m observations, the observing procedure was position-switching, the OFF-position being RA(J2000)= 03:36:39.571 Dec: 29:59:53.30 for Barnard 1b. This position was checked to be empty of emission in the observed bandwidths before the observations. In the following, line intensities are in main beam temperature, T_{MB}, for all observations. Calibration errors are estimated to be ~20% for the IRAM

30m telescope and ~ 30% for the Yebes 40m telescope. In order to constrain the gas physical conditions and the sulphur chemistry, in this paper we use the observed lines of CS and SO, in addition to H_2S (see the list of lines in Table 5.1 and the corresponding spectra in Fig. 5.14, Fig. 5.15, and Fig. 5.16).

5.4 Multi-transition study of CS and SO

A precise knowledge of the gas physical conditions is required to determine accurate molecular abundances. For TMC 1, we adopted the gas kinetic temperatures and molecular hydrogen densities derived in Paper I. These values are summarized in Table 5.6, together with the CS column densities also derived in our previous work.

Table 5.1: Measured transitions

Species	Transition	Frequency (MHz)	Beam (arcsec)
^{13}CS	$1 \rightarrow 0$	46247.563	42"
^{13}CS	$2 \rightarrow 1$	92494.308	27"
^{13}CS	$3 \rightarrow 2$	138739.335	18"
C^{34}S	$1 \rightarrow 0$	48206.941	42"
C^{34}S	$2 \rightarrow 1$	96412.950	26"
C^{34}S	$3 \rightarrow 2$	144617.101	17"
CS	$1 \rightarrow 0$	48990.955	42"
CS	$2 \rightarrow 1$	97980.953	25"
CS	$3 \rightarrow 2$	146969.029	17"
$H_2{}^{34}$S	$1_{1,0} \rightarrow 1_{0,1}$	167910.516	15"
H_2S	$1_{1,0} \rightarrow 1_{0,1}$	168762.753	15"
SO	$2_2 \rightarrow 1_1$	86093.96	29"
SO	$2_3 \rightarrow 1_2$	99299.89	25"
SO	$3_2 \rightarrow 2_1$	109252.18	23"
SO	$3_4 \rightarrow 2_3$	138178.66	18"
SO	$4_4 \rightarrow 3_3$	172181.42	14"
^{34}SO	$2_3 \rightarrow 1_2$	97715.40	25"
^{34}SO	$3_2 \rightarrow 2_1$	106743.37	23"
^{34}SO	$4_4 \rightarrow 3_3$	168815.11	15"

We estimate the physical conditions towards Barnard 1b from a multi-transition analysis of CS and SO following the same procedure as in Chapter 4. We fit the intensities of the observed CS, C^{34}S, and ^{13}CS J = $1 \rightarrow 0$, $2 \rightarrow 1$, and $3 \rightarrow 2$ lines using the molecular excitation and radiative transfer code RADEX (van der Tak et al. 2007). During the fitting process, the isotopic ratios are fixed to $^{12}C/^{13}C = 60$ and $^{32}S/^{34}S = 22.5$ (Gratier et al. 2016), and we assume a beam filling factor of 1 for all transitions (the emission is more extended than the beam size). Then, we let T_k, n_{H_2}, and N(CS) vary as free parameters. The parameter space (T_k, n_{H_2}, N(CS)) is then explored following the Monte Carlo Markov Chain (MCMC) methodology with

a Bayesian inference approach, as described in Rivière-Marichalar et al. (2019). In particular, we use the *emcee* (Foreman-Mackey et al. 2013) implementation of the Invariant MCMC Ensemble sampler methods by Goodman & Weare (2010). While n_{H_2} and N(CS) are allowed to vary freely, we need to introduce a prior distribution to limit the gas kinetic temperatures to reasonable values in this cold region and, hence, break the temperature-density degeneracy that is usual in this kind of calculations. As estimated by Friesen et al. (2017), the gas kinetic temperature in a wide sample of molecular clouds, based on the NH_3 (1,1) and (2,2) inversion lines, is found to be systematically 1 or 2 K lower than that obtained from Hershel maps. This is indeed corroborated in Section 5. Thus, we set a Gaussian prior distribution with mean $\mu = T_d$ and $\sigma = 2$ K for the gas kinetic temperature. The collisional rate coefficients for the molecular excitation calculations that involve ^{13}CS and C^{34}S isotopologues are those of CS. They include collisions with para and ortho-H_2 as reported by Denis-Alpizar et al. (2018), with a ortho-to-para ratio of 3, and He, taken from Lique et al. (2006a). The gas temperature and the density derived for Barnard 1b from the multi-line fitting of CS and its isotopologues are shown in Table 5.7.

A similar multi-transition analysis is carried out to derive SO column densities. In this case we have used the collisional coefficients derived by Lique & Spielfiedel (2007). The derived molecular gas densities and SO column densities are shown in Table 5.8. In most positions, the densities derived from the SO fitting fully agree with those derived from CS. However, in the vicinity of the visual extinction peak ($A_v > 30$ mag), the molecular hydrogen densities derived from SO data are systematically higher than those derived with CS. Daniel et al. (2013) derived the density structure of the core by fitting the CSO 350 μm continuum map and the IRAM 1.2mm image with a power-law radial density profile, and assuming standard values of the dust-to-gas mass ratio and dust opacity. The densities derived from the continuum images fitting are consistent with those derived from our SO observations and a factor $5-10$ higher than those derived from CS. Therefore, we adopt the densities derived from SO for the inner Barnard 1b core. The lower densities derived from CS are very likely the consequence of a high depletion of this molecule in the densest part of the core.

It is interesting to compare the SO column density obtained in this paper towards Barnard 1b with the S^{18}O column density derived by Fuente et al. (2016). Comparing both values, we obtain $N(SO)/N(S^{18}O) = 78 \pm 45$, much lower than the isotopic ratio, $^{16}O/^{18}O = 550$. Recent chemical calculations (Loison et al. 2019) using the gas-grain chemical code Nautilus (Ruaud et al. 2016) in typical conditions for dark molecular clouds, showed that the isotopic fractionation might be important in the case of SO, which yields a $^{16}O/^{18}O$ ratio between 500 and 80. Following their predictions, the $N(SO)/N(S^{18}O)$ ratio is expected to vary with time with changes of more than a factor of 5. The ratio measured in Barnard 1b would be consistent with a chemical age of a few 0.1 Myr.

5.5 Gas kinetic temperatures from NH_3 data

The low densities found in the translucent phase, with n_H of the order of a few 10^3 cm^{-3}, might cast some doubts on our assumption that gas and dust are close to thermal equilibrium. To check that this is indeed the case, we have independently derived the gas kinetic

Table 5.2: Kinetic temperatures, T_k(CS), in Kelvin, of several $A_v < 20$ mag positions in Barnard 1b, compared to the estimated rotation temperature $T_R(NH_3)$ and the corresponding kinetic temperature $T_k(NH_3)$ from the ammonia (1,1) and (2,2) inversion lines.

Offset (",")	T_k(CS) (K)	$T_R(NH_3)$ (K)	$T_k(NH_3)$ (K)
(+80", 0")	13.2 ± 1.8	11.5 ± 1.5	12.0 ± 2.1
(+110", 0")	14.4 ± 1.9	11.6 ± 1.8	12.1 ± 2.4
(+140", 0")	14.2 ± 1.0	12.7 ± 1.9	13.4 ± 2.6

temperature using the NH_3 (1,1) and (2,2) inversion lines as observed with the 40m Yebes telescope towards the positions with $A_v < 20$ mag in Barnard 1b. To derive the gas kinetic temperatures, first we follow the method described by Bachiller et al. (1987) to derive the rotation temperature $T_R(NH_3)$, and then we use the prescription which relates the gas kinetic temperature $T_k(NH_3)$ with $T_R(NH_3)$ found by Swift et al. (2005). Gas kinetic temperatures thus derived from ammonia data (Table 5.2) fully agree within the error with those derived from the CS multi-transition study (Table 5.7). Previous measurements of the gas kinetic temperature (Lis et al. 2002) are in agreement with our values. Thus, we adopt the gas kinetic temperatures derived from CS for our further analysis. It should be noted that we have not observed ammonia lines towards the $A_v > 20$ mag positions precluding an independent gas kinetic temperature estimate. However, taking into account the high molecular hydrogen densities measured in these regions, our assumption of gas and dust being close to thermal equilibrium is a plausible approximation. We have not detected the NH_3 lines towards the positions with $A_v < 10$ mag.

5.6 H_2S abundance

The gas physical conditions derived in previous sections are used to compute the H_2S column densities. First, we estimate the ortho-H_2S column density using RADEX with the ortho-H_2O collisional coefficients calculated by Dubernet et al. (2009), scaled to ortho-H_2S. The H_2S abundance is then calculated adopting an ortho-to-para ratio of 3. The resulting molecular abundances are listed in Table 5.6 and Table 5.7, and shown in Fig. 5.2.

In these plots, we try to find correlations between the H_2S abundance and physical quantities like visual extinction, gas temperature, and H density. Here, hydrogen nuclei number density is twice the n_{H_2} density obtained with the MCMC approach described earlier. As seen in such plots, the relationship between the H_2S abundance and the physical parameters is mostly monotonic. To assess the degree of correlation, we compute the Kendall's tau coefficient (Kendall 1938) in each case: 1 for perfect correlation, 0 means no correlation, and -1 stands for perfect anti-correlation. Fig. 5.2 shows the estimated H_2S abundances as a function of the visual extinction towards the observed positions. They are loosely anti-correlated (Kendall test results: $\tau_K = -0.3$, p-value = 0.06), as the H_2S abundance is, in general, at its minimum towards the visual extinction peak, with values of the order of 10^{-10}, and increases towards lower visual extinctions (Fig. 5.2). In TMC 1, the maximum H_2S abundance is mea-

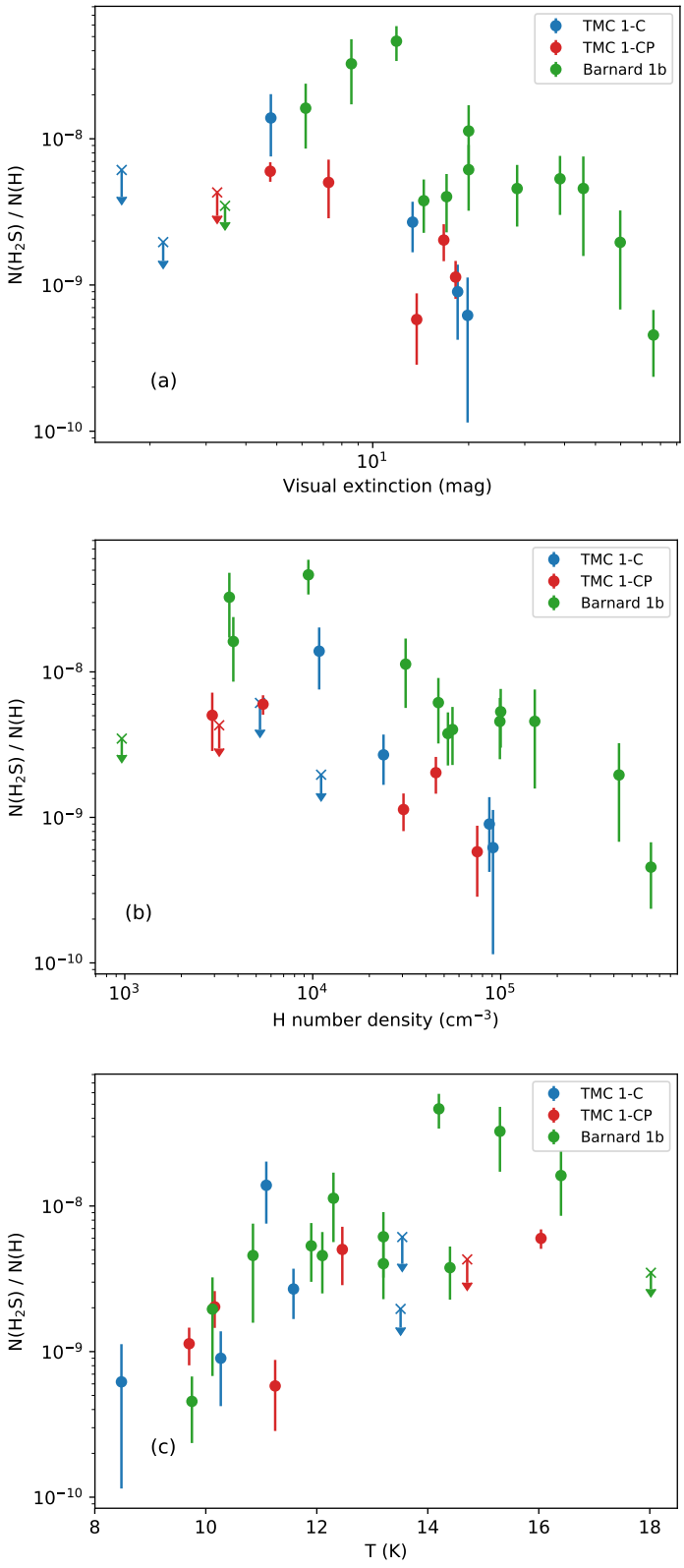

Figure 5.2: In (a), the observed H_2S abundance is plotted as a function of visual extinction in TMC 1-C (blue), TMC 1-CP (red), and Barnard 1b (green). In a similar fashion, in (b) the observed H_2S gas-phase abundance against the H number density in TMC 1 and Barnard 1b cores is shown. Crosses represent upper bound values. Finally, (c) displays the H_2S abundance plotted against the gas kinetic temperature.

sured at $A_v \sim 5$ mag, with values of $\sim 2\times10^{-8}$. In Barnard 1b, the H_2S abundance peaks at $A_v \sim 10$ mag with values of $\sim 5\times10^{-8}$ and then, decreases again, reaching values of $\sim 2\times10^{-8}$ at $A_v \sim 5$ mag. We do not detect H_2S when $A_v < 5$ mag (Fig. 5.2).

The H_2S gas-phase abundance is moderately anti-correlated with the hydrogen nuclei density ($\tau_K = -0.4$, p-value $< 10^{-2}$). This kind of anti-correlation is expected when the freeze-out of molecules on grain surfaces is determining the molecular abundance. The probability of collisions between gas and grains is proportional to the gas density and the thermal velocity. Assuming that the sticking efficiency is ~ 1, that is, the H_2S molecules stick on grains in every collision, we can define a depletion timescale given by the inverse of this probability such as

$$X(H_2S) \propto t_{dep} \propto \frac{1}{n_{gas}\sigma_{gr}v} \propto \frac{1}{n_{gas}\sqrt{T_{kin}}}, \tag{5.1}$$

where $X(H_2S)$ is the abundance of H_2S respect to H nuclei, n_{gas} is the density of the gas, σ_{gr} is the grain cross-section, and v is the thermal velocity of the species, related to the kinetic temperature T_{kin}. In Fig. 5.3 we plot the H_2S gas-phase abundance against $n_{gas}\sqrt{T_{kin}}$. The H_2S abundance decreases with $n_{gas}\sqrt{T_{kin}}$ following a power-law with index $m \approx -1$ in the three studied cores, which confirms this behavior (we do not include upper bound values in this analysis). Interestingly, the abundance of H_2S in Barnard 1b is more than a factor of ~ 3 higher than towards TMC 1 for each density, suggesting a higher formation rate or lower destruction rate in Barnard 1b. In Fig. 5.2 we plot the H_2S gas-phase abundance as a function of the kinetic temperature. The H_2S abundance is strongly correlated with the gas kinetic temperature (Kendall test gave $\tau_K = 0.6$ and p-value $p < 10^{-3}$) as long as $A_v > 5$ mag, which translates into a lower abundance towards the cooler quiescent region TMC 1 compared with slightly warmer Barnard 1b core that is located in an active star forming region. In the following we determine the physical structure and model the chemistry of these two regions.

5.7 Physical structure: core density profiles

The densities at the observed positions in TMC 1 and Barnard 1b (those marked in Fig. 5.1) were derived using the procedure described in Section 4. To fully characterize the density structure of the cores along the line of sight, we consider the simplest case of spherically symmetric, thermally supported, and gravitationally bound clouds. The solution for such a cloud is the well-known Bonnor-Ebert sphere (BE, hereafter). We assume that the radial density structure of the filament is that of a BE, which has been widely parameterized by the approximate analytical profile (see e.g., Priestley et al. 2018; Tafalla et al. 2002):

$$n_H(r) = \frac{n_0}{1+\left(\frac{r}{r_c}\right)^{\alpha}}, \tag{5.2}$$

where r is the distance from the origin, that is , either TMC 1-C, TMC 1-CP, or Barnard 1b, n_0 is the hydrogen nuclei number density at the origin $r = 0$, r_c is the flat radius of the BE, and α is the asymptotic power index. At high distances, density falls as $\propto r^{-\alpha}$. As Fig. 5.4

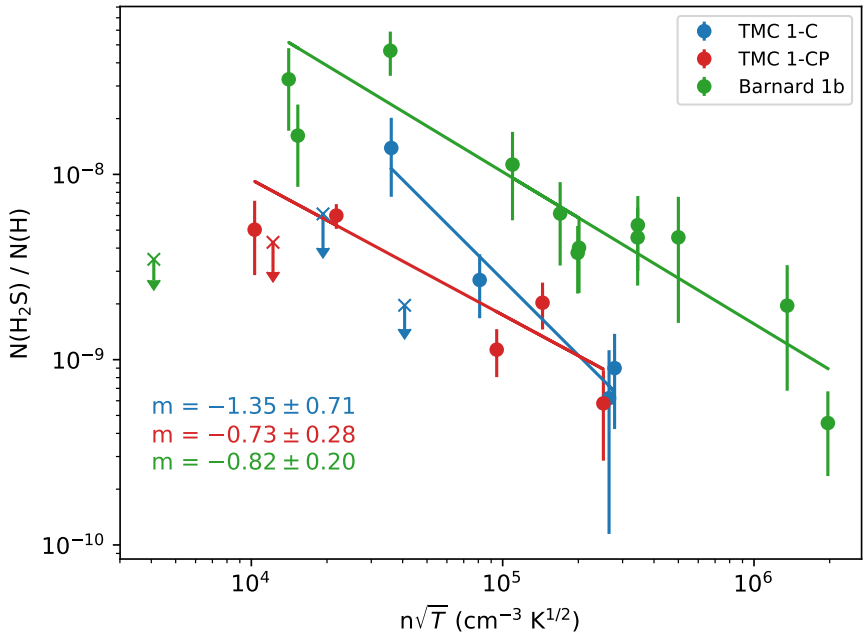

Figure 5.3: Observed H_2S gas-phase abundance plotted against $n_{\rm gas}\sqrt{T}$ (cm^{-3} K$^{1/2}$) in log scale, showing the sticking behavior described by Eq. (5.1). Crosses mark upper bound values, which were not taken into account in this analysis.

shows, the family of curves defined by Eq. (5.2) is in good agreement with the observed values (to include the origin in a logarithmic scale, we use the symmetrical logarithmic scale from Matplotlib Python library, which by default uses a linear scale between 0 and 1 and the logarithmic scale for the rest of the data range). The central density, n_0, ranges between $(5.23-7.55)\times10^4$ cm^{-3} in TMC 1 and $(3.43-9.11)\times10^5$ cm^{-3} in Barnard 1b. The value of r_c, the flat radius of the BE sphere, is found to be $(0.28\pm0.11)\times10^4$ au and $(1.11\pm0.32)\times10^4$ au in Barnard 1b and TMC 1, respectively. Finally, the asymptotic power index α ranges from 1.76 in the case of Barnard 1b to 4.29 in TMC 1. In a simple parametrization of a BE collapse, a larger flat radius corresponds to a younger, less evolved BE (Aikawa et al. 2005; Priestley et al. 2018). This is in agreement with our parameterizations, since TMC 1-C and TMC 1-CP, starless cores, have larger flat radii than Barnard 1b, which hosts a first hydrostatic core (FHSC for short) and is, therefore, a more evolved core than TMC 1-C and TMC 1-CP. Similarly, the higher asymptotic power index α of TMC 1 is indeed a feature of younger BEs, according to the parameterizations derived by Priestley et al. (2018).

The visual extinction along the line of sight of the selected positions in TMC 1 and Barnard 1b cores is taken from the visual extinction maps in Fig. 5.1. A parameter that will be needed in the chemical modeling of the cores (Section 9) is the shielding from the external UV field at each point. Assuming spherical symmetry and isotropic UV illumination, each point inside the cloud is shielded from the external UV field by an extinction that is, approximately, half of that measured in the extinction maps. We thus define an effective visual extinction

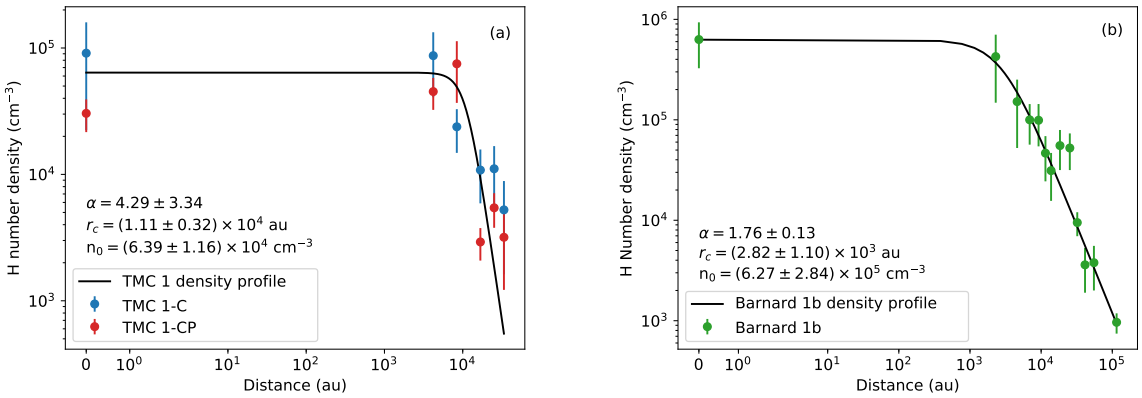

Figure 5.4: H number density profiles of TMC 1-C and TMC 1-CP (a) and Barnard 1b (b) as the result of fitting the data in Table 5.6 and Table 5.7, respectively, to the Eq. (5.2).

$A_{\rm veff}$ as half of the visual extinction measured in the extinction maps: $A_{\rm veff}(r) = A_{\rm v}(r)/2$. In Fig. 5.5, the effective visual extinction is plotted as a function of the distance towards the origin. The effective visual extinction across TMC 1 is interpolated using a cubic spline passing through the average of the effective extinction at each position (Fig. 5.5). In Barnard 1b, we fit the effective visual extinction with the following family of functions:

$$A_{\rm veff}(r) = \frac{A_{0\,\rm eff}}{\sqrt{1 + r/r_{\rm c}}}, \tag{5.3}$$

where r is the distance from the origin, $A_{0\,\rm eff}$ is the effective visual extinction at the origin, and $r_{\rm c}$ is the flat radius of the profile, the distance at which effective visual extinction starts falling significantly. This kind of profile is well-suited for BEs with an asymptotic power index $\alpha \sim 2$ (see Dapp & Basu 2009). The flat radius of Barnard 1b is found to be in agreement with the one previously estimated via BE fitting. Finally, as shown in Fig. 5.6, we parameterize the gas temperature of the observed positions.

Incident UV field in TMC 1 and Barnard 1b

The incident UV field is a key parameter in the photodesorption of H_2S. The increase of the grain temperature at the cloud borders is only understood as the consequence of dust heating by the interstellar radiation field (ISRF). However, to our knowledge, it is not straightforward to derive the incident UV field from the dust temperature. On the one hand, the exact relation between dust temperature and the ISRF is dependent on the poorly known grain composition and its detailed variation across the cloud. On the other hand, in our part of the Galaxy, the dust heating is dominated by the visible part of the ISRF, and the visible and IR parts of the ISRF do not scale in a simple way with the UV part. Remaining aware of all these problems, in Paper I we obtain a first guess of the local UV flux in TMC 1 using the analytical expression by Hocuk et al. (2017). This expression relates the dust temperature of a region with a given visual extinction and the incident UV field in units of the Draine

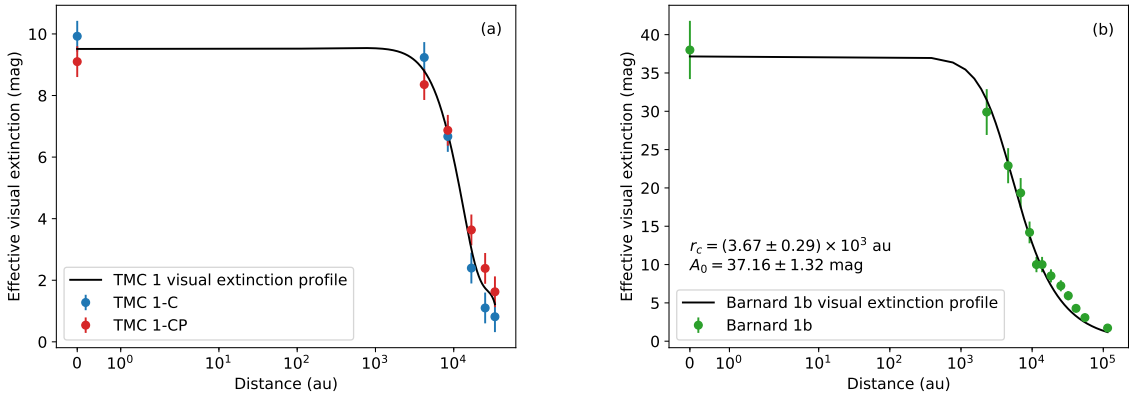

Figure 5.5: Effective visual extinction in magnitudes of TMC 1-C and TMC 1-CP (a) and Barnard 1b (b) as the result of fitting the data in Table 5.6 and Table 4.7, respectively, to the Eq. (5.3).

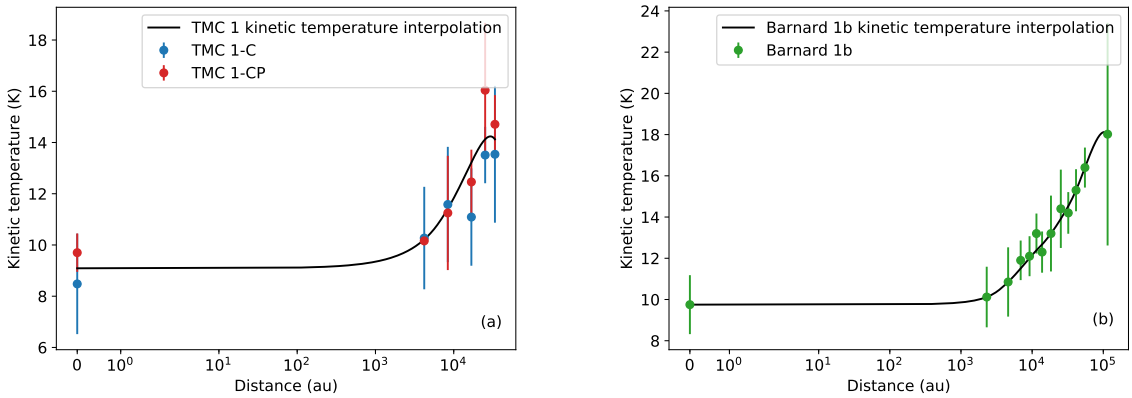

Figure 5.6: Kinetic temperature in the observed positions of TMC 1-C and TMC 1-CP (a) and Barnard 1b (b) and the quadratic spline interpolation of the error-weighted average at each position (solid black line).

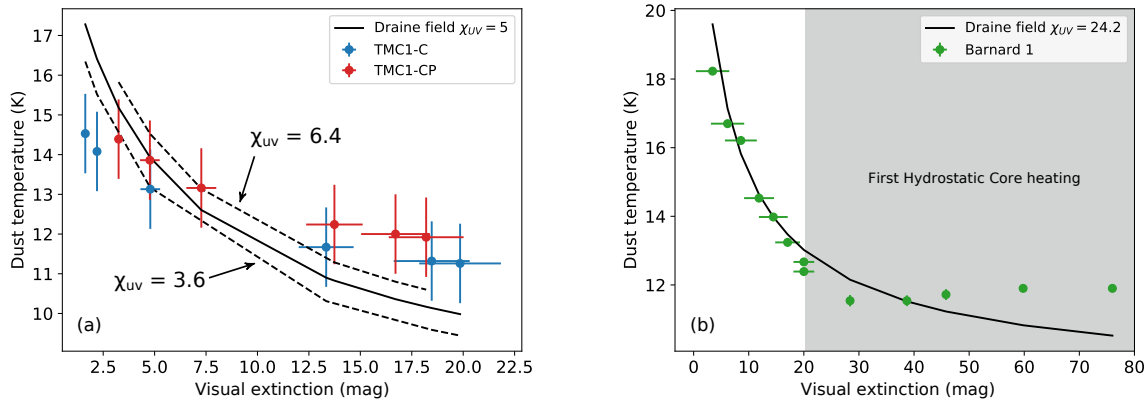

Figure 5.7: (a) shows the values of the UV field following the Hocuk et al. (2017) parameterization for TMC 1-C (blue) and TMC 1-CP (red) cuts (dashed lines). We also show the best fit (solid line) for the whole TMC 1 region, with χ_{UV}(TMC1) = 5. Similarly, in (b), the parameterization yields a Draine field of χ_{UV}(B1b) ~ 24 for Barnard 1b. It is worth noticing the raise of dust temperature in the $A_v > 30$ mag region, probably due to the FHSC heating of dust or the presence of a thick ice covering.

field (Draine 1978). In this paper, we use the same procedure to estimate the incident UV radiation in Barnard 1b.

Fig. 5.7 shows the $T_{dust} - A_v$ plots for the three cuts considered in this paper. None of the cuts can be fitted with a single value of the UV field. In TMC 1, the dust temperature of the dense core ($A_v > 7.5$ mag) is better fitted with an illuminating UV field such that $\chi_{UV} \sim 6.4$, while the translucent region ($A_v < 7.5$ mag) is better fitted with $\chi_{UV} \sim 3.6$. In Barnard 1b, dust temperatures are best fitted with $\chi_{UV} = 24$ in the region $A_v < 20$ mag. However, this value of the incident UV field underestimates the dust temperature in the region $A_v > 30$ mag. The reason for this underestimation is unclear. A thick layer of ice would allow the dust to be warmer by up to 15% at high visual extinctions (Hocuk et al. 2017). It is interesting to note that Barnard 1b is located in an active star forming region, and hosts the two very young protostellar cores B1b-N and B1b-S. In fact, as seen with ALMA, dust temperatures above 60 K have been detected in scales of 0.6" in the Barnard 1b core. Therefore, we cannot exclude an additional dust heating because of the presence of these young protostars. Due to the large column density $N(H_2) \sim 7.6 \times 10^{22}$ cm^{-2} in Barnard 1b, this heating would only affect high extinction areas. Since we are interested in the effects of photo-desorption in the low-extinction layers of the cloud, we will adopt $\chi_{UV} = 5$ in TMC 1 and $\chi_{UV} = 24$ in Barnard 1b in our calculations.

5.8 Photodesorption of H_2S: a simple accretion and photodesorption model

To study the role of photodesorption in the formation of gas-phase H_2S, we adapted the simplified PDR model proposed by Hollenbach et al. (2009) to the case of H_2S. In this model, the grains are supposed to be covered by an ice layer, from where H_2S is released into the gas phase via photodesorption. Only two processes, freezing onto grain mantles and photodissociation, are considered for gas-phase H_2S destruction. The gas-phase H_2S formation rate is then proportional to the attenuated local UV interstellar flux $1.7\chi_{\rm UV}F_0e^{-0.9A_{\rm v}}+\Phi_{\rm SP}$, where F_0 is the local interstellar flux, $A_{\rm v}$ the visual extinction in magnitudes, $\Phi_{\rm SP}$ is the flux of secondary photons, and $\chi_{\rm UV}$ is the incident UV field in Draine units. This rate is also proportional to the photodesorption efficiency $Y_{\rm H_2S}$, which is set to 1.2×10^{-3} molecules per incident photon, as calculated by Fuente et al. (2017), the fraction of desorption sites occupied by H_2S ice ($f_{s,\rm H_2S}$), and the probability of collision ($n_{\rm gr}\sigma_{\rm gr}$). The destruction rate however must account for dissociation and freezing of H_2S molecules. The probability of a UV photon to dissociate a H_2S molecule is given by the attenuated UV field flux times the density of H_2S, $1.7\chi_{\rm UV}R_{\rm H_2S}e^{-0.9A_{\rm v}}n({\rm H_2S})$, where R_{H_2S} is the H_2S photodissociation rate, and $n(H_2S)$ is the H_2S number density. As discussed previously, the freezing probability is given by the probability of collision between grains and H_2S molecules ($n({\rm H_2S})\upsilon_{H_2S}n_{\rm gr}\sigma_{\rm gr}$). In the stationary state, both creation and destruction rates are equal, and therefore:

$$(1.7\chi_{\rm UV}F_0e^{-0.9A_{\rm v}}+\Phi_{\rm SP})\,Y_{\rm H_2S}f_{s,\rm H_2S}n_{\rm gr}\sigma_{\rm gr} = \\ = 1.7\chi_{\rm UV}R_{\rm H_2S}e^{-0.9A_{\rm v}}n({\rm H_2S})+n({\rm H_2S})\upsilon_{H_2S}n_{\rm gr}\sigma_{\rm gr}. \quad (5.4)$$

It should be noted that secondary photons are not considered to contribute to the photodissociation rate, R_{H_2S}, and are assumed to follow the same extinction law as the FUV radiation. Defining $\sigma_{\rm H}\equiv\frac{n_{\rm gr}(A_{\rm v})\sigma_{\rm gr}}{n_{\rm H}(A_{\rm v})}$, and assuming that the ratio $\frac{n_{\rm gr}(A_{\rm v})}{n_{\rm H}(A_{\rm v})}$ is constant for the range of $A_{\rm v}$ considered,

$$X({\rm H_2S})=\frac{(1.7\chi_{\rm UV}F_0\;e^{-0.9A_{\rm v}}+\Phi_{\rm SP})\;Y_{\rm H_2S}\,f_{s,\rm H_2S}\,\sigma_{\rm H}}{1.7\chi_{\rm UV}R_{\rm H_2S}\;e^{-0.9A_{\rm v}}+\upsilon_{H_2S}\,n_{\rm H}(A_{\rm v})\,\sigma_{\rm H}}. \quad (5.5)$$

The fractional coverage of the surface by H_2S ice, $f_{s,\rm H_2S}$, is given by equating the sticking of S atoms to grain surfaces to the photodesorption rate of H_2S

$$(1.7\chi_{\rm UV}F_0e^{-0.9A_{\rm v}}+\Phi_{\rm SP})\,Y_{\rm H_2S}f_{s,\rm H_2S}n_{\rm gr}\sigma_{\rm gr}=n({\rm S})\upsilon_{\rm S}n_{\rm gr}\sigma_{\rm gr},$$

and therefore,

$$f_{s,\rm H_2S}=\frac{n({\rm S})\upsilon_{\rm S}}{Y_{\rm H_2S}(1.7\chi_{\rm UV}F_0e^{-0.9A_{\rm v}}+\Phi_{\rm SP})}. \quad (5.6)$$

Combining Eqs. (5.5) and (5.6), we are able to predict the H_2S abundance for given physical conditions. The abundance relative to water found in comets is of the order of 2% (Bockelée-Morvan et al. 2000), thus we take as saturation value, $f_{s,\rm H_2S}=0.02$. We obtain

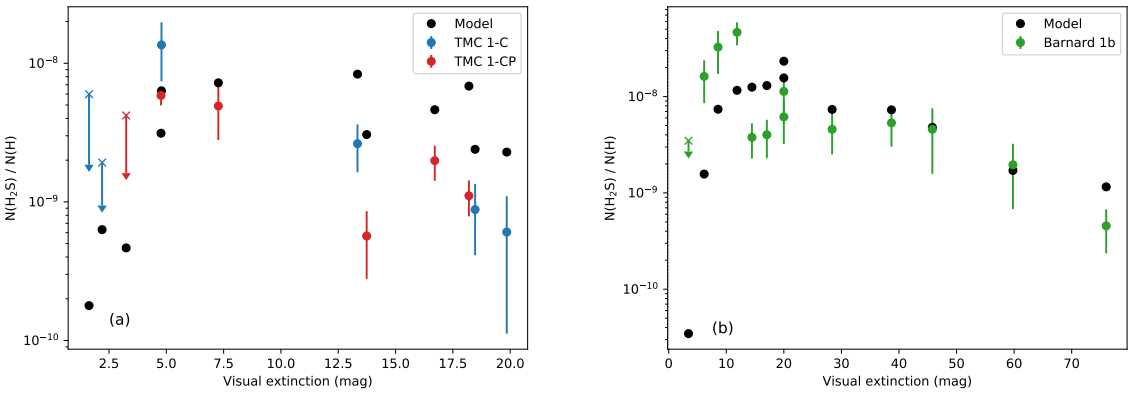

Figure 5.8: Observed H_2S gas-phase abundance in TMC 1-C, TMC 1-CP, and Barnard 1b (blue, red, and green, respectively), compared to the PDR model prediction (black). The abundances are calculated using Eq. (5.5) and assuming $\Phi_{SP} = 2 \times 10^4$ photons cm^{-2} s^{-1} in TMC 1 and $\Phi_{SP} = 7 \times 10^4$ photons cm^{-2} s^{-1} in Barnard 1b. The value of Φ_{SP} has been selected to match the observations.

the best fitting of the observed H_2S abundances in TMC 1 with $\Phi_{SP} = 2 \times 10^4$ photons cm^{-2} s^{-1} (Fig. 5.8). However, we do not reproduce the H_2S abundances in Barnard 1b with the same flux of secondary photons, specially at higher extinction regions (see Fig. 5.8). To explain the abundances observed in Barnard 1b we should adopt a higher value, $\Phi_{SP} = 7 \times 10^4$ photons cm^{-2} s^{-1}. Secondary photons are generated by the interaction of H_2 with cosmic rays (Prasad & Tarafdar 1983). While the UV photons are absorbed by dust, cosmic rays penetrate deeper into the cloud maintaining a flux of UV photons even in the densest part of starless cores. The flux of UV secondary photons in dense clouds has a typical value of 10^4 photons cm^{-2} s^{-1}, with a cosmic ray molecular hydrogen ionization rate of 3.1×10^{-17} s^{-1}, and a factor of 3 uncertainty (Shen et al. 2004). Recent works point to a lower cosmic ionization molecular hydrogen rate in Barnard 1b than in TMC 1 (Fuente et al. 2016, 2019) which is in contradiction with assuming higher Φ_{SP} in Barnard 1b, rendering our assumptions very unlikely. It is true, however, that the uncertainties of these estimates are large, of around a factor of ~ 5, not allowing us to fully discard this explanation.

As we have seen, this simple model presents several difficulties. It neglects the chemically active nature of the icy grains, as it does not include any chemical reaction on grain surfaces. Furthermore, recent studies have shown that chemical desorption might be an important source of gas-phase H_2S (Oba et al. 2018), which is not included here. Finally, due to the many ad-hoc parameters introduced, it lacks of any predicting power. It is therefore necessary to consider a more complete chemical modeling of these cores. In the next section we carry out a 1D modeling of the cores using a full gas-grain chemical network to have a deeper insight into the H_2S chemistry.

5.9 Complete modeling of the TMC 1 and Barnard 1b chemistry

NAUTILUS 1.1 (Ruaud et al. 2016) is a numerical model suited to study the chemistry in astrophysical environments. It solves the kinetic equations for the gas-phase and the heterogeneous chemistry at the surface of interstellar dust grains. NAUTILUS is now a three-phase model, in which gas, grain surface and grain mantle phases, and their interactions, are considered. Given a set of physical and chemical parameters, NAUTILUS computes the evolution of chemical abundances. In the following, we adopt the physical properties of TMC 1 and Barnard 1b derived in Section 7. Since both TMC 1-C and TMC 1-CP are described with identical physical parameters, we consider a common chemical model for them.

5.9.1 Chemical network

We have developed an up-to-date sulfur chemical network, based on the KInetic Database for Astrochemistry (KIDA), including recent updates (Fuente et al. 2017; Le Gal et al. 2017; Vidal et al. 2017; Le Gal et al. 2019). Our chemical network is composed of 1126 species (588 in the gas phase and 538 in solid phase) linked together via 13155 reactions, with 8526 reactions in gas phase and 4629 reactions in solid phase. The gas-phase reactions are composed of (i) bi-molecular reactions, such as radiative associations, ion-neutral and neutral-neutral reactions), (ii) recombinations with electrons, (iii) ionization and dissociation reactions by direct by UV-photons, cosmic rays, and secondary photons (i.e., photons induced by cosmic rays). The solid phase reactions are composed of both surface and bulk iced grain mantle reactions that occurs for most of them through the diffusive Langmuir-Hinshelwood mechanism. The bulk and surface of the grain mantle interact via swapping processes (Garrod 2013; Ruaud et al. 2016). Desorption into the gas phase is only allowed for the surface species, considering both thermal and non-thermal mechanisms. The latter include desorption induced by cosmic-rays (Hasegawa & Herbst 1993), photodesorption, and chemical desorption (Garrod et al. 2007). We further describe this last process in Section 9.2. The binding energies considered in this work can be found in Table 2 of Wakelam et al. (2017) and on the KIDA database website[1].

5.9.2 Chemical desorption: 1D modeling

In Fig. 5.9 and Fig. 5.10, we show the comparison of our model with the observations of TMC 1 and Barnard 1b, respectively. We have computed the chemical abundances of different sulphuretted molecules in TMC 1 and Barnard 1b using the physical structures derived in Section 7. As initial abundances, we adopt undepleted sulphur abundance (see Table 5.3). Dust and gas temperatures are assumed to be equal. Other relevant parameters are χ_{UV} = 5 and $\zeta_{CR} = 1.15 \times 10^{-16}$ s^{-1} for TMC 1 (Fuente et al. 2019), and $\chi_{UV} = 24$ and $\zeta_{CR} = 6.5 \times 10^{-17}$ for Barnard 1b (Fuente et al. 2016). To compare the output of the chemical model with the observations, we compute a weight-averaged abundance over the line of sight, weighted

[1] http://kida.obs.u-bordeaux1.fr/

Table 5.3: Initial abundances

He	9.00×10^{-2}
N	6.20×10^{-5}
O	2.40×10^{-4}
C^+	1.70×10^{-4}
S^+	1.50×10^{-5}
Si^+	8.00×10^{-9}
Fe^+	3.00×10^{-9}
Na^+	2.00×10^{-9}
Mg^+	7.00×10^{-9}
P^+	2.00×10^{-10}
Cl^+	1.00×10^{-9}
F	6.68×10^{-9}

with the density at each position. Assuming the spherically symmetric density profiles n_H given in Fig. 5.4, the weight-averaged abundance $[X]_{ac}$ of an element X along the line of sight with offset r is calculated here as:

$$[X]_{ac}(r) = \frac{\sum_i (l_{i+1} - l_i)\,(n_H(s_i)[X](s_i) + n_H(s_{i+1})[X](s_{i+1}))}{\sum_j \left(l_{j+1} - l_j\right)\left(n_H(s_j) + n_H(s_{j+1})\right)}, \tag{5.7}$$

where $s_i = \sqrt{r^2 + l_i^2}$, l_i is a discretization of the segment along the line of sight $l_{max} > \cdots > l_{i+1} > l_i > \cdots > 0$, with $l_{max} = \sqrt{r^2 + r_{max}^2}$ and r_{max} being the radius of the density profile $n_H(r)$.

In dark clouds, where the temperature of grain particles is below the sublimation temperature of most species, non-thermal desorption processes are needed to maintain significative abundances of molecules in gas phase. This is especially important in the case of H_2S that is thought to be mainly formed on the grain surfaces. Differently from the other processes, chemical desorption links the solid and gas phases without the intervention of any external agents such as photons, electrons, or other energetic particles (Garrod et al. 2007). In other words, it could be efficient in UV-shielded and low-CR environments where photodesorption or sputtering cannot be efficient, becoming more likely the most efficient mechanism in dark cores. This mechanism seems also to be responsible for the abundance of complex molecules such as methanol and formaldehyde in dense cores and PDRs, becoming dominant against phototodesorption (Esplugues et al. 2019; Le Gal et al. 2017; Vasyunin et al. 2017; Esplugues et al. 2016). New laboratory experiments proved that chemical desorption might be important for H_2S formation on water ice (Oba et al. 2018).

Achieving the correct inclusion of chemical desorption in chemical models is difficult. The efficiency of this process depends not only on the specific molecule involved, but also on the detailed chemical composition of the grain surface on which the reaction occurs, making a correct estimate of its value very difficult to obtain. The chemical desorption process starts from the energy excess of some reactions. In bare grains, as described in Minissale & Dulieu

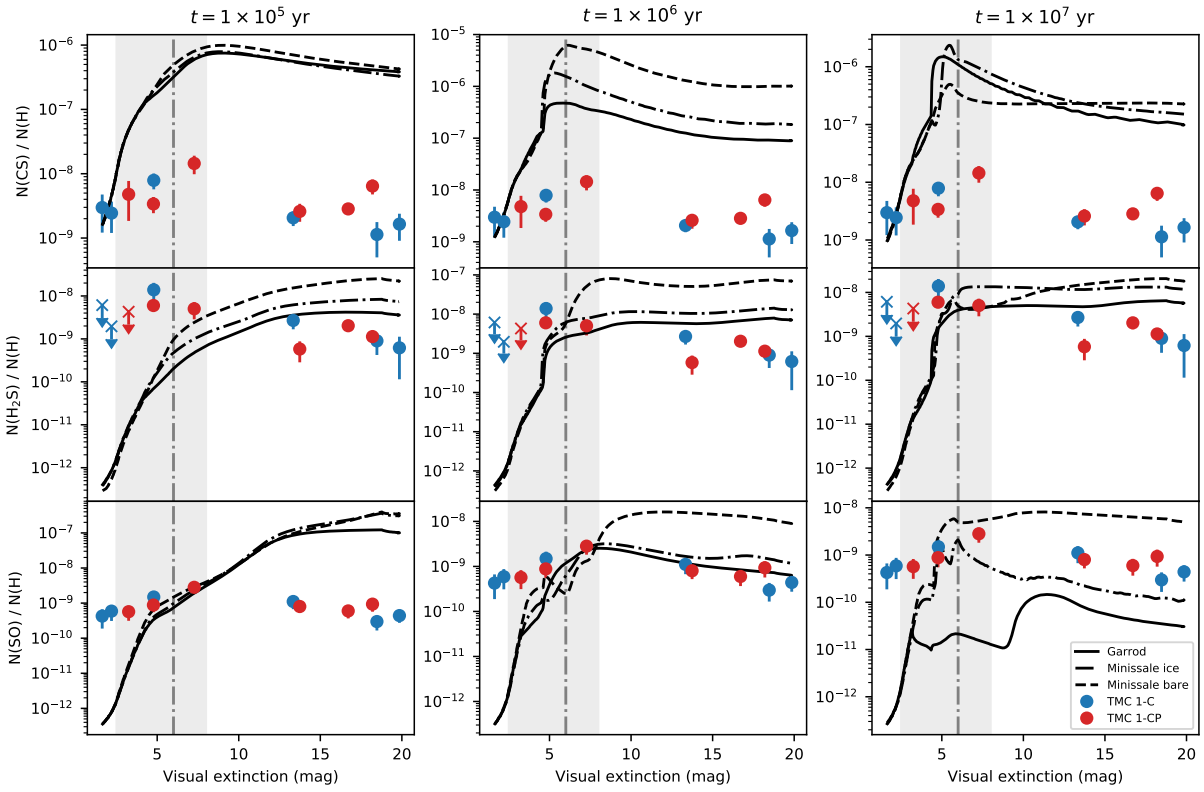

Figure 5.9: Predicted abundances (solid lines) of the CS (top row), H_2S (middle row), and SO (bottom row) by models with different chemical desorption schemes, together with the observed abundances in TMC 1, at times 0.1 – 1 – 10 Myrs. It should be noted that there is an extinction interval in which the observed H_2S fit to different chemical desorption schemes. This can be interpreted as a change in the grain surface composition. The vertical dashed line corresponds to $A_v = 6$ mag. The interval 2.5 – 8 mag around this value is shaded in all plots.

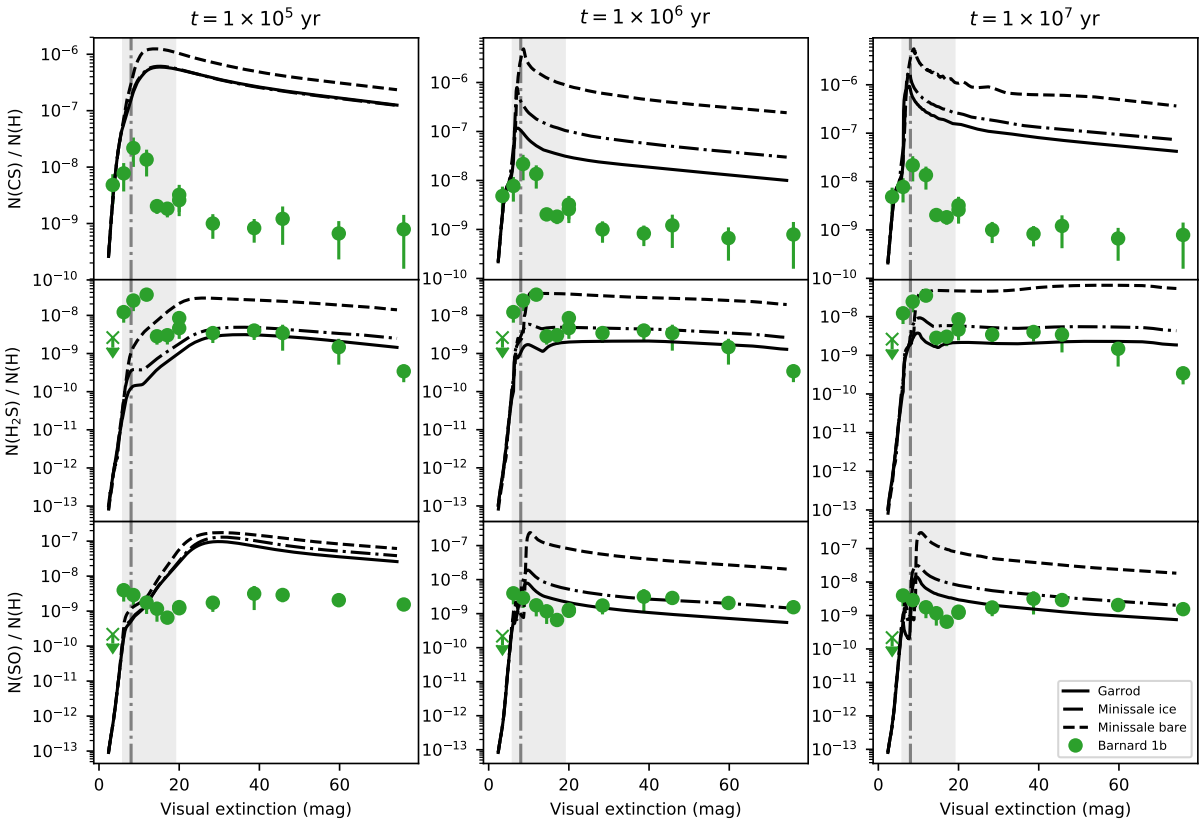

Figure 5.10: Plots that show the predicted abundances (solid lines) of the CS (top row), H_2S (middle row), and SO (bottom row) by models with different chemical desorption schemes, together with the observed abundances in Barnard 1b, at times 0.1 – 1 – 10 Myrs. The vertical dashed line represents A_v = 8 mag, and the shaded area encloses the range of extinctions 6 – 19 mag.

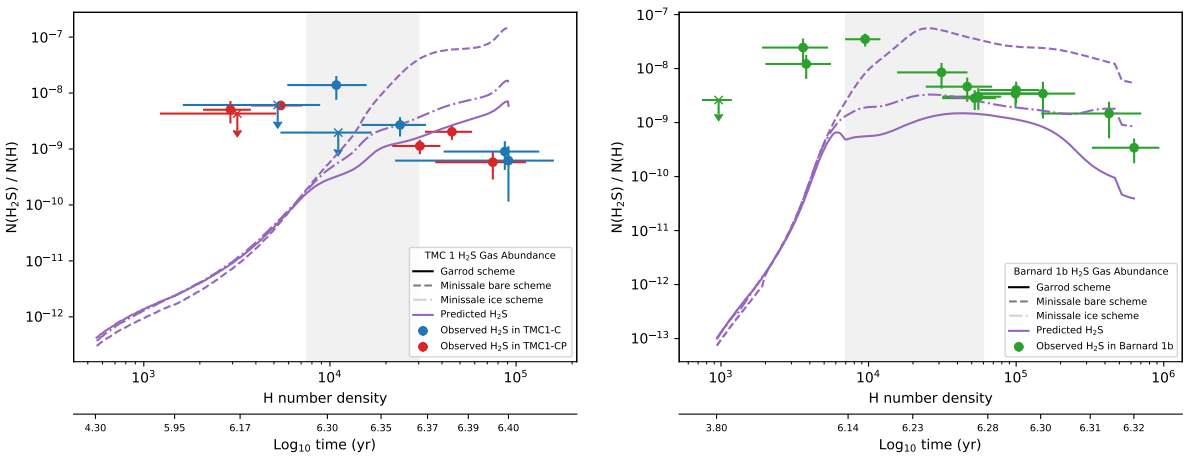

Figure 5.11: Detail of the predicted H_2S gas-phase abundance in TMC 1 (left) and Barnard 1b (right) according to the different desorption schemes in a 0-dimensional simulation, and the observed H_2S gas-phase abundances, plotted as a function of density and the time according to a freefall collapse. The shaded band encloses the density interval where the change in desorption scheme occur.

(2014), its efficiency essentially depends on four parameters: enthalpy of formation, degrees of freedom, binding energy, and mass of newly formed molecules. However, this efficiency becomes lower when dust grains are covered with an icy mantle because part of the energy released in the process is absorbed by the ice matrix. Minissale et al. (2016), based on experimental results, suggested that when taking into account the icy surface, the efficiency of the chemical desorption should be reduced to 10% of the value calculated for a bare grain, when dealing with the water-dominated icy coated mantles of dense regions. We run our chemical model to compare with our observations considering the three chemical desorption scenarios, i) bare grains following Minissale prescription, ii) icy coated grains following Minissale prescription, and iii) ice coated grains assuming Garrod prescription, in which the ratio of the surface–molecule bond-frequency to the frequency at which energy is lost to the grain surface is set to 0.01. The calculations following these three different scenarios are shown in Fig. 5.9 and Fig. 5.10.

The observed H_2S abundances are in reasonable agreement with those predicted by NAUTILUS at 1 Myr. At this time, the main reactions that lead to the creation and destruction of gas-phase H_2S at low and high extinctions in TMC 1 and Barnard 1b are found in Table 5.4. In all scenarios, chemical desorption is the main formation mechanism of gas-phase H_2S, and its prevalence diminishes at high extinctions, where density increases and gas-phase reactions become more important to form gas-phase H_2S.

Interestingly, the H_2S observations cannot be fitted using the same chemical desorption scheme at every position. In fact, we see that the observational data are in better agreement with the bare grain chemical desorption scheme as described by Minissale et al. (2016) towards the edge of the clouds and to an ice-covered grain chemical desorption scheme towards the more shielded regions. This suggests a change in the chemical composition of

grain surfaces, which become covered by a thick ice mantle as the density increases towards the core center, and opens the possibility to use the H_2S abundance to estimate the transition from bare to ice coated grains. Based on our observations, grains become coated with a thick ice mantle at $A_v \sim 8$ mag ($A_{v\,\mathrm{eff}} = A_v/2 \sim 4$ mag) in TMC 1 and $A_v \sim 12$ mag ($A_{v\,\mathrm{eff}} \sim 6$ mag) in Barnard 1b. As a sanity check for our interpretation, we compute a rough estimation of the upper bound of the visual extinction required to photodesorb the ice covering the grains with the expression (Tielens 2005):

$$A_{v\mathrm{eff}}^{\mathrm{ice}} < 4.1 + \ln\left[1.7\chi_{\mathrm{UV}}\left(\frac{Y_{\mathrm{pd}}}{10^{-2}}\right)\frac{10^4\ \mathrm{cm}^{-3}}{n}\right], \tag{5.8}$$

with χ_{UV} the incident UV field in Draine units, Y_{pd} the photodesorption yield, and n the number density. Assuming $Y_{\mathrm{pd}} = 10^{-3}$ photon^{-1} (Hollenbach et al. 2009), we obtain that grains would mainly remain bared for $A_{v\,\mathrm{eff}}^{\mathrm{ice}} < 6$ mag in TMC 1 and for $A_{v\,\mathrm{eff}}^{\mathrm{ice}} < 8$ mag in Barnard 1b. These values are in qualitative agreement with our results, within a factor of ~ 2, as grains are expected to remain bare deeper in Barnard 1b than in TMC 1 because of the higher incident UV field. However, this simple expression does not quantitatively reproduce our values of $A_{v\,\mathrm{eff}}^{\mathrm{ice}}$. This is not surprising taking into account that our estimate of the local ISRF is uncertain. Furthermore, the above expression is an approximation based on the equilibrium between photo-desorption and freeze-out of water molecules on the grain surfaces. To test the consistency of our result, we will use our chemical model to investigate the ice composition in Section 10.

It is also interesting to compare the output of our models with the observations of the other two most abundant S-bearing molecules, CS and SO. One first result is that our models overestimate by more than one order of magnitude the CS abundance in TMC 1 and Barnard 1b. The problem of the overestimation of the CS abundance was already pointed out by Vidal et al. (2017) and Laas & Caselli (2019). Vidal et al. (2017) suggested that it could come from wrong branching ratios of the dissociative recombination of HCS^+ or a potentially new sink for CS that might be the O + CS reaction whose reaction rate has not been measured at low temperatures. The predicted SO abundances are in reasonable agreement with the observed values if we assume the Garrod prescription to describe chemical desorption even at low visual extinctions. The difficult match between chemical model predictions for S-bearing species and observations make it challenging to determine the sulphur elemental abundance with an accuracy better than a factor of 10.

5.10 Discussion: Is H_2S tracing the snow line in dark cores?

As commented above, the H_2S chemical desorption efficiency seems to decay at a visual extinction of $A_v \sim 8$ mag in TMC 1 and $A_v \sim 12$ mag in Barnard 1b. We propose that this jump in the chemical desorption efficiency might be caused by a change in the chemical composition on the surface of grains, in particular the formation of a thick ice mantle. In this section, we use our chemical model to explore the link between the efficiency of the H_2S chemical desorption as traced by our observations and the ice chemical composition in TMC 1 and Barnard 1b.

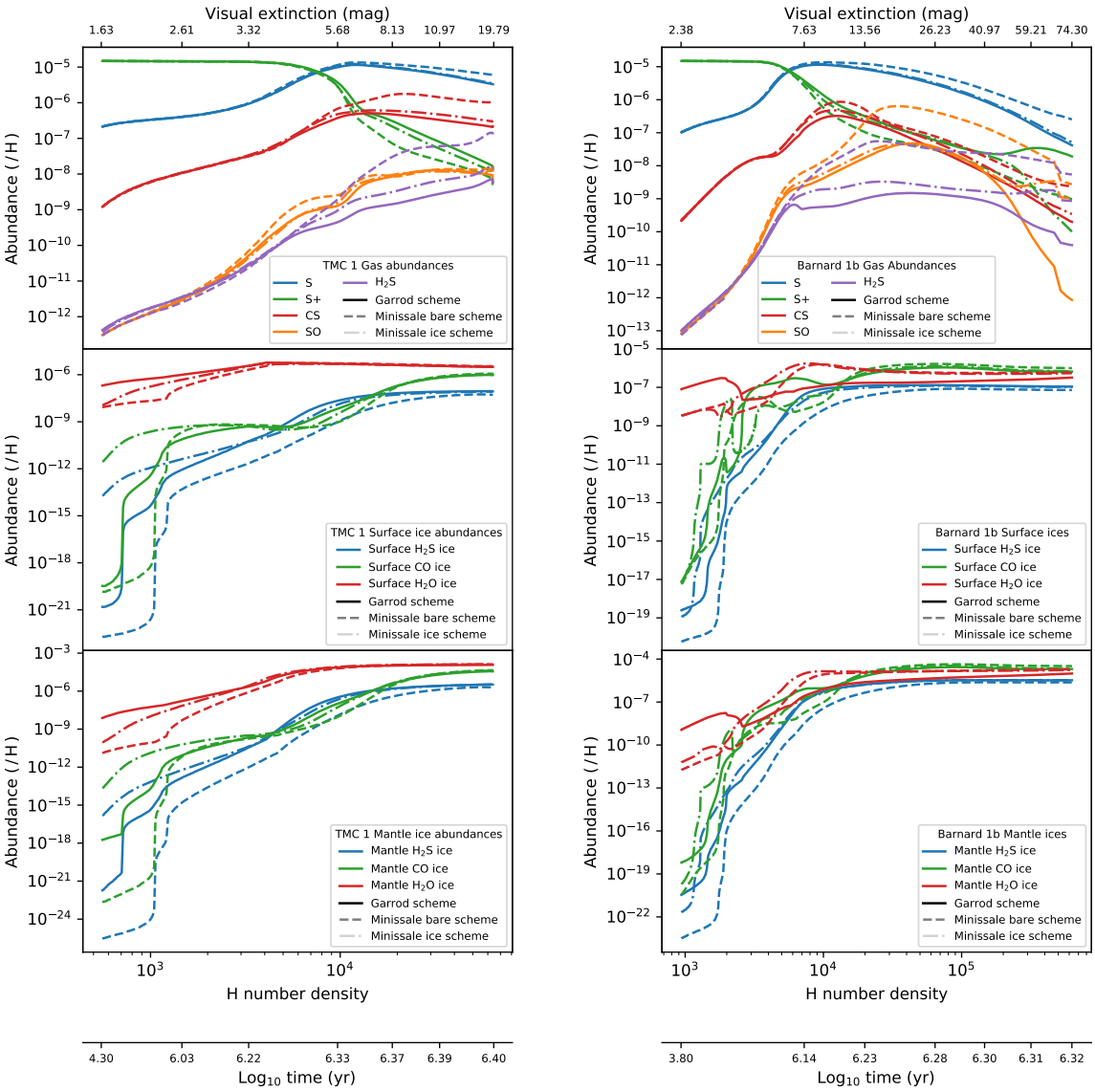

Figure 5.12: Predicted abundances of different molecules in gas phase (top row), ice surfaces (middle row), and ice mantles (bottom row) of TMC 1 (left column), and Barnard 1b (right column), according to the different desorption schemes. They are plotted as a function of the number density, together with the visual extinction that corresponds to such densities (see Fig. 5.4 and Fig. 5.5), and the time according to a freefall collapse.

In NAUTILUS, two ice phases are considered, the mantle and the surface. The mantle is assumed to grow by incorporating material from the surface. The mantle is hence a fossil record of the grain history. To determine the chemical composition of the ice mantle we should reproduce the trajectory of a cell of gas and dust during the core contraction. As a reasonable approximation, we have converted our 1D profile in a cell trajectory as follows. First, the density, temperature, and visual extinction profiles shown in Fig. 5.4, Fig. 5.5, and Fig. 5.6 are divided in 300 bins that we use to define the cell trajectory. Second, the time elapsed by the material to reach a bin i is equal to the difference between the free-fall time $t_{\rm ff}(\rho) \approx \sqrt{3/2\pi G\rho}$ of the initial bin and the current bin, that is, $t(i) = t_{\rm ff}(\rho_0) - t_{\rm ff}(\rho_i)$, and consequently, the duration of the whole trajectory is equal to the free-fall time assuming the density of the first bin. This time, for the lowest density in our cuts $n_{\rm H} \sim 1 \times 10^3$ cm^{-3} (see Table 4.7), is $t_{\rm ff} \sim 10^6$ yr. It is remarkable that this is the time that best fit the observations in Section 9, thus suggesting this choice to be a good guess of the collapse time. Third, in each time-step, the chemical abundances of the previous bin are taken as initial abundances for the next step. These trajectories describe the changes in density, temperature and local UV radiation experienced by a given cell once the collapse has started. Finally, we need to establish the chemical composition of the initial molecular cloud. To set the initial abundances of the cloud, we run the chemical model in a pre-phase, using the physical conditions of the first bin and letting chemistry evolve during 1 Myr, the typical time for this stage. The abundances at the beginning of the cloud collapse are then those that result from the pre-phase.

Following this procedure, we predict the chemical composition of the gas and dust as a function of time. In Fig. 5.11 we show the H_2S abundance as a function of H number density in TMC 1 and Barnard 1b. The density is continuously increasing with time and provides an easier comparison with observations. We recall, however, that in this comparison we are not taking into account the different physical and chemical conditions along the line-of-sight. According to our results in Section 9, for the low densities prevailing in the cloud border, we need to assume the chemical desorption prescription for bare grains to account for the high observed H_2S abundances, but at higher densities, our model overestimates the H_2S abundance. In both sources we find the same behavior with a break point at densities around $n_{\rm H} = 2 \times 10^4$ cm^{-3}. In the case of Barnard 1b, the abundances are well accounted using the Minissale prescription for ice coated grains for $n_{\rm H} > 2 \times 10^4$ cm^{-3}. In TMC 1, the observed abundances are 5−10 times lower than our predictions in any of the scenarios. To relate the H_2S abundance with the ice composition, we show the surface and mantle chemical composition as a function of density in TMC 1 and Barnard 1b in Fig. 5.12. It is worth noting that the density $n_{\rm H} = 2 \times 10^4$ cm^{-3} corresponds to the phase in which basically the whole ice mantle is formed, achieving the highest values for the s-H_2O and s-CO abundances. Moreover, solid H_2S (s-H_2S) becomes the most abundant S-bearing molecule locked in the ices, with an abundance of $\sim 3 \times 10^{-6}$ in both targets, one fifth of the cosmic value. Furthermore, according to our predictions, the main sulphur reservoir is gaseous atomic sulphur all along the cores.

One additional result is the different ice composition predicted in TMC 1 and Barnard 1b. While the predicted abundance of water ice is as high as $\sim 1.3 \times 10^{-4}$ in TMC 1, its abundance is 1.7×10^{-5} in Barnard 1b. In Barnard 1b, the oxygen is found mainly in the form of CO_2 ice, with an abundance of X(s-CO_2)$\sim 7.4 \times 10^{-5}$. Vasyunin et al. (2017) proposed, based on ex-

trapolations from Minissale's experimental results, that, in general, chemical desorption is enhanced if the ice surface is rich in CO or CH_3OH (instead of water). This could explain the higher abundance of H_2S in the high-density regions of Barnard 1b compared to TMC 1. However, this is not in agreement with Spitzer data on the ice composition towards the young stellar object Barnard 1b-S (Boogert et al. 2008), a star in the moderate density neighborhood of Barnard 1b, which do not show any sign of low s-H_2O abundance or s-CO_2 overabundance. This might be caused by several factors such as, for example, that Spitzer observations might show the ice composition of only the envelope of these objects instead of the dense core. It should be noted, however, that the chemistry on grain surfaces is not very well understood yet and, in addition to the surface chemical network, depends on many poorly known parameters such as the diffusivity of the grain surface. Indeed, the ratio s-CO_2/s-H_2O is very sensitive to the diffusivity of the surface and the grain temperature since the efficiency of surface processes involving O, S, CO, and SO is enhanced when surface diffusivities and ice mobilities are increased (Semenov et al. 2018). The same remains true for s-OCS abundance whose abundance is very sensitive to high mobility of heavy atoms. Further observational constraints are required to fine-tune models and give a more accurate description of the ice composition.

Under the assumption that comets are pristine tracers of the outer parts of the protosolar nebula, it is interesting to compare the composition of comets with that predicted for the ice mantles in the high extinction peaks of TMC 1 and Barnard 1b (see Table 5.5). There are significant variations in the observed abundances of S-bearing species among different comets. To account for this variation, we compare our predictions with a range of values derived from the compilation by Bockelée-Morvan & Biver (2017). In addition, we have added a specific column to compare with the most complete dataset on comet 67P/Churyumov-Gerasimenko (Calmonte et al. 2016). The ice abundances predicted for TMC 1 and Barnard 1b at the end of the simulation are, in general, close to the values observed in comets (see Table 5.5 and Fig. 5.13). These values, however, need to be taken with caution. The abundances of the species in comets are usually calculated relative to water. Our calculations show that the abundance of water in solid phase varies of about one order of magnitude from TMC 1 and Barnard 1b, making the comparison with comets very dependent on the abundance of solid water itself.

Sulphur abundance

A large theoretical and observational effort has been done in the last five years to understand the sulphur chemistry that is progressively leading to a new paradigm (Vidal et al. 2017; Fuente et al. 2016, 2019; Le Gal et al. 2019; Laas & Caselli 2019). Gas-grain models provide a new vision of the interstellar medium in which both gaseous and ice species are predicted. Vidal et al. (2017) updated the sulphur chemistry network and used this new chemical network to interpret previous observations towards the prototypical dark core TMC 1-CP. They found that the best fit to the observations was obtained when adopting the cosmic abundance of S as initial condition, and an age of 1 Myr. At this age, more than 70 % of the sulphur would remain in gas phase and only 30% would be in ice. Using the same chemical network but with 1D modeling, Vastel et al. (2018) tried to fit the abundances of twenty-one

Table 5.4: Most important reactions to H_2S in the model

Visual Extinction	**TMC 1**	
	Minissale bare	Minissale ice
	H_2S Production	
$A_v \sim 5$ mag	s-H + s-HS → H_2S (91.0%) $H_3CS^+ + e^- \rightarrow H_2S + CH$ (8.2%)	s-H + s-HS → H_2S (90.3%) $H_3CS^+ + e^- \rightarrow H_2S + CH$ (9.2%)
$A_v \sim 20$ mag	s-H + s-HS → H_2S (55.1%) $H_3S^+ + e^- \rightarrow H + H_2S$ (31.9%)	s-H + s-HS → H_2S (43.6%) $H_3S^+ + e^- \rightarrow H + H_2S$ (43.3%)
	H_2S Destruction	
$A_v \sim 5$ mag	$H_2S + S^+ \rightarrow H_2 + S_2^+$ (40.1%) $C + H_2S \rightarrow HCS + H$ (16.7%)	$H_2S + S^+ \rightarrow H_2 + S_2^+$ (39.1%) $C + H_2S \rightarrow HCS + H$ (18.0%)
$A_v \sim 20$ mag	$H_2S + H_3^+ \rightarrow H_2 + H_3S^+$ (51.7%)[†] $H_2S + S^+ \rightarrow H_2 + S_2^+$ (11.2%)	$H_2S + H_3^+ \rightarrow H_2 + H_3S^+$ (72.9%) $H_2S + H^+ \rightarrow H + H_2S^+$ (6.4%)
Visual Extinction	**Barnard 1b**	
	Minissale bare	Minissale ice
	H_2S Production	
$A_v \sim 5$ mag	s-H + s-HS → H_2S (99.2%) $S + H_2S^+ \rightarrow H_2S + S^+$ (0.3%)	s-H + s-HS → H_2S (85.4%) s-H_2S → H_2S (0.3%)
$A_v \sim 70$ mag	$H_3S^+ + e^- \rightarrow H + H_2S$ (48.4%) s-H + s-HS → H_2S (42.8%)	$H_3S^+ + e^- \rightarrow H + H_2S$ (47.0%) s-H + s-HS → H_2S (46.8%)
	H_2S Destruction	
$A_v \sim 5$ mag	$H_2S + S^+ \rightarrow H_2 + S_2^+$ (39.2%) $C + H_2S \rightarrow HCS + H$ (32.1%)	$H_2S + S^+ \rightarrow H_2 + S_2^+$ (38.0%) $C + H_2S \rightarrow HCS + H$ (32.4%)
$A_v \sim 70$ mag	$H_2S + H_3^+ \rightarrow H_2 + H_3S^+$ (73.8%) $H_2S + H^+ \rightarrow H + H_2S^+$ (10.9%)	$H_2S + H_3^+ \rightarrow H_2 + H_3S^+$ (69.8%) $H_2S + H^+ \rightarrow H + H_2S^+$ (20.6%)

[†] This reaction recycles H_2S since the products are reactants in the production reactions.

Table 5.5: Abundances of selected molecules in ice mantles

Molecule	Predicted abundances (/ H)		Predicted abundances (/ s-H_2O)		Abundance in comets (/ s-H_2O)[2]	67P/Churyumov-Gerasimenko[3]
	TMC 1	Barnard 1b	TMC 1	Barnard 1b		
CO	4.0×10^{-5}	2.2×10^{-5}	3.0×10^{-1}	1.3	0.002 – 0.23	–
CO_2	9.0×10^{-6}	7.4×10^{-5}	6.8×10^{-2}	4.2	0.025 – 0.30	–
H_2S	3.4×10^{-6}	3.3×10^{-6}	2.5×10^{-2}	1.9×10^{-1}	0.0013 – 0.015	0.0067 – 0.0175
OCS	3.8×10^{-7}	1.1×10^{-6}	2.9×10^{-3}	6.2×10^{-2}	$(0.3-4)\times10^{-3}$	0.00017 – 0.00098
SO	5.5×10^{-9}	6.3×10^{-8}	4.1×10^{-5}	3.6×10^{-3}	$(0.4-3)\times10^{-3}$	0.00004 – 0.000014
SO_2	4.0×10^{-11}	1.4×10^{-8}	3.0×10^{-7}	8.0×10^{-4}	2×10^{-3}	0.00011 – 0.00041
CS	3.7×10^{-8}	7.9×10^{-8}	2.8×10^{-4}	4.6×10^{-3}	$(0.2-2)\times10^{-3}$	–
H_2CS	4.0×10^{-8}	5.2×10^{-8}	3.0×10^{-4}	3.0×10^{-3}	$(0.9-9)\times10^{-4}$	–
NS	1.8×10^{-6}	2.7×10^{-6}	1.3×10^{-2}	1.5×10^{-1}	$(0.6-1.2)\times10^{-4}$	–
S_2	1.2×10^{-9}	2.8×10^{-9}	8.7×10^{-6}	1.6×10^{-4}	$(0.1-25)\times10^{-4}$	0.000004 – 0.000013
H_2O	1.3×10^{-4}	1.7×10^{-5}	1	1	–	–

[2] Data taken from Bockelée-Morvan & Biver (2017)
[3] Taken from Calmonte et al. (2016)

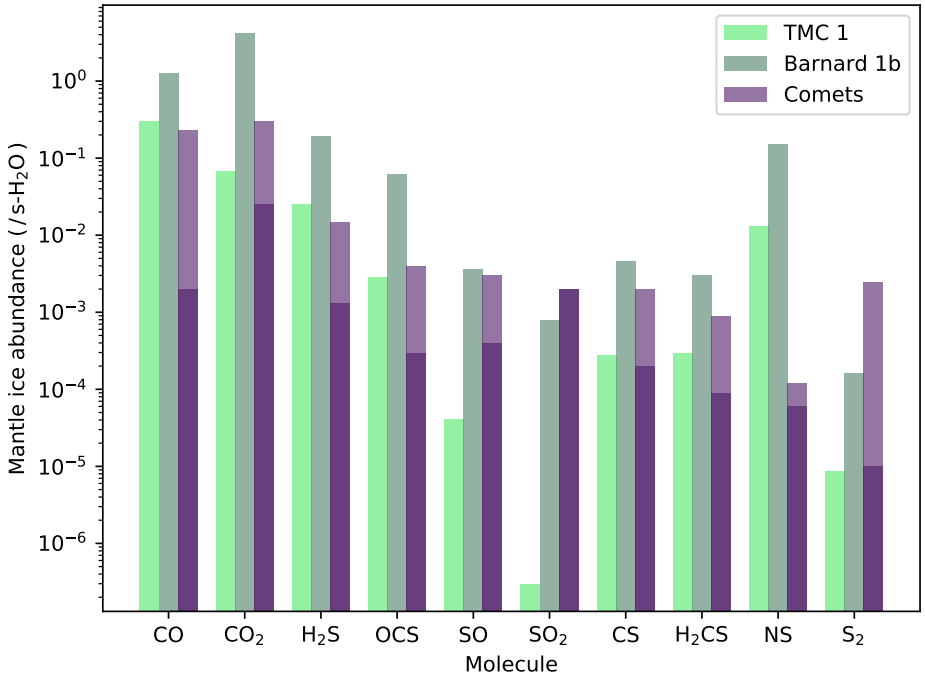

Figure 5.13: Predicted ice abundances in the mantle of grains in TMC 1 (light green) and Barnard 1b (dark green) of selected molecules and those observed in comets (dark and light purple) from Table 5.5.

S-bearing species towards the starless core L1544. The authors found that all the species cannot be fitted with the same sulphur abundance, with variations of a factor of 100, being models with S/H = 8.0×10^{-8} at an age of 1 - 3 Myr, those that best fitted the abundances of all the twenty-one species. A new gas-grain astrochemical network was proposed by Laas & Caselli (2019) to account for the complex sulphur chemistry observed in comets.

In this paper, we attempt to carry out a comprehensive study of the sulphur chemistry in TMC 1 and Barnard 1b by modeling the CS, SO, and H_2S observations in three cold cores using a fully updated gas-grain chemical network. Our chemical model is unable to fit the observations of the three species with the same parameters. By assuming a cosmic abundance of sulphur, we have a reasonable agreement between H_2S and SO observations with model predictions. However, we overestimate the CS abundance by more than one order of magnitude. Adopting a different approach, Fuente et al. (2019) obtained S/H $\sim (0.4 - 2.2) \times 10^{-6}$, one order of magnitude lower than the cosmic sulphur abundance, in the translucent part of the the TMC 1 filament. Given the uncertainty in the sulphur chemistry, we can conclude that the value of S/H that best fits our data $\sim$ a few 10^{-6} to 1.5×10^{-5}.

5.11 Summary and Conclusions

We performed a cloud depth dependent observational and modeling study, determining the physical structure and chemistry of three prototypical dense cores, two of them located in Taurus (TMC 1-C, TMC 1-CP) and the third one in Perseus (Barnard 1b).

- We used the dust temperature to carry out a rough estimate of the incident UV field which is $\chi = 3 - 10$ Draine field in TMC 1 and $\chi = 24$ in Barnard 1b. Moreover, we modeled the physical conditions of TMC 1- C, TMC 1- CP and Barnard 1b assuming a BE sphere. TMC 1- C and TMC 1- CP are well-fitted with the same parameters while Barnard 1b requires a higher central density consistent with a more evolved collapse.

- Using the full gas-grain model NAUTILUS and the physical structure derived from our observations, we investigated the chemistry of H_2S in these cores. Chemical desorption reveals as the most efficient release path for H_2S in cold cores. Our results show that the abundance of H_2S is well-fitted assuming high values of chemical desorption (bare grains) for densities $n_H < 2 \times 10^4$ cm^{-3}. For higher densities, our model overestimates the H_2S abundance suggesting that chemical desorption becomes less efficient. We propose that this critical density is related with a change in the chemical composition of the surface of the grains.

- To further investigate the relationship between the H_2S and grains properties, we examined the chemical composition of the icy mantles along the cores, as predicted by our model. Interestingly, the decrease of the H_2S chemical desorption occurs when the abundance of s-H_2O and s-CO achieves the maximum value in both molecular clouds.

- One additional result is that our model predicts different ice compositions in TMC 1 and Barnard 1b. While the abundance of s-H_2O is as high as $\sim 10^{-4}$ in TMC 1, its

abundance is ~10^{-5} in Barnard 1b. The abundances of s-H_2S are however very similar in the two clouds, about one fifth of the sulphur cosmic abundance.

- In addition to H_2S, we compared the abundances of CS and SO with model predictions. Our chemical model is unable to fit the observations of the three species simultaneously. Given the uncertainty in the sulphur chemistry, we can only conclude that the value of S/H that best fits our data is the cosmic value within a factor of 10.

This paper presents an exhaustive study of the sulphur chemistry in TMC 1 and Barnard 1b by modeling the CS, SO, and H_2S observations. Our chemical model is unable to fit the observations of the three species at a time, but it does manage to fit, with reasonable accuracy, our H_2S and SO observations. More theoretical and experimental work needs to be done in this area, especially in improving the constraints on the chemistry of CS. Given the uncertainty in the sulphur chemistry, we can only conclude that the value of S/H that best fit our data is the cosmic value within a factor of 10.

5.12 Tabulated data and line spectra

5.12.1 Physical conditions and chemical abundances in TMC 1

Table 5.6: TMC 1 physical conditions and chemical abundances

Source name	T_{dust} (K)	A_v (mag)	T_{gas}(K)	n_H (cm^{-3})	N(^{13}CS) (cm^{-2}) [a]	N(^{13}CS) / N(H_T) [c]	N(ortho $-H_2S$)(cm^{-2})	N(H_2S) / N(H_T)
TMC 1-CP+0	11.92	18.20	9.7 ± 0.8	$(3.0 \pm 0.8) \cdot 10^4$	$(3.9 \pm 1.0) \cdot 10^{12}$	$(1.1 \pm 0.3) \cdot 10^{-10}$	$(3.1 \pm 0.9) \cdot 10^{13}$	$(1.1 \pm 0.3) \cdot 10^{-9}$
TMC 1-CP+30	12.00	16.71	10.2 ± 0.2	$(4.6 \pm 0.4) \cdot 10^4$	$(1.6 \pm 0.2) \cdot 10^{12}$	$(4.7 \pm 0.6) \cdot 10^{-11}$	$(5.1 \pm 1.4) \cdot 10^{13}$	$(2.0 \pm 0.6) \cdot 10^{-9}$
TMC 1-CP+60	12.24	13.74	11.3 ± 2.2	$(7.6 \pm 3.8) \cdot 10^4$	$(1.2 \pm 0.4) \cdot 10^{11}$	$(4.3 \pm 1.4) \cdot 10^{-11}$	$(1.2 \pm 0.6) \cdot 10^{13}$	$(5.7 \pm 0.3) \cdot 10^{-10}$
TMC 1-CP+120	13.16	7.27	12.5 ± 1.3	$(3.0 \pm 0.8) \cdot 10^3$	$(2.8 \pm 1.1) \cdot 10^{12}$	$(1.9 \pm 0.8) \cdot 10^{-10}$	$(5.5 \pm 1.6) \cdot 10^{13}$	$(5.1 \pm 1.4) \cdot 10^{-9}$
TMC 1-CP+180	13.86	4.77	16.0 ± 2.6	$(5.4 \pm 1.6) \cdot 10^3$	$(5.4 \pm 1.5) \cdot 10^{12}$	$(5.7 \pm 1.6) \cdot 10^{-11}$	$(4.3 \pm 1.3) \cdot 10^{13}$	$(5.9 \pm 1.8) \cdot 10^{-9}$
TMC 1-CP+240	14.39	3.25	14.7 ± 1.1	$(3.2 \pm 2.0) \cdot 10^3$	$(5.2 \pm 3.2) \cdot 10^{11}$	$(8.0 \pm 5.0) \cdot 10^{-12}$	$(2.1 \pm 1.3) \cdot 10^{13}$	$(4.2 \pm 2.1) \cdot 10^{-9}$ [b]
TMC 1-C+0	11.26	19.85	8.5 ± 2.0	$(9.2 \pm 6.8) \cdot 10^4$	$(1.1 \pm 0.5) \cdot 10^{12}$	$(2.8 \pm 1.2) \cdot 10^{-11}$	$(2.0 \pm 1.5) \cdot 10^{13}$	$(6.0 \pm 4.9) \cdot 10^{-10}$
TMC 1-C+30	11.32	18.47	10.3 ± 2.0	$(8.8 \pm 4.6) \cdot 10^4$	$(7.0 \pm 3.9) \cdot 10^{11}$	$(1.9 \pm 1.1) \cdot 10^{-11}$	$(2.5 \pm 1.3) \cdot 10^{13}$	$(8.6 \pm 5.0) \cdot 10^{-10}$
TMC 1-C+60	11.67	13.34	11.6 ± 2.2	$(2.4 \pm 1.0) \cdot 10^4$	$(9.2 \pm 2.3) \cdot 10^{11}$	$(3.5 \pm 0.9) \cdot 10^{-11}$	$(5.4 \pm 2.0) \cdot 10^{13}$	$(2.6 \pm 1.0) \cdot 10^{-9}$
TMC 1-C+120	13.13	4.79	11.1 ± 1.9	$(1.1 \pm 0.5) \cdot 10^4$	$(6.2 \pm 1.8) \cdot 10^{11}$	$(6.5 \pm 1.9) \cdot 10^{-11}$	$(1.0 \pm 0.5) \cdot 10^{13}$	$(1.4 \pm 0.6) \cdot 10^{-8}$
TMC 1-C+180	14.08	2.20	13.5 ± 1.1	$(1.1 \pm 2.8) \cdot 10^4$	$(1.8 \pm 0.9) \cdot 10^{11}$	$(4.1 \pm 2.1) \cdot 10^{-11}$	$(6.5 \pm 3.3) \cdot 10^{12}$ [b]	$(1.9 \pm 1.0) \cdot 10^{-9}$ [b]
TMC 1-C+240	14.53	1.63	13.5 ± 2.7	$(5.2 \pm 1.8) \cdot 10^3$	$(1.6 \pm 1.0) \cdot 10^{11}$	$(4.9 \pm 3.0) \cdot 10^{-11}$	$(1.5 \pm 1.0) \cdot 10^{13}$ [b]	$(6.0 \pm 4.2) \cdot 10^{-9}$ [b]

Notes:
[a] When ^{13}CS or C^{34}S isotopologues are not detected, ^{13}CS column densities are determined from that of C^{34}S or CS, applying the ratios CS/^{13}CS ≈ 60 and C^{34}S/^{13}CS $\approx 8/3$.
[b] Upper bound values.
[c] N(H_T) stands for the total hydrogen column density: N(H_T) = N(H) + 2 N(H_2).

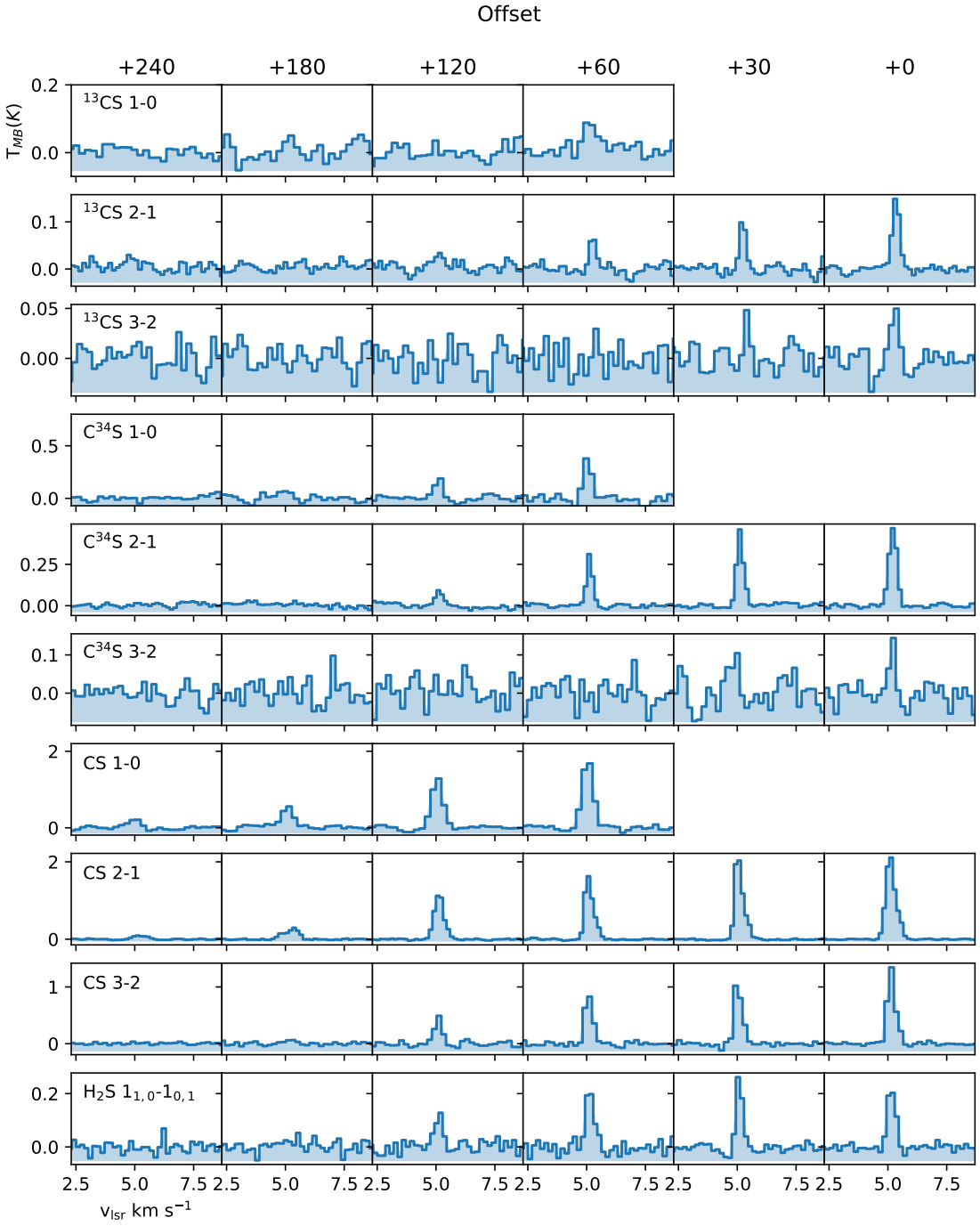

Figure 5.14: Single dish spectra of ^{13}CS 1 → 0, ^{13}CS 2 → 1, ^{13}CS 3 → 2, C^{34}S 1 → 0, C^{34}S 2 → 1, C^{34}S 3 → 2, CS 1 → 0, CS 2 → 1, C^{34}S 3 → 2 transitions towards TMC 1-C positions with offsets (+0",0"), (+30",0"), (+60",0"), (+120",0"), (+180",0"), (+240",0"). The systemic velocity is $v_{\rm lsr} = 6.5$ km s^{-1}.

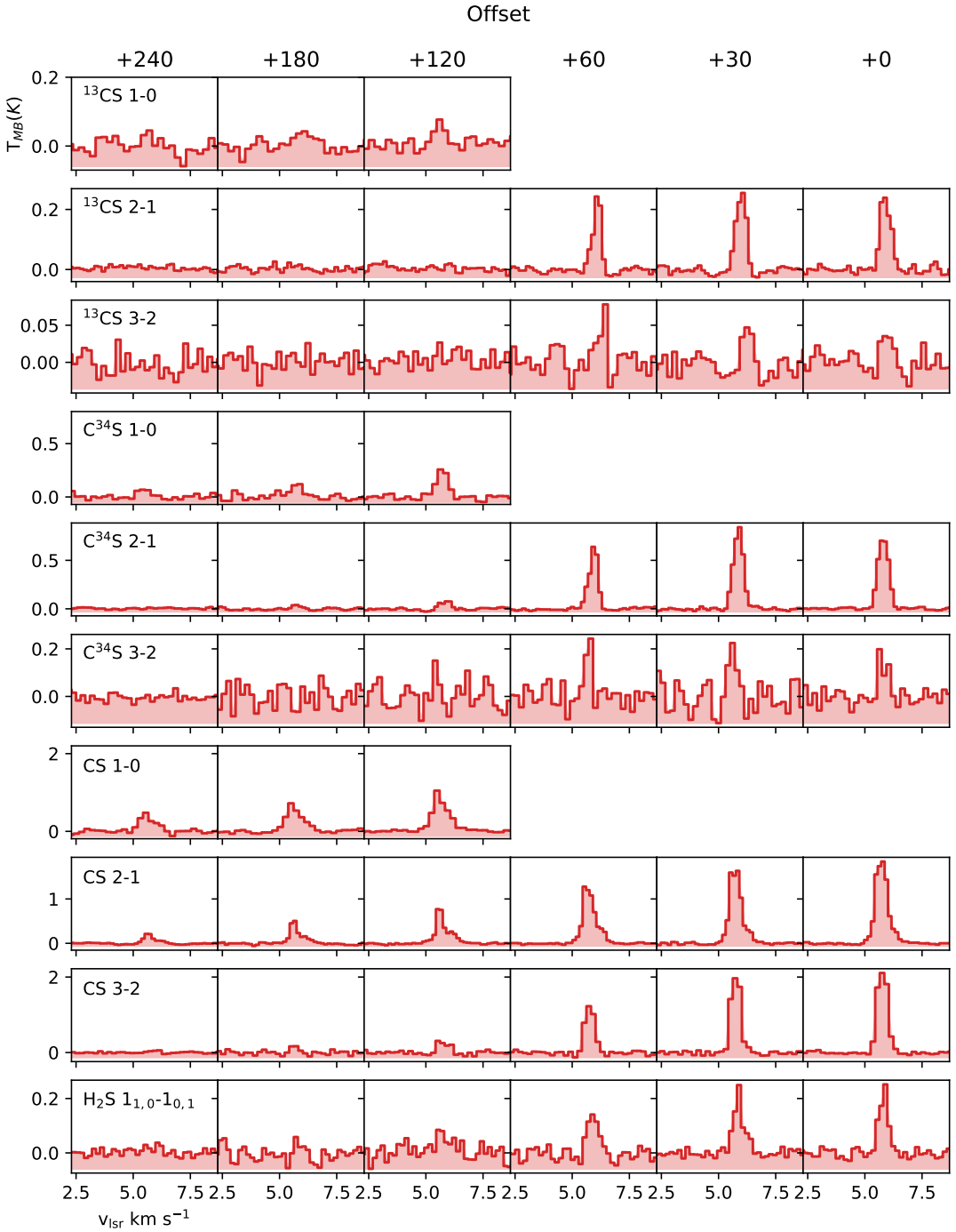

Figure 5.15: Single dish spectra of ^{13}CS 1 → 0, ^{13}CS 2 → 1, ^{13}CS 3 → 2, C^{34}S 1 → 0, C^{34}S 2 → 1, C^{34}S 3 → 2, CS 1 → 0, CS 2 → 1, C^{34}S 3 → 2 transitions towards TMC 1-CP positions with offsets (+0",0"), (+30",0"), (+60",0"), (+120",0"), (+180",0"), (+240",0"). The systemic velocity is $v_{\rm lsr} = 6.5$ km s^{-1}.

5.12.2 Physical conditions and chemical abundances in Barnard 1b

Table 5.7: Barnard 1b physical conditions. ^{13}CS and H_2S abundances.

Source name	T_{dust} (K)	A_v (mag)	T_{gas}(K)	n_H (cm^{-3})	N(^{13}CS) (cm^{-2}) [a]	N(^{13}CS) / N(H_T)	N(ortho$-H_2S$)(cm^{-2})	N(H_2S) / N(H_T)
B1B-cal-0_0	11.90	76.00	9.8 ± 1.4	$(6.3 \pm 3.0) \cdot 10^5$	$(2.0 \pm 1.6) \cdot 10^{12}$	$(2.6 \pm 2.1) \cdot 10^{-11}$	$(5.2 \pm 2.5) \cdot 10^{13}$	$(4.5 \pm 2.1) \cdot 10^{-10}$
B1B-cal-10_0	11.72	59.80	10.1 ± 1.5	$(4.2 \pm 2.8) \cdot 10^5$	$(1.3 \pm 0.9) \cdot 10^{12}$	$(2.2 \pm 1.5) \cdot 10^{-11}$	$(1.8 \pm 1.2) \cdot 10^{14}$ [c]	$(1.9 \pm 1.2) \cdot 10^{-9}$ [c]
B1B-cal-20_0	11.72	45.80	10.9 ± 1.7	$(1.6 \pm 0.9) \cdot 10^5$	$(1.9 \pm 1.2) \cdot 10^{12}$	$(4.0 \pm 2.6) \cdot 10^{-11}$	$(3.2 \pm 2.1) \cdot 10^{14}$ [c]	$(4.5 \pm 2.9) \cdot 10^{-9}$ [c]
B1B-cal-30_0	11.54	38.70	11.9 ± 1.0	$(1.0 \pm 0.4) \cdot 10^5$	$(1.1 \pm 0.5) \cdot 10^{12}$	$(2.8 \pm 1.2) \cdot 10^{-11}$	$(3.1 \pm 1.4) \cdot 10^{14}$	$(5.2 \pm 2.3) \cdot 10^{-9}$
B1B-cal-40_0	11.54	28.39	12.1 ± 1.1	$(1.0 \pm 0.4) \cdot 10^5$	$(9.5 \pm 4.4) \cdot 10^{11}$	$(3.3 \pm 1.6) \cdot 10^{-11}$	$(2.0 \pm 0.9) \cdot 10^{13}$	$(4.5 \pm 2.0) \cdot 10^{-9}$
B1B-cal-50_0	12.39	20.00	13.2 ± 1.3	$(4.7 \pm 2.2) \cdot 10^4$	$(1.7 \pm 0.8) \cdot 10^{11}$	$(8.7 \pm 4.2) \cdot 10^{-11}$	$(1.9 \pm 0.9) \cdot 10^{13}$	$(6.0 \pm 2.9) \cdot 10^{-9}$
B1B-cal-60_0	12.67	20.00	12.3 ± 0.9	$(3.1 \pm 1.6) \cdot 10^4$	$(2.2 \pm 1.1) \cdot 10^{12}$	$(1.1 \pm 0.5) \cdot 10^{-10}$	$(3.4 \pm 1.7) \cdot 10^{14}$	$(1.1 \pm 0.6) \cdot 10^{-8}$
B1B-cal-80_0	13.24	17.05	13.2 ± 1.8	$(5.5 \pm 2.4) \cdot 10^4$	$(1.0 \pm 0.3) \cdot 10^{12}$	$(6.1 \pm 1.8) \cdot 10^{-11}$	$(1.0 \pm 0.4) \cdot 10^{14}$	$(3.9 \pm 1.7) \cdot 10^{-9}$
B1B-cal-110_0	13.98	14.46	14.4 ± 1.9	$(5.2 \pm 2.1) \cdot 10^4$	$(9.8 \pm 2.7) \cdot 10^{11}$	$(6.8 \pm 1.9) \cdot 10^{-11}$	$(8.2 \pm 3.3) \cdot 10^{13}$	$(3.7 \pm 1.5) \cdot 10^{-9}$
B1B-cal-140_0	14.53	11.87	14.2 ± 1.0	$(9.5 \pm 2.5) \cdot 10^3$	$(5.4 \pm 2.7) \cdot 10^{12}$	$(4.5 \pm 2.3) \cdot 10^{-10}$	$(8.3 \pm 2.2) \cdot 10^{14}$	$(4.5 \pm 1.2) \cdot 10^{-8}$
B1B-cal-180_0	16.21	8.57	15.3 ± 1.2	$(3.6 \pm 1.7) \cdot 10^3$	$(6.2 \pm 3.3) \cdot 10^{12}$	$(7.3 \pm 3.9) \cdot 10^{-10}$	$(4.2 \pm 2.0) \cdot 10^{14}$	$(3.2 \pm 1.5) \cdot 10^{-8}$
B1B-cal-240_0	16.70	6.16	16.4 ± 1.0	$(3.8 \pm 1.8) \cdot 10^3$	$(1.6 \pm 0.8) \cdot 10^{12}$	$(2.6 \pm 1.4) \cdot 10^{-10}$	$(1.5 \pm 0.7) \cdot 10^{14}$	$(1.6 \pm 0.8) \cdot 10^{-8}$
B1B-cal-500_0	18.23	3.44	18.0 ± 5.4	$(9.6 \pm 2.2) \cdot 10^2$	$(5.5 \pm 3.0) \cdot 10^{11}$	$(1.6 \pm 0.9) \cdot 10^{-10}$	$(1.8 \pm 0.4) \cdot 10^{13}$ [b]	$(3.4 \pm 0.8) \cdot 10^{-9}$ [b]

Notes

[a] When ^{13}CS or C^{34}S isotopologues are not detected, ^{13}CS column densities are determined from that of C^{34}S or CS, applying the isotopic ratios CS/^{13}CS ≈ 60 and C^{34}S/^{13}CS $\approx 8/3$.

[b] Upper bound values.

[c] Column densities are obtained from that of the isotopologue $H_2{}^{34}S$, using $H_2S/H_2{}^{34}S \approx 22.5$.

Table 5.8: Barnard 1b physical conditions and SO abundances.

Source name	T_{dust} (K)	A_v (mag)	T_{gas}(K)	n_H (cm^{-3})	N(SO) (cm^{-2})	N(SO) / $N(H_T)$
B1B-cal-0_0	11.90	76.00	9.8 ± 1.4	$(6.3 \pm 3.0) \cdot 10^5$	$(2.4 \pm 0.6) \cdot 10^{14}$	$(1.5 \pm 0.4) \cdot 10^{-9}$
B1B-cal-10_0	11.72	59.80	10.1 ± 1.5	$(4.2 \pm 2.8) \cdot 10^5$	$(2.5 \pm 0.9) \cdot 10^{14}$	$(2.1 \pm 0.8) \cdot 10^{-9}$
B1B-cal-20_0	11.72	45.80	10.9 ± 1.7	$(1.6 \pm 0.9) \cdot 10^5$	$(2.7 \pm 1.0) \cdot 10^{14}$	$(2.9 \pm 1.1) \cdot 10^{-9}$
B1B-cal-30_0	11.54	38.70	11.9 ± 1.0	$(1.0 \pm 0.4) \cdot 10^5$	$(2.4 \pm 1.6) \cdot 10^{14}$	$(3.2 \pm 2.1) \cdot 10^{-9}$
B1B-cal-40_0	11.54	28.39	12.1 ± 1.0	$(1.0 \pm 0.4) \cdot 10^5$	$(9.9 \pm 4.5) \cdot 10^{13}$	$(1.7 \pm 0.8) \cdot 10^{-9}$
B1B-cal-50_0	12.39	20.00	13.2 ± 1.0	$(4.7 \pm 2.2) \cdot 10^4$	$(5.2 \pm 1.7) \cdot 10^{13}$	$(1.3 \pm 0.4) \cdot 10^{-9}$
B1B-cal-60_0	12.67	20.00	12.3 ± 1.0	$(3.1 \pm 1.6) \cdot 10^4$	$(4.8 \pm 1.6) \cdot 10^{13}$	$(1.2 \pm 0.4) \cdot 10^{-9}$
B1B-cal-80_0	13.24	17.05	13.2 ± 1.8	$(5.5 \pm 2.4) \cdot 10^4$	$(2.2 \pm 0.8) \cdot 10^{13}$	$(6.5 \pm 2.3) \cdot 10^{-10}$
B1B-cal-110_0	13.98	14.46	14.4 ± 1.9	$(5.2 \pm 2.1) \cdot 10^4$	$(3.4 \pm 1.9) \cdot 10^{13}$	$(1.2 \pm 0.7) \cdot 10^{-9}$
B1B-cal-140_0	14.53	11.87	14.2 ± 1.0	$(9.5 \pm 2.5) \cdot 10^3$	$(4.2 \pm 2.2) \cdot 10^{13}$	$(1.8 \pm 0.9) \cdot 10^{-9}$
B1B-cal-180_0	16.21	8.57	15.3 ± 1.2	$(3.6 \pm 1.7) \cdot 10^3$	$(4.9 \pm 2.4) \cdot 10^{13}$	$(2.9 \pm 1.4) \cdot 10^{-9}$
B1B-cal-240_0	16.70	6.16	16.4 ± 1.0	$(3.8 \pm 1.8) \cdot 10^3$	$(4.9 \pm 2.6) \cdot 10^{13}$	$(4.0 \pm 2.1) \cdot 10^{-9}$
B1B-cal-500_0	18.23	3.44	18.0 ± 5.4	$(9.6 \pm 2.2) \cdot 10^2$	$(1.5 \pm 0.3) \cdot 10^{12}$ [a]	$(2.2 \pm 0.5) \cdot 10^{-10}$ [a]

Notes

[a] Upper bound values

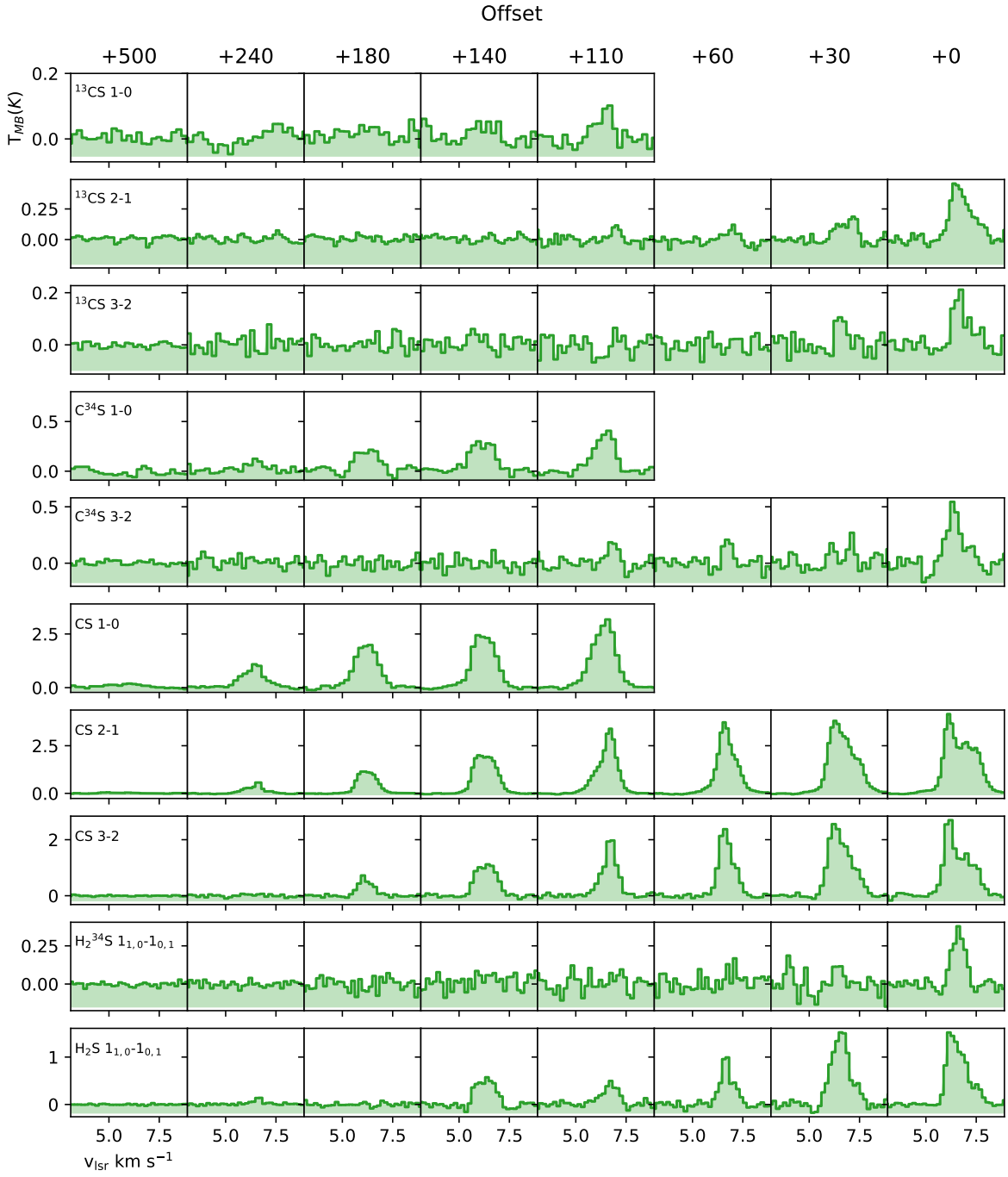

Figure 5.16: Single dish spectra of ^{13}CS 1 → 0, ^{13}CS 2 → 1, ^{13}CS 3 → 2, C^{34}S 1 → 0, C^{34}S 2 → 1, C^{34}S 3 → 2, CS 1 → 0, CS 2 → 1, C^{34}S 3 → 2 transitions towards positions with offsets (+0",0"), (+30",0"), (+60",0"), (+120",0"), (+180",0"), (+240",0") in the Barnard 1b filament. The systemic velocity is $v_{\rm lsr} = 6.5$ km s^{-1}.

Chapter 6

Evolutionary view through the starless cores in Taurus: deuteration in TMC 1

Adapted from Navarro-Almaida, D., Fuente, A., Majumdar, L., et al. 2021, A&A, 653, A15

Abstract

Context: The chemical and physical evolution of starless and pre-stellar cores are of paramount importance to understanding the process of star formation. The Taurus Molecular Cloud cores TMC 1-C and TMC 1-CP share similar initial conditions and provide an excellent opportunity to understand the evolution of the pre-stellar core phase.

Aims: We investigated the evolutionary stage of starless cores based on observations towards the prototypical dark cores TMC 1-C and TMC 1-CP.

Methods: We mapped the prototypical dark cores TMC 1-C and TMC 1-CP in the CS $3 \rightarrow 2$, $C^{34}S$ $3 \rightarrow 2$, ^{13}CS $2 \rightarrow 1$, DCN $1 \rightarrow 0$, DCN $2 \rightarrow 1$, DNC $1 \rightarrow 0$, DNC $2 \rightarrow 1$, $DN^{13}C$ $1 \rightarrow 0$, $DN^{13}C$ $2 \rightarrow 1$, N_2H^+ $1 \rightarrow 0$, and N_2D^+ $1 \rightarrow 0$ transitions. We performed a multi-transitional study of CS and its isotopologs, DCN, and DNC lines to characterize the physical and chemical properties of these cores. We studied their chemistry using the state-of-the-art gas-grain chemical code NAUTILUS and pseudo time-dependent models to determine their evolutionary stage.

Results: The central n_H volume density, the N_2H^+ column density, and the abundances of deuterated species are higher in TMC 1-C than in TMC 1-CP, yielding a higher N_2H^+ deuterium fraction in TMC 1-C, thus indicating a later evolutionary stage for TMC 1-C. The chemical modeling with pseudo time-dependent models and their radiative transfer are in agreement with this statement, allowing us to estimate a collapse timescale of $\sim$ 1 Myr for TMC 1-C. Models with a younger collapse scenario or a collapse slowed down by a magnetic support are found to more closely reproduce the observations towards TMC 1-CP.

Conclusions: Observational diagnostics seem to indicate that TMC 1-C is in a later evolutionary stage than TMC 1-CP, with a chemical age $\sim$1 Myr. TMC 1-C shows signs of being an evolved core at the onset of star formation, while TMC 1-CP appears to be in an earlier evolutionary stage due to a more recent formation or, alternatively, a collapse slowed down by a magnetic support.

6.1 Introduction

Starless cores are the seeds of star formation, and are the result of fragmentation and contraction of molecular clouds. A detailed knowledge of the physical and chemical conditions in a starless core is then crucial to understand the subsequent stellar evolution. Starless cores are characterized by densities of around $n_{\rm H} = 10^5$ cm^{-3}, and cold ($T \leq 10$ K) temperatures (Ward-Thompson 1996; Tafalla et al. 2004; Crapsi et al. 2005; Keto & Caselli 2008). In these particular physical conditions, species like CO, are expected to be heavily depleted from the gas, being frozen out onto dust grain surfaces (Leger 1983), and thus becoming inadequate tracers of mass, hydrogen number density $n_{\rm H}$, and kinetic temperature $T_{\rm kin}$. Fortunately, some species remain abundant even in the dense and cold inner regions of starless cores. One of these cases is molecular ion N_2H^+, rapidly destroyed through reactions with CO in molecular clouds. Once CO is depleted, the N_2H^+ abundance increases, remaining in the gas phase even at high densities. The anti-correlation between N_2H^+ and CO line emissions (see, e.g., Pagani et al. 2007; Caselli et al. 1999), and the high critical density of N_2H^+ $1 \rightarrow 0$ line ($n_{\rm crit} \sim 1.5 \times 10^5$ cm^{-3} at 10 K, Lin et al. 2020), make this molecule suitable to probe inside dense cores.

Deuterated compounds are also thought to be good tracers of the cold gas inside dense starless cores (Millar et al. 1989). At the low temperatures prevailing in these environments, the exothermicity of the reaction

$$H_3{}^+ + HD \leftrightharpoons H_2D^+ + H_2 \tag{6.1}$$

in the forward direction (of ~ 232 K, see Gerlich & Schlemmer 2002) promotes the formation of H_2D^+ and inhibits the reverse reaction. The deuteration proceeds further via formation of D_2H^+ and D_3^+ in reactions with HD and D_2. These deuterated ions react with a variety of neutral molecules, such as CO and N_2, leading to high abundances of other deuterated species (see, e.g., Ceccarelli et al. 2014; Roueff et al. 2014). As a result, the deuteration fraction, which is the abundance of a given deuterated compound relative to its hydrogenated counterpart, can be enhanced by more than three orders of magnitude (see, e.g., Turner 2001; Bacmann et al. 2003; Crapsi et al. 2005; Pagani et al. 2007; Spezzano et al. 2013) compared to the solar elemental D/H ratio ($1.51^{+0.39}_{-0.33} \times 10^{-5}$, see, e.g., Linsky 2003; Oliveira et al. 2003). Deuterated molecules thus become important diagnostic tools of dense and cold interstellar clouds.

The N_2H^+ deuteration fraction (the ratio of the column density of N_2D^+ to its non-deuterated counterpart N_2H^+) has been found in moderate anti-correlation with the gas temperature (Emprechtinger et al. 2009; Chen et al. 2011; Fontani et al. 2015) and in correlation with the density (Daniel et al. 2007). These dependencies are also tightly related to the evolutionary stage of the object. Using a chemical model, Caselli (2002) concluded that the N_2D^+/N_2H^+ column density ratio is a chemical clock, working as an indicator for the evolutionary stage in low-mass star formation sites. Increasing attention is being paid to the accurate modeling of the deuterium chemistry as a tool to probe the evolution of the dense gas during the starless core phase (see, e.g., Sipilä et al. 2010, 2015; Roueff et al. 2015; Majumdar et al. 2017). One key aspect is the realization of the importance of the spin state in deuterium chemistry (Sipilä et al. 2019), since multiply-hydrogenated or deuterated molecules can exist in several forms due to the different nuclear spin states. Majumdar et al. (2017) presented the

first publicly available chemical network for NAUTILUS (Ruaud et al. 2016) with deuterated species and spin chemistry in its two-phase implementation where the gas phase and grain phase interact.

The chemical properties of star-forming regions are best constrained with chemical models of well-known objects. The Taurus molecular cloud (TMC), at a distance of 141.8 ± 0.2 pc (Galli et al. 2018), is one of the closest molecular cloud complexes and is considered an archetypal low-mass star-forming region. The most massive molecular cloud in Taurus is the Heiles cloud 2 (HCL 2), which hosts the well-known region TMC 1. TMC 1-C and TMC 1-CP are two starless dense cores embedded in the translucent filament TMC 1 (see Figure 6.1). These two nearby cores have similar masses (~ 1 $M_\odot$), gas kinetic temperatures of 8−10 K (Kirk et al., in prep.), and share similar initial conditions. Moreover, Navarro-Almaida et al. (2020) obtained a similar density profile for the two cores from a multi-transition analysis of CS and its isotopologs. In spite of these similarities, several spectroscopic studies points to significant chemical and dynamical differences between them. TMC 1-CP has been the target of numerous chemical studies and is considered as prototype of a C-rich (C/O∼1) starless core (Fehér et al. 2016; Gratier et al. 2016; Agúndez & Wakelam 2013). With a rich carbon chemistry, it is the preferred site for hunting new organic molecules (McGuire et al. 2020; Lee et al. 2021). Less studied from the chemical point of view, TMC 1-C has been identified as an accreting starless core with high depletion of CO (Schnee et al. 2007, 2010). In addition to CO, other dense gas tracers like CS are expected to be depleted in dense cores (Kim et al. 2020). In line with this statement, Fuente et al. (2019) measured a higher depletion of CS towards TMC 1-C, based on data from the Gas phase Elemental abundances in Molecular CloudS (GEMS) IRAM 30m Large Program. One compelling explanation of these measurements is that the differences are due to different evolutionary stages of the two cores (e.g., Sipilä & Caselli 2018). If confirmed, these nearby cores would constitute a valuable site to investigate the evolution of gas and dust during the pre-stellar phase, avoiding the confusion due to possible differences in the initial conditions or environment when using cores placed in different molecular clouds.

In this paper we investigate the evolutionary stage of TMC 1-C and TMC 1-CP based on spectroscopic observations. Several observational diagnostics have been proposed to determine the evolutionary stage of starless and pre-stellar cores (Crapsi et al. 2005), among which the volume density at the core center, the N_2H^+ column density at the visual extinction peak, the depletion of CO and CS, and the deuterium fraction of N_2H^+. We mapped the two cores in several lines of CS, N_2H^+, N_2D^+, DCN, and DNC to derive an accurate estimate of the central density. Moreover, we used the CS/N_2H^+ and N_2D^+/N_2H^+, and DCN/DNC column density ratios as chemical clocks for the core evolution. Finally, we performed pseudo-dynamical modeling and 3D radiative transfer to synthesize the spectra towards TMC 1-C to compare with observations.

6.2 Observational strategy

In order to determine the morphology of the dense gas and the peak hydrogen densities in TMC 1-C and TMC 1-CP, we mapped these starless cores in a selection of molecular lines

(see Table 6.1) using the IRAM 30m telescope (Pico Veleta, Spain). The observations were carried out during May 2019 using the on-the-fly (OTF) technique to cover a field of view of 9 and 6.8 arcmin^2 towards TMC 1-C and TMC 1-CP, respectively. We used 2 mm and 3 mm bands in dual polarization mode using the EMIR receivers (Carter et al. 2012) with the Fast Fourier Transform Spectrometer (FFTS) at 50 kHz resolution. The emission from the sky was subtracted using reference positions located at offsets (600", 0") relative to the map centers ($\alpha = 04^h41^m37^s58$, δ= 26°00'31".10 for TMC 1-C; $\alpha = 04^h41^m40^s.10$, $\delta = 26°00'05''.00$ for TMC 1-CP, see Table 6.2). In addition to the maps, long integration spectra were taken towards the map centers to improve the S/N of the 2 mm lines. In this paper we use the main beam brightness temperature $T_{\rm MB}$ as intensity scale, while the output of the telescope is calibrated in antenna temperature $T_{\rm A}$. The conversion between $T_{\rm MB}$ and $T_{\rm A}$ is done using the Ruze equation utility provided in the data reduction and line analysis package GILDAS-CLASS[1].

Table 6.1: Observed lines, beam sizes, and efficiencies

Line	Frequency (MHz)[a]	$\theta_{\rm beam}$(")[b]	$F_{\rm eff}/B_{\rm eff}$
^{13}CS 2 → 1	92494.28	27	0.95/0.81
C^{34}S 3 → 2	144617.10	17	0.93/0.74
CS 3 → 2	146969.03	17	0.93/0.73
DN^{13}C 1 → 0	73367.75	34	0.95/0.83
DN^{13}C 2 → 1	146734.00	17	0.93/0.73
DNC 1 → 0	76305.68	32	0.95/0.83
DNC 2 → 1	152609.74	16	0.93/0.72
DCN 1 → 0	72414.93	34	0.95/0.83
DCN 2 → 1	144828.11	17	0.93/0.74
N_2H^+ 1 → 0	93173.38	26	0.95/0.81
N_2D^+ 1 → 0	77109.61	32	0.95/0.83

(*a*) When hyperfine splitting is present, the frequency shown here is that of the main component. The frequencies are taken from the CDMS catalog except those of the DN^{13}C lines, taken from SLAIM catalog.

(*b*) The HPBW(") is computed as 2460/Freq(GHz), see IRAM 30m Efficiencies

6.3 Results

Figure 6.1 shows the visual extinction maps towards the starless cores TMC 1-C and TMC 1-CP as derived from Herschel maps (J. Kirk, private communication). The overplotted black

[1]GILDAS home page: www.iram.fr/IRAMFR/GILDAS/

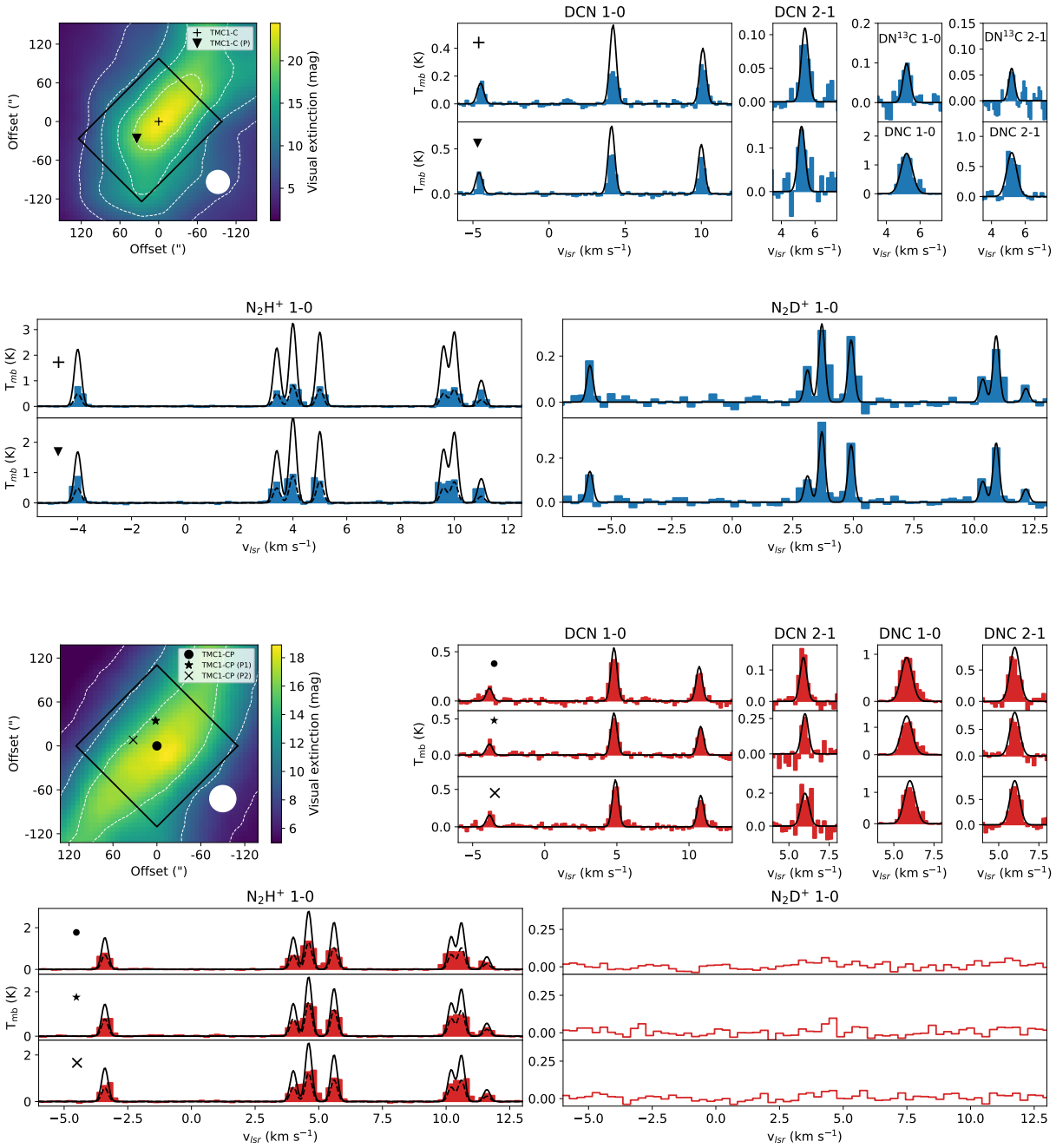

Figure 6.1: *Top left and third row, left:* Visual extinction maps from Herschel data (Jason Kirk, private communication) of the TMC 1-C and TMC 1-CP cores, respectively, with the areas mapped in the transitions presented in Table 6.1. Contour lines show levels of extinction of 6, 10, 15, and 20 mag. The blue and red spectra show the observed molecular lines in TMC 1-C and TMC 1-CP, respectively. The solid lines show synthetic spectra created with the model parameters present in Table 6.3.

Table 6.2: Target positions

Source	RA (2000)	Dec (2000)	v_{LSR} (km s^{-1})
TMC 1-C	04:41:37.58	26:00:31.10	5.2
TMC 1-C (P)	04:41:40.10	26:00:05.00	5.2
TMC 1-CP	04:41:41.90	25:41:27.10	5.8
TMC 1-CP (P1)	04:41:42.56	25:42:02.40	5.8
TMC 1-CP (P2)	04:41:44.07	25:41:42.43	5.8

rectangles indicate the areas mapped in molecular lines with the 30m telescope. The spectra from the positions in Table 6.2 are also shown. The map center positions of TMC 1-C and TMC 1-CP correspond to the Herschel extinction peaks of each core (see extinction maps in Figure 6.1). We also included the spectra towards the DNC 1 → 0 emission peak positions TMC 1-C (P), TMC 1-CP (P1), and TMC 1-CP (P2) to compare with the map centers (see Figure 6.2). It should be noted that the N_2D^+ 1 → 0, $DN^{13}C$ 1 → 0, and $DN^{13}C$ 2 → 1 lines were only detected towards TMC 1-C. The integrated areas and main-beam temperatures of the observed lines are shown in Table 6.6 to 6.10.

The integrated intensity maps of the DNC 1 → 0, N_2H^+ 1 → 0, and the CS 3 → 2 lines towards the studied cores are shown in Figure 6.2. Integration was performed over the whole hyperfine structure for those lines that present it. The DNC 2 → 1, DCN 2 → 1, N_2D^+ 1 → 0, $DN^{13}C$ 1 → 0, and $DN^{13}C$ 2 → 1 lines were too weak to produce maps. In Figure 6.2, we present maps of integrated intensity of different lines to analyze their morphology. Although the discussion of emission morphology from optically thick lines is, in general, uncertain, the morphologies of the integrated intensity maps shown in Figure 6.2, which include integration over all hyperfine components, are similar to those that only include integration over the weakest optically thin hyperfine component, and thus the following analysis is not affected by opacity. The emission of the CS 3 → 2 line is quite uniform near the position TMC 1-C. This flat map is expected because the CS 3 → 2 line is optically thick in this dense core. Moreover, Fuente et al. (2019) found that the CS abundance is depleted towards the visual extinction peak. The N_2H^+ 1 → 0 emission presents an elongated structure following the direction of the molecular filament. The bright area in the N_2H^+ 1 → 0 emission is not coincident with the location of the the visual extinction peak, but shifted ~10" SW (see visual extinction maps in Figure 6.1). Contrary to CS and N_2H^+, the morphology of the DNC 1 → 0 map resembles that observed in the visual extinction maps (Figure 6.1). In spite of this, the position of the emission peak of the DNC 1 → 0 line in TMC 1-C, called TMC 1-C (P), is not located towards the position of the extinction peak, as measured with the Herschel extinction maps at an angular resolution of ~ 30", but to the south. Interestingly, this position is ~ 19" SW away (within the DNC 1 → 0 line beam size) from the visual extinction peak derived by Schnee & Goodman (2005) based on SCUBA observations of the dust continuum emission at 450 μm (half power beam width HPBW ~7.5") and 850 μm (HPBW~14"), and therefore the effective core center.

In TMC 1-CP, the emission of the CS 3 → 2 presents a featureless structure, wide and flat on the top, consistent with the emission of this line being optically thick. Similarly to DNC,

Table 6.3: Kinetic temperatures, hydrogen nuclei number densities, and column densities of the species resulting from the multi-transition analysis described in Section 4.

		TMC 1-C	TMC 1-C (P)	TMC 1-CP	TMC 1-CP (P1)	TMC 1-CP (P2)
CS	T_k(K) [a]	**7.4 ± 2.1**	**8.7 ± 1.9**	**9.0 ± 2.1**	**9.3 ± 1.8**	**9.1 ± 1.6**
	n_H (cm^{-3})	$(1.4 \pm 0.8) \times 10^5$	$(8.8 \pm 6.0) \times 10^4$	$(6.2 \pm 2.0) \times 10^4$	$(6.7 \pm 2.5) \times 10^4$	$(7.0 \pm 4.6) \times 10^4$
	N (cm^{-2})	$(1.0 \pm 0.5) \times 10^{14}$	$(1.2 \pm 0.9) \times 10^{14}$	$(2.9 \pm 1.8) \times 10^{14}$	$(1.6 \pm 1.2) \times 10^{14}$	$(2.5 \pm 0.9) \times 10^{14}$
DNC	n_H (cm^{-3})	$(1.8 \pm 0.5) \times 10^5$	**$(2.4 \pm 0.5) \times 10^5$**	**$(4.0 \pm 1.0) \times 10^5$**	**$(3.0 \pm 0.6) \times 10^5$**	**$(4.0 \pm 0.8) \times 10^5$**
	N (cm^{-2})	$(3.0 \pm 0.9) \times 10^{12}$	$(3.2 \pm 0.7) \times 10^{12}$	$(2.0 \pm 0.5) \times 10^{12}$	$(2.8 \pm 0.5) \times 10^{12}$	$(2.5 \pm 0.4) \times 10^{12}$
DN^{13}C	n_H (cm^{-3})	**$(4.1 \pm 1.2) \times 10^5$**	–	–	–	–
	N (cm^{-2})	$(8.5 \pm 2.4) \times 10^{10}$				
DCN	N (cm^{-2})	$(2.5 \pm 0.7) \times 10^{12}$	$(5.0 \pm 1.1) \times 10^{12}$	$(2.3 \pm 0.5) \times 10^{12}$	$(3.5 \pm 0.7) \times 10^{12}$	$(3.5 \pm 0.6) \times 10^{12}$
N_2H^+	N_{upp} (cm^{-2}) [b]	$(1.2 \pm 0.3) \times 10^{13}$	$(1.0 \pm 0.2) \times 10^{13}$	$(6.0 \pm 1.4) \times 10^{12}$	$(6.0 \pm 1.2) \times 10^{12}$	$(5.0 \pm 0.9) \times 10^{12}$
	N_{low} (cm^{-2}) [c]	$(8.0 \pm 2.0) \times 10^{12}$	$(5.0 \pm 1.0) \times 10^{12}$	$(3.5 \pm 0.8) \times 10^{12}$	$(4.2 \pm 0.8) \times 10^{12}$	$(3.0 \pm 0.6) \times 10^{12}$
N_2D^+	N (cm^{-2})	$(1.8 \pm 0.5) \times 10^{12}$	$(1.5 \pm 0.3) \times 10^{12}$	$< 3.5 \times 10^{11}$	$< 3.0 \times 10^{11}$	$< 3.0 \times 10^{11}$
N(DNC)/N(DCN)		2.04 ± 0.82	0.64 ± 0.20	0.87 ± 0.29	0.80 ± 0.22	0.71 ± 0.18
$N(N_2D^+)/N(N_2H^+)_{upp}$		0.15 ± 0.06	0.15 ± 0.04	< 0.06	< 0.05	< 0.06
$N(N_2D^+)/N(N_2H^+)_{low}$		0.23 ± 0.08	0.30 ± 0.08	< 0.10	< 0.07	< 0.10
$N(N_2H^+)_{upp}/N$(CS)		0.09 ± 0.05	0.08 ± 0.06	0.02 ± 0.01	0.04 ± 0.03	0.02 ± 0.01

[a] We assume the kinetic temperature T_k and the hydrogen nuclei number densities n_H obtained from CS and DNC multi-transition fitting (in bold) to derive the DCN, N_2H^+, and N_2D^+ column densities.

[b] Upper bound value for the column density obtained assuming the T_k and n(H_2) values in bold and fitting the opacity of the main component and the brightness of the weakest hyperfine component as explained in Section 4.1.

[c] Lower bound value for the column density obtained in the low excitation temperature scenario discussed in Section 6.

the N_2H^+ emission is more intense in an elongated structure parallel to the dust filament. The DNC filament is farther from the visual extinction filament than N_2H^+, forming some kind of DNC–N_2H^+ layered structure. In addition to the map center, we selected two positions, TMC 1-CP (P1) and TMC 1-CP (P2), for their detailed study.

In the two cores the morphologies observed in the DNC 1 → 0 line are more similar to those observed in the visual extinction maps. In TMC 1-C, the emission of DNC shows a rounded core, with an intense peak in the southwest part of the core. In TMC 1-CP, the DNC 1 → 0 emission is elongated, following the filament similarly to N_2H^+, but shifted as a function of radius with respect to the main axis of the core. Assuming that DNC is coming from the denser gas, the DNC 1 → 0 images point to a difference in the dense gas morphology between the TMC 1-C and TMC 1-CP cores. The more compact distribution of the dense gas in TMC 1-C argues in favor of this core being in a more evolved stage.

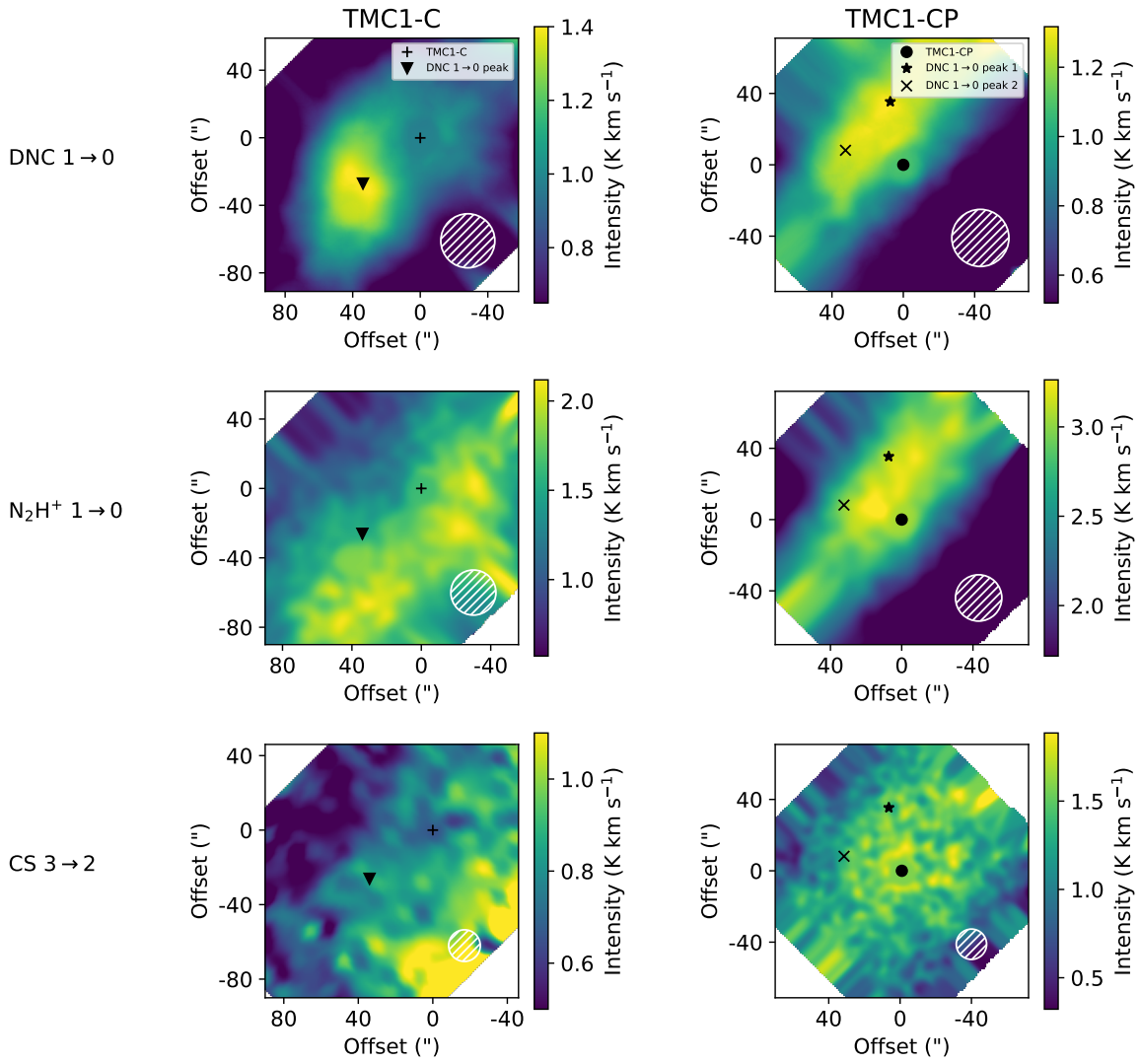

Figure 6.2: Velocity-integrated intensity maps of TMC 1-C (left) and TMC 1-CP (right) molecular emission of DNC $1 \rightarrow 0$, N_2H^+ $1 \rightarrow 0$, and CS $3 \rightarrow 2$. The integration was performed from 4 to 8 km s^{-1} when no hyperfine structure is present. Otherwise, the emission is integrated to cover all hyperfine components. Also shown are the selected positions from Table 6.2 and the beam sizes from Table 6.1 in each map.

6.4 Molecular column densities

As discussed previously, deuterated molecules are suitable for tracing dense and cold regions inside dark molecular clouds. Given the necessity to characterize these regions for future modeling, we estimated the temperature, density, and column densities across our targets. We derived the column density of CS by fitting the emission of the ^{13}CS 2 → 1, C^{34}S 3 → 2, and CS 3 → 2 lines following the procedure already described in Fuente et al. (2019) and Navarro-Almaida et al. (2020). Briefly, this method explores a parameter space consisting in kinetic temperatures (T_k), molecular hydrogen densities (n_{H_2}), and column densities of the species following the Markov Chain Monte Carlo (MCMC) methodology with a Bayesian inference approach, described in Rivière-Marichalar et al. (2019). To be consistent, we smoothed the maps of the C^{34}S 3 → 2 and CS 3 → 2 lines to the angular resolution of those of the ^{13}CS 2 → 1 line. This method uses the radiative transfer code RADEX (van der Tak et al. 2007) to reproduce all the line temperatures. Since our observations include different isotopologs, for this method to work we need to reduce the degrees of freedom that these different species introduce. To do so we assume the isotopic ratios N(C^{34}S)/N(^{13}CS) = 8/3 and N(CS)/N(^{13}CS) = 60 (Gratier et al. 2016). For consistency in the radiative transfer calculations presented in this paper, we only considered H_2 as the collisional partner for CS and isotopologs, with the collisional coefficients described in Denis-Alpizar et al. (2013). The effect of ignoring collisions with helium would translate in densities that are ~20% higher (He/H_2=0.20), which is within the uncertainties of our calculations. The resulting kinetic temperatures, hydrogen nuclei densities, and CS column densities are shown in Table 6.3. The synthetic ^{13}CS 2 → 1, C^{34}S 3 → 2, and CS 3 → 2 line profiles resulting from these parameters are shown in Figure 6.7, together with the observations.

Since our setup only considers up to two lines of DCN and DNC, it is necessary to assume the kinetic temperature at each position to derive reliable hydrogen nuclei densities and molecular column densities. We assumed the kinetic temperatures at these positions as those given by the multi-transition analysis of the CS (and isotopologs) lines, as they are in agreement with those calculated in Fuente et al. (2019) and Navarro-Almaida et al. (2020). The observation of two lines of DNC and DN^{13}C allows for an independent estimate of the hydrogen nuclei density. We derived the hydrogen nuclei density and DNC (DN^{13}C) column density at each region using the radiative transfer code RADEX and the HNC collisional coefficients by Dumouchel et al. (2010). As mentioned in the previous section, the DNC 1 → 0 line is expected to be optically thick towards the position TMC 1-C. In this position, the multi-transition study of the rarer isotopolog DN^{13}C provides more accurate values. To calculate the DNC column density, it is assumed that DNC/DN^{13}C ~ 60, a value commonly accepted for TMC1. We recall however that the DNC/DN^{13}C ratio itself is uncertain to a factor of 1.3 (Liszt & Ziurys 2012; Roueff et al. 2015). The densities derived from CS are a factor ~ 3 to ~ 6 lower than those derived from DNC and DN^{13}C (see Table 6.3). This discrepancy could be due to different radial distributions with the deuterated compounds coming mainly from the densest regions where CS is expected to be depleted. Since DCN and DNC are expected to trace the innermost regions of our targets, we take the densities we derived from these molecules as more appropriate to describe the cores. The volume densities in TMC 1-CP and TMC 1-C differ by a factor of 2. This difference is within the uncertainties of our calcu-

lations, and we cannot conclude that TMC 1-C is more evolved than TMC 1-CP only on the basis of the density estimations. Interestingly, we do not find any significant difference in volume density between the different positions within the same core, indicating a uniform density distribution for R < 6000 au. We recall that our beam is ~5000 au at frequencies of the deuterated species lines.

We adopted the densities derived from DNC and estimate the DCN column density by fitting the weakest hyperfine component of the J=1 → 0 line. This is a good approximation as long as the opacity of this line is moderate. Assuming that the excitation temperature is the same for all the hyperfine components, we can estimate the opacity of the DCN 1 → 0 line using the HFS method of GILDAS-CLASS (see Table 6.11). In the case of TMC 1-C, the opacities are so high that we might be still underestimating the DCN column density. The opacity of the main lines is $\tau_m \gtrsim 4$, implying that the opacity of the weakest line would be ~1. Thus, our fitting could underestimate the DCN column density by a factor of ~2. Therefore, we consider the derived DCN column density towards TMC 1-C as a lower limit to the real value. Synthetic spectra are created using the values in Table 6.3, which are compared with observations in Figure 6.1.

6.4.1 N_2H^+ and N_2D^+

In the cases of N_2H^+ and N_2D^+, we observed one transition and therefore we cannot carry out a multi-transition study. We can however take advantage of the hyperfine splitting to quantify the opacities. As explained above, we can use the GILDAS-CLASS HFS method to estimate the line opacities and calculate accurate column densities (Figure 6.1). This method computes the line profiles of a species and the opacity of the main component given the relative velocities and intensities of the components to the most intense component. In our analysis the relative intensities and velocities are fixed to laboratory values. This method assumes a Gaussian velocity distribution and the same line width and excitation temperature for each component. However, the N_2H^+ 1 → 0 spectra towards TMC 1-C and TMC 1-CP cannot be reproduced using this technique, which suggests that we need more sophisticated modeling with at least two gas layers to account for the N_2H^+ observations. Nevertheless, we can obtain a first estimate of the N_2H^+ column density by exploring two different scenarios that can be considered as limit cases. First, assuming the values of T_k and n_H derived from the CS and DNC fitting, we estimate the N_2H^+ column density in such a way that the brightness of the weakest hyperfine component matches the observations. We fit the intensity of the weakest hyperfine component N_2H^+ $J_{F_1,F} = 1_{1,0} \rightarrow 0_{1,1}$ because it is the least affected by opacity effects. This can be considered as a high excitation temperature scenario, where the N_2H^+ column density is an upper bound value (see Table 6.3). The resulting spectrum of N_2H^+ 1 → 0 is plotted in Figure 6.1, and overestimates the temperatures of the rest of components. For these to be fitted, a second scenario of low excitation temperatures should be considered. The appropriate excitation temperatures are obtained solving the radiative transfer equation for spectral lines with RADEX. These low temperatures, of around $T_{ex} \sim 4$ K in TMC 1-C and $T_{ex} \sim 5$ K in TMC 1-CP, correspond to environments with either low kinetic temperatures (~ 5 K in TMC 1-C and ~ 6−7 K in TMC 1-CP) or relative low densities ($n_H \sim 10^4$ cm^{-3}). Thus, the N_2H^+ emission would be linked to dense regions at extremely low temper-

atures, lower than the temperatures derived from our observations (see Table 6.3). Alternatively, the emission could originate in an optically thick envelope at low density. Proceeding as before, we obtain a lower bound for the N_2H^+ column density such that both the brightness temperature and the opacity of the main component match the observations. In this case, the intensity of the weakest hyperfine line is underestimated, especially for TMC 1-C. The column densities obtained in the two scenarios are found to agree within a factor of two and are summarized in Table 6.3. To better interpret our results we must take into account that self-absorption features are present in the spectra of other transitions in our setup, such as DCN $1 \rightarrow 0$. These features point towards the presence of an absorbing envelope around TMC 1-C. This possibility has been already discussed in Fuente et al. (2019), and its effect on the observations is explored in Section 10. We propose that the low brightness temperatures of the optically thick N_2H^+ hyperfine lines is the consequence of self-absorption by the optically thick low-density envelope. Self-absorption has less affect on the optically thin emission of the weakest hyperfine line. If our interpretation is correct, the high excitation temperature scenario is more representative of the TMC 1-C and TMC 1-CP environments. Thus, we adopt the upper bound values for the N_2H^+ column density as the ones that best describe the observations with an uncertainty of a factor of 2.

In addition to N_2H^+ $1 \rightarrow 0$, we also include the N_2D^+ $1 \rightarrow 0$ line in our setup. This time, however, the spectra have the appropriate line intensity ratios. As before, we obtain the N_2D^+ column density in TMC1-C by matching the opacity of the main component and the brightness of the hyperfine components, assuming the values of T_k and n_H derived from the CS and DNC fitting. We obtain $N(N_2D^+)/N(N_2H^+) \sim 0.15 \pm 0.06$ in TMC 1-C assuming the high value of $N(N_2H^+)$ (see Table 6.3). We did not detect N_2D^+ towards TMC 1-CP with $N(N_2D^+)/N(N_2H^+) < 0.06$. Crapsi et al. (2005) analyzed the N_2H^+ and N_2D^+ abundances in a large sample of starless cores. They calculated the N_2H^+ deuteration fraction in TMC 1-C, obtaining a N_2D^+/N_2H^+ ratio of 0.07 ± 0.02, consistent with our results. Their estimation in their position named TMC 1, which is near the cyanopolyyne peak, yields a lower N_2D^+/N_2H^+ ratio 0.04 ± 0.01, compatible with our estimated upper bound in the position TMC 1-CP.

As noted before, the N_2H^+ column density and the $N(N_2D^+)/N(N_2H^+)$ ratio are considered evolutionary diagnostics for starless cores. Regardless of the different scenarios proposed to estimate the N_2H^+ column density, $N(N_2H^+)$ is higher in TMC 1-C than in TMC 1-CP, suggesting that the former is in a more evolved stage, although the difference is within the uncertainties. Similarly, the higher value of $N(N_2D^+)/N(N_2H^+)$ estimated towards TMC 1-C, taking into account all possible values of $N(N_2H^+)$, does confirm the more evolved stage of this core.

6.5 Physical and chemical modeling of starless cores

The physical and chemical diagnostics used in the previous section (i.e., the volume density at the center of the core), the N_2H^+ column density, and the N_2D^+/N_2H^+ column density ratio indicate that TMC 1-C is in a later evolutionary stage. We test and develop this idea with the help of chemical models in the following sections.

Table 6.4: Model parameters and initial fractional abundances with respect to total hydrogen nuclei.

Parameter		Model A	Model B	Model C	Model D
T_k (K)	Temperature		9		
A_v (mag)	Visual extinction		20 mag		
HD	Hydrogen deuteride abundance		1.60×10^{-5}		
He	Helium abundance		9.00×10^{-2}		
N	Nitrogen abundance		6.20×10^{-5}		
O	Oxygen abundance		2.40×10^{-4}		
C^+	Carbon abundance		1.70×10^{-4}		
S^+	Sulfur abundance		1.50×10^{-5}		
Si^+	Silicon abundance		8.00×10^{-9}		
Fe^+	Iron abundance		3.00×10^{-9}		
Na^+	Sodium abundance		2.00×10^{-9}		
Mg^+	Magnesium abundance		7.00×10^{-9}		
P^+	Phosphorus abundance		2.00×10^{-10}		
Cl^+	Chlorine abundance		1.00×10^{-9}		
F	Fluorine abundance		6.68×10^{-9}		
χ_{UV}	UV field strength (Draine units)		5		
o-H_2/p-H_2	Initial ortho-to-para ratio of H_2	3	3	10^{-3}	10^{-3}
$\zeta(H_2)$ (s^{-1})	Cosmic-ray ionization rate	1.3×10^{-17}	1×10^{-16}	1.3×10^{-17}	1×10^{-16}

6.5.1 Chemical network and general considerations

We modeled the chemistry of TMC 1-CP and TMC 1-C using the NAUTILUS gas-grain chemical code (Ruaud et al. 2016). NAUTILUS is a three-phase model in which gas, grain surface, and grain mantle phases, and their interactions, are considered. NAUTILUS solves the kinetic equations for both the gas-phase and the surface of interstellar dust grains and computes the evolution with time of chemical abundances for a given physical structure. We use the chemical network presented by Majumdar et al. (2017), which considers multiple deuterated molecules and includes the spin chemistry in NAUTILUS. In all models, we adopted the initial abundances and the ambient UV field strength χ_{UV}=5 (in Draine units), determined by Fuente et al. (2019), and shown in Table 6.4. In the next section we use zero-dimensional (0D) chemical models to explore the influence of each parameter in the deuterium chemistry. In Section 6.5.3 we carry out one-dimensional (1D) pseudo-dynamical calculations to constrain the evolutionary stage of these cores.

Modeling CS observations with chemical models is challenging due to well-known uncertainties in the chemistry of CS (see, e.g., Vidal et al. 2017; Laas & Caselli 2019; Navarro-Almaida et al. 2020; Bulut et al. 2021). Based on H_2S, SO, and CS observations, Navarro-Almaida et al. (2020) conclude that sulfur elemental abundance in TMC 1 is equal to the solar value within a factor of 10. Recent calculations by Bulut et al. (2021) concluded that CS abundance in TMC 1 is overestimated when assuming the solar sulfur abundance; in order to reproduce observations of CO, CS, and HCS^+ consistently, a sulfur depletion by a factor of 20 is needed. In this section we assume undepleted sulfur abundances as in Navarro-Almaida

et al. (2020), and we discuss the effect of possible sulfur depletion in Sect 6.6. Taking into account the uncertainties in the chemical modeling of CS, we base our discussion of the best model mainly on the abundances of N_2H^+ and the deuterated species N_2D^+, DCN, and DNC. The abundances of these molecules remain essentially unaffected by a variation of the sulfur elemental abundance of a factor of 20.

6.5.2 Zero-dimensional models

Chemistry has become an essential tool in determining the physical conditions along starless cores. However, pseudo-time dependent and time-dependent chemical models show that chemical abundances depend on parameters that are usually not well constrained, such as the cosmic-ray ionization rate $\zeta(H_2)$ and the ortho-to-para ratio (OPR) of H_2 (Roueff et al. 2007, 2015; Majumdar et al. 2017; Sipilä & Caselli 2018). In the following, we use 0D models to explore the parameter space and determine suitable parameters for our pseudo-dynamical calculations.

Table 6.4 summarizes the grid of models considered in our exploratory study. In dense cores where most of the hydrogen is expected to be in molecular form, cosmic rays ionize H_2 to yield $H_3{}^+$ ions (Herbst & Klemperer 1973; Dalgarno 2006), enhancing the deuteration through Eq. (6.1). Fuente et al. (2019) estimated $\zeta(H_2)$= (0.5-1.8) $\times$ 10^{-16} s^{-1} in TMC 1 based on the chemical modeling of the moderate density gas (n_H~2×10^4 cm^{-3}). This value, however, is not representative of the central regions of TMC 1-CP and TMC 1-C where we estimate densities one order of magnitude higher and the visual extinction is higher (Padovani et al. 2013; Galli & Padovani 2015; Ivlev et al. 2015; Padovani et al. 2020). Consequently, in our grid of models we considered two values of $\zeta(H_2)$, the average interstellar value 1.3×10^{-17} s^{-1} and 1×10^{-16} s^{-1}. The reverse of Eq. (6.1) is more efficient when involving the ortho-H_2 species than the para-H_2 analogs (see, e.g., Gerlich & Schlemmer 2002; Flower et al. 2006). Thus, the ortho-H_2 abundance sets the availability of H_2D^+, the main parent species of deuterated molecules, at low temperatures. Although ortho- and para-H_2 are formed on the surfaces of interstellar grains with a statistical ratio of 3:1 (Watanabe et al. 2010), under the physical conditions prevailing in dark clouds (T_k < 10 K) the OPR decreases to values ~10^{-3} after 0.1 Myr (Majumdar et al. 2017). In the case of a static pre-phase before collapse, the initial OPR would be closer to ~10^{-3} than to 3. In order to explore the impact of this parameter in our modeling, we considered two values of initial OPR, 3 and 10^{-3} in the 0D calculations.

Using the models in Table 6.4, we ran NAUTILUS to predict the chemical evolution of the DNC, DCN, N_2H^+, N_2D^+ for two densities, $n_H = 10^5$ cm^{-3} and $n_H = 4\times10^5$ cm^{-3}, which are the values estimated for TMC 1-CP and TMC 1-C. The predicted abundances for each model up to t = 10 Myr are shown in Figure 6.3. In addition, we indicate the abundances observed towards TMC 1-C and TMC 1-CP with colored horizontal bands. The comparison of models A and B (C and D) inform us about the influence of $\zeta(H_2)$ on the molecular abundances. Once the chemistry has reached a steady state, the abundances of the deuterated molecules DCN and DNC are enhanced in Models B and D, relative to A and C. However, the reverse stands for the ionized species N_2H^+ and N_2D^+ that are rapidly destroyed via dissociative recombination with electrons (Dalgarno 2006). Navarro-Almaida et al. (2020) estimated t ~ 1 Myr for these cores based on the abundances of the S-bearing species. Assuming that the

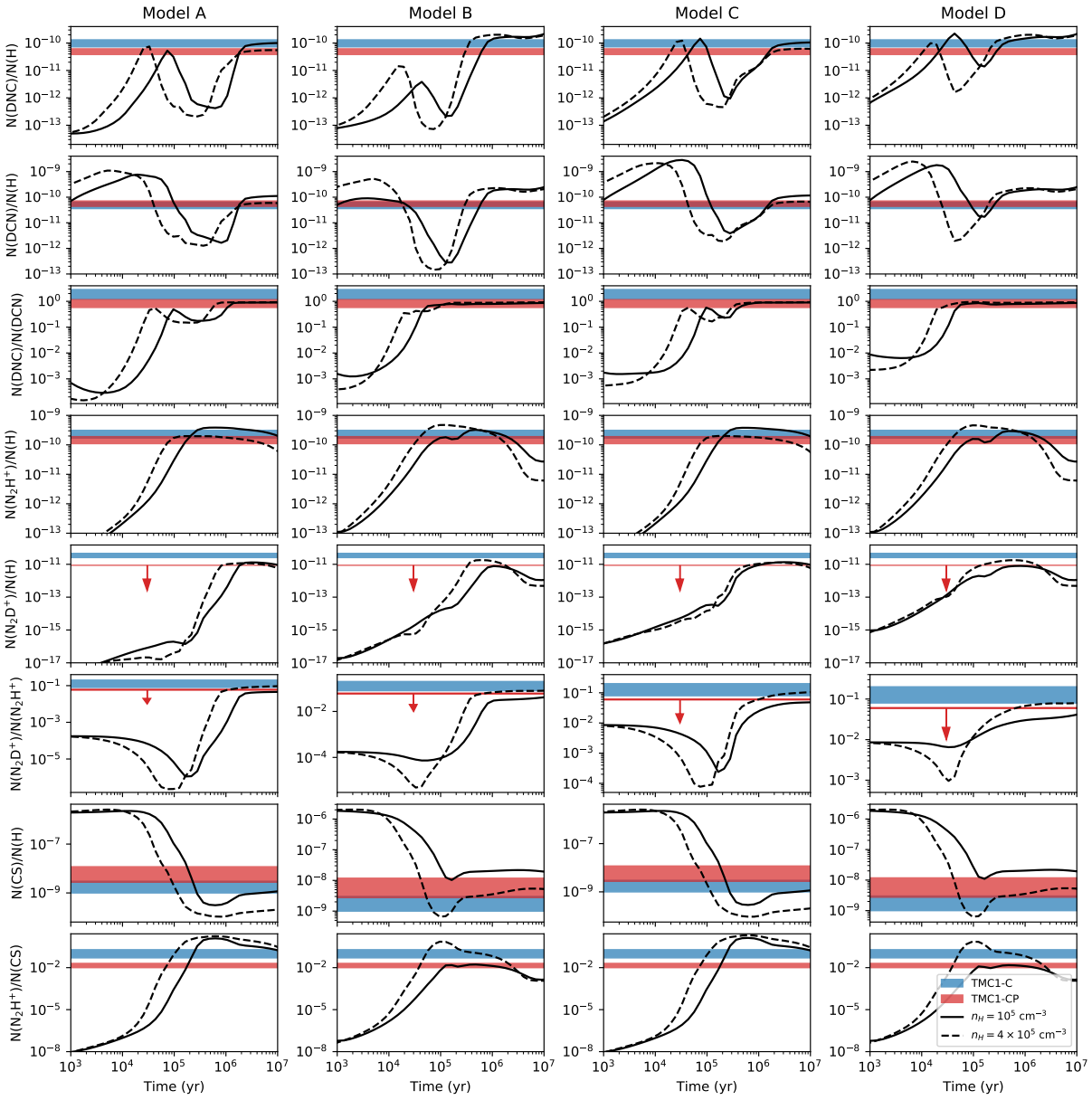

Figure 6.3: Abundances and abundance ratios of the different molecules, as predicted by the models described in Table 6.4. The predicted values are shown in solid (model with $n_{\rm H} = 10^5$ cm^{-3}) and dashed lines (model with $n_{\rm H} = 4 \times 10^5$ cm^{-3}). The blue and red areas show the observed abundances in TMC 1-C and TMC 1-CP, respectively. The arrows indicate upper bound values.

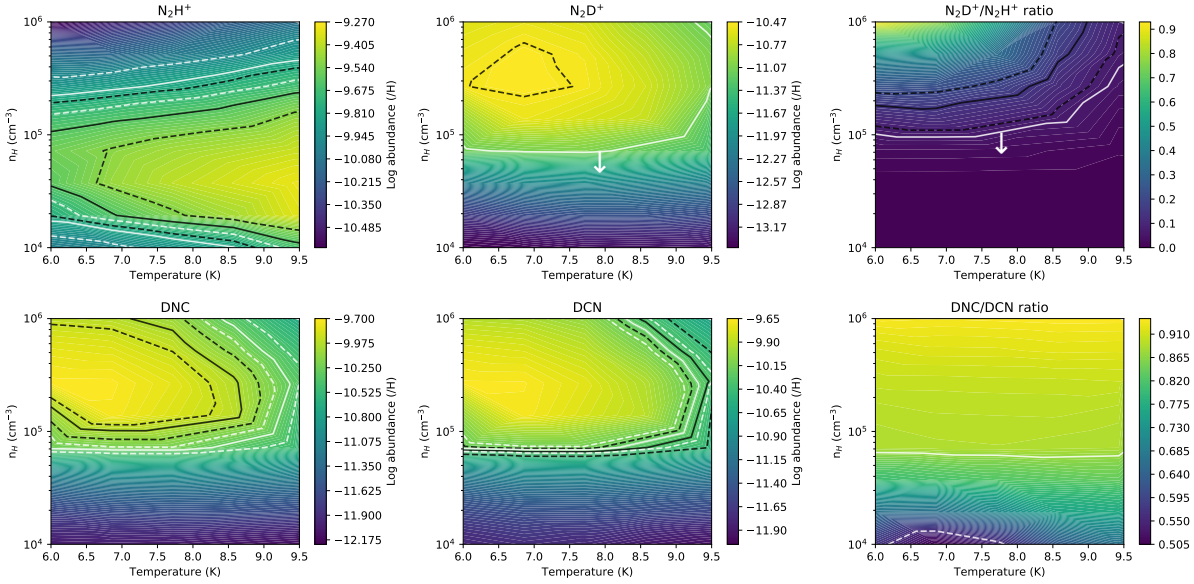

Figure 6.4: Grids of NAUTILUS models with varying temperature and hydrogen nuclei density. Each plot shows the contour levels of the N_2H^+ (top left), N_2D^+ (top middle), DNC (bottom left), and DCN (bottom middle) abundances; the N_2H^+ deuterium fraction (top right); and the DNC/DCN ratio (bottom right) at time $t \approx 10^6$ yr. Additionally, we show the contours that correspond to the abundances derived from the N_2H^+, N_2D^+, DNC, and DCN column densities in TMC 1-C (black) and TMC 1-CP (white), their uncertainties (dashed lines), and the upper bound values if present (white arrows). The model does not reproduce our estimated DNC/DCN ratio towards TMC 1-C, and thus the black contours are missing from that panel.

chemical age of TMC 1-CP and TMC 1-C is ∼ 1 Myr, the abundances of DCN, DNC, N_2H^+, and N_2D^+ are better reproduced with $\zeta(H_2) = 1.3 \times 10^{-17}$ s^{-1}, which is a factor of $\sim 5-10$ lower than that estimated by Fuente et al. (2019) in the TMC 1 translucent filament. Several works have investigated the attenuation of $\zeta(H_2)$ with the H_2 column density into the cloud (Galli & Padovani 2015; Ivlev et al. 2015; Padovani et al. 2020). Galli & Padovani (2015), based on observations ranging from diffuse clouds to molecular cloud cores, concluded that the cosmic-ray ionization rate decreases towards higher column density objects. Neufeld & Wolfire (2017) also established a dependence of the cosmic-ray ionization rate with the visual extinction, allowing a change of a factor of 5−10 of this rate in the extinction gradients found in our targets.

We selected a high ortho-to-para ratio of H_2 of 3 (models A and B) and a low value of $\sim 10^{-3}$ (models C and D) to estimate the influence of this parameter in the predicted chemical abundances. In Figure 6.3 we see that the abundances of the deuterated molecules in all models reach similar values beyond 0.1 Myr. This result was already found by Majumdar et al. (2017) who concluded that the OPR decreases to values $<10^{-3}$ for $t > 0.1$ Myr, regardless of its initial value. For times $t < 0.1$ Myr there is an enhancement in the abundance of deuterated molecules of the models C and D compared to models A and B. Our cores are expected to be older than 0.1 Myr (Navarro-Almaida et al. 2020; Bulut et al. 2021); therefore, an OPR=10^{-3} is adopted in the following calculations.

One crucial point for our study is to check the ability of the observed deuterated species to constrain the chemical age. Figure 6.3 shows that the abundances of DCN, DNC, and N_2D^+, as well as the DNC/DCN and N_2D^+/N_2H^+ ratios, are strongly dependent on the time evolution. Interestingly, the DNC/DCN ratio reaches its equilibrium value at earlier times than N_2D^+/N_2H^+. The combination of the two ratios therefore provides a useful tool for constraining the value of $\zeta(H_2)$ and the chemical age of the cores with $t \sim 0.1-1$ Myr.

Once the values of key parameters such as the cosmic-ray ionization rate and the initial ortho-to-para ratio of H_2 are constrained, we can proceed to investigate the behavior of the N_2H^+, N_2D^+, DNC, and DCN with variations in density and temperature. We carry out an exploration of the n_H-T parameter space considering 0D models with varying densities and temperatures, a cosmic-ray ionization rate of $\zeta(H_2) = 1.3 \times 10^{-17}$ s^{-1}, an OPR of 10^{-3}, and a chemical age of ∼ 1 Myr. In Figure 6.4, we show the abundances of N_2H^+, N_2D^+, DCN, DNC, as well as the N_2D^+/N_2H^+ and DNC/DCN abundance ratios, as a function of the gas kinetic temperature and density. The abundances of N_2D^+, DCN, and DNC depend on the gas kinetic temperature. In particular, the abundances derived towards TMC 1-CP and TMC 1-C are consistent with model predictions in the range of T_k∼6−9 K, in agreement with the temperatures derived in our CS multi-transition study. Interestingly, the abundance of N_2H^+ and the DNC/DCN ratio have a very weak dependence with the temperature. The abundances of the deuterated isomers DCN and DNC, and mainly the DNC/DCN ratio, increase with the number density of total hydrogen nuclei. According to our modeling, these abundances are expected for gas densities, $n_H \sim 2 \times 10^5$ cm^{-3}, a factor of 2 lower than those calculated from our multi-transition study of DCN and DNC. The deuterated compound N_2D^+ has only been detected towards TMC 1-C, and its abundance is consistent with a density, $n_H \sim 5 \times 10^5$ cm^{-3}, compatible with our density estimate using the DN^{13}C isotopolog. N_2D^+ was not detected in TMC 1-CP, with an upper limit to the N_2D^+/N_2H^+ ratio that would correspond to $n_H <$

Table 6.5: Model parameters, including the collapse time t, the central hydrogen nuclei number density n_0, the flat radius r_0, and the asymptotic power index a.

Model	$n_0 = 5\times10^4$ cm^{-3}	$n_0 = 1\times10^5$ cm^{-3}	$n_0 = 4\times10^5$ cm^{-3}	$n_0 = 1\times10^6$ cm^{-3}
BES1	$t = 5.73\times10^5$ yr $r = 9.58\times10^3$ au $a = 2.40$	$t = 8.29\times10^5$ yr $r = 6.96\times10^3$ au $a = 2.40$	$t = 1.06\times10^6$ yr $r = 3.67\times10^3$ au $a = 2.40$	$t = 1.12\times10^6$ yr $r = 2.41\times10^3$ au $a = 2.40$
BES4	–	$t = 3.18\times10^4$ yr $r = 1.23\times10^4$ au $a = 2.26$	$t = 1.28\times10^5$ yr $r = 5.59\times10^3$ au $a = 2.04$	$t = 1.56\times10^5$ yr $r = 3.31\times10^3$ au $a = 2.00$
AD	$t = 1.57\times10^7$ yr $r = 1.89\times10^4$ au $a = 2.34$	$t = 1.58\times10^7$ yr $r = 1.35\times10^4$ au $a = 2.30$	$t = 1.60\times10^7$ yr $r = 6.88\times10^3$ $a = 2.25$	$t = 1.61\times10^7$ yr $r = 4.13\times10^3$ au $a = 2.23$

2×10^5 cm^{-3}, slightly lower than our density estimate.

6.5.3 One-dimensional pseudo-dynamical modeling

Several works have simulated the chemical evolution of a core undergoing collapse with different hydrodynamical models and with different treatments for the coupling between dynamics and chemistry (Rawlings et al. 1992; Bergin & Langer 1997; Aikawa et al. 2001, 2005; Sipilä & Caselli 2018; Priestley et al. 2018). In some cases the simulations were continued until the formation of the Larson core, describing the evolution from the pre-stellar to the proto-stellar phase (Aikawa et al. 2008; Hincelin et al. 2016). The large chemical network used in our modeling, with 7700 reactions on grain surfaces linked with the 111000 reactions in gas phase, precludes its usage in chemo-hydrodynamical calculations. Instead, we used the parametric expression derived by Priestley et al. (2018) to reproduce the results of 1D simulations of collapsing cores. In particular, they adopted the gravitational collapse of a spherical cloud described by Aikawa et al. (2005). In this model, the collapse is induced by a density increase by a factor of either 1.1 (BES1 model) or 4 (BES4 model) to produce a gravitational free-fall (t~1 Myr) in model BES1 or a rapid collapse induced by cloud compression (t~0.1 Myr) in model BES4. A similar study was carried out by Fiedler & Mouschovias (1993), but adding ambipolar diffusion to a magnetically supported core (AD model), which translated into a larger timescale t~10 Myr. These models were parameterized as a sequence of progressively dense Plummer-like spheres whose peak densities depend on the time elapsed since the onset of the collapse (Priestley et al. 2018). Plummer-like profiles have been successfully used to model the density of the TMC 1 cores (see, e.g., Schnee et al. 2010; Navarro-Almaida et al. 2020) which makes it plausible to assume this model.

In the parameterization proposed by Priestley et al. (2018), the density in the core center and the radial density profile is determined by the time since the onset of collapse. In Table 6.5 we show the models considered to compare with the molecular abundances observed in TMC 1-C and TMC 1-CP. Given the central density (n_0) and the type of collapse

(BES1, BES4, AD), the density profile is described by the parameters a and r_0 by the expression

$$n(r) = n_0/(1 + r/r_0)^a, \tag{6.2}$$

where n_0 is the central density, r_0 is the flat radius, and a is the asymptotic power index. The gas temperature across the core is assumed equal to the dust temperature that is described by

$$T_d(r) = T_0(1 + r/r_1), \tag{6.3}$$

with $T_0 = 8.5$ K and $r_1 = 3.66 \times 10^4$ au, representative central temperature and size of the cores (Navarro-Almaida et al. 2020). These density and temperature profiles are used as the physical structure for our 1D chemical modeling. Our simulations start with the gas in atomic form and the chemistry is allowed to evolve during the collapse time shown in Table 6.5. Following our findings, we adopt $\zeta(H_2) = 1.3 \times 10^{-17}$ s^{-1} and OPR = 10^{-3} in our 1D calculations. The initial elemental abundances are the same as in Navarro-Almaida et al. (2020). As output of our simulations we obtain the molecular abundances as a function of the radius for the eight models shown in Table 6.5. In order to compare models with observations, we assume a spherical geometry and calculate weight-average column densities along the line of sight as

$$[\mathrm{X}]_{\mathrm{ac}}(r) = \frac{\sum_i \Delta l_i \left(n_{\mathrm{H}}(s_i)[\mathrm{X}](s_i) + n_{\mathrm{H}}(s_{i+1})[\mathrm{X}](s_{i+1})\right)}{\sum_j \Delta l_j \left(n_{\mathrm{H}}(s_j) + n_{\mathrm{H}}(s_{j+1})\right)},$$

where r is the impact parameter; $\Delta l_i = l_{i+1} - l_i$; $s_i = \sqrt{r^2 + l_i^2}$; and l_i is a discretization of the segment along the line of sight $l_{\mathrm{max}} > \cdots > l_{i+1} > l_i > \cdots > 0$, with $l_{\mathrm{max}} = \sqrt{r_{\mathrm{max}}^2 - r^2}$, and r_{max} the radius of the density profile. The obtained abundance ratios as a function of the impact parameter are shown in Figures 6.8, 6.9, and 6.10.

To assess how well models reproduce the observations, we compute the relative difference Δ between the modeled weight-average column densities and those observed towards TMC 1-C and TMC 1-CP. For convenience, we define this quantity to be in the $[0,1]$ interval $\Delta = \frac{|\text{model} - \text{measurement}|}{\text{model} + \text{measurement}}$ such that differences closer to zero indicate well-fitted empirical data while those closer to one mean a poor agreement between the model and the observations. The values of Δ for each target are shown in Figure 6.5. The results show the poor performance of the fast collapse model BES4 compared to the BES1 and AD models. This is not surprising since the time since collapse in BES4 are < 1 Myr (i.e., the timescale for deuteration). This lack of compatibility favors the scenario of a slower collapse in TMC 1.

For TMC 1-C the best model is found to be BES1 with a density of $n_{\mathrm{H}} \sim 1 \times 10^6$ cm^{-3}, consistent with the results obtained in the 0D modeling. The AD models with $n_{\mathrm{H}} > 4 \times 10^5$ cm^{-3} underestimate the N_2D^+ abundance. However, we also find a good match with observations for AD with density of $n_{\mathrm{H}} = 1 \times 10^5$ cm^{-3}. Since the density of this model is lower than that estimated from our observations, we are prone to favor the BES1 model with higher density. Due to the increasing depletion of molecules with density and projection effects along the line of sight, we would expect the density at the center to be higher than the estimated

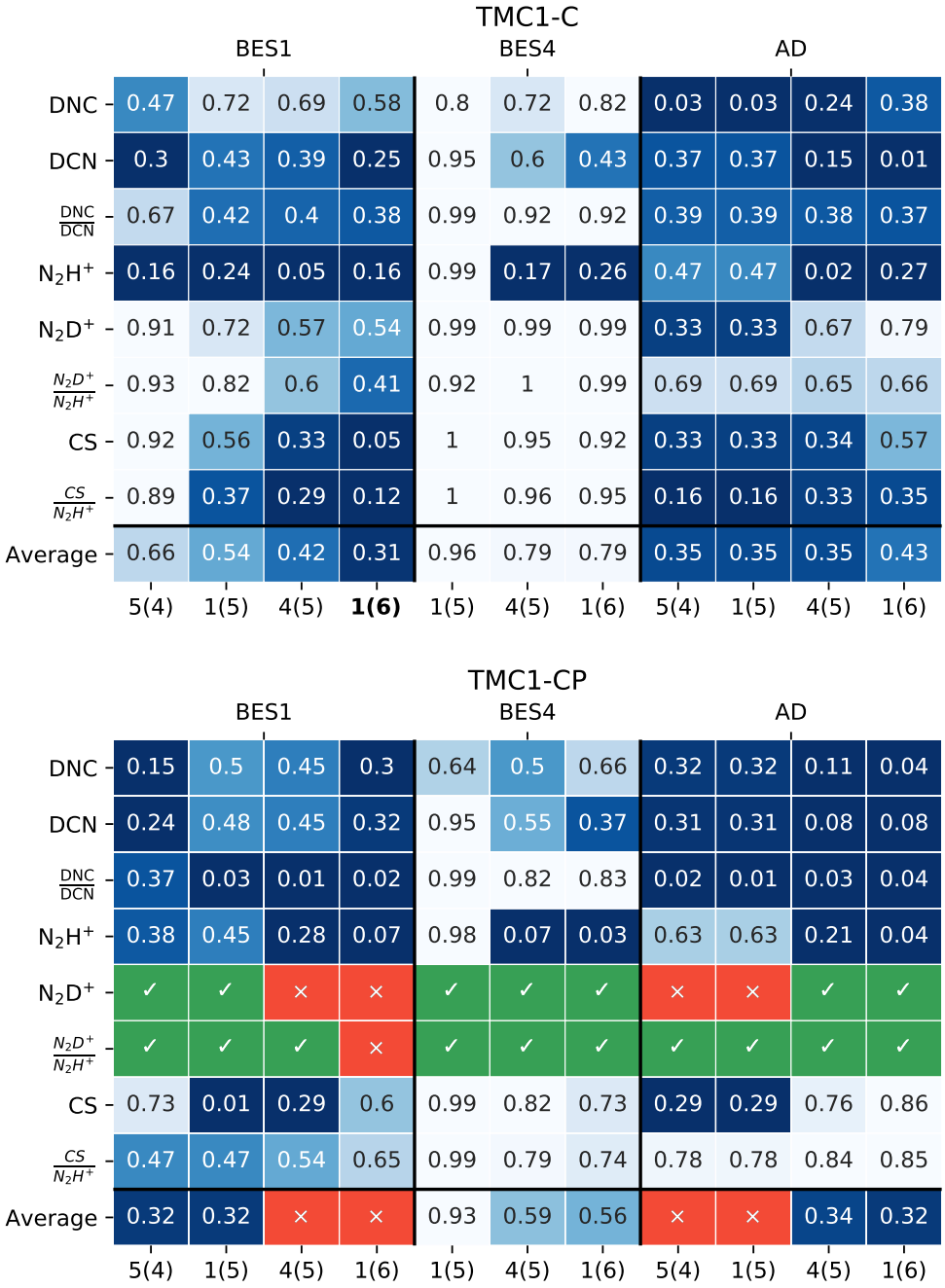

Figure 6.5: Heat maps of relative differences $\Delta = \frac{|\text{model} - \text{measurement}|}{\text{model} + \text{measurement}}$ (dark blue means better agreement) and their averages between the predictions of each model (BES1, BES4, and AD, upper x-axis) and the observed abundances and ratios. Each column corresponds to a model with density $n_{\rm H} = a \times 10^b$, displayed as $a(b)$. *Top:* heat map of relative differences in TMC 1-C. The best-fitting model is shown in bold. *Bottom:* heat map of relative differences in TMC 1-CP. The green and red models are those in agreement and disagreement, respectively, with the observed N_2D^+ and N_2D^+/N_2H^+ upper bounds.

from our multi-transition study. Moreover, Schnee et al. (2010) proposed that the peak density could be as large as $n_{\rm H} \sim 2\times10^6$ cm^{-3} based on the modeling of the dust continuum emission. Furthermore, the evolutionary time corresponding to this model, $t \sim 1$ Myr (see Table 6.5), is in better agreement with the previous estimation by Bulut et al. (2021) based on CO, CS, and HCS^+ observations. In order to test this hypothesis, in Section 6.6 we perform 3D radiative transfer calculations to produce synthetic lines to compare with our observations.

In TMC 1-CP we need to take into account the upper bound values of the N_2D^+ abundance and N_2D^+/N_2H^+ ratio in order to constrain the central density and the chemical age. Assuming the BES1 model, we derive an upper bound to the density of $n_{\rm H} < 4\times10^5$ cm^{-3} and $t < 1$ Myr. We also find good agreement with the AD models with $n_{\rm H} \sim 4\times10^5 - 1\times10^6$ cm^{-3}, which provide a better fit of the DCN, DNC, and N_2H^+ abundances. The AD models, however, do a poor job of predicting the CS abundances. One may think that this disagreement is due to our assumption of undepleted sulfur abundance, but this is not the case because assuming sulfur depletion would produce smaller CS abundances and larger discrepancies with observations. Recent fitting of the CS column densities by Bulut et al. (2021) concluded that we need to assume a sulfur depletion of a factor of 20 and chemical ages $\leq$ 1 Myr to account for the observed CS abundance.

6.6 Mock observations: TMC 1-C

TMC 1-C has been revealed to be an evolved collapsing core on the verge of forming a star, similar to the well-known L1544 (Caselli et al. 2002a,b; Caselli & Ceccarelli 2012). Given its relevance in the study of low-mass star formation processes, in this section we carry out a deeper characterization of this core. In Figure 6.5 we found that the BES1 model with a central density of $n_{\rm H} = 10^6$ cm^{-3} fits best the observed molecular abundances in TMC 1-C. AD models with moderate densities $n_{\rm H} = 10^5$ cm^{-3} also provide good approximations to the obtained chemical abundances of the species. It is therefore worth investigating how they perform in the radiative transfer of the observed lines. To further test the adequacy of the collapse models presented in the previous section, we post-processed our models to generate the synthetic spectra of a subset of the molecular lines from Table 6.1. In order to fully account for the physical structure and the abundance profiles of the different models, we used the radiative transfer code RADMC-3D (Dullemond et al. 2012).

For each density profile we created a spherically symmetric model consisting of a spherical grid divided by spherical shells in an onion-like structure. The spherical shells are endowed with a velocity field following the law $v \sim \alpha \times r^{-0.5}$, where α is chosen to yield line widths similar to those of the observed lines once we take into account the thermal and non-thermal line widths. The thickness of each shell follows a logarithmic law, with thinner layers near the origin and coarser layers towards the edge of the grid. The number of shells was chosen so that the Doppler shift between a layer and its closest neighbors is smaller than the total width of the lines, preventing abnormal ray-tracing (see "Doppler catching" in the RADMC-3D documentation). The adopted non-thermal dispersion is $\sigma_{\rm NT} = 0.1$ km s^{-1}, which fits the line widths of our observations and is in agreement with the results in Schnee et al. (2007). Finally, the temperature, density, and chemical abundance profiles are interpolated

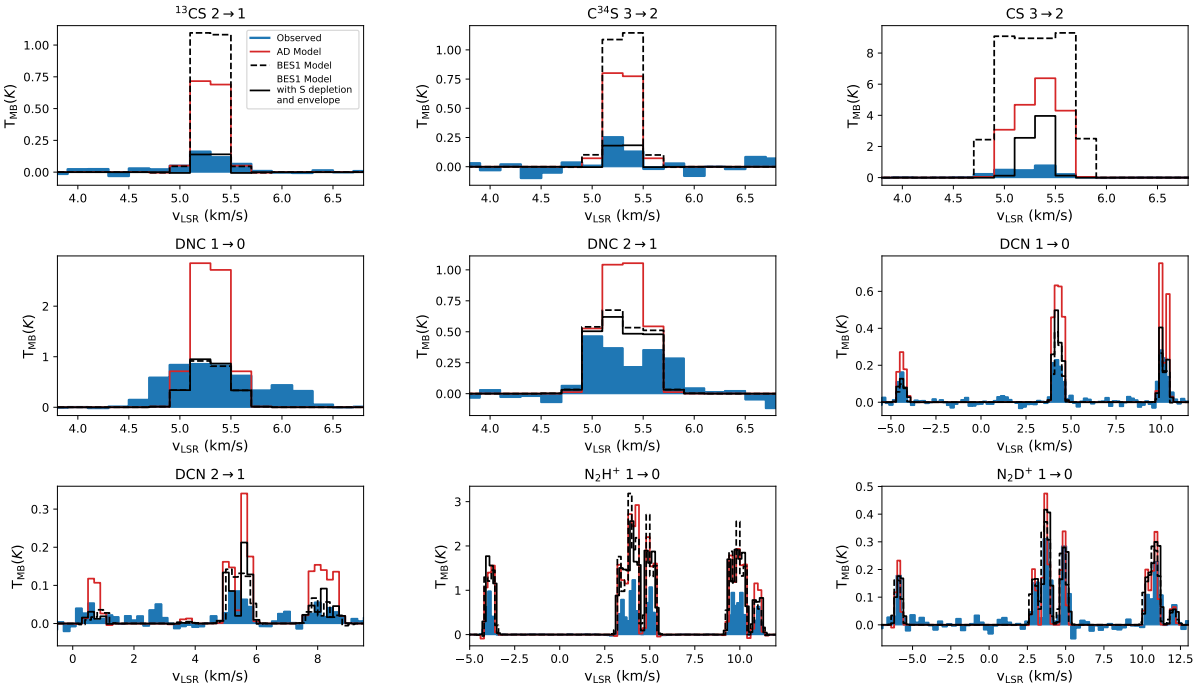

Figure 6.6: Observed spectra (blue), and the synthetic spectra of different transitions for the AD (red) and BES1 models (black, solid and dashed lines), as results from RADMC-3D. The BES1 model is highlighted as it is the one that, in general, fits the observations better.

to assign each cell the corresponding value.

To estimate the level populations, we used the RADMC-3D Large Velocity Gradient approximation (LVG) implementation (Shetty et al. 2011a,b) with the same collision coefficients as in the multi-transition study of Section 5. In Figure 6.6 we show the results of the line radiative transfer of different models following the LVG mode of RADMC-3D after convolving them with the appropriate beam sizes (Table 6.1). We first compared the performance of pure BES1 model with central density $n_H = 10^6$ cm^{-3} and the AD model with $n_H = 10^5$ cm^{-3}. While the BES1 and AD model overestimate the temperatures of the observed CS and isotopolog line temperatures, the AD model performs worse at describing the majority of deuterated lines except N_2D^+, where both show good agreement with the observations. It is worth noting that the difference between the synthesized and observed profiles of the DNC 1 → 0 line, the observed profile being wider with a secondary component, arises because the hyperfine splitting is not considered in the calculations. We are unable to reproduce these features, due to the absence of collisional coefficient files with hyperfine splitting. In the case of the N_2H^+ 1 → 0 line, both BES1 and AD models perform poorly. This poor performance suggests uncertainties in the dynamics of the core or in its physical structure. The low observed intensities of the optically thick N_2H^+ and DCN lines might be due to the existence of a thick absorbing layer that is not accounted for by our profiles. The existence of this thick absorbing layer would also be consistent with the deep self-absorption features detected by Fuente et al. (2019) in the HCN 1 → 0 line. To test this idea we added an

envelope to the BES1 profile by setting the density, temperature, and chemical abundances constant beyond the point where the density reaches $n_{H_2} = 10^4$ cm^{-3}. The thickness of this envelope was chosen so that the N_2H^+ column density would yield the observed opacity of the N_2H^+ 1 → 0 line. The resulting spectra is shown against the observations in Figure 6.6. From the results we conclude that the presence of an envelope provides a better agreement to the observations, but still overestimates the N_2H^+ line temperatures by a factor of ~ 1.5.

Thus far, the models do a poor job of reproducing the spectra of CS and isotopologs. As noted above, there is a large uncertainty on the value of the initial sulfur abundance. Following the most recent results in Bulut et al. (2021), we introduced a sulfur depletion of a factor of 20 in the BES1 model with envelope. The resulting line profiles are found to provide the best agreement to the CS 3 → 2 line and excellent agreement to the J=3 → 2 line of $C^{34}S$ and the J=2 → 1 line of ^{13}CS. Thus, we adopt the BES1 model with a density of $n_H = 10^6$ cm^{-3} and sulfur depletion as the one that best describes the chemical abundances and spectra of the TMC 1-C starless core.

Although our model is successful at reproducing the observed spectra, we should use caution before concluding about the collapse timescale in TMC 1-C because there are still some uncertainties that should be considered. On the one hand, our single-dish observations provide beam-averaged (~4000−5000 au) physical and chemical properties, hindering the variations in the density profile and chemical signatures within the core. Higher angular resolution dust continuum emission maps of TMC 1-C show an elongated structure and inhomogeneities within the core that are taken into account in our model (Schnee & Goodman 2005; Schnee et al. 2010). Clumpiness of the densest gas ($n_H > 10^5$ cm^{-3}) within the 30m telescope beam would produce lower brightness temperatures and help reconcile N_2H^+ predictions and observations. There is still room for improvement. As suggested by Sipilä & Caselli (2018), it is necessary to couple the chemistry with the dynamics to reproduce the molecular abundances in dense and small regions formed at the latest stages of the core evolution. Finally, our analysis helped constrain several parameters that are generally poorly known such as $\zeta(H_2)$, the initial OPR of H_2, or the initial S abundance. The influence of other initial abundances and quantities, such as the initial C/O ratio, was not taken into account in our study, and could be further constrained with the observation of a larger number of species.

6.7 Discussion

The classification of starless cores according to their evolutionary stage has been revealed to be a formidable problem. An accurate measurement of the gas density at the core center is challenging since the abundances of all molecules are depleted and the emerging line intensities are weak due to the low kinetic temperature. Moreover, the emission from the center can be absorbed by the outer lower density layers of the envelope. Chemistry has become an essential tool in determining the physical conditions along these dense cores, and chemical diagnostics such as the N_2D^+/N_2H^+ have been successfully used to classify pre-stellar cores. Although extremely useful, chemical models show that all these diagnostics depend on parameters that are usually not well constrained, such as $\zeta(H_2)$, the initial OPR of H_2, and the

initial elemental abundances.

We used spectroscopic observations to investigate the evolutionary stage of the cores TMC 1-C and TMC 1-CP, located in the nearby region of Taurus. These cores are located in the same molecular cloud at a separation of ~ 19′, and are expected to share the same initial conditions. Furthermore, the acquired knowledge of the initial gas ionization degree and chemical composition by Fuente et al. (2019) and Navarro-Almaida et al. (2020) allowed us to carry out a more precise modeling of their chemistry. In addition to species commonly used to probe the evolutionary stage of starless cores such as CS, N_2H^+, and N_2D^+, we mapped the deuterated isomers DCN and DNC to further constrain the physical and chemical conditions of the dense gas. The inclusion of these two isomers provided valuable information for the modeling. First, the comparison of the abundances of deuterated neutral and ionic species allowed us to have an estimate of $\zeta(H_2)$ in the dense gas. Interestingly, the value derived from these species, $\zeta(H_2) = 1.3 \times 10^{-17}$ s^{-1}, is a factor of 5−10 lower than that derived by Fuente et al. (2019) in the translucent cloud. Moreover, the chemistry of these deuterated isomers is very sensitive to the physical conditions of starless cores. At low temperatures $T_k < 10$ K, the DNC/DCN abundance ratio is a good tracer of the gas density, which itself is an indicator of the starless core evolutionary stage. The abundances of DNC and DCN reach the steady state at earlier times than N_2D^+. Combining the three species, we are able to distinguish chemical ages ranging from ~0.1 to ~1 Myr.

In an attempt to characterize the contraction of starless cores in TMC 1, we used analytic approximations to the density evolution of starless cores to predict the evolution of the gas chemistry during the collapse. In particular we considered three collapse models: i) the BES1 model, which describes a gravitational collapse with a characteristic time, $t \sim 1$ Myr; ii) the BES4 model, which describes a rapid collapse, $t \sim 0.1$ Myr, induced by the cloud compression; and iii) the AD model, which describes a collapse slowed down by a magnetic support, with $t \sim 10$ Myr. We find that the BES4 model is not compatible with the observations. The abundances measured towards TMC 1-C and TMC 1-CP can only be explained with the BES1 and AD models. Although the BES1 and AD models provide a reasonable fit to the observed chemical abundances, in the case of TMC 1-C our results are best explained by the BES1 model, which simulates the contraction of a near-equilibrium core with a typical time of collapse of ~1 Myr.

Thus far, only a few starless cores have been studied in detailed using dust continuum emission and molecular spectroscopy. Of these targets, the pre-stellar core L1544, stands out as the prototype of low-mass evolved core on the verge of collapse (Caselli et al. 2002a; Caselli & Ceccarelli 2012); L1544 is a prototypical low-mass pre-stellar core in Taurus. It shows signs of contraction (Caselli et al. 2002a; Caselli & Ceccarelli 2012) that would eventually evolve into gravitational collapse, making it an ideal target to study the earliest phases of low-mass star formation. There are many studies that analyze the deuteration in this pre-stellar core (see, e.g., Caselli et al. 2002b; Crapsi et al. 2005; Chacón-Tanarro et al. 2019; Redaelli et al. 2019). L1544 was also a subject of study in Crapsi et al. (2005), where they estimate a N_2H^+ deuteration fraction of 0.23 ± 0.04, in accordance with other works. More recently, Redaelli et al. (2019) estimated the N_2H^+ and N_2D^+ column densities at the dust peak, yielding $N_2D^+/N_2H^+ \approx 0.19^{+0.16}_{-0.19}$. This value is consistent with that measured towards TMC 1-C, suggesting that L1544 and TMC1-C are at a similar evolutionary stage. Crapsi et al.

(2005) carried out a N_2H^+ and N_2D^+ survey towards 31 low-mass stars using the 30m telescope. Out of this large sample, only five targets presents N_2H^+ deuterium fractions similar to L1544 and TMC 1-C, which testifies to the exceptionality of this evolved object that deserves further study.

The observation of several deuterated species together with N_2H^+ and CS allowed us to constrain the chemistry of the TMC 1-C. However, there are uncertainties in the physical structure of this core that must be solved for a more accurate description. First of all, the moderate spatial resolution of our observations (~4000−5000 au) hinders the detection of the density and chemical gradients expected within the cores. High spatial resolution molecular observations are mandatory to reveal their complex morphology, density, and chemical structure. At the scales probed by interferometric observations (<4000−5000 au), the abundances predicted by our pseudo-dynamic model would not be reliable, and a dynamical model is necessary to describe the gas chemical evolution. The comparison of high spatial resolution molecular observations with state-of-the-art 3D chemo-magnetohydrodynamical simulations is necessary to progress in our understanding of the formation and evolution of starless cores.

6.8 Summary and conclusions

Our goal was to investigate the evolution of starless cores based on observations towards the prototypical dense cores TMC 1-C and TMC 1-CP. These two cores are located in the same molecular cloud and share similar initial conditions. Located at a distance of 141.8 pc, these cores provide an excellent opportunity to understand the physical and chemical evolution in this phase. Our results can be summarized as follows:

- We mapped the prototypical dense cores TMC 1-C and TMC 1-CP in the J=2 → 1 and 3 → 2 lines of CS (and its isotopologs); the J=1 → 0 and 2 → 1 lines of DCN, DNC, and $DN^{13}C$; and the J= 1 → 0 line of N_2H^+ and N_2D^+. The emission of DNC 1 → 0 has revealed to be an excellent probe to identify the densest region within these cores. Moreover, we detected $DN^{13}C$ 1 → 0 and 2 → 1 lines towards TMC 1-C. Based on these observations, we selected five positions for a detailed study.

- A multi-transitional study of CS (and isotopologs), DCN, and DNC allowed us to estimate the density and molecular abundances towards the selected positions. The densities derived from CS (and isotopologs) range from n_H=6×10^4 cm^{-3} in TMC 1-CP to n_H=1×10^5 cm^{-3}. Based on DNC and DCN observations, we derive n_H=(4±1)×10^4 cm^{-3} towards all positions. The abundances of deuterated compounds are higher in TMC 1-C. In particular, the N_2D^+/N_2H^+ ratio is ~ 0.14 in TMC 1-C and < 0.06 in TMC 1-CP.

- We modeled the chemistry using a gas-grain network that includes deuterium with implemented spin chemistry. As a first step, we explored the parameter space using in a 0D modeling. Our model is able to reproduce the observed abundances, assuming $\zeta(H_2)$=1.3×10^{-17} s^{-1} and a time of ~0.8 Myr for TMC 1-CP and ~2 Myr for TMC 1-C. The initial OPR ratio does not have a strong impact on our calculations since we only consider evolution times higher than 0.1 Myr, for which the OPR evolves to 10^{-3}.

- By using analytic approximations to describe density evolution starless cores as a physical basis for our chemical modeling, we conclude that the TMC 1 filament is not undergoing a rapid collapse. Our results are more consistent with the model BES1 of Aikawa et al. (2005), which simulates the contraction of a near-equilibrium core with a typical time of collapse of ~1 Myr. TMC 1-CP is in an earlier evolutionary stage due to a shorter time since formation or, alternatively, due to a collapse led by ambipolar diffusion in a magnetically supported core.

- The 3D radiative transfer of the chemo-dynamical profiles presented in this work supports our conclusions about TMC 1-C. The comparison of the observed spectra with the radiative transfer of the chemo-dynamical profiles from Aikawa et al. (2005) points to a dynamical behavior best described by the BES1 model. This analysis also allowed us to conclude that sulfur-bearing molecular lines are best reproduced with a factor 20 of initial sulfur depletion, in agreement with the most recent results on the subject (Bulut et al. 2021). Finally, the radiative transfer modeling of the N_2H^+ $1 \rightarrow 0$ line suggests the possible existence of an absorbing envelope in front of this core, which could explain why the observed peak temperatures are lower than expected.

We investigated the chemistry of the starless cores TMC 1-C and TMC 1-CP, which are thought to be in a different evolutionary stage, using CS, N_2H^+, and the deuterated compounds N_2D^+, DCN, and DNC as chemical diagnostics. Our data allowed us to reject the possibility that these cores are undergoing a rapid collapse. Moreover, the 3D radiative transfer of pseudo time-dependent collapse models allowed us to discard a collapse timescale longer than ~ 1 Myr for TMC 1-C. However, this analysis does not allow us to definitely differentiate between a nearly equilibrium contraction with a timescale shorter than ~ 1 Myr or a longer collapse slowed down by a magnetic support in TMC 1-CP. A full chemo-magnetohydrodynamical modeling, high angular resolution observations, and an accurate estimate of the magnetic flux could help us figure out a more accurate picture of the collapse history in these regions.

6.9 Tabulated and complementary data

6.9.1 Line properties

In this section we show the obtained integrated areas and main-beam temperatures of the DCN $1 \rightarrow 0$, DCN $2 \rightarrow 1$, DNC $1 \rightarrow 0$, DNC $2 \rightarrow 1$, $DN^{13}C$ $1 \rightarrow 0$, $DN^{13}C$ $2 \rightarrow 1$, N_2D^+ $1 \rightarrow 0$, and N_2H^+ $1 \rightarrow 0$ lines at the different positions listed in Table 6.2. The frequencies and line properties are from the CDMS catalog, except those of the $DN^{13}C$ lines, which are from SLAIM catalogue. We also show the results of the HFS-CLASS method applied to the DCN, N_2H^+, and N_2D^+.

Table 6.6: Properties, main beam temperatures, and integrated intensities of the detected spectral lines in TMC 1-C

Species	Transition	Frequency (MHz)	E_{up} (K)	$\log(A_{ij})$	θ_{MB} (")	g_{up}	T_{MB} (K)	$\int T_{MB}\,dv$ (K km s^{-1})
DCN	$1_1 \rightarrow 0_1$	72413.50	3.5	-4.88	34	3	0.289 ± 0.015	0.164 ± 0.008
	$1_2 \rightarrow 0_1$	72414.93		-4.88		5	0.249 ± 0.015	0.166 ± 0.008
	$1_0 \rightarrow 0_1$	72417.03		-4.88		1	0.170 ± 0.015	0.073 ± 0.006
DCN	$2_2 \rightarrow 1_2$	144826.58	10.4	-4.50	17	5	0.085 ± 0.019	0.056 ± 0.009
	$2_1 \rightarrow 1_0$	144826.82		-4.15		3		
	$2_2 \rightarrow 1_1$	144828.00		-4.02		5		
	$2_3 \rightarrow 1_2$	144828.11		-3.90		7		
	$2_1 \rightarrow 1_2$	144828.91		-5.45		3		
	$2_1 \rightarrow 1_1$	144830.33		-4.28		3		
DNC	$1 \rightarrow 0$	76305.70	3.7	-4.80	34	3	0.870 ± 0.010	1.009 ± 0.007
DNC	$2 \rightarrow 1$	152609.74	11.0	-3.81	17	5	0.382 ± 0.048	0.365 ± 0.029
$DN^{13}C$	$1 \rightarrow 0$	73367.7540	3.4.	-4.90	34	3	0.068 ± 0.013	0.098 ± 0.022
$DN^{13}C$	$2 \rightarrow 1$	146734.0020	10.25	-3.92	27	5	0.022 ± 0.005	0.063 ± 0.021
N_2D^+	$1_{1,0} \rightarrow 0_{1,1}$	77107.46	3.7	-4.69	34	1	0.199 ± 0.027	0.152 ± 0.014
	$1_{1,2} \rightarrow 0_{1,1}$	77107.76		-5.50		5		
	$1_{1,2} \rightarrow 0_{1,2}$	77107.76		-4.76		5		
	$1_{1,1} \rightarrow 0_{1,0}$	77107.90		-4.98		3		
	$1_{1,1} \rightarrow 0_{1,1}$	77107.90		-5.45		3		
	$1_{1,1} \rightarrow 0_{1,2}$	77107.90		-5.61		3		
	$1_{2,2} \rightarrow 0_{1,1}$	77109.32		-5.11		5	0.302 ± 0.027	0.126 ± 0.009
	$1_{2,2} \rightarrow 0_{1,2}$	77109.32		-5.50		5		
	$1_{2,3} \rightarrow 0_{1,2}$	77109.61		-4.69		7	0.352 ± 0.026	0.151 ± 0.014
	$1_{2,1} \rightarrow 0_{1,0}$	77109.81		-5.19		3		
	$1_{2,1} \rightarrow 0_{1,1}$	77109.81		-4.87		3		
	$1_{2,1} \rightarrow 0_{1,2}$	77109.81		-6.09		3		
	$1_{0,1} \rightarrow 0_{1,1}$	77112.11		-5.32		3	0.181 ± 0.026	0.072 ± 0.014
	$1_{0,1} \rightarrow 0_{1,2}$	77112.11		-4.92		3		
	$1_{0,1} \rightarrow 0_{1,0}$	77112.11		-5.44		3		
N_2H^+	$1_{1,0} \rightarrow 0_{1,1}$	93171.62	4.5	-4.44	26	1	0.640 ± 0.025	0.219 ± 0.035
	$1_{1,2} \rightarrow 0_{1,1}$	93171.91		-5.25		5	0.734 ± 0.025	0.582 ± 0.035
	$1_{1,2} \rightarrow 0_{1,2}$	93171.91		-4.51		5		
	$1_{1,1} \rightarrow 0_{1,0}$	93172.05		-4.73		3		
	$1_{1,1} \rightarrow 0_{1,1}$	93172.05		-5.36		3		
	$1_{1,1} \rightarrow 0_{1,2}$	93172.05		-4.87		3		
	$1_{2,2} \rightarrow 0_{1,1}$	93173.47		-4.51		5	0.759 ± 0.025	0.293 ± 0.035
	$1_{2,2} \rightarrow 0_{1,2}$	93173.47		-5.25		5		
	$1_{2,3} \rightarrow 0_{1,2}$	93173.77		-4.44		7	0.610 ± 0.025	0.658 ± 0.035
	$1_{2,1} \rightarrow 0_{1,0}$	93173.96		-4.95		3		
	$1_{2,1} \rightarrow 0_{1,1}$	93173.96		-4.63		3		
	$1_{2,1} \rightarrow 0_{1,2}$	93173.96		-5.84		3		
	$1_{0,1} \rightarrow 0_{1,0}$	93176.26		-5.19		3	0.811 ± 0.025	0.282 ± 0.035
	$1_{0,1} \rightarrow 0_{1,1}$	93176.26		-5.07		3		
	$1_{0,1} \rightarrow 0_{1,2}$	93176.26		-4.67		3		

Table 6.7: Properties, main beam temperatures, and integrated intensities of the detected spectral lines in TMC 1-C (P)

Species	Transition	Frequency (MHz)	E_{up} (K)	$\log(A_{ij})$	θ_{MB} (")	g_{up}	T_{MB} (K)	$\int T_{MB}\,dv$ (K km s^{-1})
DCN	$1_1 \rightarrow 0_1$	72413.50	3.5	-4.88	34	3	0.408 ± 0.012	0.185 ± 0.007
	$1_2 \rightarrow 0_1$	72414.93		-4.88		5	0.484 ± 0.012	0.243 ± 0.007
	$1_0 \rightarrow 0_1$	72417.03		-4.88		1	0.271 ± 0.012	0.091 ± 0.006
DCN	$2_2 \rightarrow 1_2$	144826.58	10.4	-4.50	17	5	0.091 ± 0.026	0.045 ± 0.015
	$2_1 \rightarrow 1_0$	144826.82		-4.15		3		
	$2_2 \rightarrow 1_1$	144828.00		-4.02		5	0.130 ± 0.026	0.079 ± 0.010
	$2_3 \rightarrow 1_2$	144828.11		-3.90		7		
	$2_1 \rightarrow 1_2$	144828.91		-5.45		3		
	$2_1 \rightarrow 1_1$	144830.33		-4.28		3	0.064 ± 0.026	0.058 ± 0.013
DCN	$3 \rightarrow 2$	217237.00	20.9	-3.34	11	21	0.071 ± 0.022	0.027 ± 0.009
DNC	$1 \rightarrow 0$	76305.70	3.7	-4.80	34	3	1.387 ± 0.120	1.299 ± 0.009
DNC	$2 \rightarrow 1$	152609.74	11.0	-3.81	17	5	0.726 ± 0.089	0.557 ± 0.018
N_2D^+	$1_{1,0} \rightarrow 0_{1,1}$	77107.46	3.7	-4.69	34	1	0.249 ± 0.033	0.098 ± 0.011
	$1_{1,2} \rightarrow 0_{1,1}$	77107.76		-5.50		5		
	$1_{1,2} \rightarrow 0_{1,2}$	77107.76		-4.76		5		
	$1_{1,1} \rightarrow 0_{1,0}$	77107.90		-4.98		3		
	$1_{1,1} \rightarrow 0_{1,1}$	77107.90		-5.45		3		
	$1_{1,1} \rightarrow 0_{1,2}$	77107.90		-5.61		3		
	$1_{2,2} \rightarrow 0_{1,1}$	77109.32		-5.11		5	0.271 ± 0.033	0.096 ± 0.012
	$1_{2,2} \rightarrow 0_{1,2}$	77109.32		-5.50		5		
	$1_{2,3} \rightarrow 0_{1,2}$	77109.61		-4.69		7	0.361 ± 0.033	0.136 ± 0.012
	$1_{2,1} \rightarrow 0_{1,0}$	77109.81		-5.19		3		
	$1_{2,1} \rightarrow 0_{1,1}$	77109.81		-4.87		3		
	$1_{2,1} \rightarrow 0_{1,2}$	77109.81		-6.09		3		
	$1_{0,1} \rightarrow 0_{1,1}$	77112.11		-5.32		3	0.152 ± 0.033	0.048 ± 0.011
	$1_{0,1} \rightarrow 0_{1,2}$	77112.11		-4.92		3		
	$1_{0,1} \rightarrow 0_{1,0}$	77112.11		-5.44		3		
N_2H^+	$1_{1,0} \rightarrow 0_{1,1}$	93171.62	4.5	-4.44	26	1	0.670 ± 0.023	0.198 ± 0.009
	$1_{1,2} \rightarrow 0_{1,1}$	93171.91		-5.25		5	0.803 ± 0.023	0.623 ± 0.052
	$1_{1,2} \rightarrow 0_{1,2}$	93171.91		-4.51		5		
	$1_{1,1} \rightarrow 0_{1,0}$	93172.05		-4.73		3		
	$1_{1,1} \rightarrow 0_{1,1}$	93172.05		-5.36		3		
	$1_{1,1} \rightarrow 0_{1,2}$	93172.05		-4.87		3		
	$1_{2,2} \rightarrow 0_{1,1}$	93173.47		-4.51		5	1.050 ± 0.023	0.323 ± 0.010
	$1_{2,2} \rightarrow 0_{1,2}$	93173.47		-5.25		5		
	$1_{2,3} \rightarrow 0_{1,2}$	93173.77		-4.44		7	0.711 ± 0.023	0.708 ± 0.015
	$1_{2,1} \rightarrow 0_{1,0}$	93173.96		-4.95		3		
	$1_{2,1} \rightarrow 0_{1,1}$	93173.96		-4.63		3		
	$1_{2,1} \rightarrow 0_{1,2}$	93173.96		-5.84		3		
	$1_{0,1} \rightarrow 0_{1,0}$	93176.26		-5.19		3	0.946 ± 0.023	0.320 ± 0.010
	$1_{0,1} \rightarrow 0_{1,1}$	93176.26		-5.07		3		
	$1_{0,1} \rightarrow 0_{1,2}$	93176.26		-4.67		3		

Table 6.8: Properties, main beam temperatures, and integrated intensities of the detected spectral lines in TMC 1-CP

Species	Transition	Frequency (MHz)	E_{up} (K)	$\log(A_{ij})$	θ_{MB} (")	g_{up}	T_{MB} (K)	$\int T_{MB}\,dv$ (K km s^{-1})
DCN	$1_1 \rightarrow 0_1$	72413.50	3.5	-4.88	34	3	0.287 ± 0.020	0.192 ± 0.012
	$1_2 \rightarrow 0_1$	72414.93		-4.88		5	0.461 ± 0.020	0.320 ± 0.011
	$1_0 \rightarrow 0_1$	72417.03		-4.88		1	0.145 ± 0.020	0.074 ± 0.010
DCN	$2_2 \rightarrow 1_2$	144826.58	10.4	-4.50	17	5	0.177 ± 0.014	0.093 ± 0.007
	$2_1 \rightarrow 1_0$	144826.82		-4.15		3		
	$2_2 \rightarrow 1_1$	144828.00		-4.02		5		
	$2_3 \rightarrow 1_2$	144828.11		-3.90		7		
	$2_1 \rightarrow 1_2$	144828.91		-5.45		3		
	$2_1 \rightarrow 1_1$	144830.33		-4.28		3		
DNC	$1 \rightarrow 0$	76305.70	3.7	-4.80	34	3	0.964 ± 0.012	1.051 ± 0.008
DNC	$2 \rightarrow 1$	152609.74	11.0	-3.81	17	5	0.722 ± 0.058	0.535 ± 0.031
N_2D^+	$1_{1,0} \rightarrow 0_{1,1}$	77107.46	3.7	-4.69	34	1	rms: 1.66×10^{-2} K	
	$1_{1,2} \rightarrow 0_{1,1}$	77107.76		-5.50		5		
	$1_{1,2} \rightarrow 0_{1,2}$	77107.76		-4.76		5		
	$1_{1,1} \rightarrow 0_{1,0}$	77107.90		-4.98		3		
	$1_{1,1} \rightarrow 0_{1,1}$	77107.90		-5.45		3		
	$1_{1,1} \rightarrow 0_{1,2}$	77107.90		-5.61		3		
	$1_{2,2} \rightarrow 0_{1,1}$	77109.32		-5.11		5		
	$1_{2,2} \rightarrow 0_{1,2}$	77109.32		-5.50		5		
	$1_{2,3} \rightarrow 0_{1,2}$	77109.61		-4.69		7		
	$1_{2,1} \rightarrow 0_{1,0}$	77109.81		-5.19		3		
	$1_{2,1} \rightarrow 0_{1,1}$	77109.81		-4.87		3		
	$1_{2,1} \rightarrow 0_{1,2}$	77109.81		-6.09		3		
	$1_{0,1} \rightarrow 0_{1,1}$	77112.11		-5.32		3		
	$1_{0,1} \rightarrow 0_{1,2}$	77112.11		-4.92		3		
	$1_{0,1} \rightarrow 0_{1,0}$	77112.11		-5.44		3		
N_2H^+	$1_{1,0} \rightarrow 0_{1,1}$	93171.62	4.5	-4.44	26	1	0.427 ± 0.007	0.170 ± 0.053
	$1_{1,2} \rightarrow 0_{1,1}$	93171.91		-5.25		5	0.955 ± 0.007	0.835 ± 0.043
	$1_{1,2} \rightarrow 0_{1,2}$	93171.91		-4.51		5		
	$1_{1,1} \rightarrow 0_{1,0}$	93172.05		-4.73		3		
	$1_{1,1} \rightarrow 0_{1,1}$	93172.05		-5.36		3		
	$1_{1,1} \rightarrow 0_{1,2}$	93172.05		-4.87		3		
	$1_{2,2} \rightarrow 0_{1,1}$	93173.47		-4.51		5	1.046 ± 0.007	0.509 ± 0.043
	$1_{2,2} \rightarrow 0_{1,2}$	93173.47		-5.25		5		
	$1_{2,3} \rightarrow 0_{1,2}$	93173.77		-4.44		7	1.191 ± 0.007	1.071 ± 0.043
	$1_{2,1} \rightarrow 0_{1,0}$	93173.96		-4.95		3		
	$1_{2,1} \rightarrow 0_{1,1}$	93173.96		-4.63		3		
	$1_{2,1} \rightarrow 0_{1,2}$	93173.96		-5.84		3		
	$1_{0,1} \rightarrow 0_{1,0}$	93176.26		-5.19		3	0.808 ± 0.007	0.423 ± 0.043
	$1_{0,1} \rightarrow 0_{1,1}$	93176.26		-5.07		3		
	$1_{0,1} \rightarrow 0_{1,2}$	93176.26		-4.67		3		

Table 6.9: Properties, main beam temperatures, and integrated intensities of the detected spectral lines in TMC 1-CP (P1)

Species	Transition	Frequency (MHz)	E_{up} (K)	$\log(A_{ij})$	θ_{MB} (")	g_{up}	T_{MB} (K)	$\int T_{MB}\,dv$ (K km s^{-1})
DCN	$1_1 \rightarrow 0_1$	72413.50	3.5	-4.88	34	3	0.358 ± 0.008	0.190 ± 0.013
	$1_2 \rightarrow 0_1$	72414.93		-4.88		5	0.530 ± 0.008	0.330 ± 0.011
	$1_0 \rightarrow 0_1$	72417.03		-4.88		1	0.222 ± 0.008	0.083 ± 0.014
DCN	$2_2 \rightarrow 1_2$	144826.58	10.4	-4.50	17	5	0.282 ± 0.016	0.110 ± 0.015
	$2_1 \rightarrow 1_0$	144826.82		-4.15		3		
	$2_2 \rightarrow 1_1$	144828.00		-4.02		5		
	$2_3 \rightarrow 1_2$	144828.11		-3.90		7		
	$2_1 \rightarrow 1_2$	144828.91		-5.45		3		
	$2_1 \rightarrow 1_1$	144830.33		-4.28		3		
DNC	$1 \rightarrow 0$	76305.70	3.7	-4.80	34	3	1.227 ± 0.080	1.215 ± 0.013
DNC	$2 \rightarrow 1$	152609.74	11.0	-3.81	17	5	0.732 ± 0.059	0.477 ± 0.027
N_2D^+	$1_{1,0} \rightarrow 0_{1,1}$	77107.46	3.7	-4.69	34	1	rms: 2.00×10^{-2} K	
	$1_{1,2} \rightarrow 0_{1,1}$	77107.76		-5.50		5		
	$1_{1,2} \rightarrow 0_{1,2}$	77107.76		-4.76		5		
	$1_{1,1} \rightarrow 0_{1,0}$	77107.90		-4.98		3		
	$1_{1,1} \rightarrow 0_{1,1}$	77107.90		-5.45		3		
	$1_{1,1} \rightarrow 0_{1,2}$	77107.90		-5.61		3		
	$1_{2,2} \rightarrow 0_{1,1}$	77109.32		-5.11		5		
	$1_{2,2} \rightarrow 0_{1,2}$	77109.32		-5.50		5		
	$1_{2,3} \rightarrow 0_{1,2}$	77109.61		-4.69		7		
	$1_{2,1} \rightarrow 0_{1,0}$	77109.81		-5.19		3		
	$1_{2,1} \rightarrow 0_{1,1}$	77109.81		-4.87		3		
	$1_{2,1} \rightarrow 0_{1,2}$	77109.81		-6.09		3		
	$1_{0,1} \rightarrow 0_{1,1}$	77112.11		-5.32		3		
	$1_{0,1} \rightarrow 0_{1,2}$	77112.11		-4.92		3		
	$1_{0,1} \rightarrow 0_{1,0}$	77112.11		-5.44		3		
N_2H^+	$1_{1,0} \rightarrow 0_{1,1}$	93171.62	4.5	-4.44	26	1	0.379 ± 0.022	0.167 ± 0.008
	$1_{1,2} \rightarrow 0_{1,1}$	93171.91		-5.25		5	1.061 ± 0.022	0.904 ± 0.013
	$1_{1,2} \rightarrow 0_{1,2}$	93171.91		-4.51		5		
	$1_{1,1} \rightarrow 0_{1,0}$	93172.05		-4.73		3		
	$1_{1,1} \rightarrow 0_{1,1}$	93172.05		-5.36		3		
	$1_{1,1} \rightarrow 0_{1,2}$	93172.05		-4.87		3		
	$1_{2,2} \rightarrow 0_{1,1}$	93173.47		-4.51		5	1.208 ± 0.022	0.542 ± 0.009
	$1_{2,2} \rightarrow 0_{1,2}$	93173.47		-5.25		5		
	$1_{2,3} \rightarrow 0_{1,2}$	93173.77		-4.44		7	1.263 ± 0.022	1.102 ± 0.015
	$1_{2,1} \rightarrow 0_{1,0}$	93173.96		-4.95		3		
	$1_{2,1} \rightarrow 0_{1,1}$	93173.96		-4.63		3		
	$1_{2,1} \rightarrow 0_{1,2}$	93173.96		-5.84		3		
	$1_{0,1} \rightarrow 0_{1,0}$	93176.26		-5.19		3	0.889 ± 0.022	0.430 ± 0.010
	$1_{0,1} \rightarrow 0_{1,1}$	93176.26		-5.07		3		
	$1_{0,1} \rightarrow 0_{1,2}$	93176.26		-4.67		3		

Table 6.10: Properties, main beam temperatures, and integrated intensities of the detected spectral lines in TMC 1-CP (P2)

Species	Transition	Frequency (MHz)	E_{up} (K)	$\log(A_{ij})$	θ_{MB} (")	g_{up}	T_{MB} (K)	$\int T_{MB}\,dv$ (K km s^{-1})
DCN	$1_1 \rightarrow 0_1$	72413.50	3.5	-4.88	34	3	0.363 ± 0.033	0.220 ± 0.015
	$1_2 \rightarrow 0_1$	72414.93		-4.88		5	0.542 ± 0.033	0.357 ± 0.018
	$1_0 \rightarrow 0_1$	72417.03		-4.88		1	0.219 ± 0.033	0.090 ± 0.014
DCN	$2_2 \rightarrow 1_2$	144826.58	10.4	-4.50	17	5	0.227 ± 0.021	0.182 ± 0.022
	$2_1 \rightarrow 1_0$	144826.82		-4.15		3		
	$2_2 \rightarrow 1_1$	144828.00		-4.02		5		
	$2_3 \rightarrow 1_2$	144828.11		-3.90		7		
	$2_1 \rightarrow 1_2$	144828.91		-5.45		3		
	$2_1 \rightarrow 1_1$	144830.33		-4.28		3		
DNC	$1 \rightarrow 0$	76305.70	3.7	-4.80	34	3	1.166 ± 0.016	1.179 ± 0.011
DNC	$2 \rightarrow 1$	152609.74	11.0	-3.81	17	5	0.778 ± 0.048	0.583 ± 0.032
N_2D^+	$1_{1,0} \rightarrow 0_{1,1}$	77107.46	3.7	-4.69	34	1	rms: 2.20×10^{-2} K	
	$1_{1,2} \rightarrow 0_{1,1}$	77107.76		-5.50		5		
	$1_{1,2} \rightarrow 0_{1,2}$	77107.76		-4.76		5		
	$1_{1,1} \rightarrow 0_{1,0}$	77107.90		-4.98		3		
	$1_{1,1} \rightarrow 0_{1,1}$	77107.90		-5.45		3		
	$1_{1,1} \rightarrow 0_{1,2}$	77107.90		-5.61		3		
	$1_{2,2} \rightarrow 0_{1,1}$	77109.32		-5.11		5		
	$1_{2,2} \rightarrow 0_{1,2}$	77109.32		-5.50		5		
	$1_{2,3} \rightarrow 0_{1,2}$	77109.61		-4.69		7		
	$1_{2,1} \rightarrow 0_{1,0}$	77109.81		-5.19		3		
	$1_{2,1} \rightarrow 0_{1,1}$	77109.81		-4.87		3		
	$1_{2,1} \rightarrow 0_{1,2}$	77109.81		-6.09		3		
	$1_{0,1} \rightarrow 0_{1,1}$	77112.11		-5.32		3		
	$1_{0,1} \rightarrow 0_{1,2}$	77112.11		-4.92		3		
	$1_{0,1} \rightarrow 0_{1,0}$	77112.11		-5.44		3		
N_2H^+	$1_{1,0} \rightarrow 0_{1,1}$	93171.62	4.5	-4.44	26	1	0.347 ± 0.019	0.133 ± 0.052
	$1_{1,2} \rightarrow 0_{1,1}$	93171.91		-5.25		5	1.005 ± 0.019	0.885 ± 0.051
	$1_{1,2} \rightarrow 0_{1,2}$	93171.91		-4.51		5		
	$1_{1,1} \rightarrow 0_{1,0}$	93172.05		-4.73		3		
	$1_{1,1} \rightarrow 0_{1,1}$	93172.05		-5.36		3		
	$1_{1,1} \rightarrow 0_{1,2}$	93172.05		-4.87		3		
	$1_{2,2} \rightarrow 0_{1,1}$	93173.47		-4.51		5	1.151 ± 0.022	0.502 ± 0.051
	$1_{2,2} \rightarrow 0_{1,2}$	93173.47		-5.25		5		
	$1_{2,3} \rightarrow 0_{1,2}$	93173.77		-4.44		7	1.183 ± 0.022	1.106 ± 0.052
	$1_{2,1} \rightarrow 0_{1,0}$	93173.96		-4.95		3		
	$1_{2,1} \rightarrow 0_{1,1}$	93173.96		-4.63		3		
	$1_{2,1} \rightarrow 0_{1,2}$	93173.96		-5.84		3		
	$1_{0,1} \rightarrow 0_{1,0}$	93176.26		-5.19		3	0.827 ± 0.022	0.461 ± 0.052
	$1_{0,1} \rightarrow 0_{1,1}$	93176.26		-5.07		3		
	$1_{0,1} \rightarrow 0_{1,2}$	93176.26		-4.67		3		

6.9.2 CS spectra and line fitting with RADEX.

Here we show the observed CS lines (see Table 6.1) and the synthetic spectra obtained with the radiative transfer code RADEX and the parameters shown in Table 6.3.

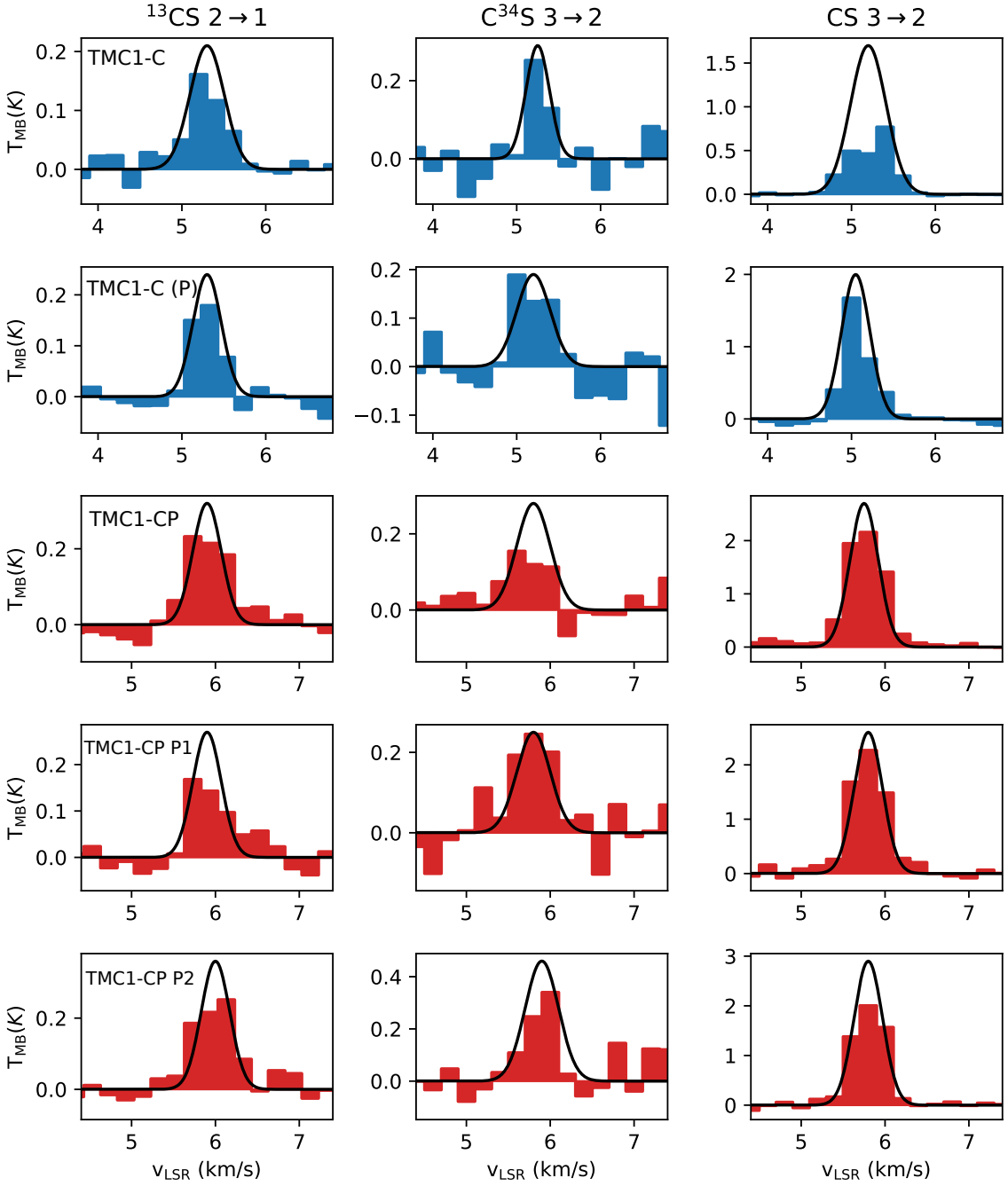

Figure 6.7: Observed ^{13}CS 2 → 1, C^{34}S 3 → 2, and CS 3 → 2 lines towards the positions listed in Table 6.2 (TMC 1-C in blue and TMC 1-CP in red), with the synthetic spectra created with RADEX and the parameters in Table 6.3.

6.9.3 HFS-CLASS results.

The HFS-CLASS method is used to derive the opacities of the DCN, N_2H^+, and N_2D^+ lines from their hyperfine structure. We list here the results of this method applied at the observed lines of our setup.

Table 6.11: HFS-CLASS method results for the DCN, N_2H^+, and N_2D^+ lines at the observed positions. T_A is the line temperature of the main component, ΔV is the line width, and τ_m is the optical depth of the main component.

Position	Species	Transition	$T_A \times \tau_m$ (K)	ΔV (km s^{-1})	τ_m
TMC 1-C	DCN	$1 \rightarrow 0$	1.36 ± 0.17	0.40 ± 0.02	5.72 ± 0.84
		$2 \rightarrow 1$	0.25 ± 0.09	0.37 ± 0.07	3.24 ± 1.53
	N_2H^+	$1 \rightarrow 0$	2.70 ± 0.08	0.33 ± 0.02	3.31 ± 0.17
	N_2D^+	$1 \rightarrow 0$	0.33 ± 0.01	0.50 ± 0.01	0.10 ± 0.04
TMC 1-C (P)	DCN	$1 \rightarrow 0$	1.57 ± 0.13	0.34 ± 0.01	3.45 ± 0.32
		$2 \rightarrow 1$	0.35 ± 0.15	0.43 ± 0.09	3.19 ± 2.05
	N_2H^+	$1 \rightarrow 0$	2.67 ± 0.07	0.33 ± 0.01	2.64 ± 0.14
	N_2D^+	$1 \rightarrow 0$	0.25 ± 0.01	0.50 ± 0.01	0.10 ± 0.02
TMC 1-CP	DCN	$1 \rightarrow 0$	0.62 ± 0.08	0.59 ± 0.03	0.69 ± 0.35
		$2 \rightarrow 1$	0.18 ± 0.07	0.38 ± 0.08	0.41 ± 0.51
	N_2H^+	$1 \rightarrow 0$	2.49 ± 0.07	0.44 ± 0.05	1.65 ± 0.10
TMC 1-CP (P1)	DCN	$1 \rightarrow 0$	0.85 ± 0.13	0.49 ± 0.03	1.14 ± 0.44
		$2 \rightarrow 1$	0.23 ± 0.04	0.33 ± 0.12	0.10 ± 0.73
	N_2H^+	$1 \rightarrow 0$	2.48 ± 0.09	0.42 ± 0.06	1.27 ± 0.11
TMC 1-CP (P2)	DCN	$1 \rightarrow 0$	0.86 ± 0.14	0.52 ± 0.04	1.07 ± 0.49
		$2 \rightarrow 1$	0.50 ± 0.20	0.50 ± 0.04	2.22 ± 1.28
	N_2H^+	$1 \rightarrow 0$	2.38 ± 0.01	0.42 ± 0.03	1.34 ± 0.06

6.9.4 Collapse models, abundance predictions, and observations.

In this section we show the observed abundances of DNC, DCN, CS, N_2H^+, and N_2D^+ at the positions in Table 6.2, and their predicted values according to the collapse models BES1, BES4, and AD presented in Section 9.

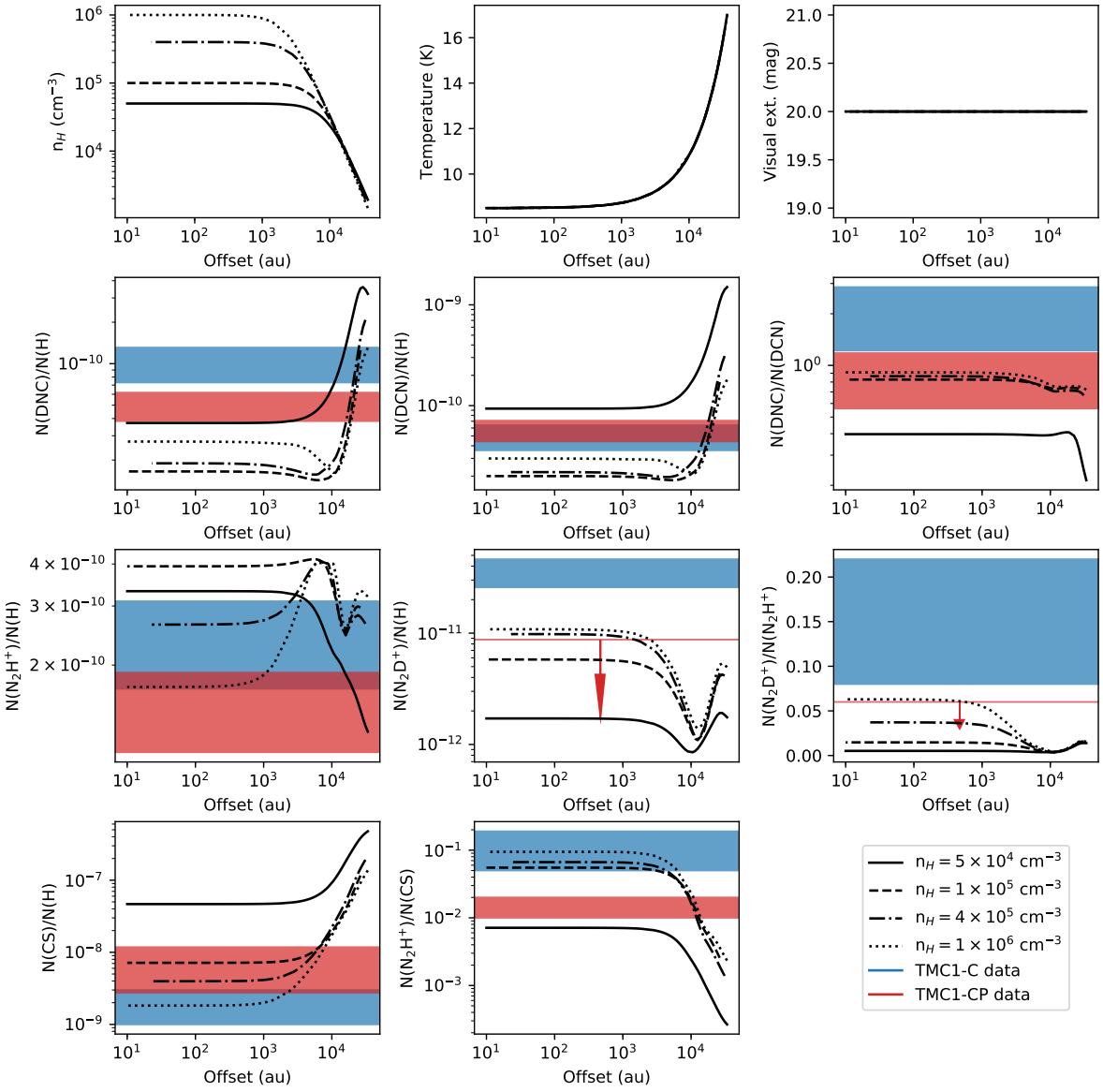

Figure 6.8: Predicted abundances along the line of sight (black) of the different BES1 collapse models with densities 5×10^4 (solid), 10^5 (dashed), 4×10^5 (dot-dashed), and 1×10^6 cm^{-3} (dotted). The observational data at the center of the starless cores are plotted in blue (TMC 1-C) and red (TMC 1-CP). The arrows indicate upper bounds.

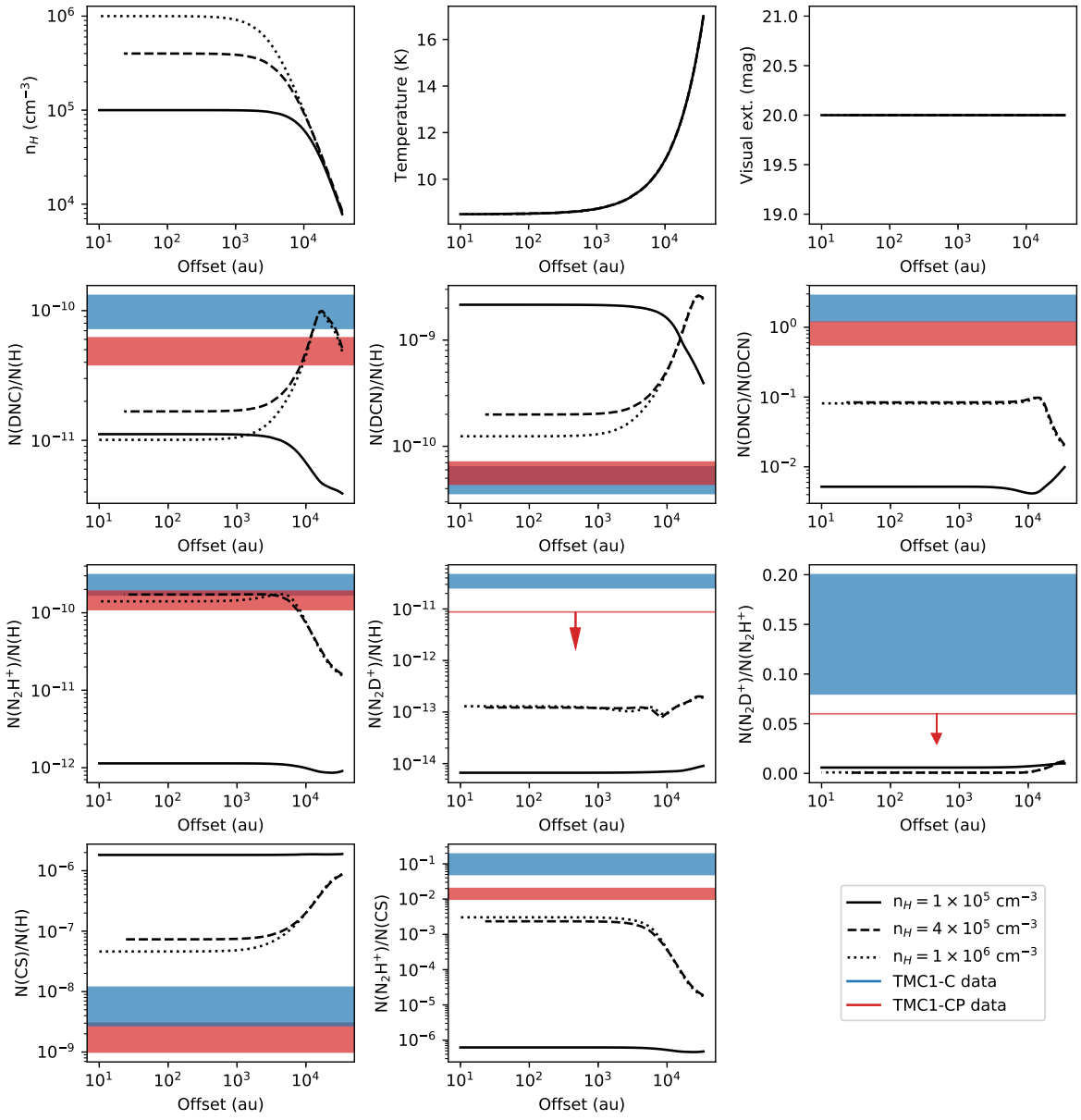

Figure 6.9: Predicted abundances (black) of the different BES4 collapse models with densities 10^5 (solid), 4×10^5 (dashed), and 1×10^6 cm^{-3} (dotted). The observational data at the center of the starless cores are plotted in blue (TMC 1-C) and red (TMC 1-CP). The arrows indicate upper bounds.

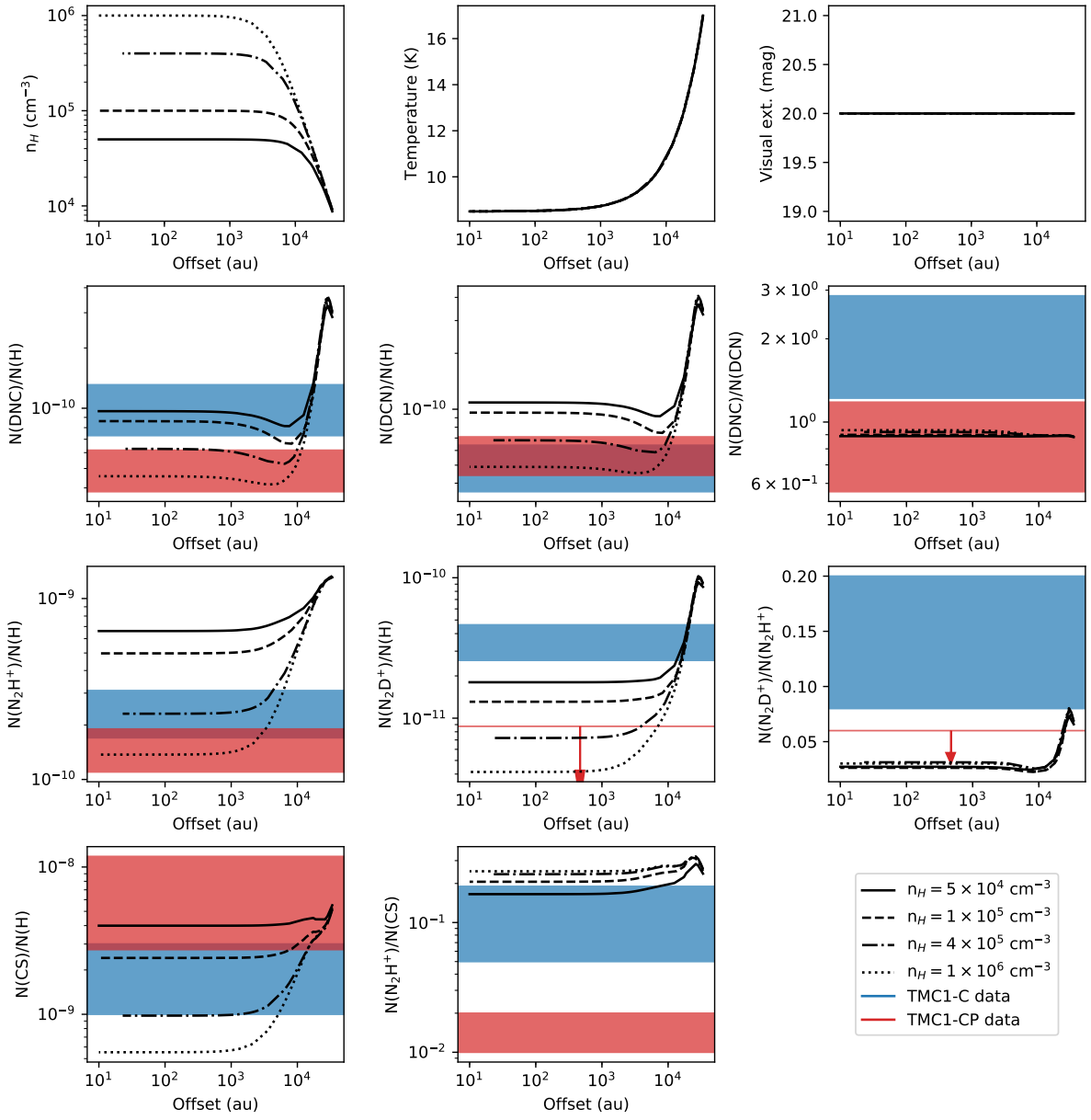

Figure 6.10: Predicted abundances (black) of the different AD collapse models with densities 5×10^4 (solid), 10^5 (dashed), 4×10^5 (dot-dashed), and 1×10^6 cm^{-3} (dotted). The observational data at the center of the starless cores are plotted in blue (TMC 1-C) and red (TMC 1-CP). The arrows indicate upper bounds.

Conclusions and future prospects

In this thesis we have explored the relationship between the chemistry of star-forming regions and their dynamics and evolution. In this relationship, the elemental depletions play a crucial role. The estimation of these quantities is not, however, straightforward, and could reveal pitfalls in our understanding of the chemistry in these regions. Sulfur chemistry is a primary example of this, with surface reactions playing an important role in the sulfur-bearing molecular make up of gas and ices. With a constrained chemistry, deuteration offers the possibility of exploring the evolutionary stage of pre-stellar cores and study their chemical evolution through time. This is key to understanding the chemical composition of young stellar objects and, ultimately, planetary systems.

We have concluded that:

- Sulphur depletion in Taurus: the estimation of fractional abundances and their comparison with chemical models provides insight about the elemental depletion factors and, consequently, about the ionization degree of the gas. Our chemical study of the prototypical TMC 1 filament shows that sulfur is depleted by factor of 10 even in the translucent region. This means that 90% of Sulphur is incorporated to grains during the transition between the diffuse gas and the translucent cloud, more likely due to electrostatic forces between grains (negatively charged) and S^+ ion.

- We analyze the emission of the H_2S molecule, a molecule only formed on dust surfaces through association of Sulfur with H atoms. The chemical modeling of TMC 1 and Barnard 1b filaments allows us to conclude that H_2S is the main sulfur reservoir on ices and is released to the gas-phase via chemical desorption. The gas-phase abundances of this molecule are sensitive to the changes in chemical desorption efficiency expected to happen when ice mantles build up. This is of great interest for the study of the grain properties since the H_2S abundance would trace the formation of thick ice mantles in molecular clouds.

- The chemical composition of pre-stellar cores is influenced by their evolutionary stage. The paradigmatic example of this is the enhancement of deuterated compounds. The emission of deuterated molecules is used to trace the inner, dense gas expected in the pre-stellar cores TMC 1-C and TMC 1-CP. The estimation of fractional abundances and the deuteration fraction, and the comparison with collapse models let us conclude that TMC 1-C is more evolved than TMC 1-CP. Moreover, we derived a cosmic ray ionization rate of $\zeta = 10^{-17}$ s^{-1}, which is one order of magnitude lower than that estimated in the

translucent part of TMC1, thus demonstrating the decrease of the cosmic ray flux with the visual extinction.

These results offer answers to some important questions in the current picture of the chemistry of star-forming regions. While doing so, they open new lines of research.

Chemical desorption efficiency and correlations

The data presented in Chapter 5, while covering a wide range of visual extinctions, is sparsely distributed near the transition zone where ices would start building up and, consequently, the desorption efficiency starts to drop. An accepted proposal for the IRAM 30m telescope is intended to deal with this issue, providing more data towards this zone.

At the same time, it would be interesting to look for more evidence to the ability of gas-phase abundances of H_2S to trace changes in the surface composition. Spectroscopic observations of methanol, a molecule that, like H_2S, is only formed efficiently over grain surfaces by hydrogenation of the frozen CO would be also useful. Comparing the evolution of the abundances of these two molecules at different extinctions with chemical models and different chemical desorption schemes would provide a more precise location of the transition zone where ice layers begin to deposit over grain surfaces. Furthermore, we could quantify the variation in the efficiency of desorption as a function of the extinction, a parameterization of great interest in future chemical studies.

High angular resolution study of pre-stellar cores

The treatment of the physical structure of pre-stellar cores has been simple, assuming spherical symmetry and a Bonnor-Ebert-like density profile. Aimed at a more realistic modeling of the pre-stellar cores in TMC 1, we submitted proposals to study the continuum emission of the cores with the 3mm MUSTANG2 camera in the Green Bank Telescope (USA). Such maps of TMC 1-C and TMC 1-CP are shown in Figure 6.11 and, as it can be readily seen, the TMC 1-C and TMC 1-CP presents different morphologies more likely related to their different evolutionary stages.

A recently accepted proposal for NOEMA is aimed at performing interferometric observations of the molecular emission coming from TMC 1-C and TMC 1-CP to determine their morphology, kinematics, and chemistry, as they show significant chemical differences coming from different evolutionary stages, as presented in this thesis. In the near future, our goal is improving our understanding of the chemistry at the earliest stages in the formation of a star with observations towards TMC 1 and new high angular resolution observations towards pre-stellar cores in different star-forming regions.

Observations at 1mm and 2mm using NIKA2 in the 30m telescope have already been carried out. The combination of these images with those at 3mm, will provide information on the grain sizes to investigate possible grain growth in pre-stellar cores. The combination of these results with NOEMA images will be eventually used to investigate the interplay between grain growth and the gas-phase chemical composition.

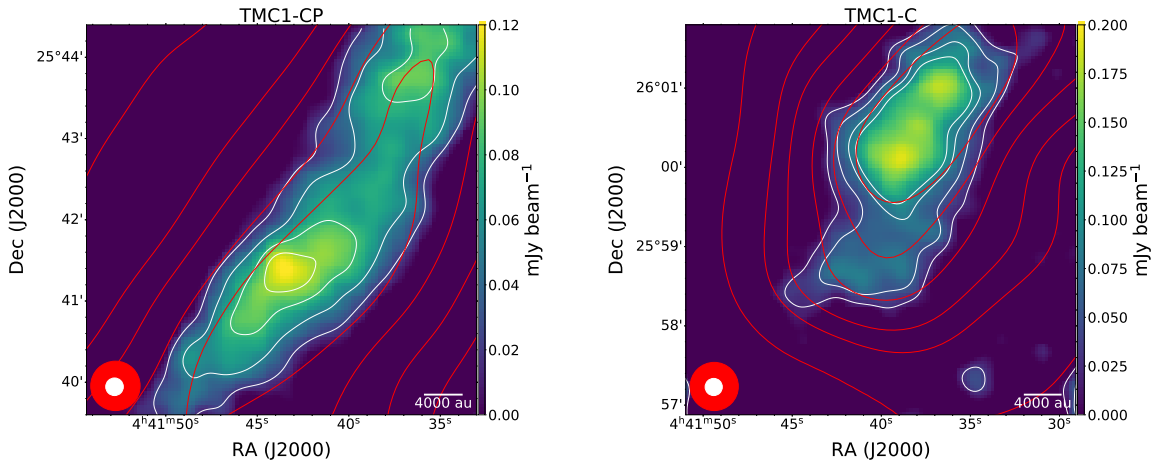

Figure 6.11: Continuum maps at 3 mm of the pre-stellar cores TMC 1-C (right) and TMC 1-CP (left) obtained with the MUSTANG-2 instrument (white contours). Herschel contours (in red) are overplotted. Note the presence of substructure in the TMC 1-C core.

Chemical evolution and magnetohydrodynamical simulations

The treatment of collapse in this thesis has been very simple, disregarding some of the effects the magnetic fields have in this process. Current models of interaction between magnetic fields and matter even include non-ideal magnetohydrodynamical features, believed to be of fundamental importance in the formation of young stellar objects.

MHD simulations offer an immediate improvement over the collapse models used here. These simulations allow leaving out commonly used assumptions like Bonnor-Ebert density profiles or sphericity of the core under collapse. So far, I have developed an interface between the chemical model Nautilus and the RAMSES MHD code (Fromang et al. 2005) that takes advantage of parallel computing in computer grids. From the RAMSES code I have extracted the physical and dynamical information in trajectories of time, density, extinction, and temperature of each one of the 10^6 particles inside the simulation. These trajectories yield a chemical evolution using the Nautilus code.

Our next goal is to classify particles in the different regions of a young stellar object: core, envelope, disk, pseudo-disk, and outflow, to perform a study of chemical differentiation between regions. Finally, these chemical abundances will be post-processed using RADMC-3D code to obtain maps and spectra of the different regions, offering an excellent tool to understand the chemistry of young stellar objects and better interpret observations.

Conclusiones y perspectivas futuras

En esta tesis hemos explorado la relación entre la química, dinámica y evolución de regiones de formación estelar. En esta relación las depleciones elementales juegan un importante papel. Sin embargo, la determinación de estas cantidades no es evidente y puede revelar limitaciones en nuestro conocimiento de estas regiones. La química del azufre es un claro ejemplo de esto, donde las reacciones sobre la superficie de los granos son responsables de la composición sólida y gaseosa de compuestos azufrados. Una vez entendidos los procesos químicos que tienen lugar en las regiones de formación estelar, la deuteración de moléculas ofrece la posibilidad de explorar el estado evolutivo de las zonas de interés y así establecer la evolución química de objetos pre-estelares. Esto es clave para entender la composición química de los futuros objetos protoestelares y sistemas planetarios.

A lo largo de la tesis hemos concluido:

- Depleción de azufre en la nube molecular de Tauro: la estimación de abundancias químicas de diferentes compuestos y su comparación con modelos químicos proporciona información sobre las depleciones elementales y, por tanto, sobre el grado de ionización del gas. El estudio de la región de formación estelar TMC 1 muestra que el azufre está depletado en un factor 10 incluso en la región traslúcida de la nube. Esto significa que el 90% del azufre se deposita sobre la superficie de los granos en la transición entre el gas difuso y el régimen traslúcido. Esto puede ser el resultado de la atracción electrostática entre iones de azufre S^+ y los granos de polvo (negativamente cargados).

- Analizamos la emisión de la molécula H_2S, una molécula que sólo se forma sobre la superficie de los granos mediante la asociación del azufre con átomos de hidrógeno. El modelado químico de los filamentos moleculares TMC 1 y Barnard 1b permite concluir que H_2S es el principal reservorio de azufre en los hielos y es liberado al gas principalmente mediante desorción química. La abundancia gaseosa de esta molécula parece ser sensible a los cambios en la eficiencia de desorción que se espera que ocurran cuando la superficie de los granos se empieza a cubrir de hielo. Esto es de gran interés para el estudio de las propiedades de los granos ya que H_2S estaría por tanto trazando la formación de hielo en nubes moleculares.

- La composición química de núcleos pre-estelares está influenciada por su estado evolutivo. El ejemplo paradigmático de esta afirmación se encuentra en el incremento de

compuestos deuterados. La emisión de moléculas deuteradas se emplea para caracterizar el gas denso que se espera en el interior de las condensaciones pre-estelares TMC 1-C y TMC 1-CP. La estimación de abundancias, la fracción de deuteración, y su comparación con modelos químicos nos permite concluir que TMC 1-C es más evolucionado que TMC 1-CP. Además, este estudio confirma el decrecimiento de la tasa de ionización por rayos cósmicos con la extinción en el interior de los núcleos a $\zeta = 10^{-17}$ s^{-1}, un orden de magnitud inferior a lo que se estima en las zonas difusas de TMC 1.

Estos resultados ofrecen respuestas a algunos problemas importantes en el conocimiento de la química en regiones de formación estelar. Además abren nuevas líneas de investigación

La eficiencia de desorción química y correlaciones

Los datos presentados en el Capítulo 5, si bien cubren un rango amplio de extinciones visuales, estos están dispersamente distribuidos cerca de la zona de transición, donde se empiezan a depositar hielos y por tanto, la eficiencia de desorción química disminuye. Una propuesta aceptada para el telescopio IRAM 30m busca solucionar esta problemática aportando más datos en la zona de transición.

A la vez, estos datos persiguen proporcionar más evidencia sobre la capacidad de la abundancia gaseosa de H_2S de trazar los cambios que se producen en la superficie de los granos. Observaciones espectroscópicas de metanol, una molécula que, al igual que H_2S, sólo se forma eficientemente mediante reacciones químicas de superficie al hidrogenar hielo de CO, serían útiles para este propósito. Comparando las abundancias de las dos moléculas a diferentes extinciones con modelos químicos ayudaría a restringir la localización de la zona de transición. Además, se podría cuantificar la variación de las eficiencias de desorción con la extinción, una parametrización de gran interés para futuros estudios químicos.

Estudios en alta resolución de núcleos pre-estelares

El tratamiento de la estructura física de las condensaciones pre-estelares que se ha hecho a lo largo de la tesis ha sido simple, asumiendo siempre simetría esférica y perfiles de densidad tipo Bonnor-Ebert. Con el objetivo de una modelización más realista de estas regiones, preparamos propuestas de observación para la emisión de contínuo a 3 mm con la cámara MUSTANG2 del telescopio de Green Bank (Virginia Occidental - EEUU). Los mapas correspondientes a los núcleos TMC 1-C and TMC 1-CP se muestran en la Figura 6.12 y, como se puede observar, presentan diferentes morfologías que pueden relacionarse con su diferente estado evolutivo.

Una propuesta recientemente aprobada para el interferómetro NOEMA está dedicada a la observación en alta resolución de la emisión molecular de TMC 1-C and TMC 1-CP para así determinar su morfología, cinemática y química, ya que presentan diferencias químicas significativas, como se ha mostrado aquí. En el futuro próximo, nuestro objetivo es mejorar nuestro entendimiento de la química en los primeros momentos de la formación de una estrella con observaciones de TMC 1 y nuevas observaciones en alta resolución de núcleos pre-estelares en otras regiones de formación estelar.

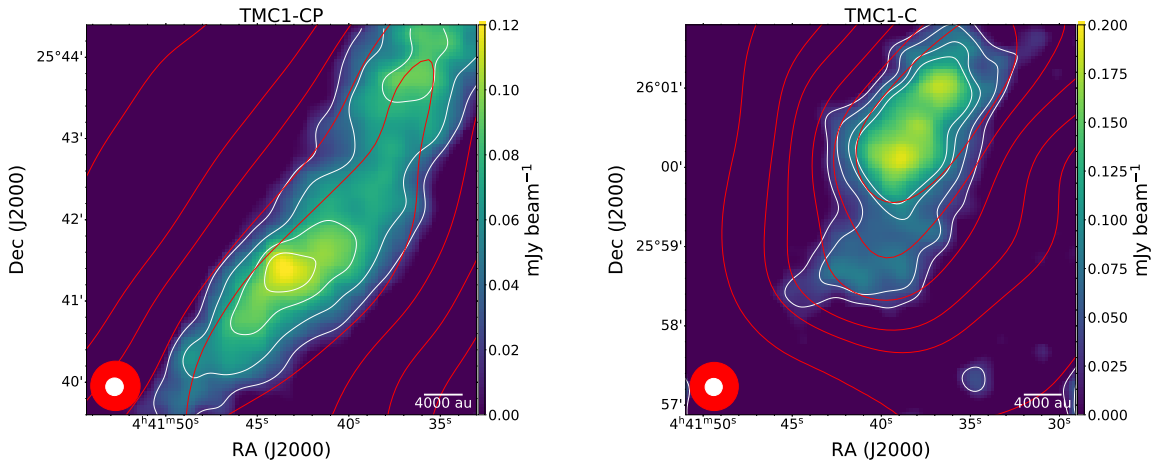

Figure 6.12: Mapas de continuo a 3 mm de los núcleos pre-estelares TMC 1-C (derecha) y TMC 1-CP (izquierda) obtenidos con el instrumento MUSTANG-2 (curvas de nivel blancas). Superpuestos se representan además los contornos del telescopio Herschel en rojo.

Adicionalmente se tienen observaciones de contínuo a 1 y 2 mm utilizando la cámara NIKA2 del telescopio IRAM 30m. La combinación de estas imágenes con las de 3 mm proporcionarán información sobre el tamaño de los granos de polvo para investigar su posible crecimiento hacia el interior de los núcleos pre-estelares. La combinación de estos resultados con las imágenes de NOEMA se utilizarán para investigar la relación entre crecimiento del polvo y la composición química.

Evolución química y simulaciones magneto-hidrodinámicas

El tratamiento del colapso en esta tesis ha sido sencillo, ignorando algunos de los efectos que los campos magnéticos tienen en el proceso. Modelos actuales de interacción entre campos magnéticos y materia incluyen fenómenos de magnetohidrodinámica (MHD) no ideales, que se cree que juegan un papel fundamental en la formación de estructuras en objetos estelares jóvenes.

Simulaciones MHD ofrecen ventajas inmediatas frente a los modelos de colapso utilizados aquí. Estas simulaciones permiten dejar fuera asunciones como la esfericidad del objeto o la presencia de un perfil de densidad tipo Bonnor-Ebert. Por el momento, he desarrollado una interfaz que permite utilizar el modelo químico Nautilus con los datos resultantes de una simulación con el código RAMSES (Fromang et al. 2005), que aprovecha la computación paralela de las redes de supercomputadores. A partir de los resultados de RAMSES, he extraído la información física y dinámica en trayectorias de tiempo, densidad, extinción y temperatura de cada una de las 10^6 partículas trazadoras que componen la simulación. Cada trayectoria produce una evolución química utilizando el modelo químico Nautilus.

Nuestro siguiente objetivo es el de la clasificación de partículas trazadoras en las diferentes regiones en las que se compone un objeto estelar joven: núcleo, envoltura, disco, pseudo-disco y outflows. Así, se podrá hacer un estudio de diferenciación química entre regiones. Finalmente, estas abundancias químicas y su distribución espacial serán post-

procesadas mediante transferencia radiativa para obtener mapas sintéticos. Estos mapas serán una excelente herramienta para entender mejor la química de estos objetos e interpretar observaciones.

Publications

Publications as first author

- **Navarro-Almaida, D., Le Gal, R., Fuente, A. et al.** ***Gas phase Elemental abundances in Molecular cloudS (GEMS). II. On the quest for the sulphur reservoir in molecular clouds: the H_2S case,*** **2020, A&A, 637, A39.**
- **Navarro-Almaida, D., Fuente, A., Majumdar, L., et al.** ***Evolutionary view through the starless cores in Taurus: deuteration in TMC 1,*** **2021, A&A, 653, A15.**

Publications as co-author

- Fuente, A., Navarro-Almaida, D., Caselli, P., et al. *Gas phase Elemental abundances in Molecular cloudS (GEMS). I. The prototypical dark cloud TMC 1*, 2019, A&A, 624, A105.
- Fuente, A., Treviño-Morales, S.P., Le Gal, R., et al. *Gas kinematics of key prebiotic molecules in GV Tau N revealed with an ALMA, PdBI, and Herschel synergy,* 2020, MNRAS, 496, 5330.
- Rivière-Marichalar, P., Fuente, A., Le Gal, R., et al. *AB Aur, a Rosetta stone for studies of planet formation. I. Chemical study of a planet-forming disk,* 2020, A&A, 642, A32.
- Bulut, N., Roncero, O., Aguado, A., et al. *Gas phase Elemental abundances in Molecular cloudS (GEMS). III. Unlocking the CS chemistry: the CS+O reaction,* 2021, A&A, 646, A5.
- Rodríguez-Baras, M., Fuente, A., Rivière-Marichalar, P., et al. *Gas phase Elemental abundances in Molecular cloudS (GEMS). IV. Observational results and statistical trends,* 2021, A&A, 648, A120.
- Rivière-Marichalar, P., Fuente, A., Le Gal, R., et al. *H_2S observations in young stellar disks in Taurus*, 2021, A&A, 652, A46.
- Wakelam, V., Dartois, E., Chabot, M., et al. *Efficiency of non-thermal desorptions in cold-core conditions. Testing the sputtering of grain mantles induced by cosmic rays*, 2021, A&A, 652, A63.
- Fuente, A., Treviño-Morales, S. P., et al., *Probing the kinematics and chemistry of the hot core Mon R2 IRS 3 using ALMA observations*, 2021, MNRAS, 507, 1886.

- Spezzano, S., Fuente, A., Caselli, P., et al., *Gas phase Elemental abundances in Molecular cloudS (GEMS) V. Methanol in Taurus*, accepted to A&A.
- Cazaux, S., Carrascosa, H., Muñoz-Caro, G. M., et al., *Photoprocessing of H_2S on dust grains: building S chains in translucent clouds and comets*, accepted to A&A.

Bibliography

"... y así, del poco dormir y del mucho leer, se le secó el cerebro de manera que vino a perder el juicio."

El Ingenioso Hidalgo Don Quijote de La Mancha - Miguel de Cervantes

Adams, F. C., Lada, C. J., & Shu, F. H. 1987, ApJ, 312, 788

Agúndez, M. & Wakelam, V. 2013, Chemical Reviews, 113, 8710

Aikawa, Y. & Herbst, E. 1999, A&A, 351, 233

Aikawa, Y., Herbst, E., Roberts, H., & Caselli, P. 2005, ApJ, 620, 330

Aikawa, Y., Ohashi, N., Inutsuka, S.-i., Herbst, E., & Takakuwa, S. 2001, ApJ, 552, 639

Aikawa, Y., Wakelam, V., Garrod, R. T., & Herbst, E. 2008, ApJ, 674, 984

Allen, C. W. 1973, Astrophysical quantities

Alonso-Albi, T., Fuente, A., Crimier, N., et al. 2010, A&A, 518, A52

Anderson, D. E., Bergin, E. A., Maret, S., & Wakelam, V. 2013, ApJ, 779, 141

André, P. 1994, in The Cold Universe, ed. T. Montmerle, C. J. Lada, I. F. Mirabel, & J. Tran Thanh Van, 179

André, P., Men'shchikov, A., Bontemps, S., et al. 2010, A&A, 518, L102

Andrews, S. M. & Williams, J. P. 2005, The Astrophysical Journal, 631, 1134

Andrews, S. M. & Williams, J. P. 2007, ApJ, 659, 705

Audit, E. & Hennebelle, P. 2005, A&A, 433, 1

Bachiller, R., Guilloteau, S., & Kahane, C. 1987, A&A, 173, 324

Bachiller, R., Martin-Pintado, J., & Fuente, A. 1991, A&A, 243, L21

Bachiller, R., Menten, K. M., & del Rio Alvarez, S. 1990, A&A, 236, 461

Bachiller, R. & Pérez Gutiérrez, M. 1997, ApJ, 487, L93

Bacmann, A., Lefloch, B., Ceccarelli, C., et al. 2002, A&A, 389, L6

Bacmann, A., Lefloch, B., Ceccarelli, C., et al. 2003, ApJ, 585, L55

Bacmann, A., Taquet, V., Faure, A., Kahane, C., & Ceccarelli, C. 2012, A&A, 541, L12

Ballester, M. & Varandas, A. 2007, Chemical Physics Letters, 433, 279

Ballester, M. Y., Orozco-Gonzalez, Y., Garrido, J. D., & Dos Santos, H. F. 2010, J. Chem. Phys., 132, 044310

Ballester, M. Y. & Varandas, A. J. C. 2005, Phys. Chem. Chem. Phys., 7, 2305

Ballesteros-Paredes, J., André, P., Hennebelle, P., et al. 2020, Space Sci. Rev., 216, 76

Balsiger, H., Altwegg, K., Bochsler, P., et al. 2007, Space Sci. Rev., 128, 745

Basu, S. & Mouschovias, T. C. 1994, ApJ, 432, 720

Bates, D. R. 1951, MNRAS, 111, 303

Bates, D. R. & Herbst, E. 1988, Radiative Association, ed. T. J. Millar & D. A. Williams, Vol. 146, 17

Beckwith, S. V. W., Sargent, A. I., Chini, R. S., & Guesten, R. 1990, AJ, 99, 924

Ben Abdallah, D., Najar, F., Jaidane, N., Dumouchel, F., & Lique, F. 2012, MNRAS, 419, 2441

Bergin, E., Calvet, N., D'Alessio, P., & Herczeg, G. J. 2003, ApJ, 591, L159

Bergin, E. A. 2003, in SFChem 2002: Chemistry as a Diagnostic of Star Formation, ed. C. L. Curry & M. Fich, 63

Bergin, E. A. 2004, in The Dense Interstellar Medium in Galaxies, ed. S. Pfalzner, C. Kramer, C. Staubmeier, & A. Heithausen, Vol. 91, 453

Bergin, E. A., Alves, J., Huard, T., & Lada, C. J. 2002, ApJ, 570, L101

Bergin, E. A. & Langer, W. D. 1997, ApJ, 486, 316

Berkhuijsen, E. M., Mitra, D., & Mueller, P. 2006, Astronomische Nachrichten, 327, 82

Bernard, J.-P., Paradis, D., Marshall, D. J., et al. 2010, A&A, 518, L88

Bettens, R. P. A. & Herbst, E. 1996, ApJ, 468, 686

Biver, N., Moreno, R., Bockelée-Morvan, D., et al. 2016, A&A, 589, A78

Black, J. H. 2000, in From Molecular Clouds to Planetary, ed. Y. C. Minh & E. F. van Dishoeck, Vol. 197, 81

Black, J. H. & Dalgarno, A. 1973, Astrophys. Lett., 15, 79

Blitz, L., Fukui, Y., Kawamura, A., et al. 2007, in Protostars and Planets V, ed. B. Reipurth, D. Jewitt, & K. Keil, 81

Blitz, L. & Shu, F. H. 1980, ApJ, 238, 148

Blitz, M. A., McKee, K. W., & Pilling, M. J. 2000, Proceedings of the Combustion Institute, 28, 2491

Bockelée-Morvan, D. & Biver, N. 2017, Philosophical Transactions of the Royal Society A: Mathematical, Physical and Engineering Sciences, 375, 20160252

Bockelée-Morvan, D., Lis, D. C., Wink, J. E., et al. 2000, A&A, 353, 1101

Boissier, J., Bockelée-Morvan, D., Biver, N., et al. 2007, A&A, 475, 1131

Bonnell, I. A., Bate, M. R., Clarke, C. J., & Pringle, J. E. 2001, MNRAS, 323, 785

Bonnor, W. B. 1956, MNRAS, 116, 351

Boogert, A. C. A., Pontoppidan, K. M., Knez, C., et al. 2008, ApJ, 678, 985

Boogert, A. C. A., Schutte, W. A., Helmich, F. P., Tielens, A. G. G. M., & Wooden, D. H. 1997, A&A, 317, 929

Booth, A. S., van der Marel, N., Leemker, M., van Dishoeck, E. F., & Ohashi, S. 2021, A&A, 651, L6

Bowyer, C. S., Field, G. B., & Mack, J. E. 1968, Nature, 217, 32

Bron, E., Daudon, C., Pety, J., et al. 2018, A&A, 610, A12

Bulut, N., Roncero, O., Aguado, A., et al. 2021, A&A, 646, A5

Calmonte, U., Altwegg, K., Balsiger, H., et al. 2016, MNRAS, 462, S253

Cambrésy, L. 1999, A&A, 345, 965

Carter, M., Lazareff, B., Maier, D., et al. 2012, A&A, 538, A89

Caselli, P. 2002, Planet. Space Sci., 50, 1133

Caselli, P. & Ceccarelli, C. 2012, A&A Rev., 20, 56

Caselli, P., Walmsley, C. M., Tafalla, M., Dore, L., & Myers, P. C. 1999, ApJ, 523, L165

Caselli, P., Walmsley, C. M., Terzieva, R., & Herbst, E. 1998, ApJ, 499, 234

Caselli, P., Walmsley, C. M., Zucconi, A., et al. 2002a, ApJ, 565, 331

Caselli, P., Walmsley, C. M., Zucconi, A., et al. 2002b, ApJ, 565, 344

Casoli, F. & Combes, F. 1982, A&A, 110, 287

Ceccarelli, C., Caselli, P., Bockelée-Morvan, D., et al. 2014, in Protostars and Planets VI, ed. H. Beuther, R. S. Klessen, C. P. Dullemond, & T. Henning, 859

Cernicharo, J., Agúndez, M., Cabezas, C., et al. 2021a, A&A, 649, L15

Cernicharo, J., Cabezas, C., Endo, Y., et al. 2021b, A&A, 650, L14

Cernicharo, J. & Guelin, M. 1987, A&A, 176, 299

Cernicharo, J., Marcelino, N., Roueff, E., et al. 2012, ApJ, 759, L43

Cernicharo, J., Thum, C., Hein, H., et al. 1990, A&A, 231, L15

Chacón-Tanarro, A., Caselli, P., Bizzocchi, L., et al. 2019, A&A, 622, A141

Charnley, S. B. 1997, ApJ, 481, 396

Chen, H.-R., Liu, S.-Y., Su, Y.-N., & Wang, M.-Y. 2011, ApJ, 743, 196

Chiang, H.-F., Looney, L. W., Tassis, K., Mundy, L. G., & Mouschovias, T. C. 2008, ApJ, 680, 474

Choi, M., Evans, Neal J., I., Gregersen, E. M., & Wang, Y. 1995, ApJ, 448, 742

Choi, M., Tatematsu, K., & Kang, M. 2010, ApJ, 723, L34

Choi, M., Tatematsu, K., Park, G., & Kang, M. 2007, ApJ, 667, L183

Codella, C., Ceccarelli, C., Bottinelli, S., et al. 2012, ApJ, 744, 164

Crapsi, A., Caselli, P., Walmsley, C. M., et al. 2005, ApJ, 619, 379

Crockett, N. R., Bergin, E. A., Neill, J. L., et al. 2014, ApJ, 781, 114

Dalgarno, A. 1988, Astrophysical Letters and Communications, 26, 153

Dalgarno, A. 2006, Proceedings of the National Academy of Sciences, 103, 12269

Dalgarno, A. & Lepp, S. 1984, ApJ, 287, L47

Daniel, F., Cernicharo, J., Roueff, E., Gerin, M., & Dubernet, M. L. 2007, ApJ, 667, 980

Daniel, F., Faure, A., Pagani, L., et al. 2016, A&A, 592, A45

Daniel, F., Gérin, M., Roueff, E., et al. 2013, A&A, 560, A3

Dapp, W. B. & Basu, S. 2009, MNRAS, 395, 1092

Dartois, E., Dutrey, A., & Guilloteau, S. 2003, A&A, 399, 773

de Jong, T., Boland, W., & Dalgarno, A. 1980, A&A, 91, 68

de Jong, T., Chu, S., & Dalgarno, A. 1975, ApJ, 199, 69

Denis-Alpizar, O., Stoecklin, T., Guilloteau, S., & Dutrey, A. 2018, MNRAS, 478, 1811

Denis-Alpizar, O., Stoecklin, T., Halvick, P., & Dubernet, M.-L. 2013, J. Chem. Phys., 139, 204304

Dickey, J. M., Salpeter, E. E., & Terzian, Y. 1978, ApJS, 36, 77

Dickman, R. L. 1978, ApJS, 37, 407

Dobashi, K., Shimoikura, T., Nakamura, F., et al. 2018, ApJ, 864, 82

Dobbs, C. L. & Pringle, J. E. 2013, MNRAS, 432, 653

Dorta-Urra, A., Zanchet, A., Roncero, O., & Aguado, A. 2015, J. Chem. Phys., 142, 154301

Douglas, A. E. & Herzberg, G. 1941, ApJ, 94, 381

Draine, B. T. 1978, ApJS, 36, 595

Draine, B. T. 2003, Annual Review of Astronomy and Astrophysics, 41, 241

Dubernet, M.-L., Daniel, F., Grosjean, A., & Lin, C. Y. 2009, A&A, 497, 911

Duley, W. W., Millar, T. J., & Williams, D. A. 1980, MNRAS, 192, 945

Dulieu, F., Congiu, E., Noble, J., et al. 2013, Scientific Reports, 3, 1338

Dullemond, C. P., Juhasz, A., Pohl, A., et al. 2012, RADMC-3D: A multi-purpose radiative transfer tool

Dumouchel, F., Faure, A., & Lique, F. 2010, MNRAS, 406, 2488

Dutrey, A., Guilloteau, S., & Bachiller, R. 1997, A&A, 325, 758

Dutrey, A., Guilloteau, S., Duvert, G., et al. 1996, A&A, 309, 493

Dutrey, A., Henning, T., Guilloteau, S., et al. 2007, A&A, 464, 615

Ebisawa, Y., Sakai, N., Menten, K. M., & Yamamoto, S. 2019, ApJ, 871, 89

Elias, J. H. 1978, ApJ, 224, 857

Elmegreen, B. G. 1987, ApJ, 312, 626

Emprechtinger, M., Caselli, P., Volgenau, N. H., Stutzki, J., & Wiedner, M. C. 2009, A&A, 493, 89

Engargiola, G., Plambeck, R. L., Rosolowsky, E., & Blitz, L. 2003, ApJS, 149, 343

Esplugues, G., Cazaux, S., Caselli, P., Hocuk, S., & Spaans, M. 2019, MNRAS, 486, 1853

Esplugues, G. B., Cazaux, S., Meijerink, R., Spaans, M., & Caselli, P. 2016, A&A, 591, A52

Esplugues, G. B., Viti, S., Goicoechea, J. R., & Cernicharo, J. 2014, A&A, 567, A95

Evans, A. 1993, The dusty universe.

Ewen, H. I. & Purcell, E. M. 1951, Nature, 168, 356

Fair, R. W. & Thrush, B. A. 1969, Trans. Faraday Soc., 65, 1557

Federman, S. R., Lambert, D. L., Sheffer, Y., et al. 2003, ApJ, 591, 986

Fehér, O., Tóth, L. V., Ward-Thompson, D., et al. 2016, A&A, 590, A75

Ferrière, K. M. 2001, Reviews of Modern Physics, 73, 1031

Fiedler, R. A. & Mouschovias, T. C. 1993, ApJ, 415, 680

Flower, D. R. 1999, MNRAS, 305, 651

Flower, D. R., Pineau Des Forêts, G., & Walmsley, C. M. 2006, A&A, 449, 621

Fontani, F., Busquet, G., Palau, A., et al. 2015, A&A, 575, A87

Foreman-Mackey, D., Hogg, D. W., Lang, D., & Goodman, J. 2013, PASP, 125, 306

Friesen, R. K., Pineda, J. E., co-PIs, et al. 2017, ApJ, 843, 63

Fromang, S., Hennebelle, P., & Teyssier, R. 2005, in SF2A-2005: Semaine de l'Astrophysique Francaise, ed. F. Casoli, T. Contini, J. M. Hameury, & L. Pagani, 743

Fuchs, G. W., Cuppen, H. M., Ioppolo, S., et al. 2009, A&A, 505, 629

Fuente, A., Cernicharo, J., Agúndez, M., et al. 2010, A&A, 524, A19

Fuente, A., Cernicharo, J., Roueff, E., et al. 2016, A&A, 593, A94

Fuente, A., Goicoechea, J. R., Pety, J., et al. 2017, ApJ, 851, L49

Fuente, A., Navarro, D. G., Caselli, P., et al. 2019, A&A, 624, A105

Fuller, G. A., Myers, P. C., Welch, W. J., et al. 1991, ApJ, 376, 135

Galli, D. & Padovani, M. 2015, arXiv e-prints, arXiv:1502.03380

Galli, P. A. B., Loinard, L., Ortiz-Léon, G. N., et al. 2018, ApJ, 859, 33

Garrod, R., Hee Park, I., Caselli, P., & Herbst, E. 2006, Faraday Discuss., 133, 51

Garrod, R. T. 2013, ApJ, 765, 60

Garrod, R. T. & Pauly, T. 2011, ApJ, 735, 15

Garrod, R. T., Wakelam, V., & Herbst, E. 2007, A&A, 467, 1103

Geballe, T. R., Baas, F., Greenberg, J. M., & Schutte, W. 1985, A&A, 146, L6

Genzel, R. 1991, in NATO Advanced Study Institute (ASI) Series C, Vol. 342, The Physics of Star Formation and Early Stellar Evolution, ed. C. J. Lada & N. D. Kylafis, 155

Genzel, R., Ho, P. T. P., Bieging, J., & Downes, D. 1982, ApJ, 259, L103

Geppert, W. D., Hamberg, M., Thomas, R. D., et al. 2006, Faraday Discussions, 133, 177

Gerin, M., de Luca, M., Goicoechea, J. R., et al. 2010, A&A, 521, L16

Gerin, M., Neufeld, D. A., & Goicoechea, J. R. 2016, ARA&A, 54, 181

Gerlich, D. & Schlemmer, S. 2002, Planet. Space Sci., 50, 1287

Goicoechea, J. R. & Le Bourlot, J. 2007, A&A, 467, 1

Goicoechea, J. R., Pety, J., Gerin, M., et al. 2006, A&A, 456, 565

Goldsmith, P. F. 2001, ApJ, 557, 736

Goldsmith, P. F., Heyer, M., Narayanan, G., et al. 2008, ApJ, 680, 428

Goldsmith, P. F. & Langer, W. D. 1999, ApJ, 517, 209

Gonzalez-Alfonso, E. & Cernicharo, J. 1993, A&A, 279, 506

Gonzalez Garcia, M., Le Bourlot, J., Le Petit, F., & Roueff, E. 2008, A&A, 485, 127

Goodman, J. & Weare, J. 2010, Communications in Applied Mathematics and Computational Science, Vol. 5, No. 1, p. 65-80, 2010, 5, 65

Gould, R. J. & Salpeter, E. E. 1963, ApJ, 138, 393

Graedel, T. E., Langer, W. D., & Frerking, M. A. 1982, ApJS, 48, 321

Gratier, P., Majumdar, L., Ohishi, M., et al. 2016, ApJS, 225, 25

Grenier, I. A., Black, J. H., & Strong, A. W. 2015, Annual Review of Astronomy and Astrophysics, 53, 199

Griffin, M. J., Abergel, A., Abreu, A., et al. 2010, A&A, 518, L3

Grozdanov, T. P. & Solovev, E. A. 1982, Journal of Physics B Atomic Molecular Physics, 15, 1195

Gueth, F., Guilloteau, S., & Bachiller, R. 1998, A&A, 333, 287

Guilloteau, S., Piétu, V., Dutrey, A., & Guélin, M. 2006, A&A, 448, L5

Guilloteau, S., Reboussin, L., Dutrey, A., et al. 2016, A&A, 592, A124

Habing, H. J. 1968, Bull. Astron. Inst. Netherlands, 19, 421

Haffner, L. M., Dettmar, R. J., Beckman, J. E., et al. 2009, Reviews of Modern Physics, 81, 969

Hartmann, L., Ballesteros-Paredes, J., & Bergin, E. A. 2001, ApJ, 562, 852

Hasegawa, T. I. & Herbst, E. 1993, MNRAS, 263, 589

Hasegawa, T. I., Herbst, E., & Leung, C. M. 1992, ApJS, 82, 167

Hatchell, J., Millar, T. J., & Rodgers, S. D. 1998a, A&A, 332, 695

Hatchell, J., Richer, J. S., Fuller, G. A., et al. 2005, A&A, 440, 151

Hatchell, J., Thompson, M. A., Millar, T. J., & MacDonald, G. H. 1998b, A&AS, 133, 29

Heitsch, F., Hartmann, L. W., & Burkert, A. 2008, ApJ, 683, 786

Helmich, F. P., van Dishoeck, E. F., & Jansen, D. J. 1996, A&A, 313, 657

Hennebelle, P. & Pérault, M. 2000, A&A, 359, 1124

Herbst, E. & Klemperer, W. 1973, ApJ, 185, 505

Herbst, E., Lee, H. H., Howe, D. A., & Millar, T. J. 1994, MNRAS, 268, 335

Herbst, E. & Leung, C. M. 1990, A&A, 233, 177

Hernandez, A. K., Tan, J. C., Caselli, P., et al. 2011, ApJ, 738, 11

Hincelin, U., Commerçon, B., Wakelam, V., et al. 2016, ApJ, 822, 12

Hiramatsu, M., Hirano, N., & Takakuwa, S. 2010, ApJ, 712, 778

Hirano, N., Kamazaki, T., Mikami, H., Ohashi, N., & Umemoto, T. 1999, in Star Formation 1999, ed. T. Nakamoto, 181–182

Hocuk, S., Szűcs, L., Caselli, P., et al. 2017, A&A, 604, A58

Hogerheijde, M. R., van Dishoeck, E. F., Blake, G. A., & van Langevelde, H. J. 1997, ApJ, 489, 293

Holdship, J., Viti, S., Jimenez-Serra, I., et al. 2016, MNRAS, 463, 802

Hollenbach, D., Kaufman, M. J., Bergin, E. A., & Melnick, G. J. 2009, ApJ, 690, 1497

Hollenbach, D. J. 1990, in Astronomical Society of the Pacific Conference Series, Vol. 12, The Evolution of the Interstellar Medium, ed. L. Blitz, 167–181

Hollenbach, D. J., Takahashi, T., & Tielens, A. G. G. M. 1991, ApJ, 377, 192

Hollenbach, D. J., Werner, M. W., & Salpeter, E. E. 1971, ApJ, 163, 165

Hoyle, F. & Ellis, G. R. A. 1963, Australian Journal of Physics, 16, 1

Huang, Y.-H. & Hirano, N. 2013, ApJ, 766, 131

Huchtmeier, W. K. 1975, A&A, 45, 259

Huettemeister, S., Wilson, T. L., Bania, T. M., & Martin-Pintado, J. 1993, A&A, 280, 255

Indriolo, N. & McCall, B. J. 2012, ApJ, 745, 91

Irvine, W. M., Schloerb, F. P., Crovisier, J., Fegley, B., J., & Mumma, M. J. 2000, in Protostars and Planets IV, ed. V. Mannings, A. P. Boss, & S. S. Russell, 1159

Ivlev, A. V., Padovani, M., Galli, D., & Caselli, P. 2015, ApJ, 812, 135

Jacq, T., Walmsley, C. M., Henkel, C., et al. 1990, A&A, 228, 447

Jenkins, E. B. 2009, ApJ, 700, 1299

Jenkins, E. B. & Meloy, D. A. 1974, ApJ, 193, L121

Jiménez-Escobar, A. & Muñoz Caro, G. M. 2011, A&A, 536, A91

Jiménez-Serra, I., Vasyunin, A. I., Caselli, P., et al. 2016, ApJ, 830, L6

Johnson, B. R. 1987, J. Chem. Phys., 86, 1445

Jørgensen, J. K., Harvey, P. M., Evans, II, N. J., et al. 2006, ApJ, 645, 1246

Jørgensen, J. K., Schöier, F. L., & van Dishoeck, E. F. 2005, A&A, 435, 177

Jourdain, J. L., Bras, G. L., & Combourieu, J. 1979, International Journal of Chemical Kinetics, 11, 569

Kalberla, P. M. W., Dedes, L., Kerp, J., & Haud, U. 2007, A&A, 469, 511

Kastner, J. H., Zuckerman, B., Weintraub, D. A., & Forveille, T. 1997, Science, 277, 67

Kendall, M. G. 1938, Biometrika, 30, 81

Keto, E. & Caselli, P. 2008, ApJ, 683, 238

Kim, S., Lee, C. W., Gopinathan, M., et al. 2020, ApJ, 891, 169

Kim, S.-H. & Martin, P. G. 1994, ApJ, 431, 783

Kirk, J. M., Ward-Thompson, D., Palmeirim, P., et al. 2013, MNRAS, 432, 1424

Kramer, C., Alves, J., Lada, C. J., et al. 1999, A&A, 342, 257

Krumholz, M. R., Bate, M. R., Arce, H. G., et al. 2014, in Protostars and Planets VI, ed. H. Beuther, R. S. Klessen, C. P. Dullemond, & T. Henning, 243

Krumholz, M. R., McKee, C. F., & Bland-Hawthorn, J. 2019, ARA&A, 57, 227

Kulkarni, S. R. & Heiles, C. 1987, The Atomic Component, ed. D. J. Hollenbach & J. Thronson, Harley A., Vol. 134, 87

Kwan, J. 1979, ApJ, 229, 567

Laas, J. C. & Caselli, P. 2019, A&A, 624, A108

Lada, C. J. & Wilking, B. A. 1984, ApJ, 287, 610

Laidler, K., Meiser, J., & Sanctuary, B. 2002, Physical Chemistry, Physical Chemistry (Houghton Mifflin)

Langer, W. D., Velusamy, T., & Xie, T. 1996, ApJ, 468, L41

Langevin, M. P. 1905, Annales de Chimie et de Physique, series, 5, 245

Larson, R. B. 1969, MNRAS, 145, 271

Larson, R. B. 1981, MNRAS, 194, 809

Larson, R. B. 1985, MNRAS, 214, 379

Le Bourlot, J., Le Petit, F., Pinto, C., Roueff, E., & Roy, F. 2012, A&A, 541, A76

Le Gal, R., Herbst, E., Dufour, G., et al. 2017, A&A, 605, A88

Le Gal, R., Öberg, K. I., Loomis, R. A., Pegues, J., & Bergner, J. B. 2019, ApJ, 876, 72

Le Petit, F., Nehmé, C., Le Bourlot, J., & Roueff, E. 2006, ApJS, 164, 506

Le Roy, L., Altwegg, K., Balsiger, H., et al. 2015, A&A, 583, A1

Lee, K. L. K., Loomis, R. A., Burkhardt, A. M., et al. 2021, ApJ, 908, L11

Leger, A. 1983, A&A, 123, 271

Lequeux, J. 2005, The Interstellar Medium

Lin, S.-J., Pagani, L., Lai, S.-P., Lefèvre, C., & Lique, F. 2020, A&A, 635, A188

Linsky, J. L. 2003, Space Sci. Rev., 106, 49

Lippok, N., Launhardt, R., Semenov, D., et al. 2013, A&A, 560, A41

Lique, F., Cernicharo, J., & Cox, P. 2006a, ApJ, 653, 1342

Lique, F. & Spielfiedel, A. 2007, A&A, 462, 1179

Lique, F., Spielfiedel, A., & Cernicharo, J. 2006b, A&A, 451, 1125

Lis, D. C., Roueff, E., Gerin, M., et al. 2002, ApJ, 571, L55

Liszt, H., Gerin, M., Beasley, A., & Pety, J. 2018, ApJ, 856, 151

Liszt, H. & Lucas, R. 1996, A&A, 314, 917

Liszt, H. & Lucas, R. 2001, A&A, 370, 576

Liszt, H. S. & Ziurys, L. M. 2012, ApJ, 747, 55

Loison, J.-C., Wakelam, V., Gratier, P., et al. 2019, MNRAS, 485, 5777

Loison, J.-C., Wakelam, V., & Hickson, K. M. 2014, MNRAS, 443, 398

Lucas, R. & Liszt, H. 1998, A&A, 337, 246

Lucas, R. & Liszt, H. S. 2002, A&A, 384, 1054

Lynden-Bell, D. 1966, The Observatory, 86, 57

Majumdar, L., Gratier, P., Ruaud, M., et al. 2017, MNRAS, 466, 4470

Malinen, J., Juvela, M., Rawlings, M. G., et al. 2012, A&A, 544, A50

Mangum, J. G., Plambeck, R. L., & Wootten, A. 1991, ApJ, 369, 169

Marcelino, N., Cernicharo, J., Roueff, E., Gerin, M., & Mauersberger, R. 2005, ApJ, 620, 308

Marcelino, N., Cernicharo, J., Tercero, B., & Roueff, E. 2009, ApJ, 690, L27

Marcelino, N., Gerin, M., Cernicharo, J., et al. 2018, A&A, 620, A80

Maret, S., Bergin, E. A., & Tafalla, M. 2013, A&A, 559, A53

Martin-Pintado, J., Bachiller, R., & Fuente, A. 1992, A&A, 254, 315

Mayo Greenberg, J. 1982, Dust in dense clouds: one stage in a cycle., 261–306

McCall, B. J. 2001, PhD thesis, Department of Chemistry and Department of Astronomy and Astrophysics, University of Chicago, 5735 S. Ellis Ave., Chicago, IL 60637

McCall, B. J., Geballe, T. R., Hinkle, K. H., & Oka, T. 1998, in Bulletin of the American Astronomical Society, Vol. 30, American Astronomical Society Meeting Abstracts, 1340

McCammon, D. & Sanders, W. T. 1990, Annual Review of Astronomy and Astrophysics, 28, 657

McGuire, B. A., Burkhardt, A. M., Loomis, R. A., et al. 2020, ApJ, 900, L10

McKee, C. F. 1989, ApJ, 345, 782

McKee, C. F. & Ostriker, J. P. 1977, ApJ, 218, 148

McKee, C. F. & Tan, J. C. 2002, Nature, 416, 59

McKellar, A. 1940, PASP, 52, 187

Mebold, U. & Hills, D. L. 1975, A&A, 42, 187

Miettinen, O. & Offner, S. S. R. 2013, A&A, 555, A41

Mihalas, D. 1978, Stellar atmospheres

Millar, T. J., Adams, N. G., Smith, D., Lindinger, W., & Villinger, H. 1986, MNRAS, 221, 673

Millar, T. J., Bennett, A., & Herbst, E. 1989, ApJ, 340, 906

Millar, T. J., Roueff, E., Charnley, S. B., & Rodgers, S. D. 1995, International Journal of Mass Spectrometry and Ion Processes, 149, 389

Minh, Y. C., Ziurys, L. M., Irvine, W. M., & McGonagle, D. 1991, ApJ, 366, 192

Minissale, M. & Dulieu, F. 2014, Journal of Chemical Physics, 141, 014304

Minissale, M., Dulieu, F., Cazaux, S., & Hocuk, S. 2016, A&A, 585, A24

Mizuno, A., Onishi, T., Yonekura, Y., et al. 1995, ApJ, 445, L161

Morris, M. & Rickard, L. J. 1982, ARA&A, 20, 517

Mouschovias, T. C. 1976, ApJ, 207, 141

Mumma, M. J. & Charnley, S. B. 2011, ARA&A, 49, 471

Mumma, M. J., Weissman, P. R., & Stern, S. A. 1993, in Protostars and Planets III, ed. E. H. Levy & J. I. Lunine, 1177

Myers, P. C. 1989, Physical Conditions in Dark Clouds, ed. G. Winnewisser & J. T. Armstrong, Vol. 331, 38

Nagai, T., Inutsuka, S.-i., & Miyama, S. M. 1998, ApJ, 506, 306

Nagy, T. & Lendvay, G. 2017, The Journal of Physical Chemistry Letters, 8, 4621, pMID: 28889751

Narayanan, G., Heyer, M. H., Brunt, C., et al. 2008, ApJS, 177, 341

Navarro-Almaida, D., Le Gal, R., Fuente, A., et al. 2020, A&A, 637, A39

Neufeld, D. A., Godard, B., Gerin, M., et al. 2015, A&A, 577, A49

Neufeld, D. A., Goicoechea, J. R., Sonnentrucker, P., et al. 2010, A&A, 521, L10

Neufeld, D. A. & Wolfire, M. G. 2017, ApJ, 845, 163

Nicastro, F., Senatore, F., Krongold, Y., Mathur, S., & Elvis, M. 2016, arXiv e-prints, arXiv:1607.08364

Oba, Y., Tomaru, T., Lamberts, T., Kouchi, A., & Watanabe, N. 2018, Nature Astronomy, 2, 228

Öberg, K. I., Bottinelli, S., Jørgensen, J. K., & van Dishoeck, E. F. 2010, ApJ, 716, 825

Öberg, K. I., Guzmán, V. V., Furuya, K., et al. 2015, Nature, 520, 198

Öberg, K. I., van Dishoeck, E. F., & Linnartz, H. 2009, A&A, 496, 281

Ohishi, M. 1997, IAU Symposium, 178, 61

Ohishi, M. & Kaifu, N. 1998, Faraday Discussions, 109, 205

Oliveira, C. M., Hébrard, G., Howk, J. C., et al. 2003, ApJ, 587, 235

Onishi, T., Mizuno, A., Kawamura, A., Ogawa, H., & Fukui, Y. 1996, ApJ, 465, 815

Onishi, T., Mizuno, A., Kawamura, A., Tachihara, K., & Fukui, Y. 2002, ApJ, 575, 950

Oort, J. H. 1954, Bull. Astron. Inst. Netherlands, 12, 177

Oppenheimer, M. & Dalgarno, A. 1974, ApJ, 192, 29

Osterbrock, D. E. 1989, Astrophysics of gaseous nebulae and active galactic nuclei

Osterbrock, D. E. & Ferland, G. J. 2006, Astrophysics of gaseous nebulae and active galactic nuclei

Pacheco-Vázquez, S., Fuente, A., Baruteau, C., et al. 2016, A&A, 589, A60

Padoan, P., Cambrésy, L., & Langer, W. 2002, ApJ, 580, L57

Padoan, P., Juvela, M., Goodman, A. A., & Nordlund, Å. 2001, ApJ, 553, 227

Padovani, M., Galli, D., & Glassgold, A. E. 2009, A&A, 501, 619

Padovani, M., Hennebelle, P., & Galli, D. 2013, A&A, 560, A114

Padovani, M., Ivlev, A. V., Galli, D., & Caselli, P. 2018, A&A, 614, A111

Padovani, M., Ivlev, A. V., Galli, D., et al. 2020, Space Sci. Rev., 216, 29

Pagani, L., Bacmann, A., Cabrit, S., & Vastel, C. 2007, A&A, 467, 179

Palumbo, M. E., Tielens, A. G. G. M., & Tokunaga, A. T. 1995, ApJ, 449, 674

Parise, B., Ceccarelli, C., Tielens, A. G. G. M., et al. 2002, A&A, 393, L49

Parker, E. N. 1966, ApJ, 145, 811

Piani, L., Marrocchi, Y., Rigaudier, T., et al. 2020, Science, 369, 1110

Piétu, V., Dutrey, A., & Guilloteau, S. 2007, A&A, 467, 163

Pineda, J. E., Maury, A. J., Fuller, G. A., et al. 2012, A&A, 544, L7

Pires, W. A. D., Garrido, J. D., Nascimento, M. A. C., & Ballester, M. Y. 2014, Physical Chemistry Chemical Physics (Incorporating Faraday Transactions), 16, 12793

Poglitsch, A., Waelkens, C., Geis, N., et al. 2010, A&A, 518, L2

Prasad, S. S. & Tarafdar, S. P. 1983, ApJ, 267, 603

Priestley, F. D., Viti, S., & Williams, D. A. 2018, The Astronomical Journal, 156, 51

Qi, C., Wilner, D. J., Aikawa, Y., Blake, G. A., & Hogerheijde, M. R. 2008, ApJ, 681, 1396

Qu, C. & Bowman, J. M. 2016, The Journal of Physical Chemistry A, 120, 4988, pMID: 26881845

Rawlings, J. M. C., Hartquist, T. W., Menten, K. M., & Williams, D. A. 1992, MNRAS, 255, 471

Reboussin, L., Wakelam, V., Guilloteau, S., & Hersant, F. 2014, MNRAS, 440, 3557

Redaelli, E., Bizzocchi, L., Caselli, P., et al. 2019, A&A, 629, A15

Rivière-Marichalar, P., Fuente, A., Goicoechea, J. R., et al. 2019, A&A, 628, A16

Rivière-Marichalar, P., Fuente, A., Le Gal, R., et al. 2021, A&A, 652, A46

Riviere-Marichalar, P., Ménard, F., Thi, W. F., et al. 2012, A&A, 538, L3

Rivilla, V. M., Jiménez-Serra, I., Zeng, S., et al. 2018, MNRAS, 475, L30

Roberts, J. F., Rawlings, J. M. C., Viti, S., & Williams, D. A. 2007, MNRAS, 382, 733

Roshi, D. A., Goss, W. M., & Jeyakumar, S. 2014, ApJ, 793, 83

Roueff, E., Loison, J. C., & Hickson, K. M. 2015, A&A, 576, A99

Roueff, E., Parise, B., & Herbst, E. 2007, A&A, 464, 245

Roueff, E., Ruaud, M., Le Petit, F., Godard, B., & Le Bourlot, J. 2014, in IAU Symposium, Vol. 297, The Diffuse Interstellar Bands, ed. J. Cami & N. L. J. Cox, 311–320

Ruaud, M., Wakelam, V., & Hersant, F. 2016, MNRAS, 459, 3756

Sanders, W. T., Boldt, E. A., Brickhouse, N. S., et al. 1998, Astronomische Nachrichten, 319, 151

Sandford, S. A. & Allamandola, L. J. 1988, Icarus, 76, 201

Sandford, S. A. & Allamandola, L. J. 1990a, ApJ, 355, 357

Sandford, S. A. & Allamandola, L. J. 1990b, Icarus, 87, 188

Sandford, S. A. & Allamandola, L. J. 1993, ApJ, 417, 815

Savage, B. D. & Sembach, K. R. 1996, ARA&A, 34, 279

Schnee, S., Caselli, P., Goodman, A., et al. 2007, ApJ, 671, 1839

Schnee, S., Enoch, M., Noriega-Crespo, A., et al. 2010, ApJ, 708, 127

Schnee, S. & Goodman, A. 2005, ApJ, 624, 254

Scoville, N. Z., Solomon, P. M., & Sanders, D. B. 1979, in The Large-Scale Characteristics of the Galaxy, ed. W. B. Burton, Vol. 84, 277

Semenov, D., Favre, C., Fedele, D., et al. 2018, A&A, 617, A28

Semenov, D., Hersant, F., Wakelam, V., et al. 2010, A&A, 522, A42

Shen, C. J., Greenberg, J. M., Schutte, W. A., & van Dishoeck, E. F. 2004, A&A, 415, 203

Shetty, R., Glover, S. C., Dullemond, C. P., & Klessen, R. S. 2011a, MNRAS, 412, 1686

Shetty, R., Glover, S. C., Dullemond, C. P., et al. 2011b, MNRAS, 415, 3253

Sipilä, O. & Caselli, P. 2018, A&A, 615, A15

Sipilä, O., Caselli, P., & Harju, J. 2015, A&A, 578, A55

Sipilä, O., Caselli, P., & Harju, J. 2019, A&A, 631, A63

Sipilä, O., Hugo, E., Harju, J., et al. 2010, A&A, 509, A98

Smith, I. 2013, Kinetics and Dynamics of Elementary Gas Reactions: Butterworths Monographs in Chemistry and Chemical Engineering (Elsevier Science)

Snow, T. P. & McCall, B. J. 2006, ARA&A, 44, 367

Sobolev, V. V. 1960, Moving envelopes of stars

Spezzano, S., Brünken, S., Schilke, P., et al. 2013, ApJ, 769, L19

Spitzer, Lyman, J. 1956, ApJ, 124, 20

Spitzer, Lyman, J. 1968, Dynamics of Interstellar Matter and the Formation of Stars, ed. B. M. Middlehurst & L. H. Aller, 1

Spitzer, L. 1978, Physical processes in the interstellar medium

Stecher, T. P. & Williams, D. A. 1967, ApJ, 149, L29

Strömgren, B. 1939, ApJ, 89, 526

Struve, O. & Elvey, C. T. 1938, ApJ, 88, 364

Sugimura, M., Yamaguchi, T., Sakai, T., et al. 2011, PASJ, 63, 459

Swift, J. J., Welch, W. J., & Di Francesco, J. 2005, ApJ, 620, 823

Swings, P. & Rosenfeld, L. 1937, ApJ, 86, 483

Tafalla, M., Myers, P. C., Caselli, P., & Walmsley, C. M. 2004, A&A, 416, 191

Tafalla, M., Myers, P. C., Caselli, P., Walmsley, C. M., & Comito, C. 2002, The Astrophysical Journal, 569, 815

Taquet, V., Ceccarelli, C., & Kahane, C. 2012, ApJ, 748, L3

Tielens, A. G. G. M. 1983, A&A, 119, 177

Tielens, A. G. G. M. 2005, The Physics and Chemistry of the Interstellar Medium

Tielens, A. G. G. M. & Allamandola, L. J. 1987, Composition, Structure, and Chemistry of Interstellar Dust, ed. D. J. Hollenbach & J. Thronson, Harley A., Vol. 134, 397

Tielens, A. G. G. M. & Hagen, W. 1982, A&A, 114, 245

Tóth, L. V., Haas, M., Lemke, D., Mattila, K., & Onishi, T. 2004, A&A, 420, 533

Turner, B. E. 1990, ApJ, 362, L29

Turner, B. E. 2001, ApJS, 136, 579

Umebayashi, T. & Nakano, T. 1981, PASJ, 33, 617

Ungerechts, H. & Thaddeus, P. 1987, ApJS, 63, 645

van der Tak, F. F. S., Black, J. H., Schöier, F. L., Jansen, D. J., & van Dishoeck, E. F. 2007, A&A, 468, 627

van Dishoeck, E. F. 1987, in Astrochemistry, ed. M. S. Vardya & S. P. Tarafdar, Vol. 120, 51–65

van Dishoeck, E. F. & Blake, G. A. 1998, ARA&A, 36, 317

van Dishoeck, E. F., Thi, W. F., & van Zadelhoff, G. J. 2003, A&A, 400, L1

Vastel, C., Ceccarelli, C., Lefloch, B., & Bachiller, R. 2014, ApJ, 795, L2

Vastel, C., Quénard, D., Le Gal, R., et al. 2018, MNRAS, 478, 5514

Vasyunin, A. I., Caselli, P., Dulieu, F., & Jiménez-Serra, I. 2017, ApJ, 842, 33

Vasyunin, A. I. & Herbst, E. 2013, ApJ, 769, 34

Vázquez-Semadeni, E., Gazol, A., & Scalo, J. 2000, ApJ, 540, 271

Vicente, S. M. & Alves, J. 2005, A&A, 441, 195

Vidal, T. H. G., Loison, J.-C., Jaziri, A. Y., et al. 2017, MNRAS, 469, 435

Wakelam, V., Castets, A., Ceccarelli, C., et al. 2004, A&A, 413, 609

Wakelam, V., Loison, J. C., Mereau, R., & Ruaud, M. 2017, Molecular Astrophysics, 6, 22

Walmsley, C. M. 1992, in Chemistry and Spectroscopy of Interstellar Molecules, ed. D. K. Bohme, 267

Ward-Thompson, D. 1996, Ap&SS, 239, 151

Watanabe, N., Kimura, Y., Kouchi, A., et al. 2010, ApJ, 714, L233

Watanabe, N. & Kouchi, A. 2002, ApJ, 571, L173

Whittet, D. C. B., Cook, A. M., Herbst, E., Chiar, J. E., & Shenoy, S. S. 2011, ApJ, 742, 28

Williams, D. A. 2005, in Journal of Physics Conference Series, Vol. 6, Journal of Physics Conference Series, 1–17

Wilson, T. L. & Rood, R. 1994, ARA&A, 32, 191

Wolfire, M. G., Hollenbach, D., McKee, C. F., Tielens, A. G. G. M., & Bakes, E. L. O. 1995, ApJ, 443, 152

Wolfire, M. G., McKee, C. F., Hollenbach, D., & Tielens, A. G. G. M. 2003, ApJ, 587, 278

Yamamoto, S. 2017, Introduction to Astrochemistry: Chemical Evolution from Interstellar Clouds to Star and Planet Formation

Yang, B., Stancil, P. C., Balakrishnan, N., & Forrey, R. C. 2010, ApJ, 718, 1062

Zanchet, A., del Mazo, P., Aguado, A., et al. 2018, Physical Chemistry Chemical Physics (Incorporating Faraday Transactions), 20, 5415

Zari, E., Lombardi, M., Alves, J., Lada, C. J., & Bouy, H. 2016, A&A, 587, A106

Zhao, B., Caselli, P., Li, Z.-Y., et al. 2016, MNRAS, 460, 2050

Zhou, S., Evans, Neal J., I., Koempe, C., & Walmsley, C. M. 1993, ApJ, 404, 232

Zubko, V., Dwek, E., & Arendt, R. G. 2004, ApJS, 152, 211

Zucconi, A., Walmsley, C. M., & Galli, D. 2001, A&A, 376, 650